

---

# Light Propagation and Many-Particle Effects in Semiconductor Nanostructures

---

vorgelegt von Diplom-Physiker

**Jens Förstner**

aus Berlin

Fakultät II - Mathematik und Naturwissenschaften  
der Technischen Universität Berlin

zur Erlangung des akademischen Grades

Dr. rer. nat.

genehmigte Dissertation

Tag der mündlichen Aussprache: 2.9.2004

Promotionsausschuss:

Vorsitzender: Prof. Dr. rer. nat M. Dähne

1. Gutachter: Prof. Dr. rer. nat A. Knorr

2. Gutachter: Prof. Dr. rer. nat. E. Schöll

Berlin 2005

D 83



---

# Light Propagation and Many-Particle Effects in Semiconductor Nanostructures

---

vorgelegt von Diplom-Physiker

**Jens Förstner**

aus Berlin

Fakultät II - Mathematik und Naturwissenschaften  
der Technischen Universität Berlin

zur Erlangung des akademischen Grades

Dr. rer. nat.

genehmigte Dissertation

Tag der mündlichen Aussprache: 2.9.2004

Promotionsausschuss:

Vorsitzender: Prof. Dr. rer. nat M. Dähne

1. Gutachter: Prof. Dr. rer. nat A. Knorr

2. Gutachter: Prof. Dr. rer. nat. E. Schöll

Berlin 2005

D 83



# Zusammenfassung

In dieser Arbeit wird eine Theorie vorgestellt, welche die quantenmechanische Vielteilchenphysik der Licht-Materie Wechselwirkung in Halbleiternanostrukturen beschreibt. Diese mikroskopische Beschreibung wird durch Kombination eines allgemeinen Dichtematrixansatzes mit speziellen Methoden zur Auswertung der Maxwellgleichungen wie der zeitaufgelösten Finite-Differenzen-Methode (FDTD) erreicht. Die Theorie wird auf verschiedene physikalische Situationen angewendet, wie z.B. Lichtausbreitung in Volumenhalbleitern, Interband- und Intersubbandübergänge in Quantenfilmstrukturen und optische Anregung von Quantenpunkten. Der Fokus liegt dabei auf der Beschreibung der linearen und nichtlinearen Antwort des Vielteilchensystems und seiner Ankopplung an das elektromagnetische Feld. In diesem Zusammenhang wird sowohl die Erzeugung als auch der Zerfall von optischen Anregungen untersucht, indem verschiedene Kopplungsmechanismen wie Elektron-Phonon-, Elektron-Photon- und Elektron-Elektron-Wechselwirkung berücksichtigt werden.

Im Bereich der linearen Optik, also für Anregung mit geringer Intensität, ermöglicht die Theorie die Berechnung von Absorptionsspektren. Verschiedene Effekte in linearer Optik werden in dieser Arbeit untersucht und beschrieben: Linienaufspaltung durch Polaritonen im Volumenmaterial, Zunahme der Linienbreite bei Intersubbandübergängen verursacht durch Elektron-Elektron- und Elektron-Phonon-Streuung in einzelnen Quantenfilmen, Bildung einer optischen Bandlücke durch starke radiative Kopplung in Vielfilmstrukturen in Bragg-Geometrie, Phononenseitenbänder verursacht durch quantenkinetische Effekte in einzelnen Quantenpunkten und schliesslich Superradianz und Interferenzeffekte in Quantenpunktgittern.

Bei nichtlinearer Anregung treten Dichte-Rabiflops als fundamentale Prozesse in allen betrachteten Systemen auf und können als kohärente Be- und Entvölkerung von quantenmechanischen Zuständen beobachtet werden. Der Einfluss von starker Lichtkopplung und verschiedenen Wechselwirkungen auf dynamische Größen wie die Besetzung wird untersucht. Bei nichtlinearer Propagation, bei der sich ein starker Lichtpuls über längere Strecken in einem System bewegt, wird selbstinduzierte Verstärkung der Transmission näher betrachtet. Des weiteren werden von der Coulombwechselwirkung verursachte nichtlineare Effekte wie exzitoninduziertes Dephasieren in Volumenmaterial und verschränkte Zustände in Quantenpunkten untersucht, die einen Zusammenbruch der Hartree-Fock-Näherung darstellen.

Zusammenfassend werden in dieser Arbeit verschiedene lineare und nichtlineare optische Effekte in Halbleiternanostrukturen verschiedener Dimensionalität mit Hilfe einer allgemeinen Theorie, die einen Dichtematrixansatz mit den Maxwell'schen Gleichungen kombiniert, untersucht.



# Abstract

This work presents a theory describing the quantum mechanical many-particle physics of light-matter interaction in semiconductor nanostructures. A microscopic description is achieved by combination of a general density matrix approach and special methods for the evaluation of Maxwell's equations like the Finite Differences Time Domain (FDTD) method. The theory is applied to several physical situations like propagation in bulk semiconductors, interband and intersubband transitions in semiconductor quantum well structures and optical excitation of quantum dots. The main focus lies on the description of the linear and nonlinear optical response of many-particle systems and their coupling via the electromagnetic field. In this context both the build-up and decay of optical excitation is studied by taking into account several coupling mechanisms like electron-phonon, electron-photon and electron-electron interaction.

In the linear optical regime, i.e. for low-intensity excitation, the theory allows calculation of absorption spectra. Several effects in linear optics are investigated and described in this work: Polariton splitting in bulk material, linewidth broadening of intersubband transitions due to electron-electron and electron-phonon scattering in single semiconductor quantum wells, formation of optical stop bands by strong radiative coupling of multiple quantum well structures in Bragg geometry, phonon sidebands caused by quantum kinetic effects in single quantum dots, and finally superradiance and interference effects in a quantum dot array.

In all considered systems density Rabi flopping occurs as fundamental process for nonlinear excitation and can be observed as coherent population and depopulation of quantum mechanical states. The influence of strong light-coupling and different many-particle interactions on nonlinear dynamical quantities like the population is investigated. Self-induced transmission enhancement is studied in nonlinear propagation setups, where a strong light pulse travels over long distances in a system. Furthermore nonlinear effects of the Coulomb interaction like exciton-induced dephasing in bulk material and generation of entangled states in quantum dots, which constitute a break-down of the Hartree-Fock approximation, are investigated.

In summary, several linear and nonlinear optical effects in semiconductor nanostructures of different dimensionality are explored using a general theory which combines the density matrix approach with the solution of Maxwell's equations.



# Contents

|          |  |           |
|----------|--|-----------|
| <b>1</b> | <b>Introduction</b>  | <b>13</b> |
| 1.1      | Basics . . . . .   | 13        |
| 1.2      | Structure of this work . . . . .   | 14        |
| 1.3      | Highlights . . . . .   | 15        |
| <b>2</b> | <b>Theoretical framework</b>   | <b>17</b> |
| 2.1      | Description of confinement . . . . .                                       | 18        |
| 2.2      | Hamiltonians . . . . .   | 19        |
| 2.2.1    | Electronic band structure . . . . .  | 19        |
| 2.2.2    | The quantized light field: photons . . . . .                               | 20        |
| 2.2.3    | Classical electron-field coupling . . . . .                                | 22        |
| 2.2.4    | Coulomb interaction . . . . .  | 24        |
| 2.2.5    | Lattice vibrations: phonons . . . . .                                      | 25        |
| 2.3      | The Heisenberg picture . . . . .   | 26        |
| 2.4      | Quantities of interest . . . . .   | 27        |
| 2.4.1    | Weakly inhomogeneous excitation, gradient expansion . . . . .              | 27        |
| 2.4.2    | The macroscopic polarization for weakly inhomogeneous excitation . . . . . | 28        |
| 2.5      | Hierarchy of equations . . . . .   | 29        |
| 2.6      | Bosonic baths . . . . .  | 30        |
| 2.7      | Hartree-Fock factorization . . . . .                                       | 31        |
| 2.8      | Markov approximation . . . . .   | 32        |
| 2.9      | Spontaneous emission of photons . . . . .                                  | 32        |
| <b>3</b> | <b>Maxwell equations</b>   | <b>35</b> |
| 3.1      | The macroscopic Maxwell equations . . . . .                                | 35        |
| 3.2      | Experimental observables . . . . .   | 35        |
| 3.3      | Linear response, Beer's law . . . . .                                      | 36        |
| 3.4      | The Finite Differences Time Domain method . . . . .                        | 38        |
| 3.4.1    | One-dimensional FDTD . . . . .   | 38        |
| 3.4.2    | Three-dimensional FDTD . . . . .   | 40        |
| 3.5      | The Slowly Varying Envelope Approximation . . . . .                        | 40        |
| <b>4</b> | <b>Bulk material</b>   | <b>43</b> |
| 4.1      | Nonlinear Polariton Pulse Propagation . . . . .                            | 43        |
| 4.1.1    | Introduction . . . . .   | 43        |
| 4.1.2    | Theoretical approach . . . . .   | 44        |

|          |  |            |
|----------|--|------------|
| 4.1.3    | Numerical Results and Discussion . . . . .                 | 45         |
| 4.1.4    | Experimental Results and Comparison . . . . .              | 47         |
| 4.1.5    | Hole burning within the exciton resonance . . . . .        | 47         |
| 4.2      | Hole-burning within the homogeneous linewidth . . . . .    | 53         |
| <b>5</b> | <b>Quantum wells</b>                                       | <b>57</b>  |
| 5.1      | Interband transitions in MQW Bragg structures . . . . .    | 57         |
| 5.1.1    | Material description . . . . .                             | 58         |
| 5.1.2    | Linear propagation two-level MQW structures . . . . .      | 59         |
| 5.1.3    | Nonlinear propagation two-level MQW structures . . . . .   | 61         |
| 5.1.4    | Two-band semiconductor quantum wells . . . . .             | 63         |
| 5.2      | Intersubband transitions . . . . .                         | 67         |
| 5.2.1    | Description of confinement, energetic structure . . . . .  | 68         |
| 5.2.2    | Free dynamics . . . . .                                    | 69         |
| 5.2.3    | Hartree-Fock contributions . . . . .                       | 71         |
| 5.2.4    | Electron-electron and electron-phonon scattering . . . . . | 73         |
| 5.2.5    | Quantum kinetic electron-phonon coupling . . . . .         | 75         |
| 5.2.6    | Intersubband Rabi oscillations . . . . .                   | 76         |
| <b>6</b> | <b>Quantum dots</b>  | <b>81</b>  |
| 6.1      | The Independent Boson Model . . . . .                      | 83         |
| 6.2      | Correlation expansion . . . . .                            | 90         |
| 6.3      | Rabi oscillations . . . . .                                | 91         |
| 6.4      | Convolution approach . . . . .                             | 96         |
| 6.4.1    | Nonpertubative linear solution for finite pulses . . . . . | 96         |
| 6.4.2    | Integro-differential approach . . . . .                    | 99         |
| 6.4.3    | Frequency domain approach . . . . .                        | 101        |
| 6.5      | Nonlinear detuning spectra . . . . .                       | 102        |
| 6.6      | Intradot Coulomb coupling (biexcitonic effects) . . . . .  | 104        |
| 6.7      | Interdot coupling by phonons . . . . .                     | 109        |
| 6.8      | Array of quantum dots: radiative coupling . . . . .        | 110        |
| 6.8.1    | Theoretical Background . . . . .                           | 110        |
| 6.8.2    | Linear properties . . . . .                                | 112        |
| 6.8.3    | Nonlinear properties . . . . .                             | 115        |
| <b>7</b> | <b>Conclusion and Outlook</b>                              | <b>119</b> |
| <b>A</b> | <b>Two-Level Systems</b>                                   | <b>121</b> |
| A.1      | Introduction . . . . .                                     | 121        |
| A.1.1    | The Hamiltonian . . . . .                                  | 121        |
| A.1.2    | Equations of motion . . . . .                              | 122        |
| A.1.3    | Field expansion . . . . .                                  | 122        |
| A.1.4    | The Rotating Wave Approximation . . . . .                  | 123        |
| A.2      | Rabi flopping . . . . .                                    | 124        |

---

|          |  |            |
|----------|--|------------|
| <b>B</b> | <b>Mathematical Tools</b>                                      | <b>127</b> |
| B.1      | Fourier transformation . . . . .                               | 127        |
| B.2      | Numerical methods for solving differential equations . . . . . | 128        |
| B.2.1    | Euler method . . . . .   | 128        |
| B.2.2    | Runge-Kutta method . . . . .                                   | 128        |
| <b>C</b> | <b>Equations of motion</b>                                     | <b>131</b> |
| C.1      | Markovian subband scattering rates . . . . .                   | 131        |
| C.2      | Quantum dots: correlation expansion . . . . .                  | 133        |
| C.2.1    | Coulomb interaction . . . . .                                  | 133        |
| <b>D</b> | <b>Notation, Symbols</b>                                       | <b>135</b> |
| D.1      | Notation . . . . .   | 135        |
| D.2      | Fundamental constants . . . . .                                | 135        |
| D.3      | Symbols . . . . .  | 136        |
| D.4      | Acronyms . . . . .   | 137        |
|          | <b>Bibliography</b>  | <b>139</b> |



# Chapter 1

## Introduction

### 1.1 Basics

Semiconductor optics is one of the fortunate disciplines in physics being able to bridge the gap between the basic description of nature and technological applications. Starting from the very fundamental quantum mechanical description of light and matter it is possible to derive a picture of large systems and to predict their physical behavior. Whereas the name “semiconductor” refers to the property of being either conductive or insulating depending on certain internal and external conditions (like temperature), semiconductors also exhibit a variety of optical features. These optical properties all rely on the existence of at least two energetic levels which are separated by a gap. By absorption or emission of light, electrons can be transferred from one level to another. For example, light coming from the sun can be absorbed within a solar cell by lifting an electron into a higher energetic level. This energy is absorbed by electrons and can be used as electric current to power electronic devices. The opposite process happens in light emitting diodes (LEDs) and semiconductor lasers where electrons are electrically injected into the higher energetic level. These electrons can fall into the lower level by emitting light quanta which can be observed subsequently.

While early semiconductor samples were homogeneous and unstructured pieces consisting of only one material type, technological process has made it possible to manufacture semiconductor heterostructures which are composed of several different material types arranged in complex structure. In nanostructures, which can generally also contain other materials like metal, this structuring is possible down to the nanometer scale today. On this scale the physical laws known from everyday experience break down and are replaced by quantum mechanics. The most prominent example is the quantum well which consists of a thin layer of a material with a lower energy gap than its surrounding. Due to quantum confinement electrons are trapped in this layer and can only move freely in the plane of the layer, effectively forming a two-dimensional electron gas. The properties emerging from this quantum confinement, like enhancement of the density of states, are exploited in most commercial semiconductor lasers. The possibility to design many optical and electric properties of such structures is utilized in perfection in the so-called quantum cascade lasers. These structures consist of many active layers in which transitions between the quantum confined states (subbands) are used. In a next step, the motion of electrons can be further constrained by adding barrier material in the remaining directions. If the motion is confined to one dimension one obtains a quantum wire. For complete confinement in all three dimension one speaks of quantum dots. Like atomic systems quantum dots have a discrete energy level structure and are therefore in principle candidates for storage and processing of qubits – the fundamental constituent of quantum computers.

This work presents a theory describing the linear and nonlinear optical properties of these semiconductor nanostructures. The theory is microscopic in the sense that it is based on the fundamental laws of quantum mechanics without relying on phenomenologic models. As application of the theory several examples of nanostructures like quantum dots, quantum wells and bulk material are investigated in detail.

## 1.2 Structure of this work

The theory used in this work is based on a combination of a general density matrix approach with Maxwell's equation. The density matrix formalism has been proven to be a powerful tool for the description of optical and transport processes in solid state materials [1, 2]. In the second quantization picture all known interactions can be intuitively expressed via quasi particle creation and destruction operators. The density matrix theory presented in the first chapter is flexible with respect to the confinement following an approach by Kuhn [1]. This also applies to the relevant Hamiltonians. This work covers the electronic band structure, the classical and quantized electron-light coupling, the Coulomb interaction between carriers and the electron-phonon coupling. By using a special confinement notation and proper integrating of the confinement wave functions into coupling elements the derivation of the Hamiltonians can be performed analogous to bulk material [3, 4]. It is therefore only sketched in section 2.2 presenting the emerging Hamiltonians and briefly reciting the underlying assumptions and approximations. A discussion of the quantities relevant for semiconductors optics is followed by several sections which outline the derivation of equations of motion for a given Hamiltonian. Methods like the bath and Markov approximations are presented and in exemplary applied to the problem of radiative decay by spontaneous emission of photons.

Investigating optical effects, the microscopic material model has to be combined with a description of the electromagnetic field. The usage of several special analytic and numeric methods allows evaluation of the Maxwell equations as presented in chapter 3. In linear optics the Maxwell equations can be solved by a plane wave approach based on a linear absorption function which is related to the linear susceptibility  $\chi$ . For nonlinear optics numerical evaluation in time domain is preferable. For a short overview the Finite Differences Time Domain method for one and three dimensions and the Slowly Varying Envelope Approximation used for unidirectional propagation are presented.

Application of the theory to various semiconductor structures is given in the chapters 4-6, starting with unconfined optically excited electron dynamics in bulk material in chapter 4. First, nonlinear polariton propagation which is affected by excitation induced dephasing is studied in semiconductor volume material in section 4.1. The theory is based on a dynamically controlled truncation scheme which includes all effects scaling cubically with the exciting light field and is therefore well suited for the intermediate nonlinear optical regime. Comparison to experiments shows good agreement. Nonlinear propagation in this regime leads to formation of the polaritons with a special phase shape which induces a novel wave-mixing effect in the material leading to lineshape narrowing and hole-burning in the homogeneous line. This effect is further studied in an extended ensemble consisting of two-level systems in section 4.2 by numerical and analytical means.

Chapter 5 considers systems with one-dimensional confinement. Section 5.1 deals with intersubband transitions in structures consisting of multiple equally spaced quantum wells. The structure's dynamics is strongly coined by the electron-light interaction, specifically, formation of a linear band gap and nonlinear self-induced transmission are explored. Additionally, a stationary solution which allows to capture light and optical excitation in the structure is discussed within a simplified two-level model. In section 5.2 transitions between subbands emerging from quantum confinement splitting

of the conduction band are investigated. The subbands have similar curvature leading to interesting properties not known from interband transitions. To calculate absorption spectra for these systems both electron-electron and electron-phonon interaction is included in a second order Born approach. The electron-phonon interaction is further studied beyond the Markov approximation. Further, the phonon-induced damping of subband Rabi-flopping is simulated.

The subject of the final chapter 6 are confinement-dominated quantum dots which constitute the main focus of the conducted work. In these quantum dots free motion is impossible leading to a discrete energy level structure. Beyond strict energy conservation, quantum kinetic intralevel scattering processes with phonons are possible. This non-Markovian electron-phonon coupling is investigated in detail using different methods. After a brief discussion of the independent Boson model (in section 6.1), which allows analytical summation of the complete electron-phonon hierarchy in linear optics, a correlation expansion approach, which additionally allows nonlinear excitation, is presented in section 6.2. The theory is used to simulate nonlinear effects like phonon-induced damping of Rabi flopping (in section 6.3). One finds that the system exhibits a reduced dephasing during nonlinear excitation if pulses of increased duration are used. This is in contrast to most known dephasing processes. After a short discussion of a nonperturbative approach for the nonlinear excitation regime (in section 6.4), the systems response for off-resonant excitation is studied (in section 6.5). By systematic variation of the pulse detuning and intensity one can obtain detailed information of the underlying electron-phonon coupling. Finally, section 6.8 considers the light-matter coupling in an ensemble of quantum dots arranged in a two-dimensional grid. The linear properties of this system, like e.g. the radiative decay, are strongly coined by interference effects between the dots. In the nonlinear excitation regime situations are investigated in which the polarization-driven dephasing is suppressed. This leads to conservation of optical excitation over long times.

Several appendices have been added to provide additional information. Appendix A describes the dynamics encountered in two- and many-level systems. The physics of two-level systems is frequently used in this work for discussions of the similarities and differences in comparison with semiconductors, because most of the fundamental linear and nonlinear effects (like e.g. Rabi oscillations) can be studied analytically in this model system. Some approximation repeatedly used in this work, like the rotating wave approximation, are explained there. Appendix B lists common mathematical knowledge relevant for this work like some properties of Fourier transformations and methods for solving differential equations. Of the appendices, only appendix C provides original content by listing several equations which were considered to be too extensive for inclusion in the main text. Finally, the last appendix gives a list of frequently used symbols and abbreviations.

## 1.3 Highlights

While I personally consider every topic in this work to be interesting, there are certainly several highlights. They all have in common that they exhibit features of the underlying theory which were initially unexpected and needed a detailed analysis before they could be understood.

Definitely one of those highlights is the capturing of light and optical excitation in multiple quantum well structures as considered in section 5.1.3. The self-evolving stationary solution can be understood by a balanced interplay of the material and Maxwell equations.

A similar effect but with different explanation is seen in quantum dot arrays arranged on an ordered grid (section 6.8). In linear optics, a dense array exhibits very strong damping due to radiative coupling. However, if the quantum dots are completely inverted by excitation with a short nonlinear pulse, this radiative dephasing is completely suppressed and the optical excitation is stored without

decaying. Using a subsequent pulse (of lower intensity) the stored energy can be released.

Likewise unexpected but explainable is the reduction of phonon-induced dephasing in semiconductor quantum dots when applying pulses of increased duration (section 6.3). This is in contrast to usual many-particle induced dephasing and has strong impact for the usability of quantum dots for quantum information processing.

Despite the fact that propagation in volume material, including atomic vapor, has been subject of both intensive experimental and theoretical research during the last decades, there are still novel features to discover. Section 4.2 describes a nonlinear wave-mixing effect which leads to lineshape narrowing and even hole-burning within the homogeneous line, an effect previously unknown.

## Chapter 2

# Theoretical framework

One of the most fundamental properties of quantum theory concerning many particle systems is the indistinguishability of identical particles. As direct consequence one obtains symmetry properties which lead to the particle classes of bosons and fermions. Second quantization provides an elegant framework to maintain the symmetry constraints while also giving the intuitive particle creation and annihilation operators.

The individual Hamiltonians which describe effects like e.g. the coupling of electrons to photons in second quantization can be derived from an appropriate Lagrangian describing the physical situation in a semiconductor. This derivation is only sketched here as it can be found in several textbooks on semiconductor many-particle theory [3, 4]. Thus, the main purpose of this chapter is to recapitulate the needed assumptions and approximations. Additionally, the derivation is generalized to semiconductors heterostructures in which the electrons can be quantum confined in an arbitrary number of dimensions. Following an approach similar to Ref. [1] it is then possible to derive Hamiltonians which are simultaneously valid for bulk material, quantum wells, quantum wires and quantum dots. This allow to use the same Hamiltonians in the very different systems which are considered in this work.

First the Lagrangian describing the semiconductor physics by embracing all relevant particles and interactions has to be proposed. On the interatomic scale solely the electromagnetic interaction is relevant. The strong and weak forces only play a role on the atomic nuclei level. It is assumed that the nucleus problem can be decoupled from the atomic and interatomic layer and that it is already solved. Gravitation is a very weak force, hence only relevant between macroscopic objects. Consequently it is not included. By extending the kinetic energies  $\frac{p_i^2}{2m_i}$  of charged particles with electromagnetic quantities under the constraint of gauge invariance one can express the complete quantum mechanical description of charged matter and light as a simple and elegant many-body Hamiltonian ([4] p.11):

$$H = \sum_i \frac{1}{2m_i} (\mathbf{p}_i - e_0 Z_i \mathbf{A}(\mathbf{r}_i))^2 + \frac{\epsilon_0}{2} \int d^3r (\mathbf{E}^2 + c_0^2 \mathbf{B}^2). \quad (2.1)$$

The sum runs over all nuclei and electrons,  $m_i$  are the masses and  $Z_i$  the charges of the particles. As electromagnetic quantities the vector potential  $\mathbf{A}$ , the electric field  $\mathbf{E}$  and the magnetic field  $\mathbf{B}$  enter the equation. Additionally the (vacuum) velocity of light  $c_0$ , the permittivity of free space  $\epsilon_0$  and the (positive defined) elementary charge  $e_0$  occur as fundamental constants. Knowing that not even the Kepler problem is solvable for more than two particles it is not surprising that despite its elegance no general analytical solution is known to the Schrödinger problem connected to the Hamiltonian from in Eq. 2.1. Direct numerical evaluation is only possible for a set of very few particles and gets

infeasible for larger problems like a solid state crystal. Also, very few sensible approximations are possible without further assumptions at this level. Therefore the complete problem is divided into smaller more manageable parts.

As a first step one can apply the Coulomb gauge which separates the electromagnetic fields into longitudinal and transversal contributions. The longitudinal part can be written as an instantaneous Coulomb potential which describes interaction between two charged particles. The remaining transversal part cannot be expressed as such a carrier-carrier interaction without introducing further particles or fields. Therefore it has to be described either classically using Maxwell equations or in second quantization leading to the photon particle. Assuming that the ion problem, i.e. the description of the atomic nucleus with the inner electrons, has already been solved, only ions and electrons are left as fundamental particles. The longitudinal Coulomb force can then be divided into ion-ion, ion-electron and electron-electron contributions, and following the Born-Oppenheimer approximation the ion motion can be decoupled from the electron dynamics in first order. It is plausible to assume that crystalline semiconductors which are exclusively considered in this work have an equilibrium structure which can be calculated by energy minimization. There are several methods to solve this problem[5]. Relevant for this work is the possibility to (at least approximatively) obtain an energy band structure and a periodic potential for single electrons. In heterogeneous material structures, it is assumed for simplicity that the existence of different materials does not completely disturb the periodicity but only leads to an additional barrier potential. If the potential exhibits a minimum, it can confine electrons into a small spatial area in that dimension. But even in the unconfined directions the electrons can not move unaffected from the ion-electron interaction. Nevertheless it is possible for periodic potentials to introduce a new fermionic quasi-particle called Bloch electron with properties similar to an electron, as the Bloch theorem shows[6].

To describe effects beyond the static lattice limit it is promising to perform a Taylor expansion of the effective ion-ion coupling potential around its energetic minimum. In the lowest relevant (second) order, this leads to harmonic oscillations of the ions contributing to collective modes of the crystal which can then be quantized leading to the bosonic phonon quasi-particle. Consequently, expansion of the effective ion-ion potential beyond the second order gives rise to interaction between these phonons.

The interaction between electrons and the (transversal) electromagnetic field can be treated in two ways: In the classical limit the field enters the Hamiltonian as time-dependent external potential, mostly within dipole approximation. The field dynamics is then determined by Maxwell's equations (also derivable from the above Hamiltonian), which are recursively coupled to the material via macroscopic polarizations, currents and charge imbalances. The full quantum optical description is obtained via field quantization of the electromagnetic potentials into bosonic photon modes and also covers incoherent light fields, which cannot consistently be described within Maxwell's equations.

After a short overview on the used notation, the different parts of the Hamiltonian in second quantization are presented in section 2.2. Subsequently, the different methods for handling the infinite hierarchy of differential equations, which emerges from application of the Heisenberg equation to the many-body problem, will be discussed.

## 2.1 Description of confinement

Since structures with confinement of different dimensions are considered in this work a notation is used which is flexible with respect to the number of confinement dimensions (roughly following Ref. [1]): First, spatial coordinates are split into free (f) and confined directions (c):  $\mathbf{r} = (\mathbf{r}_f, \mathbf{r}_c)$ . It is

assumed that the electrons are strongly localized disallowing free motion in the confined directions. Therefore also the wave vector has no components in these directions. Instead the band splits into subbands due to the confinement. Electron wave number vectors with reduced dimensionality, are denoted by the character  $\mathbf{k}$  while three-dimensional wave vectors, which are needed for unconfined particles like phonons or photons are denoted as  $\mathbf{q}$  and can be decomposed according to  $\mathbf{q} = (\mathbf{q}_f, \mathbf{q}_c)$ . The exact notation for band and subband indices depends on the special case. In general a compound index which includes the band ( $\bar{i}$ ), subband ( $\lambda_i$ ) and spin ( $s_i$ ) is used and denoted  $i = (\bar{i}, \lambda_i, s_i)$ . Accordingly “electron in band  $i$ ” in fact means: “Bloch electron in band  $\bar{i}$ , subband  $\lambda_i$ , spin  $s_i$ ”. For an even more compact notation the wave vector is sometimes combined with the other indices in a single compound index:  $1 = (\bar{1}, \lambda_1, s_1, \mathbf{k}_1)$ .

Not considered in this work are any effects that occur due to the existence of surfaces in the free directions. It is assumed that in these dimensions the considered material can be described using the Born-van-Karman assumption (cyclic boundary conditions).

## 2.2 Hamiltonians

### 2.2.1 Electronic band structure

In a first step the ion-ion and ion-electron coupling is considered. Following the Born-Oppenheimer approach one can decouple the fast electronic from the slow ion motion. On a slow timescale the ions form a crystal lattice structure at their equilibrium positions. Motion of ions around these equilibrium positions is described within the phonon picture as presented in section 2.2.5. In a first step the ions are assumed to be fixed and to provide a periodic static background potential for the electrons. Calculation of the energy dispersion alone can already be arbitrarily complex for real materials, thus one must either use numerical techniques or reduce the structure to an analytically solvable case (e.g. tight binding approximation, Kronig-Penney model). All methods have in common that they use the periodicity of the crystal lattice and by that allow application of the Bloch theorem for the description of the electronic wave functions.

Assuming that this periodicity is also partly valid for heterostructures, where the presence of different but similar materials is expected to give only an additional barrier potential  $U(\mathbf{r}_c)$  limiting the motion of the electrons to the unconfined directions. Considering only confined states and using the above notation the general electronic wave function in second quantization can be written as<sup>1</sup>:

$$\psi(\mathbf{r}) = \frac{1}{\sqrt{V_f}} \sum_{i,\mathbf{k}} e^{i\mathbf{k}\cdot\mathbf{r}_f} \phi_i(\mathbf{r}_c) u_{\bar{i}}(\mathbf{r}) a_{i,\mathbf{k}}.$$

Here the annihilation operator  $a_{i,\mathbf{k}}$  of an Bloch electron with (reduced) wave vector  $\mathbf{k}$  in band  $i$  is introduced.  $u_{\bar{i}}(\mathbf{r})$  are the lattice-periodic Bloch functions (obeying  $\int_{V_{ec}} d^3r u_{\bar{i}}^*(\mathbf{r}) u_{\bar{j}}(\mathbf{r}) = V_{ec} \delta_{\bar{i},\bar{j}}$  with  $V_{ec}$  being the volume of an elementary cell). The electronic envelope functions  $\phi(\mathbf{r}_c)$  are the solutions to the Schrödinger problem for the confinement potential  $U_{\bar{i}}(\mathbf{r}_c)$ . They are orthonormal with respect to the subband index within the same band, i.e.  $\int d\mathbf{r}_c \phi_{i,\lambda,s}^*(\mathbf{r}_c) \phi_{i,\lambda',s'}(\mathbf{r}_c) = \delta_{\lambda,\lambda'} \delta_{s,s'}$ .  $V_f$  is given by the extensions of the crystal in the direction of free motion (periodicity according to Born-van-Karman approach is used) and can be eliminated by transition from sums over the quasi-continuous wave vector to integrals. With these definitions  $\psi(\mathbf{r})$  itself is normalized to 1.

<sup>1</sup>some notational notes: Operators are not specially marked by a symbol (like  $\hat{\phantom{a}}$ ) but should be identifiable from their definition or context. Vectors, with the exception of indices, are specially marked (e.g.  $\mathbf{v}$ ), so are tensors (e.g.  $\underline{\mathbf{Z}}$ ). Temporal derivatives are sometimes written as  $\partial_t x(t)$  or  $\dot{x}$ . The commutator for two operators  $A, B$  is defined as  $[A, B] = [A, B]_- = AB - BA$  and the anti commutator (for fermions) as  $[A, B]_+ = AB + BA$ .

The Bloch electrons are fermionic and therefore obey the anticommutator relation:

$$[a_{i,\mathbf{k}}, a_{i',\mathbf{k}'}^+]_+ = \delta_{i,i'} \delta_{\mathbf{k},\mathbf{k}'}. \quad (2.2)$$

The second-quantization Hamiltonian arising from the coupling of the electrons to the static lattice can always be diagonalized since it does not involve direct interaction with other particles. Hence the resulting Hamiltonian simply sums up the electronic number operators weighted by the respective single particle energies  $\varepsilon_{i\mathbf{k}}$ :

$$H_{0e} = \sum_{i,\mathbf{k}} \varepsilon_{i,\mathbf{k}} a_{i\mathbf{k}}^+ a_{i\mathbf{k}}. \quad (2.3)$$

This work only considers direct semiconductor materials where the absolute maxima and minima of the optically relevant valence and conduction bands are located around the  $\Gamma$ -point. The energies  $\varepsilon_{i\mathbf{k}}$  can therefore be expanded into Taylor series in  $\mathbf{k}$  around 0 with a vanishing linear term. In most cases it is sufficient to truncate the series after the quadratic term leading to a parabolic dispersion resembling the free particle kinetic energy (with a possible negative effective mass  $\tilde{m}$ ) plus an energy offset  $\varepsilon_{i0}$ :

$$\varepsilon_{i\mathbf{k}} = \varepsilon_{i0} + \frac{\hbar^2 k^2}{2\tilde{m}_i}. \quad (2.4)$$

The energy offset  $\varepsilon_{i0}$  consists of material-specific band energies plus a confinement energy offset for each subband. In order to induce optical transitions between two states, the frequency of the exciting electric field must be comparable to the frequency difference of these states. As known from the derivation of Fermi's Golden rule this energy selection is not strict for finite times. But, if the probability of transitions into a band is sufficiently small due to strongly mismatching energies and no processes contribute to electron transfer from or to other bands, it is plausible to only consider bands with strong, i.e. roughly resonantly excited transitions. Hence, usually only a strongly reduced band structure has to be taken into account.

### 2.2.2 The quantized light field: photons

Starting from Eq. 2.1 the transversal part of the electromagnetic interaction with Bloch electrons can be described in second quantization. For this the vector potential  $\mathbf{A}$  (being transversal in the used Coulomb gauge) is expanded into plane wave modes ([4] p.19, [7] p.199):

$$\mathbf{A}(\mathbf{r}, t) = \sum_{\lambda\mathbf{q}} \sqrt{\frac{\hbar}{2\varepsilon_0\omega_{\mathbf{q}}V}} \varepsilon_{\lambda\mathbf{q}} \left( c_{\lambda\mathbf{q}}(t) + c_{\lambda,-\mathbf{q}}^+(t) \right) e^{i\mathbf{q}\cdot\mathbf{r}}.$$

Here, the dispersion  $\omega_{\mathbf{q}} = c_0 |\mathbf{q}|$  of light has been introduced. The index  $\lambda$  runs over the two orthogonal transversal modes with polarization vectors  $\varepsilon_{\lambda\mathbf{q}}$ . By treating the vector potential as canonical variable one can derive the commutator relation for the creation ( $c_{\lambda\mathbf{q}}^+$ ) and annihilation ( $c_{\lambda\mathbf{q}}$ ) operators ([8] p.82):

$$\left[ c_{\lambda,\mathbf{q}}, c_{\lambda',\mathbf{q}'}^+ \right]_- = \delta_{\lambda,\lambda'} \delta_{\mathbf{q},\mathbf{q}'} \quad (2.5)$$

Obeying the regular commutator relation the modes can be identified as bosonic particles called photons. The contributions in Eq. 2.1 describing the transversal electromagnetic field and its coupling to electrons can accordingly be rewritten and consist of three parts. The first part describes the energy stored within the electromagnetic field in analogy to decoupled harmonic oscillator modes and is given by:

$$H_{0,p} = \sum_{\lambda\mathbf{q}} \hbar\omega_{\mathbf{q}} c_{\lambda,\mathbf{q}}^+ c_{\lambda,\mathbf{q}}. \quad (2.6)$$

The second part originating from  $\mathbf{A} \cdot \mathbf{p}$  describes the coupling between photons and electrons and can be written as:

$$H_{el-p} = \sum_{i,i',\mathbf{k},\mathbf{k}',\lambda,\mathbf{q}} G_{\mathbf{k},\mathbf{k}',\mathbf{q}}^{ii'\lambda} a_{i,\mathbf{k}}^+ (c_{\lambda,\mathbf{q}} + c_{\lambda,-\mathbf{q}}^+) a_{i',\mathbf{k}'}. \quad (2.7)$$

The electron-photon coupling element, given in general by  $G_{\mathbf{k},\mathbf{k}',\mathbf{q}}^{ii'\lambda} = \frac{e_0}{m_0} \sqrt{\frac{\hbar}{2\varepsilon_0\omega_{\mathbf{q}}V}} \varepsilon_{\lambda\mathbf{q}} \cdot \langle i\mathbf{k}|\mathbf{p} e^{i\mathbf{q}\cdot\mathbf{r}}|i'\mathbf{k}'\rangle$ , decomposes into three contributions:

### 1. Interband transitions:

$$G_{\mathbf{k},\mathbf{k}',\mathbf{q}}^{ii'\lambda,(1)} = -\frac{1}{m_0} \sqrt{\frac{\hbar}{2\varepsilon_0\omega_{\mathbf{q}}V}} (\varepsilon_{i\mathbf{k}} - \varepsilon_{i'\mathbf{k}'}) \delta_{\mathbf{k},\mathbf{k}'+\mathbf{q}} F_{i,i'}(\mathbf{q}_c) \varepsilon_{\lambda\mathbf{q}} \cdot \mu_{i,\bar{i}'}^{IB}.$$

The interband dipole element  $\mu_{i,\bar{i}'}^{IB}$  is a material-specific function that does not depend on the confinement and describes the local polarizability on the scale of an elementary cell of the semiconductor lattice:

$$\mu_{i,\bar{i}'}^{IB} = \frac{e_0}{V_{ec}} \int_{V_{ec}} d^3r u_i^*(\mathbf{r}) \mathbf{r} u_{\bar{i}'}(\mathbf{r}) \quad (2.8)$$

The dipole approximation has been applied by assuming that the plane wave factor  $e^{i\mathbf{q}\cdot\mathbf{r}}$  is constant within the elementary cell. Following from symmetry considerations the dipole element must be non-diagonal in the band indices ( $\bar{i} \neq \bar{i}'$ ). The wave vector dependency is generally weak and therefore neglected in this work ([4] p.79). By multiplication with an appropriate phase factor it can always be chosen to be real [2].

The confinement enters the coupling element via a form factor  $F$ :

$$F_{i,i'}(\mathbf{q}_c) = \int d\mathbf{r}_c \phi_i^*(\mathbf{r}_c) e^{i\mathbf{q}_c \cdot \mathbf{r}_c} \phi_{i'}(\mathbf{r}_c). \quad (2.9)$$

If the confinement region is small compared to the optical wave length, the wave vector dependency is also small and can, as above, be neglected.

### 2. Intersubband transitions:

$$G_{\mathbf{k},\mathbf{k}',\mathbf{q}}^{ii'\lambda,(2)} = -\frac{1}{m_0} \sqrt{\frac{\hbar}{2\varepsilon_0\omega_{\mathbf{q}}V}} (E_{i\mathbf{k}} - E_{i'\mathbf{k}'}) \delta_{\mathbf{k},\mathbf{k}'+\mathbf{q}} \delta_{\bar{i},\bar{i}'} \varepsilon_{\lambda\mathbf{q}} \cdot \mu_{i,\bar{i}'}^{ISB}(\mathbf{q}_c)$$

Due to the Kronecker delta  $\delta_{\bar{i},\bar{i}'}$  only transitions between two subbands in the same band are described. Therefore a dipole coupling element occurs which is solely determined by the confinement functions and independent of the material:

$$\mu_{i,\bar{i}'}^{ISB}(\mathbf{q}_c) = \left( \begin{array}{c} 0 \\ e_0 \int d\mathbf{r}_c \phi_i^*(\mathbf{r}_c) \mathbf{r}_c e^{i\mathbf{q}_c \cdot \mathbf{r}_c} \phi_{i'}(\mathbf{r}_c) \end{array} \right). \quad (2.10)$$

The wave vector dependency can again be neglected for small structures. Accordingly the phase factor  $e^{i\mathbf{q}_c \cdot \mathbf{r}_c}$  is approximatively constant and a non-diagonality in the subband indices becomes evident. Since the intersubband dipole moment vanishes in the free directions only photon modes with polarization components in the confined directions couple to intersubband transitions.

### 3. Intraband currents:

$$G_{\mathbf{k},\mathbf{k}',\mathbf{q}}^{ii'\lambda,(3)} = i\frac{e_0}{m_0}\sqrt{\frac{\hbar}{2\varepsilon_0\omega_q V}}(\varepsilon_{i\mathbf{k}} - \varepsilon_{i'\mathbf{k}'})\delta_{\bar{i},\bar{i}'}F_{i'i'}(\mathbf{q}_c)\varepsilon_{\lambda\mathbf{q}} \cdot \begin{pmatrix} \nabla_{\mathbf{k}'} \\ 0 \end{pmatrix} \delta_{\mathbf{k},\mathbf{k}'+\mathbf{q}_f}.$$

As above, this is an intraband contribution, but since no optical dipole elements occur, it can be viewed as a current which couples only to photon modes with polarization components in the free directions. In contrast to the previous part, intrasubband transitions are allowed.

Since the photon energy has to approximatively match the energy difference of the involved states in order to induce transitions, it is plausible to assume  $\omega_q \approx E_{i\mathbf{k}} - E_{i'\mathbf{k}'}$  for sufficiently large  $\omega_q$ . Combining interband and intersubband transitions into a single dipole transition element the Hamilton operator reads:

$$H_{el-p} = \sum_{i,i',k,\lambda,q} G_q^{ii'\lambda,(opt)} a_{i,k+q_f}^+ (c_{\lambda,q} + c_{\lambda,-q}^+) a_{i',k} \quad (2.11)$$

$$-i \sum_{i,i',k,\lambda,q} G_q^{ii'\lambda,(cur)} \varepsilon_{\lambda\mathbf{q}} \cdot a_{i,k+q_f}^+ (c_{\lambda,q} + c_{\lambda,-q}^+) \nabla_k a_{i',k},$$

$$G_q^{i,i'\lambda,(opt)} = \frac{1}{m_0}\sqrt{\frac{\hbar\omega_q}{2\varepsilon_0 V}}\varepsilon_{\lambda\mathbf{q}} \cdot (F_{i,i'}(\mathbf{q}_c)\mu_{i,i'}^{IB} + \delta_{\bar{i},\bar{i}'}\mu_{i,i'}^{ISB}), \quad (2.12)$$

$$G_q^{ii'\lambda,(cur)} = \frac{e_0}{m_0}\sqrt{\frac{\hbar\omega_q}{2\varepsilon_0 V}}F_{i'i'}(\mathbf{q}_c)\varepsilon_{\lambda\mathbf{q}}. \quad (2.13)$$

The distinction between optical transition and electric current is based on the resulting equations of motion. The optical part is nondiagonal in the band indices and therefore only couples effectively to an oscillating field which induces coherent transitions between two (sub)bands. In general the photon momentum  $\mathbf{q}$  is small compared to the electron momenta  $\mathbf{k}$  and can be neglected ( $\mathbf{k} + \mathbf{q}_f \approx \mathbf{k}$ ). The current part mainly results in changes of the electron distribution driven by slowly varying electric fields. The gradient breaks the momentum symmetry and hence can lead to macroscopic motion of the charge carriers in the free directions. In agreement to the focus of this work only the contributions describing optical processes are evaluated in this work.

The third part of the transversal electromagnetic contribution of the original Hamiltonian (Eq. 2.1) can be derived from the  $\mathbf{A}^2$  term and translation into second quantization results in a Hamiltonian with the rough shape  $H \approx \sum \langle \cdot | \mathbf{A}^2 | \cdot \rangle a^+ (c + c^+) (c + c^+) a$ . From this structure one can deduce that it describes two-photon-processes which are not further considered as they only occur for very intense fields.

Direct coupling of the transversal electromagnetic field to the ions is considered by introducing a background dielectric function. For excitation at optical frequencies the dielectric function varies only weakly and can therefore be approximated by a constant background refractive index. For low-frequency excitation (THz), which is needed in some situations to induce intersubband transitions, the field can directly couple to phonon modes. This has to be considered by either quantization of the phonon-photon coupling part of the Hamiltonian or approximatively by an appropriate frequency dependent background dielectric function as done in this work.

### 2.2.3 Classical electron-field coupling

Constraining to coherent optical fields a semiclassical approach can be used by describing the electromagnetic fields classically and treating only the remaining particles (electrons, phonons) quantum

mechanically [2]. From the general Hamiltonian (Eq. 2.1) one can derive Maxwell's equations (see chapter 3) which determine the physics of the classical light field. This allows usage of several well-known analytical and numerical methods for the calculation of light propagation effects. As a resulting disadvantage one is no longer able to describe incoherent light fields which are necessary to explain several effects like photo-luminescence or light squeezing.

As a second consequence, the quantum mechanical Hamiltonian in second quantization only contains the light field as a time dependent external potential. In addition to neglecting of the  $\mathbf{A}^2$  term from Eq. 2.1 the vector potential is replaced by the (transversal part of the) electric field  $\mathbf{E}$  and a dipole approximation is applied. In analogy to the quantized light field the matrix elements divide into (IB,ISB) optical and current contributions. Allowing spatially inhomogeneous electric fields the optical part of the respective Hamiltonian reads:

$$H_{e.m.} = - \sum_{i,i',k,q} \mathbf{d}_{i,i'}(\mathbf{q}_c) \cdot \mathbf{E}(t, \mathbf{q}) a_{\mathbf{k}+\mathbf{q}_f}^+ a_{i' \mathbf{k}}. \quad (2.14)$$

With the definitions from section 2.2.2 (Eqs. 2.8, 2.10, 2.9) the combined dipole transition element is given by:

$$\mathbf{d}_{i,i'}(\mathbf{q}_c) = F_{i,i'}(\mathbf{q}_c) \mu_{i,i'}^{IB} + \delta_{i,i'} \mu_{i,i'}^{ISB}(\mathbf{q}_c). \quad (2.15)$$

The first part of  $\mathbf{d}_{i,i'}$  describes interband transitions between different bands. The second part leads to transitions between different subbands in the same band. Because of the structure of  $\mu_{i,i'}^{ISB}$  it is only driven by the components of the electric field in the confined direction. The wave-vector dependent electric field is defined by a slightly modified Fourier transformation and is given by  $\mathbf{E}(t, \mathbf{q}) = \frac{(2\pi)^3}{V} \int d^3 r \mathbf{E}(\mathbf{r}) e^{-i\mathbf{q}\cdot\mathbf{r}}$ . Excitation by a plane wave with a spatially homogeneous envelope function (i.e.  $\mathbf{E}(t, \mathbf{r}) \propto e^{i\mathbf{q}_0\cdot\mathbf{r}}$ ) is therefore accomplished by  $\mathbf{E}(t, \mathbf{q}) = \mathbf{E}(t) \delta_{\mathbf{q}, \mathbf{q}_0}$ . As in the quantized picture the Hamiltonian can be further simplified by assuming  $|\mathbf{q}| \ll |\mathbf{k}|$ , i.e. by neglecting the photon momenta compared to electron momenta. Very commonly the so called Rabi frequency

$$\Omega_{ii'}(t, \mathbf{q}) = \mathbf{d}_{i,i'}(\mathbf{q}_c) \cdot \mathbf{E}(t, \mathbf{q}) / \hbar, \quad (2.16)$$

is introduced during the derivation of equations of motion. If only two (sub)bands are considered, the band indices are omitted, for homogeneous excitation also the wavevector dependency.

If the electric field cannot be described as a plane wave with a constant envelope function in the confinement direction and if one wants to evaluate Maxwell's equations in space domain, as e.g. in chapter 6.8, it is more suitable to use a spatial integration instead of the  $\mathbf{q}$ -sum. This inhibits the separation into a form factor and the electric field, see Eq. 6.13. If the electric field envelope is sufficiently slowly varying in the free dimensions a similar approach can be performed by decoupling the relative from the center-of-mass motion and subsequent Fourier transformation of the center-of-mass motion back into space domain ([4] p.88). This is demonstrated in section 2.4.1.

Often a combination of the classical and quantized description of the light field is used. This is applicable if the system is driven by a strong coherent laser pulse and the incoherent signals (by emission and re-absorption) are small. Even if small, the quantized light field can be of interest, either to study the secondary emission itself or simply in order to include spontaneous emission as decay channel for the polarization. Mostly the incoherent part of the light field is supposed to be in a thermal equilibrium initially and the driving coherent light field is described by the time-dependent external potential approach as described above.

### 2.2.4 Coulomb interaction

The remaining longitudinal electromagnetic contributions between (Bloch) electrons can be quantized into a two-particle Hamiltonian describing a momentum and energy exchange:

$$H_{el-el} = \frac{1}{2} \sum_{i1,i2,i3,i4,\mathbf{k},\mathbf{k}',\mathbf{q}_f} V_{\mathbf{q}_f}^{i1,i2,i3,i4} a_{i1,\mathbf{k}+\mathbf{q}_f}^+ a_{i2,\mathbf{k}'-\mathbf{q}_f}^+ a_{i3,\mathbf{k}} a_{i4,\mathbf{k}}. \quad (2.17)$$

If the considered system is not charged and has no macroscopic charge imbalances the contribution of the sum for  $\mathbf{q}_f = 0$  cancels out with a corresponding term from the ion problem and consequently has to be excluded from the sum [2]. If there are charge imbalances the  $\mathbf{q}_f = 0$  contribution has no exact counterpart with the ions and therefore has to be considered appropriately. As demonstrated in section 5.2 this leads to a so-called depolarization contributions. For  $\mathbf{q}_f \neq 0$  the Coulomb matrix element  $V_{\mathbf{q}_f}^{i1,i2,i3,i4}$  mediating the electron-electron interaction can be expressed as ( $\mathbf{q} = (\mathbf{q}_f, \mathbf{q}_c)$ ):

$$V_{\mathbf{q}_f}^{i1,i2,i3,i4} = \delta_{i1,i4} \delta_{i2,i3} \sum_{\mathbf{q}_c} V_{\mathbf{q}}^{3D} F_{i1,i4}(\mathbf{q}_c) F_{i2,i3}^*(\mathbf{q}_c), \quad (2.18)$$

$$\text{with } V_{\mathbf{q}}^{3D} = \frac{4\pi e^2}{V \epsilon_0 \epsilon_s(\mathbf{q}, t) q^2}. \quad (2.19)$$

This is the leading (monopole-monopole) contribution of a Taylor expansion of the Coulomb potential ( $\frac{1}{r}$ ) on the scale of an elementary cell. Higher-order contributions describe Förster (dipole-dipole) processes [9, 10] and are not considered further. As for the other interactions the confinement is taken into account via the form factor  $F_{i\gamma}(\mathbf{q}_c)$  as defined in Eq. 2.9. The dielectric function  $\epsilon_s(\mathbf{q}, t)$  allows inclusion of screening effects as e.g. described by the Lindhard formula [11]. In principle the screening can depend on the actual state of the system and is therefore implicitly time dependent. Whereas screening may not be a negligible effect, there is no consistent microscopic screening theory which is generally applicable, known to quantitatively describe the physical situation and to be numerically feasible. Since a quantitatively better description is not necessarily achieved by more complex theories, only simple static screening functions have been used in this work, either described by a constant background value or by  $\epsilon_s(q) = \epsilon_{st}(q^2 + \kappa^2)/q^2$  (corresponding to an exponential screening in space domain, [12]).

Like electrons and protons conjoin as hydrogen atoms due to the Coulomb interaction, Bloch electrons and holes in semiconductors form a bound state which is called exciton. In quantum dots where electron-hole pairs are already spatially confined by the three dimensional barrier potential this effect is secondary but in higher-dimensional semiconductors the difference between free electrons/holes and bound electron-hole pairs completely changes the optical properties. E.g. the continuous absorption spectrum of a free moving electron gas is replaced by a hydrogen-like series of discrete absorption peaks ending in a reshaped and suppressed continuum. In contrast to these interband excitons the Coulomb interaction between subbands with the same curvature sign (i.e. electron-electron or hole-hole interaction) exposes different properties: For example repulsive forces can occur or the Coulomb interaction may even vanish completely (compare section 5.11). Beyond the exciton picture which is retrieved within the first order mean-field approximation, many-particle correlations may become relevant. They give rise to electron-electron scattering (second Born approximation, section 5.2), biexcitonic effects (DCT, section 4.1.2) or other entangled many-particle states (e.g. in quantum dots, section 6.6).

### 2.2.5 Lattice vibrations: phonons

The motion of ions around their equilibrium positions can be considered by Taylor expansion of the ionic potential around the energetic minimum that must exist for the formation of a stable crystal. The second order contribution of the expansion represents a harmonic oscillator for each ion. All ions together form an ensemble of coupled oscillators whose energy can be expressed using an expansion into bosonic modes called phonons. With phonon creation (annihilation) operators  $b_{\mu,\mathbf{q}}^+$  ( $b_{\mu,\mathbf{q}}$ ) the Hamiltonian in second quantization is hence given by [8]:

$$H_{0,ph} = \sum_{\mu,\mathbf{q}} \hbar\omega_{\mu,\mathbf{q}} b_{\mu,\mathbf{q}}^+ b_{\mu,\mathbf{q}}. \quad (2.20)$$

Depending on the number and masses of the ions in a lattice unit cell, different degrees of freedom exist and different classes of motion for the ions are possible, leading to distinctive phonon dispersion branches. In this work only bulk phonons which are assumed to be unaffected by the electronic confinement are considered. Then, for  $p$  ions in a cell there are  $3p$  of these branches (index  $\mu$ ), dividing into 3 so-called acoustic branches (with a vanishing dispersion  $\omega_{\mu,\mathbf{q}}$  for small wave vectors  $\mathbf{q}$ ) and  $3p - 3$  optical branches (with  $\omega_{\mu,0} \neq 0$ ). Depending on the direction of the ionic motion with respect to their propagation direction (wave vector  $\mathbf{q}$ ) one differs between longitudinal and transversal branches. Since only longitudinal phonons couple effectively to electrons, transversal branches are not further considered here as they are mainly relevant for phonon-phonon coupling. Longitudinal optical phonons (LO) often have a weak wave vector dependency around the  $\Gamma$ -point and can therefore be approximated by a constant value  $\omega_{LO}$ . In contrast longitudinal acoustic (LA) phonons have an approximatively linear dependency for small wave numbers and, assuming isotropy, can be described by  $\omega_{LA,q} \approx c_{LA}|\mathbf{q}|$ , where  $c_{LA}$  is given by the sound propagation velocity of the material. Only bulk phonons, i.e. phonons which are not substantially influenced by the material heterogeneity, are considered.

Going beyond the Born-Oppenheimer approximation the mutual impact of the motion of electrons and ions can be described using the phonon mode expansion:

$$H_{el-ph} = \sum_{i,i',\mathbf{q},\mathbf{k},\mu} g_{\mu,\mathbf{q}}^{ii'} a_{i,\mathbf{k}+\mathbf{q}}^+ (b_{\mu,\mathbf{q}} + b_{\mu,-\mathbf{q}}^+) a_{i',\mathbf{k}}, \quad (2.21)$$

$$\text{with } g_{\mu,\mathbf{q}}^{ij} = g_{\mu,\mathbf{q}}^{3d,ii'} F^{ii'}(\mathbf{q}_c). \quad (2.22)$$

As usual, the electronic confinement is considered by modulation with the form factor defined in Eq. 2.9. The electron-phonon matrix element  $g_{\mu,\mathbf{q}}^{ij}$  strongly depends on the type of phonons and the specific material system. In polar crystals, which are considered in this work, the coupling of electrons to optical phonons is well described by the Fröhlich coupling element [13, 8, 4, 3]:

$$g_{LO,\mathbf{q}}^{3d,ii'} = \sqrt{\frac{e^2 \hbar \omega_{LO}}{2\epsilon_0 V} \left( \frac{1}{\epsilon_b} - \frac{1}{\epsilon_{st}} \right) \frac{1}{q}} \quad (2.23)$$

Emerging from a dipole interaction between electrons and ions the optical (high frequency) dielectric constant  $\epsilon_b$  enters the equation in addition to the static (“low frequency”) dielectric constant  $\epsilon_{st}$ . The Fröhlich coupling is not principally diagonal in the band index  $\bar{i}$ , but due to energy considerations generally no direct interband transitions are possible. Transitions within and between subbands on the other hand are very likely, provided that the energy of a single or a cascade of phonons matches the intra-/intersubband energy.

Coupling to acoustic phonons is described in this work by a deformation potential approach with coupling elements given by:[3]

$$g_{\text{LA},\mathbf{q}}^{3\text{d},i\bar{i}'} = \delta_{i\bar{i}'} \sqrt{\frac{\hbar q}{2\rho c_{\text{LA}} V}} D_{\bar{i}} \quad (2.24)$$

The deformation potential constant  $D_{\bar{i}}$  quantifies the change of the electronic band structure energies for small volume variations. The density of the material appears as  $\rho$ , the sound velocity as  $c_{\text{LA}}$ . Generally the coupling of electrons to LA phonons is much weaker than to LO phonons. But for special cases LA phonons may be relevant due to their typically lower energy spectrum (up to few meV). E.g. coupling of phonons to the discrete energy levels in quantum dots is only possible by non-Markovian kinetics which favors lower energies and by that LA phonons.

### 2.3 The Heisenberg picture

For transition from Schrödinger to Heisenberg picture, the temporal dependency is transferred from wavefunctions to operators by an unitary transformation  $U(t) = \exp(-iHt/\hbar)$  leading to static wavefunctions  $|\psi_H\rangle = U^\dagger(t)|\psi_S\rangle$  and time dependent operators  $X_H = U^\dagger X_S U$ . Accordingly the Schrödinger equation for wavefunctions is replaced by Heisenberg's equation of motion for operators (assuming an operator  $X = X_H$  that is not explicitly time dependent):

$$i\hbar \frac{d}{dt} X = [X, H]. \quad (2.25)$$

Conveniently the structure of the Hamiltonian is identical in Schrödinger and in Heisenberg picture since  $U$  and  $H$  commute. The expectation value of an operator is given by the trace over its product with the statistical operator:  $\langle X \rangle = \text{tr}(\rho X)$  [14]. If no ensemble average is wanted the trivial statistical operator  $\rho = |\psi\rangle\langle\psi|$  can be used. Either way, the Ehrenfest equation, describing the dynamics of expectation values can be directly derived from the Heisenberg equation (Eq. 2.25):

$$i\hbar \frac{d}{dt} \langle X \rangle = \langle [X, H] \rangle. \quad (2.26)$$

If many-particle interactions are considered, usually further operators in addition to  $X$  occur in the commutator  $[X, H]$ . Therefore one has to derive equations for the additionally appearing quantities as well. In special cases one directly gets a closed set of equations, but usually one is confronted with an infinite hierarchy of equations (see section 2.5). Dealing with this hierarchy is the real challenge of many-particle physics. In this work, several methods are used to approach the problem: For the special situation of electron-phonon coupling in quantum dots an analytical summation of the complete hierarchy is possible using the independent Boson model (section 6.1). In most other cases a truncation scheme has to be applied. This is done either by a Hartree-Fock factorization (see section 2.7) or by other projection operator techniques like a system-reservoir decomposition (see section 2.6). Remainders of a specific order are then neglected. This truncation can be controlled either by the number of involved particles, the order of the correlation expansion (i.e. the number of occurring operators of a particle class) or the order of a specific interaction, like e.g. the driving electrical field (dynamics controlled scheme) or the electron-phonon coupling.

For some rare cases, the evolving equations of motion can then be solved analytically or by Fourier transformation. Else, parts of the equations are solved within the Markov approximation by adiabatically neglecting the memory kernel of the particle coupling (section 2.8). Also a bath approximation can replace a subset of the differential equations by demanding an equilibrium state with constant

expectation values, e.g. for the particle numbers which are then given by the distribution function of the bath particles (section 2.6). The remaining equations are then solved numerically, which is usually done in this work using a fourth order Runge Kutta method (section B.2.2).

## 2.4 Quantities of interest

The set of relevant quantities strongly depends on the considered problem. For coherent optics the Maxwell equations as described in chapter 3 have to be solved at some level. They are driven by the macroscopic polarization, which emerges from a spatial averaging of microscopic charge imbalances. As leading (dipole) contribution of a multiple expansion the polarization is therefore given by  $\mathbf{P} = \langle e_0 \mathbf{r} \rangle_{qm,em}$  (see e.g. [15]). In addition to an electromagnetic averaging, which is performed on the level of single elementary cells here, the quantum mechanical expectation value has to be taken. Without further assumptions and allowing arbitrary inhomogeneous excitation the transition to second quantization of the macroscopic polarization can be written most compactly in the wave vector representation using the dipole moment definition from Eq. 2.15, which includes both inter- and intersubband transitions:

$$\mathbf{P}(t, -\mathbf{q}) = \sum_{i,i',k} \mathbf{d}_{i,i'}(\mathbf{q}_c) \left\langle a_{i\mathbf{k}+\mathbf{q}_f}^+ a_{i'\mathbf{k}} \right\rangle_{qm}. \quad (2.27)$$

It can be seen that the macroscopic polarization is built up from single-particle coherences, which are defined by  $\sigma_{\mathbf{k},\mathbf{k}'}^{i,i'} = \langle a_{i,\mathbf{k}}^+ a_{i',\mathbf{k}'} \rangle$  in second quantization picture. For a given Hamiltonian the equation of motion for this quantity can be derived using the Heisenberg equation of motion.

### 2.4.1 Weakly inhomogeneous excitation, gradient expansion

An exemplary derivation of the equations of motion is given here for excitation of electrons with an electric field which is weakly varying in the directions of free electron motion[4, 16]. This derivation is demonstrated for a Hamiltonian consisting of the energy structure (Eq. 2.3) and coupling to the classical light field (Eq. 2.14):

$$H = H_{0e} + H_{e.m.} = \sum_{i\mathbf{k}} \varepsilon_{i\mathbf{k}} a_{i\mathbf{k}}^+ a_{i\mathbf{k}} - \sum_{i,i',\mathbf{k},\mathbf{q}} \mathbf{d}_{i,i'}(\mathbf{q}_c) \cdot \mathbf{E}(t, \mathbf{q}) a_{i,\mathbf{k}+\mathbf{q}_f}^+ a_{i'\mathbf{k}}.$$

Multiple applications of the electronic anti-commutator relation (Eq. 2.2) lead to:

$$i\hbar \dot{\sigma}_{\mathbf{k},\mathbf{k}'}^{i,i'} = -(\varepsilon_{i,\mathbf{k}} - \varepsilon_{i',\mathbf{k}'}) \sigma_{\mathbf{k},\mathbf{k}'}^{i,i'} + \sum_{j,\mathbf{q}} \left( d_{i'j}(\mathbf{q}_c) \cdot \mathbf{E}(\mathbf{q}) \sigma_{\mathbf{k},\mathbf{k}'-\mathbf{q}_f}^{i,j} - d_{ji}(\mathbf{q}_c) \cdot \mathbf{E}(\mathbf{q}) \sigma_{\mathbf{k}+\mathbf{q}_f,\mathbf{k}'}^{j,i'} \right). \quad (2.28)$$

Next a separation of relative and center of mass motion is performed by introducing  $\mathbf{l}(\mathbf{k}, \mathbf{k}') = \alpha\mathbf{k} + \beta\mathbf{k}'$  and  $\mathbf{L}(\mathbf{k}, \mathbf{k}') = \mathbf{k}' - \mathbf{k}$  with  $\alpha + \beta = 1$  ( $\Rightarrow \mathbf{k} = \mathbf{l} - \beta\mathbf{L}, \mathbf{k}' = \mathbf{l} + \alpha\mathbf{L}$ ). The weights  $\alpha$  and  $\beta$  take the different effective masses into account, their specific values will be obtained later. By definition of  $\sigma_1^{i,i'}(\mathbf{L}) = \sigma_{\mathbf{l}+\beta\mathbf{L},\mathbf{l}-\alpha\mathbf{L}}^{i,i'}$  one can rewrite Eq. 2.28:

$$\begin{aligned} i\hbar \dot{\sigma}_1^{i,i'}(\mathbf{L}) &= -(\varepsilon_{i,\mathbf{l}-\beta\mathbf{L}} - \varepsilon_{i',\mathbf{l}+\alpha\mathbf{L}}) \sigma_1^{i,i'}(\mathbf{L}) \\ &+ \sum_{j,\mathbf{q}} \left( d_{i'j}(\mathbf{q}_c) \cdot \mathbf{E}(\mathbf{q}) \sigma_{\mathbf{l}-\beta\mathbf{q}_f}^{i,j}(\mathbf{L} - \mathbf{q}_f) - d_{ji}(\mathbf{q}_c) \cdot \mathbf{E}(\mathbf{q}) \sigma_{\mathbf{l}+\alpha\mathbf{q}_f}^{j,i'}(\mathbf{L} - \mathbf{q}_f) \right). \end{aligned} \quad (2.29)$$

The weak spatial inhomogeneity of the electric field is used to separate the electronic motion on the different scales. As a first consequence one can neglect the photon momentum  $\mathbf{q}_f$  in comparison to the relative electron momentum  $\mathbf{l}$ . The center of mass electron momentum  $\mathbf{L}$  is given by a difference of wave vectors and is therefore not necessarily larger than  $\mathbf{q}_f$ , but potentially of the same order. The  $\mathbf{L}$  dependence in the energy dispersion can either be completely neglected or for an isotropic situation it can be treated using a Taylor expansion approach giving  $\varepsilon_{i,1-\beta\mathbf{L}} - \varepsilon_{i',1+\alpha\mathbf{L}} \approx \varepsilon_{i,l} - \varepsilon_{i',l} - 2(\beta\partial_l\varepsilon_{i,l} + \alpha\partial_l\varepsilon_{i',l})L + (\beta^2\partial_l^2\varepsilon_{i,l} - \alpha^2\partial_l^2\varepsilon_{i',l})L^2$ . The linear term can be eliminated by demanding that  $\alpha$  and  $\beta$  obey  $\beta\partial_l\varepsilon_{i,l} + \alpha\partial_l\varepsilon_{i',l} = 0$  in addition to  $\alpha + \beta = 1$ . For  $i = i'$  this is generally fulfilled by  $\alpha = \beta = \frac{1}{2}$ . For  $i \neq i'$  the specific band structure has to be known, e.g. a quadratic dispersion  $\varepsilon_{i,k} = \varepsilon_{i,0} + \hbar k^2/(2m_i)$  requires  $\alpha = m_{i'}/(m_{i'} - m_i)$  and  $\beta = m_i/(m_i - m_{i'})$ . This leaves the  $L^2$ -term with a prefactor  $\Xi_l^{i,i'} = (\beta^2\partial_l^2\varepsilon_{i,l} - \alpha^2\partial_l^2\varepsilon_{i',l})$ . This term vanishes for  $i = i'$ . For  $i \neq i'$  and a quadratic dispersion it is  $\Xi_l^{i,i'} = \frac{\hbar}{2(m_i - m_{i'})}$ . Fourier transformation of the above equation with respect to  $\mathbf{L}$  yields :

$$\begin{aligned} i\hbar\sigma_{\mathbf{l}}^{i,i'}(\mathbf{r}_f) &= -(\varepsilon_{i,1} - \varepsilon_{i',1} - \Xi_{\mathbf{l}}^{i,i'}\nabla_{\mathbf{r}_f}^2)\sigma_{\mathbf{l}}^{i,i'}(\mathbf{r}_f) \\ &+ \sum_{j,\mathbf{q}_c} \left( d_{i'j}(\mathbf{q}_c) \cdot \mathbf{E}(\mathbf{r}_f, \mathbf{q}_c) \sigma_{\mathbf{l}}^{i,j}(\mathbf{r}_f) - d_{ji}(\mathbf{q}_c) \cdot \mathbf{E}(\mathbf{r}_f, \mathbf{q}_c) \sigma_{\mathbf{l}}^{j,i'}(\mathbf{r}_f) \right). \end{aligned} \quad (2.30)$$

This can be interpreted as a set of locally defined equations of motion, which are only coupled by the gradient term. For homogeneous excitation it becomes evident, that also the material's response is homogeneous and that the spatial dependence vanishes. As can be seen from 2.28 such a homogeneous excitation only induces coherences with  $\mathbf{k} = \mathbf{k}'$ , i.e. without spatial correlation.

#### 2.4.2 The macroscopic polarization for weakly inhomogeneous excitation

Because of the confinement of the electrons the material's response is always concentrated in a small spatial region in the confinement dimension. Therefore the macroscopic polarization is always strongly inhomogeneous in these directions. For an excitation with a homogeneous or weakly inhomogeneous field one can use Eq. 2.30 to transform the macroscopic polarization back into space domain:

$$\mathbf{P}(t, \mathbf{r}) = \frac{1}{V_f} \sum_{i,i',\mathbf{k}} \phi_i^*(\mathbf{r}_c) \phi_{i'}(\mathbf{r}_c) \left[ \mu_{i,i'}^{IB} + e_0 \mathbf{r}_c \delta_{i,i'} \right] \sigma_{\mathbf{k}}^{i,i'}(\mathbf{r}_f). \quad (2.31)$$

If additionally the spatial dependence of the polarization on scales below the confinement length is not of interest, one can represent the confinement functions by a delta function after averaging over the confined region. For a confinement wavefunctions  $\phi_i$  localized around  $\mathbf{r}_c = 0$  this leads to:

$$\mathbf{P}(t, \mathbf{r}) = \frac{\delta(\mathbf{r}_c)}{V_f} \sum_{i,i',\mathbf{k}} \mathbf{d}_{i,i'}(0) \sigma_{\mathbf{k}}^{i,i'}(\mathbf{r}_f). \quad (2.32)$$

For completely uniform excitation in the direction of free motion the dependence on  $\mathbf{r}_f$  can be omitted.

If the indices  $i, i'$  of the coherences  $\sigma_{\mathbf{k}}^{i,i'}(\mathbf{r}_f)$  differ, one generally speaks of a microscopic polarization. If specifically  $\bar{i} = \bar{i}'$  and  $\lambda_i \neq \lambda_{i'}$  (same band, different subbands) it is called intersubband coherence or polarization, if  $\bar{i} \neq \bar{i}'$  (different bands) interband coherence or polarization. If  $i = i'$  then  $f_{i,\mathbf{k}} = \langle a_{i\mathbf{k}}^\dagger a_{i\mathbf{k}} \rangle$  is the state occupation (number density) of electrons in band  $i$  and wave vector  $\mathbf{k}$  (sometimes also called intraband or intrasubband coherence). The  $\mathbf{k}$ -integrated number density  $f_i = \sum_{\mathbf{k}} f_{i,\mathbf{k}}$  is denoted as (sub)band population, the difference between populations is called inversion. The occupation is effectively an internal quantity describing the energetic state and is therefore

important for the system's dynamics but not an observable which is directly available in optical experiments. The polarization on the other hand appears in Maxwell's equations and hence can be observed more directly. In contrast to the density, the polarization also carries phase information which is an essential ingredient for coherent optics.

## 2.5 Hierarchy of equations

The derivation in section 2.4.1 directly leads to a closed set of equations (Eq. 2.28) because the used Hamiltonian is build up from single particle contributions alone. If many-particle interactions are considered the emerging equations of motion are not closed anymore. This is illustrated for the coupling of electrons to the quantized light field. The respective Hamiltonian consists of Eqs. 2.3, 2.6 and 2.7:

$$H = \sum_{\mathbf{k}} \varepsilon_{i\mathbf{k}} a_{i\mathbf{k}}^{\dagger} a_{i\mathbf{k}} + \hbar \sum_{\mathbf{q}} \omega_{\mathbf{q}} c_{\mathbf{q}}^{\dagger} c_{\mathbf{q}} + \sum_{i,i',\mathbf{k},\mathbf{q}} G_{\mathbf{q}}^{i,i'} a_{i,\mathbf{k}}^{\dagger} (c_{\mathbf{q}} + c_{-\mathbf{q}}^{\dagger}) a_{i'\mathbf{k}}.$$

Here the photon momentum has been neglected compared to the electron momentum. The equation of motion for the single-electron coherence  $\langle a_{i\mathbf{k}}^{\dagger} a_{i'\mathbf{k}} \rangle$  can then be derived using the commutator relations for electrons (Eq. 2.2) and photons (Eq. 2.5):

$$\begin{aligned} i\hbar \partial_t \langle a_{i\mathbf{k}}^{\dagger} a_{i'\mathbf{k}} \rangle &= -(\varepsilon_{i\mathbf{k}} - \varepsilon_{i'\mathbf{k}}) \langle a_{i\mathbf{k}}^{\dagger} a_{i'\mathbf{k}} \rangle \\ &+ \sum_{j,\mathbf{q}} \left[ G_{\mathbf{q}}^{i,j} (\langle a_{i\mathbf{k}}^{\dagger} a_{j\mathbf{k}} c_{\mathbf{q}} \rangle + \langle a_{i\mathbf{k}}^{\dagger} a_{j\mathbf{k}} c_{-\mathbf{q}}^{\dagger} \rangle) - G_{\mathbf{q}}^{j,i} (\langle a_{j\mathbf{k}}^{\dagger} a_{i'\mathbf{k}} c_{\mathbf{q}} \rangle + \langle a_{j\mathbf{k}}^{\dagger} a_{i'\mathbf{k}} c_{-\mathbf{q}}^{\dagger} \rangle) \right]. \end{aligned}$$

Evidently, the equation couples to further, photon-assisted coherences  $\langle a_{i\mathbf{k}}^{\dagger} a_{j\mathbf{k}} c_{\mathbf{q}} \rangle$  and  $\langle a_{i\mathbf{k}}^{\dagger} a_{j\mathbf{k}} c_{-\mathbf{q}}^{\dagger} \rangle$ . Their equations of motion read:

$$\begin{aligned} i\hbar \partial_t \langle a_{i\mathbf{k}}^{\dagger} a_{i'\mathbf{k}} c_{\mathbf{q}} \rangle &= -(\varepsilon_{i\mathbf{k}} - \varepsilon_{i'\mathbf{k}} - \hbar \omega_{\mathbf{q}}) \langle a_{i\mathbf{k}}^{\dagger} a_{i'\mathbf{k}} c_{\mathbf{q}} \rangle \\ &+ \sum_{j,j'} G_{-\mathbf{q}}^{ij} \langle a_{i\mathbf{k}}^{\dagger} a_{j\mathbf{k}} \rangle - \sum_{j,j',\mathbf{k}'} G_{-\mathbf{q}}^{j,j'} \langle a_{i\mathbf{k}}^{\dagger} a_{j\mathbf{k}'}^{\dagger} a_{i'\mathbf{k}'} a_{j'\mathbf{k}'} \rangle \\ &+ \sum_{j,\mathbf{q}'} \{ G_{\mathbf{q}'}^{i,j} (\langle a_{i\mathbf{k}}^{\dagger} a_{j\mathbf{k}} c_{\mathbf{q}'} c_{\mathbf{q}} \rangle + \langle a_{i\mathbf{k}}^{\dagger} a_{j\mathbf{k}} c_{-\mathbf{q}'}^{\dagger} c_{\mathbf{q}} \rangle) \\ &\quad - G_{\mathbf{q}'}^{j,i} (\langle a_{j\mathbf{k}}^{\dagger} a_{i'\mathbf{k}} c_{\mathbf{q}'} c_{\mathbf{q}} \rangle + \langle a_{j\mathbf{k}}^{\dagger} a_{i'\mathbf{k}} c_{-\mathbf{q}'}^{\dagger} c_{\mathbf{q}} \rangle) \}, \\ i\hbar \partial_t \langle a_{i\mathbf{k}}^{\dagger} a_{i'\mathbf{k}} c_{\mathbf{q}}^{\dagger} \rangle &= -(\varepsilon_{i\mathbf{k}} - \varepsilon_{i'\mathbf{k}} + \hbar \omega_{\mathbf{q}}) \langle a_{i\mathbf{k}}^{\dagger} a_{i'\mathbf{k}} c_{\mathbf{q}}^{\dagger} \rangle \\ &- \sum_{j,j'} G_{\mathbf{q}}^{ij} \langle a_{i\mathbf{k}}^{\dagger} a_{j\mathbf{k}} \rangle + \sum_{j,j',\mathbf{k}'} G_{\mathbf{q}}^{j,j'} \langle a_{i\mathbf{k}}^{\dagger} a_{j\mathbf{k}'}^{\dagger} a_{i'\mathbf{k}'} a_{j'\mathbf{k}'} \rangle \\ &+ \sum_{j,\mathbf{q}'} \{ G_{\mathbf{q}'}^{i,j} (\langle a_{i\mathbf{k}}^{\dagger} a_{j\mathbf{k}} c_{\mathbf{q}'} c_{\mathbf{q}}^{\dagger} \rangle + \langle a_{i\mathbf{k}}^{\dagger} a_{j\mathbf{k}} c_{-\mathbf{q}'}^{\dagger} c_{\mathbf{q}}^{\dagger} \rangle) \\ &\quad - G_{\mathbf{q}'}^{j,i} (\langle a_{j\mathbf{k}}^{\dagger} a_{i'\mathbf{k}} c_{\mathbf{q}'} c_{\mathbf{q}}^{\dagger} \rangle + \langle a_{j\mathbf{k}}^{\dagger} a_{i'\mathbf{k}} c_{-\mathbf{q}'}^{\dagger} c_{\mathbf{q}}^{\dagger} \rangle) \}. \end{aligned}$$

As can be seen these equations couple to further coherences which contain two phonon operators like  $\langle a_{i\mathbf{k}}^{\dagger} a_{j\mathbf{k}} c_{-\mathbf{q}'}^{\dagger} c_{\mathbf{q}} \rangle$  or four electronic operators like  $\langle a_{i\mathbf{k}}^{\dagger} a_{j\mathbf{k}'}^{\dagger} a_{i'\mathbf{k}'} a_{j'\mathbf{k}'} \rangle$ . For a closed evaluation one would also need the equation of motion for these quantities, which of course couple to further coherences. Hence, one is confronted with a infinite hierarchy of equations of motion. Only in rare situations one

can sum up the whole hierarchy. Such a case is discussed in section 6.2, where the electron-phonon coupling in quantum dots in linear optics is solved using the independent boson model. Usually one needs a truncation criterion to decide which parts of an equation are kept and which are neglected. Two methods, the bath approximation and the Hartree-Fock approximation are presented in the following. The DCT approach, which uses the order in the electric field as criterion, is discussed for a two-level model in section A.1.3 and for a semiconductor material in section 4.1.2.

## 2.6 Bosonic baths

Considering an ensemble of bosonic particles with energies  $\hbar\omega_{\mathbf{q}}$  one knows that the equilibrium of the ensemble can be described by a Bose distribution:

$$n_{\mathbf{q}}^0 = \frac{1}{\exp(\beta\hbar\omega_{\mathbf{q}}) - 1}. \quad (2.33)$$

The factor  $\beta = k_B T$  is related to a temperature  $T$ . The basic idea of the correlation expansion approach is the assumption that the bosonic ensemble is only slightly affected by coupling to the electron dynamics. Consequently the full state of the system is described by a separation into a static equilibrium part and the deviations, denoted as correlations. This procedure can be performed within a projection operator formalism [14]. For this the statistical operator is split into two parts. The so-called relevant part is obtained by mapping the full state on the bosonic equilibrium which is determined by the canonical statistical operator  $\rho_R^0 = \exp(-\beta H_R)/Z_R$  with the Hamilton operator  $H_R$  of an interaction-free boson reservoir and  $Z_R = \text{tr}[\exp(-\beta H_R)]$ . This projection is performed using the projection operator  $Px = \rho_R^0 \text{tr}_R(x)$  which applies a partial trace over the reservoir states. The complementary projection operator  $Q = 1 - P$  hence maps out the so-called irrelevant part, which describes the dynamics resulting from deviation from the equilibrium position.

Accordingly, using these projection operators one can separate every expectation values into a relevant and an irrelevant part:  $\langle X \rangle = \langle X \rangle^{rel} + \langle X \rangle^{irr}$ . Considering a reservoir Hamiltonian  $H_R = \sum_{\mathbf{q}} \hbar\omega_{\mathbf{q}} c_{\mathbf{q}}^{\dagger} c_{\mathbf{q}}$  and a typical coupling to the electronic system (section 2.7) one can derive:

$$\begin{aligned} \langle c_{\mathbf{q}}^{\dagger} \rangle &= \langle c_{\mathbf{q}}^{\dagger} \rangle^{irr}, \\ \langle c_{\mathbf{q}}^{\dagger} c_{\mathbf{q}'} \rangle &= n_{\mathbf{q}}^0 \delta_{\mathbf{q}, \mathbf{q}'} + \langle c_{\mathbf{q}}^{\dagger} c_{\mathbf{q}'} \rangle^{irr}, \\ \langle c_{\mathbf{q}}^{\dagger} c_{\mathbf{q}'}^{\dagger} \rangle &= \langle c_{\mathbf{q}}^{\dagger} c_{\mathbf{q}'}^{\dagger} \rangle^{irr}, \\ \langle a_1^{\dagger} a_2 c_{\mathbf{q}}^{\dagger} \rangle &= \langle a_1^{\dagger} a_2 c_{\mathbf{q}}^{\dagger} \rangle^{irr}, \\ \langle a_1^{\dagger} a_2 c_{\mathbf{q}}^{\dagger} c_{\mathbf{q}'} \rangle &= \langle a_1^{\dagger} a_2 \rangle^{rel} n_{\mathbf{q}}^0 \delta_{\mathbf{q}, \mathbf{q}'} + \langle a_1^{\dagger} a_2 c_{\mathbf{q}}^{\dagger} c_{\mathbf{q}'} \rangle^{irr}. \end{aligned} \quad (2.34)$$

Evidently only expectation values which contain the same number of phonon creation and destruction operators give a nonvanishing contribution to the relevant part and produce the equilibrium Bose distribution  $n_{\mathbf{q}}^0$ . Expectation values containing only electronic operators are called system observables and have a vanishing irrelevant part, i.e.  $\langle a_1^{\dagger} a_2 \rangle = \langle a_1^{\dagger} a_2 \rangle^{rel}$ .

This formalism allows systematic application of approximations. For example, one can neglect all irrelevant quantities, also called correlations, on some level. This is equivalent to the bath approximation and results in a neglect of all deviations of the boson dynamics from the equilibrium. This is valid if either the electronic system has very little effect on the boson system in the first place or if the equilibrium situation is reestablished on short time scales. Applying the bath approximation to the

electron-phonon problem which has been discussed above, one can simplify the equations of motion by including only the lowest nonvanishing order (i.e. one neglects correlations with more than one phonon operator):

$$\begin{aligned}
i\hbar\partial_t \langle a_{i\mathbf{k}}^+ a_{i'\mathbf{k}} \rangle &= -(\varepsilon_{i\mathbf{k}} - \varepsilon_{i'\mathbf{k}}) \langle a_{i\mathbf{k}}^+ a_{i'\mathbf{k}} \rangle \\
&+ \sum_{j,\mathbf{q}} G_{\mathbf{q}}^{ij} \left( \langle a_{i\mathbf{k}}^+ a_{j\mathbf{k}} c_{\mathbf{q}} \rangle^{irr} + \langle a_{i\mathbf{k}}^+ a_{j\mathbf{k}} c_{-\mathbf{q}}^+ \rangle^{irr} \right) \\
&- \sum_{j,\mathbf{q}} G_{\mathbf{q}}^{ji} \left( \langle a_{j\mathbf{k}}^+ a_{i'\mathbf{k}} c_{\mathbf{q}} \rangle^{irr} + \langle a_{j\mathbf{k}}^+ a_{i'\mathbf{k}} c_{-\mathbf{q}}^+ \rangle^{irr} \right),
\end{aligned} \tag{2.35}$$

$$\begin{aligned}
i\hbar\partial_t \langle a_{i\mathbf{k}}^+ a_{i'\mathbf{k}} c_{\mathbf{q}} \rangle^{irr} &= -(\varepsilon_{i\mathbf{k}} - \varepsilon_{i'\mathbf{k}} - \hbar\omega_{\mathbf{q}}) \langle a_{i\mathbf{k}}^+ a_{i'\mathbf{k}} c_{\mathbf{q}} \rangle^{irr} \\
&+ \sum_{j,j'} G_{-\mathbf{q}}^{ij} \langle a_{i\mathbf{k}}^+ a_{j\mathbf{k}} \rangle - \sum_{j,j',\mathbf{k}'} G_{-\mathbf{q}}^{jj'} \langle a_{i\mathbf{k}}^+ a_{j\mathbf{k}'}^+ a_{i'\mathbf{k}'} a_{j'\mathbf{k}'} \rangle \\
&+ \sum_j \left[ G_{\mathbf{q}}^{ij} \langle a_{i\mathbf{k}}^+ a_{j\mathbf{k}} \rangle - G_{\mathbf{q}'}^{ji} \langle a_{j\mathbf{k}}^+ a_{i'\mathbf{k}} \rangle \right] n_{\mathbf{q}}, \\
i\hbar\partial_t \langle a_{i\mathbf{k}}^+ a_{i'\mathbf{k}} c_{\mathbf{q}}^+ \rangle &= -(\varepsilon_{i\mathbf{k}} - \varepsilon_{i'\mathbf{k}} + \hbar\omega_{\mathbf{q}}) \langle a_{i\mathbf{k}}^+ a_{i'\mathbf{k}} c_{\mathbf{q}}^+ \rangle \\
&- \sum_{j,j'} G_{\mathbf{q}}^{ij} \langle a_{i\mathbf{k}}^+ a_{j\mathbf{k}} \rangle + \sum_{j,j',\mathbf{k}'} G_{\mathbf{q}}^{jj'} \langle a_{i\mathbf{k}}^+ a_{j\mathbf{k}'}^+ a_{i'\mathbf{k}'} a_{j'\mathbf{k}'} \rangle \\
&+ \sum_j \left[ G_{\mathbf{q}}^{ij} \langle a_{i\mathbf{k}}^+ a_{j\mathbf{k}} \rangle - G_{\mathbf{q}'}^{ji} \langle a_{j\mathbf{k}}^+ a_{i'\mathbf{k}} \rangle \right] (n_{\mathbf{q}} + 1).
\end{aligned}$$

These equations constitute the quantum kinetic dynamics of the electron-photon problem in bath approximation and are suitable for calculating optical dephasing due to spontaneous and reservoir-stimulated emission. For the description of further quantum optical effects like squeezing or photoluminescence higher order contributions have to be taken into account. A systematic control of the truncation based on the order of the system-reservoir coupling can be achieved using the Nakajima-Zwanzig formalism [14]. For the electron-phonon problem in quantum dots (section 6.2) a cluster expansion scheme, which truncates according to the number of bosonic operators, is applied in order to obtain higher order expansions [2].

## 2.7 Hartree-Fock factorization

The Hartree-Fock factorization is extensively covered in many basic textbooks on semiconductors [2, 5, 17, 8, 3, 11]. A formal derivation based on the projection operator formalism leads to the Robertson equation as discussed in Refs. [18, 14]. On the level of the expectation values it corresponds to separation into one part which can be written as a product of single particle expectation values and a remainder:

$$\langle a_1^+ a_2^+ a_3 a_4 \rangle = \langle a_1^+ a_4 \rangle \langle a_2^+ a_3 \rangle - \langle a_1^+ a_3 \rangle \langle a_2^+ a_4 \rangle + \langle a_1^+ a_2^+ a_3 a_4 \rangle^c.$$

Neglect of the correlation term  $\langle a_1^+ a_2^+ a_3 a_4 \rangle^c$  is denoted in this work as Hartree-Fock approximation and is equivalent to the mean-field approximation.

## 2.8 Markov approximation

The electron-photon problem can be further evaluated by performing the Markov approximation. Equations 2.35 can be reduced to the following basic structure:

$$\begin{aligned}\dot{x} &= i\omega_x x + i \sum_j c_j y_j, \\ y_j &= i\omega_j y + id_j x.\end{aligned}$$

Formal integration of the  $x$ -equation (assuming  $x(-\infty) = 0$ ) yields:

$$y_j(t) = id_j e^{i\omega_j t} \int_{-\infty}^t e^{-i\omega_j t'} x(t') dt' = id_j \int_0^{\infty} e^{i\omega_j s} x(t-s) ds$$

The essence of the Markov approximation is to neglect the so called memory kernel of the integral by replacing the full dynamics of the quantity  $y$  in the integral by its free oscillation  $\Rightarrow x(t-s) \approx x(t) e^{-\omega_x s}$ . This is equivalent to neglect the interaction which connects  $x$  and  $y$  on third order as can be formally shown using the Nakajima-Zwanzig equation [14]. This substitution results in:

$$y(t) = id_j x(t) \int_0^{\infty} e^{-i(\omega_x - \omega_j)s} ds = d_j x(t) \zeta(\omega_x - \omega_j),$$

$$\text{with } \zeta(\omega) = \lim_{\gamma \rightarrow 0} \frac{i}{\omega + i\gamma} = \lim_{\gamma \rightarrow 0} \frac{\gamma + i\omega}{\omega^2 + \gamma^2} = \pi\delta(\omega) + iPV \left( \frac{1}{\omega} \right)$$

The integral can be identified as the generalized delta function (rarely called Heitler Zeta function [19]) which evaluates according to the Sokhotskii formula to the Dirac  $\delta$ -function plus the Cauchy integral principal value  $PV$ . While the  $\delta$ -function can be used to reduce integrals and generally leads to dephasing contributions, the second term is more demanding but in most cases only results in frequency shifts. As an approximation, one can assume that this shift is already included in the one-particle energies as renormalizations. This solution for  $y_j$  can now be substituted into the differential equation for  $x$ :

$$\dot{x} = i\omega_x x + i \sum_j c_j d_j x(t) \zeta(\omega_x - \omega_j).$$

In an iterative approach one can use the newly calculated  $x(t)$  for better describing the motion of  $y(t)$  (instead of the free motion).

## 2.9 Spontaneous emission of photons

The Markov approximation can be applied to the electron-phonon problem (Eqs. 2.35). Using the definition  $\sigma_{\mathbf{k}}^{ij} = \langle a_{\mathbf{i}\mathbf{k}}^+ a_{\mathbf{i}'\mathbf{k}} \rangle$  the phonon-assisted quantities evaluate to:

$$\begin{aligned}\langle a_{\mathbf{i}\mathbf{k}}^+ a_{\mathbf{i}'\mathbf{k}} c_{\mathbf{q}} \rangle^{irr} &= \frac{1}{\hbar} \sum_j \left[ \delta(\varepsilon_{j\mathbf{k}} - \varepsilon_{\mathbf{i}'\mathbf{k}} - \hbar\omega_{\mathbf{q}}) G_{\mathbf{q}}^{i'j} \sigma_{\mathbf{k}}^{ij} - \delta(\varepsilon_{\mathbf{i}\mathbf{k}} - \varepsilon_{j\mathbf{k}} - \hbar\omega_{\mathbf{q}}) G_{\mathbf{q}}^{ji} \sigma_{\mathbf{k}}^{j'i'} \right] n_{\mathbf{q}}, \\ \langle a_{\mathbf{i}\mathbf{k}}^+ a_{\mathbf{i}'\mathbf{k}} c_{\mathbf{q}}^+ \rangle^{irr} &= \frac{1}{\hbar} \sum_j \left[ \delta(\varepsilon_{j\mathbf{k}} - \varepsilon_{\mathbf{i}'\mathbf{k}} + \hbar\omega_{\mathbf{q}}) G_{\mathbf{q}}^{i'j} \sigma_{\mathbf{k}}^{ij} - \delta(\varepsilon_{\mathbf{i}\mathbf{k}} - \varepsilon_{j\mathbf{k}} + \hbar\omega_{\mathbf{q}}) G_{\mathbf{q}}^{ji} \sigma_{\mathbf{k}}^{j'i'} \right] (n_{\mathbf{q}} + 1).\end{aligned}$$

Substituting this into the equation of motion for the coherence gives:

$$\begin{aligned}
i\hbar\dot{\sigma}_{\mathbf{k}}^{ii'} &= -(\varepsilon_{i\mathbf{k}} - \varepsilon_{i'\mathbf{k}})\sigma_{\mathbf{k}}^{ii'} \\
&+ \frac{i}{\hbar} \sum_{j,j',\mathbf{q}} G_{\mathbf{q}}^{i'j} \left[ \delta(\varepsilon_{j'\mathbf{k}} - \varepsilon_{j\mathbf{k}} - \hbar\omega_{\mathbf{q}}) G_{\mathbf{q}}^{jj'} \sigma_{\mathbf{k}}^{jj'} - \delta(\varepsilon_{i\mathbf{k}} - \varepsilon_{j'\mathbf{k}} - \hbar\omega_{\mathbf{q}}) G_{\mathbf{q}}^{j'i} \sigma_{\mathbf{k}}^{j'j} \right] n_{\mathbf{q}} \\
&+ \frac{i}{\hbar} \sum_{j,j',\mathbf{q}} G_{\mathbf{q}}^{i'j} \left[ \delta(\varepsilon_{j'\mathbf{k}} - \varepsilon_{j\mathbf{k}} + \hbar\omega_{\mathbf{q}}) G_{\mathbf{q}}^{jj'} \sigma_{\mathbf{k}}^{jj'} - \delta(\varepsilon_{i\mathbf{k}} - \varepsilon_{j'\mathbf{k}} + \hbar\omega_{\mathbf{q}}) G_{\mathbf{q}}^{j'i} \sigma_{\mathbf{k}}^{j'j} \right] (n_{\mathbf{q}} + 1) \\
&- \frac{i}{\hbar} \sum_{j,j',\mathbf{q}} G_{\mathbf{q}}^{ji} \left[ \delta(\varepsilon_{j'\mathbf{k}} - \varepsilon_{i'\mathbf{k}} - \hbar\omega_{\mathbf{q}}) G_{\mathbf{q}}^{i'j'} \sigma_{\mathbf{k}}^{j'j'} - \delta(\varepsilon_{j\mathbf{k}} - \varepsilon_{j'\mathbf{k}} - \hbar\omega_{\mathbf{q}}) G_{\mathbf{q}}^{j'i} \sigma_{\mathbf{k}}^{i'j'} \right] n_{\mathbf{q}} \\
&- \frac{i}{\hbar} \sum_{j,j',\mathbf{q}} G_{\mathbf{q}}^{ji} \left[ \delta(\varepsilon_{j'\mathbf{k}} - \varepsilon_{i'\mathbf{k}} + \hbar\omega_{\mathbf{q}}) G_{\mathbf{q}}^{i'j'} \sigma_{\mathbf{k}}^{j'j'} - \delta(\varepsilon_{j\mathbf{k}} - \varepsilon_{j'\mathbf{k}} + \hbar\omega_{\mathbf{q}}) G_{\mathbf{q}}^{j'i} \sigma_{\mathbf{k}}^{i'j'} \right] (n_{\mathbf{q}} + 1).
\end{aligned} \tag{2.36}$$

Further evaluation is only possible knowing details of a specific system. Hence, the frequently used model of a system with two-bands, a valence (c) and a conduction (c) band with  $\varepsilon_{c,\mathbf{k}} > \varepsilon_{v,\mathbf{k}}$  is considered. The indices also can denote two subbands, important is a non-diagonality of the electron-photon coupling. For optical frequencies and realistic temperature the photon population is negligible ( $n_{\mathbf{q}} \ll 1$ ) thus the dynamics is dominated by spontaneous photon emission processes. The  $\delta$ -functions only contribute for  $\varepsilon_{c,\mathbf{k}} - \varepsilon_{v,\mathbf{k}} = \hbar\omega_{\mathbf{q}}$ , with the positive definite photon dispersion  $\omega_{\mathbf{q}} = c_0|\mathbf{q}|$ . With these considerations the equations for the microscopic polarization and occupations evaluate to:

$$\begin{aligned}
\dot{\sigma}_{\mathbf{k}}^{vc} &= i(\varepsilon_{v\mathbf{k}} - \varepsilon_{c\mathbf{k}})\sigma_{\mathbf{k}}^{vc} - \Gamma_{\mathbf{k}}\sigma_{\mathbf{k}}^{vc}, \\
\dot{\sigma}_{\mathbf{k}}^{cc} &= -2\Gamma_{\mathbf{k}}\sigma_{\mathbf{k}}^{cc}, \\
\dot{\sigma}_{\mathbf{k}}^{vv} &= +2\Gamma_{\mathbf{k}}\sigma_{\mathbf{k}}^{cc}.
\end{aligned}$$

These equations describe a radiatively damped system. The solution are exponentially decaying functions for the polarization (dephasing, phase relaxation) and the occupation of the upper band (energy relaxation). Apparently the occupations decays by factor 2 faster than the polarization for these energy relaxation processes. The decay rate is given by:

$$\Gamma_{\mathbf{k}} = \frac{1}{\hbar^2} \sum_{\mathbf{q}} |G_{\mathbf{q}}^{vc}|^2 \delta(\varepsilon_{c,\mathbf{k}} - \varepsilon_{v,\mathbf{k}} - \hbar\omega_{\mathbf{q}}).$$

This dephasing rate has been microscopically derived from the general electron-photon coupling Hamiltonian solely by applying a Markovian approximation and assuming a photonic bath. It is still valid for all confinement situations. For an explicit evaluation the electron-phonon coupling element  $G_{\mathbf{q}}^{vc}$  from Eq. 2.12, which contains the confinement form factor, and the energy band structure for the given problem have to be inserted.

Equations of motion for other coupling mechanisms can be obtained analogous to the presented derivation. However, depending on the specific system, the bath or mean-field approximation may not be appropriate. Also the Markov approximation may not always be applicable. E.g. this is the case for the electron-phonon interaction in quantum dots (chapter 6) and to some extend for intersubband transitions (sections 5.2.5 and 5.13).



## Chapter 3

# Maxwell equations

### 3.1 The macroscopic Maxwell equations

From the general Hamiltonian (Eq. 2.1) one can also obtain the microscopic Maxwell equations. They describe the dynamics of electromagnetic fields and have elementary charges and currents as external inhomogeneity. By averaging over microscopic currents and charge imbalances within small spatial regions, one can derive the macroscopic Maxwell equations. In dipole approximation they are given by [15, 20]:<sup>1</sup>

$$\begin{aligned}\nabla \times \mathbf{E} &= -\dot{\mathbf{B}} & \nabla \cdot \mathbf{D} &= \rho \\ \nabla \times \mathbf{H} &= \dot{\mathbf{D}} + \mathbf{J} & \nabla \cdot \mathbf{B} &= 0\end{aligned}\quad (3.1)$$

Here,  $\mathbf{E}$  is the electric field,  $\mathbf{D} = \epsilon_0 \mathbf{E} + \mathbf{P}$  the displacement field,  $\epsilon_0$  the permittivity of free space and  $\mathbf{P}$  the (macroscopic) polarization.  $\mathbf{B}$  is the magnetic flux density,  $\mathbf{H} = \mathbf{B}/\mu_0 - \mathbf{M}$  the magnetic field,  $\mu_0$  the permeability of free space and  $\mathbf{M}$  the magnetization, which is assumed to be zero throughout this work, because no magnetic effects are considered. Also the density of (macroscopic) electric charges  $\rho$  and the (macroscopic) current density  $\mathbf{J}$  are mostly not needed for the description of optics in the considered materials. This leaves the macroscopic polarization as the only external quantity in the Maxwell equations. The polarization represents the material dipole response to optical excitation and is given by the electromagnetic average over microscopic dipoles  $\mathbf{P} = \langle e\mathbf{r} \rangle_{em}$  [15]. The dipoles are modeled in this work using the quantum mechanical density matrix theory from chapter 2. Therefore additionally a quantum mechanical expectation value and a statistical averaging is introduced.

There are countless analytical and numerical techniques which allow evaluation of Maxwell's equations. A few methods, which are relevant for this work, are sketched here in a compact overview.

### 3.2 Experimental observables

While static electric fields can be directly measured, fast oscillating light fields can only be detected with special experimental setups using interference effects or indirectly by measuring their energy. The energy flux density of an electromagnetic field is given by the Poynting vector  $\mathbf{S}(\mathbf{r}, t) = \mathbf{E}(\mathbf{r}, t) \times \mathbf{H}(\mathbf{r}, t)$ . The signal of standard light detectors can be represented by the temporal averaged absolute value of the Poynting vector and is called intensity:

$$I(\mathbf{r}, t) = \langle |\mathbf{S}(\mathbf{r}, t)| \rangle_t = \langle \mathbf{E}(\mathbf{r}, t) \times \mathbf{H}(\mathbf{r}, t) \rangle_t . \quad (3.2)$$

<sup>1</sup>SI/MKS units are used in this work

In dielectric media (see e.g. Eq. 3.8, section 3.3) the intensity of a propagating mode (with a weakly varying envelope function  $\hat{E}$  and carrier frequency  $\omega_0$ , see Eq. A.7) can be written as:

$$I(\mathbf{r}, t) = \frac{1}{2} \frac{\epsilon_0 c_0}{\sqrt{\epsilon(\omega_0)}} \hat{E}^2(\mathbf{r}, t). \quad (3.3)$$

The temporal averaging (which may e.g. correspond to a detector speed) is supposed to cover some oscillations of the light but to be shorter than the dynamics of the envelope - otherwise  $\hat{E}$  has to be treated as an averaged quantity itself. Eq. 3.3 is only valid in the given form, if the square root of the dielectric function  $\sqrt{\epsilon(\omega)} = n(\omega)$  as the response of the material is weakly frequency dependent and can be represented by a simple background refractive index  $n_b$  for each carrier frequency. If the response depends strongly on the frequency, like for excitation near a resonance, Eq. 3.3 can only be used as an approximation to Eq. 3.2 within that material. But, in contrast to the electric field, which strongly depends on the material properties like the refractive index, the intensity as energy density is comparable in different materials for the same light pulse (assuming it could transit between materials without losses).

Based on intensity definition one can introduce the transmittivity, reflectivity, and absorbance of a sample. If  $I_{in}$  is the incident intensity and  $I_R$  is the intensity reflected by the material then  $R = I_R/I_{in}$  is the reflectivity. Accordingly  $T = I_T/I_{in}$  is the transmittivity if  $I_T$  is the intensity of the transmitted light. If  $I_R + I_T < I_{in}$  the remaining part  $I_A$  accounts for energy loss in the material and an absorbance  $A = 1 - T - R$  can be defined.

In linear optics (see e.g. section 3.3) the extinction of a light pulse propagating as plane wave (here in  $z$ -direction) within a homogeneous optical medium can be described using Beer's law:

$$I_\alpha(z) = I_0 e^{-\alpha z}, \quad (3.4)$$

with the (possibly frequency dependent) absorption coefficient  $\alpha$ , which is a material property and hence independent of the sample size. If  $L$  is the full propagation length in the material, the absorbed intensity is given by  $I_A = I_0(1 - e^{-\alpha L})$ , and the absorption coefficient can be expressed approximatively in terms of the transmittivity and the possibly negligible reflectivity:

$$\alpha = -\frac{1}{L} \ln\left(\frac{T}{1+R}\right) \approx -\frac{1}{L} \ln(T). \quad (3.5)$$

If the absorption coefficient is frequency dependent it is generally called (linear) spectral absorption, or -simpler but ambiguous- (linear) spectrum.

### 3.3 Linear response, Beer's law

In general, the so-called (local) susceptibility tensor  $\underline{\chi}(\mathbf{r}, \omega, E(\mathbf{r}, \omega))$  relates the macroscopic polarization  $\mathbf{P}(\mathbf{r}, \omega)$ , i.e. the local response of the material, to the exciting electric field  $\mathbf{E}(\mathbf{r}, \omega)$ :

$$\mathbf{P}(\mathbf{r}, \omega) = \epsilon_0 \underline{\chi}(\mathbf{r}, \omega, \mathbf{E}(\mathbf{r}, \omega)) \cdot \mathbf{E}(\mathbf{r}, \omega). \quad (3.6)$$

An extension to nonlocal response is considered in section 6.8. In an isotropic material, the susceptibility tensor reduces to a scalar function. In a homogeneous environment also the direct space dependence can be omitted. In the so-called linear optical regime, the susceptibility does not depend on the electric field leading to a response proportional to the field.

For discussing semiconductor optics it is useful to split the material response in a frequency independent background response function  $\chi_b$ , which contains all off-resonant contributions, and the dynamic response  $\chi_d(\omega)$ , which includes the resonant electronic dynamics, needed as a spectral function here. For the linear, isotropic and homogeneous system the (spectral) displacement field can then be written as:

$$\begin{aligned} \mathbf{D}(\omega) &= \varepsilon_0 \mathbf{E}(\omega) + \chi_b \mathbf{E}(\omega) + \chi_d(\omega) \mathbf{E}(\omega) = \varepsilon_0 \varepsilon(\omega) \mathbf{E}(\omega), \\ \text{with } \varepsilon(\omega) &= (1 + \chi_b) + \chi_d(\omega) = \varepsilon_b + \chi_d(\omega) = \varepsilon_b (1 + \chi_d(\omega)/\varepsilon_b). \end{aligned} \quad (3.7)$$

Here, the complex-valued (relative) dielectric function  $\varepsilon(\omega)$  and the background dielectric constant  $\varepsilon_b$  have been introduced. The background refractive index is then given by  $n_b = \sqrt{\varepsilon_b}$ . For vanishing macroscopic charges and currents, one can derive the wave equation for the electric field from the Maxwell Equations in frequency domain:

$$\Delta \mathbf{E}(\mathbf{r}, \omega) = \frac{\varepsilon(\omega) \omega^2}{c_0^2} \mathbf{E}(\mathbf{r}, \omega). \quad (3.8)$$

This equation has plane waves  $\mathbf{E}(\mathbf{r}, \omega) = \mathbf{E}(\mathbf{q}, \omega) e^{i\mathbf{q}\cdot\mathbf{r}}$  with (possibly complex-valued) wave vectors  $\mathbf{q}$  as solution, provided that the dispersion relation  $c_0^2 q^2 = \omega^2 \varepsilon(\omega)$  holds. Assuming propagation in the  $z$ -direction, the intensity of a spectral mode (see Eq. 3.3) is given by:  $I(z, \omega) = \frac{1}{2} \varepsilon_0 c_0 / \sqrt{\varepsilon(\omega)} |\mathbf{E}(z, \omega)|^2 = I(0, \omega) e^{iqz} e^{-iq^*z} = I(0, \omega) e^{-2\text{Im}(q)z}$ . Introducing the absorption coefficient  $\alpha(\omega)$  this can be written in form of Beer's law (Eq. 3.4):

$$\begin{aligned} I(z, \omega) &= I_0(\omega) e^{-\alpha(\omega)z}, \\ \text{with } \alpha(\omega) &= -2\text{Im}(q(\omega)) = -2 \frac{\omega}{c_0} n_b \text{Im} \left( \sqrt{1 + \chi_d(\omega)/\varepsilon_b} \right) \\ &\approx - \frac{\omega}{c_0 n_b} \text{Im}(\chi_d(\omega)) \propto \text{Im} \left( \frac{P_d(\omega)}{E(\omega)} \right). \end{aligned} \quad (3.9)$$

In the last step a second order Taylor expansion of the square root has been applied. The validity of this expansion has to be checked for every special case. If only a small spectral region is considered and if the bandwidth of this region is small compared to its absolute spectral energy one can replace  $\omega$  by a typical frequency of the region, mostly by  $\omega_g$ . Additionally it should be noted, that the background refractive index itself can be frequency dependent. However, the complete dynamics at the optical resonance is included in the dynamical polarization  $P_d$ . Hence the frequency dependence of the background refractive index only gets important for very far-resonant excitation or in the low-frequency regime where the lattice itself can be excited. This equation relates the absorption coefficient, which is one of the most important material characteristics in linear optics, to the electron dynamics in form of the macroscopic polarization, which can be obtained using the density matrix formalism. For brevity in the following  $P$  is written instead of  $P_d$ , the background part only appears as  $\varepsilon_b$ .

If the susceptibility depends on the spacial position either directly (material inhomogeneity) or because of a nonlinear response, usually a general explicit solution of the wave equation (Eq. 3.8) cannot be given, but one can show (e.g. starting from Eq. 3.17), that Beer's law (Eq. 3.9) still holds approximatively for small distances  $z$  and can therefore be applied to thin layers of material like quantum wells or quantum dot layers. Since such a solution only describes the electric field within the thin layer, it does not include surface effects like reflections or interference.

### 3.4 The Finite Differences Time Domain method

All previous solutions presented in this chapter are either limited to homogeneous situations or to linear excitation. In order to simulate propagation of strong light pulses through semiconductor material for either inhomogeneous excitation or more complex material structures, Maxwell's equations have to be evaluated without further assumption. Analytical solutions are therefore only available in situations with special symmetries. For general geometries numerical evaluation is inevitable. Since in the density matrix approach the material response is given in time domain by Heisenberg's equation and spatial inhomogeneous light fields have to be considered, a time-space domain approach is most suitable. Hence in this work the so called Finite-Differences-Time-Domain (FDTD) method, which is based on a direct spatial and temporal discretization of Maxwell's equations on a interleaved grid, is used [21]. The method has second order precision and its numerical characteristic have been subject of extensive research [22]. Like all approaches, which spatially and temporally resolve Maxwell's equations on the carrier oscillation level, it is computational very demanding and memory consuming if larger three-dimensional regions have to be simulated. Also, special boundary conditions at the borders of the computed simulation regions have to be introduced. But, the FDTD method has several advantages, like relatively easy realization and good stability, compared to other algorithms.

#### 3.4.1 One-dimensional FDTD

If the incident light field can be represented by a plane wave, homogeneous in the directions perpendicular to the propagation direction, the rotational Maxwell's equations can be reduced to:

$$\begin{aligned}\partial_z E_y(z, t) &= \mu_0 \partial_t H_x(z, t), \\ \partial_z H_x(z, t) &= \epsilon_0 \epsilon_b \partial_t E_y(z, t) + \partial_t P_y(t, z).\end{aligned}\quad (3.10)$$

Here  $z$  is chosen as the propagation direction, only  $E_y$  and  $B_x$  are considered and a constant background dielectric constant is assumed. Introducing a shorthand notation for grid positions using  $z = i\Delta z$  and  $t = n\Delta t$  with grid spacings  $\Delta z$  and  $\Delta t$ , the fields can be written as  $E_i^n := E_y(i\Delta z, n\Delta t)$  and  $H_i^n := H_x(i\Delta z, n\Delta t)$ . Using second order Taylor series expansions, the temporal and spatial derivatives can then expressed by central finite differences using:

$$\partial_t E_i^n \approx \frac{E_i^{n+\frac{1}{2}} - E_i^{n-\frac{1}{2}}}{\Delta t}, \quad \partial_z E_i^n \approx \frac{E_{i+\frac{1}{2}}^n - E_{i-\frac{1}{2}}^n}{\Delta z}.\quad (3.11)$$

By the chosen construction, the quadratic contributions from the Taylor expansion exactly cancel out, hence the approximation is despite its appearance exact in second order. Looking for an update algorithm for the fields a so-called leapfrog scheme as depicted in Fig. 3.1 (left), in which electric and magnetic fields are temporally and spatially interleaved, is most suitable [23, 21]. Using this scheme Eqs. 3.10 read:

$$\begin{aligned}E_{i+\frac{1}{2}}^{n+\frac{1}{2}} &= E_{i+\frac{1}{2}}^{n-\frac{1}{2}} + \frac{\Delta t}{\epsilon_0 \epsilon_b \Delta z} (H_{i+1}^n - H_i^n) - \frac{1}{\epsilon_0 \epsilon_b} \left( P_{i+\frac{1}{2}}^{n+\frac{1}{2}} - P_{i+\frac{1}{2}}^{n-\frac{1}{2}} \right), \\ H_i^{n+1} &= H_i^n + \frac{\Delta t}{\mu_0 \Delta z} \left( E_{i+\frac{1}{2}}^{n+\frac{1}{2}} - E_{i-\frac{1}{2}}^{n+\frac{1}{2}} \right)\end{aligned}\quad (3.12)$$

Hence, knowing the magnetic field at a time  $t = n\Delta t$  and the electric field at a time  $t = (n + \frac{1}{2})\Delta t$ , the updated magnetic field at a later time  $t = (n + 1)\Delta t$  can be calculated. Accordingly the electric

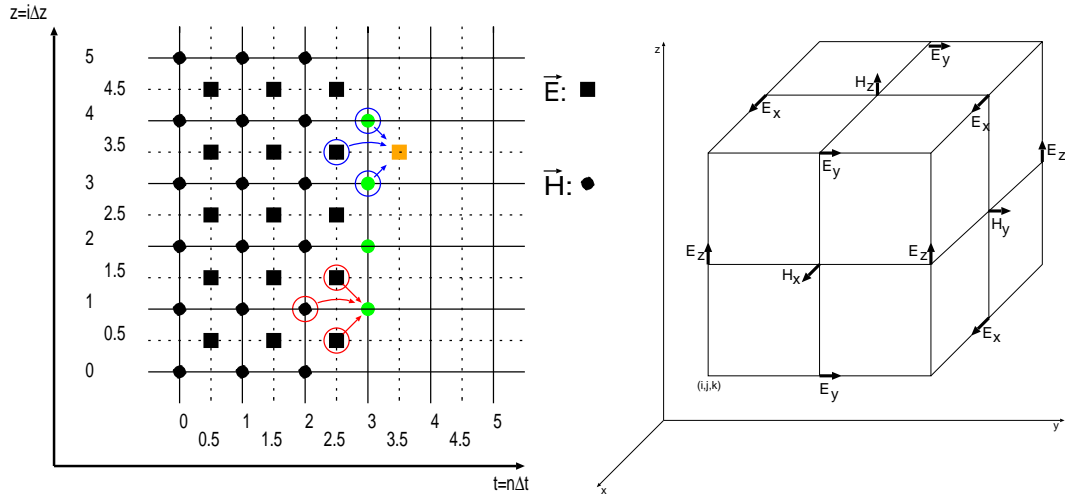


Figure 3.1: Interleaved discretization scheme of the FDTD method. Left: Update scheme, Right: Yee grid for the three-dimensional FDTD [23]

field can be updated, but for this additionally the polarization has to be known for the past and the next time step. This has to be achieved by either directly updating  $P$  using an Euler scheme, i.e.  $P_{i+\frac{1}{2}}^{n+\frac{1}{2}} = P_{i+\frac{1}{2}}^{n-\frac{1}{2}} + \Delta t \dot{P} \left( E_{i+\frac{1}{2}}^{i-\frac{1}{2}} \right)$ , which is only correct in first order. Alternatively a higher order approach like the Runge Kutta method (see chapter B.2.2) can be employed, but then the electric field which is only known for times  $t \leq (n - \frac{1}{2})\Delta t$  has to be extrapolated if needed for later times. Since the Euler scheme breaks the second order correctness of the FDTD approach the Runge Kutta method with a quadratic Lagrange extrapolation [24] has been used in this work.

The grid spacings  $\Delta t$  and  $\Delta z$  should be at least a factor 20 smaller than the oscillation period and the wavelength in the material [22]. The spacial discretization must of course also be small enough to sufficiently resolve the material structure. For numerical stability of the FDTD algorithm, the time step  $\Delta t$  also should not exceed a critical limit, the so called Magic Time Step, which depends on the spacial discretization, the velocity of light and the considered dimensionality. To be safe, a time step  $\Delta t = \frac{\Delta z}{2c}$ , being below the critical value has been used.

Being a numerical method the simulation space of FDTD is always limited by the finite computer memory. Therefore special care of the borders of the simulated region has to be taken. The simplest approach of setting all fields outside the considered region to zero, effectively results in simulation of an perfect metallic wall which reflects all incident waves. This behaviour is usually not wanted, since the reflected fields would interfere with the dynamics of the material in the simulated area. Instead one would prefer a border which absorbs the waves without any reflection. This would be equivalent to an unlimited empty space into which the waves vanish. Several algorithms for implementing such absorbing boundary conditions have been proposed. For the one-dimensional situation the Mur approach, which is based on a simple plane wave propagation and subtraction scheme, is appropriate [25]. Alternatively periodic boundary conditions are possible, which connect the left side of a region with the right side to form an infinite region with periodic internal structure. For two or three dimensions this periodicity may reflect a symmetry of the geometry, for a one-dimensional problem it is intrinsically unphysical.

### 3.4.2 Three-dimensional FDTD

If either the excitation or the material is not homogeneous in the propagation direction the FDTD method has to be extended to two or three dimensions to resolve the spatial variations. Using the Yee scheme [23] from Fig. 3.1 (right) this extension is straightforward and can be found in the literature [21]. As in the one-dimensional FDTD approach the polarization is included additionally via a central differences scheme. Consequently, the emerging equations resemble those from the one-dimensional approach, however all three components of the fields have to be considered. Also, the fields now depend on three spatial coordinates which are arranged according to the Yee scheme, respective indices  $(j,k)$  have to be added. The emerging update equations have similar structures, as an example the  $x$ -component of the electric field is given here [26]:

$$E_x|_{i+\frac{1}{2},j,k}^{n+\frac{1}{2}} = E_x|_{i+\frac{1}{2},j,k}^{n-\frac{1}{2}} - \frac{1}{\epsilon_0 \epsilon_b} \left( P_x|_{i+\frac{1}{2},j,k}^{n+\frac{1}{2}} - P_x|_{i+\frac{1}{2},j,k}^{n-\frac{1}{2}} \right) + \frac{\Delta t}{\epsilon_0 \epsilon_b \Delta s} \left( H_y|_{i+\frac{1}{2},j+\frac{1}{2},k}^n - H_y|_{i+\frac{1}{2},j-\frac{1}{2},k}^n - H_z|_{i+\frac{1}{2},j,k+\frac{1}{2}}^n + H_z|_{i+\frac{1}{2},j,k-\frac{1}{2}}^n \right). \quad (3.13)$$

As for the one-dimensional case the time step  $\Delta t$  and the spatial discretization  $\Delta s$  cannot be chosen independently. Also, the boundaries of the material have to be appropriately described. While the Mur approach works well in one dimension it tends to a high error rate in the sense of nonvanishing unwanted reflections, especially when exposed to near-fields. Instead the UPML scheme has been proven to be very successful [21, 22]. It is based on an artificial material model which has the property to perfectly absorb incident light without reflections. This is achieved by introducing special anisotropic unidirectional tensors for the dielectric and magnetic susceptibility, which in theory leads to the perfect absorption even for very thin layers with appropriate parameters. In numerical implementations one has to keep in mind the finite precision of the FDTD scheme. Therefore the UPML layer usually consists of several grid points which gradually interpolate from the interior material to a highly absorbing material.

### 3.5 The Slowly Varying Envelope Approximation

The Slowly Varying Envelope Approximation (SVEA) provides a framework for the easy yet effective evaluation of the Maxwell equations for nonlinear propagation. Starting from a plane wave ansatz it is first assumed, that only propagation in one direction is possible and both external (at surfaces) and internal (by backscattering) reflections can be neglected. Under the assumption that the envelope of the pulse is slowly varying compared to the underlying carrier oscillation one can derive the SVEA equation for the electric field envelope  $\tilde{E}$  [27, 16]:

$$\partial_\eta \tilde{E}(\eta, \zeta) = i\beta \tilde{P}(\eta, \zeta). \quad (3.14)$$

A transformation into the moving frame of a light pulse that travels with reduced speed of light  $v_g = c_0/n_b$  has been performed by introducing  $\eta = t - z/v_g$  and  $\zeta = z$ . The electric field and polarization appear via their envelope functions  $\tilde{E}$  and  $\tilde{P}$ . The factor  $\beta$  is given by

$$\beta = \frac{2\pi\omega_0}{c_0 n_b}, \quad (3.15)$$

and combines the carrier's angular frequency  $\omega_0$  and the background refractive index  $n_b$ . With a forward discretization scheme, the SVEA equation can be written as propagation rule for the electric

field:

$$\tilde{E}(\eta, \zeta + \Delta\zeta) = \tilde{E}(\eta, \zeta) + i\beta\tilde{P}(\eta, \zeta)\Delta\zeta. \quad (3.16)$$

If the electric field is known at position  $\zeta$  one can calculate the polarization at this position. Using Eq. 3.16 one can then determine the electric field at a position  $\zeta + \Delta\zeta$ . Hence, one can simulate pulse propagation by iterative application of the equation.

From the practical point of view, the SVEA promises several advantages: The envelope functions (rotating frame quantities) allow application of the RWA in the material equations, considerably reducing the computational effort. Also, the spacial discretization can be much coarser than e.g. for the FDTD method since only the changes of the envelope functions have to be considered. On the other hand, the complete neglect of reflection limits the usability of the method to special situations where surface reflections are minimal and also the internal structure is mainly homogeneous like in bulk material (chapter 4) or quantum dot ensembles [28, 29].

The SVEA can also be used to achieve an approximate solution for a thin layer of a material neglecting surface reflections. In a limiting case, the material layer of width  $l$  could be modeled by one numerical discretization step, then the transmitted field  $E_T$  can be related to the incident field  $E_{in}$  by:

$$E_T = E_{in} + i\beta l P. \quad (3.17)$$

Methods, like the Forward Backward Propagation Algorithm [30], which work in the rotating frame but incorporate reflection and backscattering have been proposed, but generally lack a correct handling of temporal retardation.



## Chapter 4

# Bulk material

### 4.1 Nonlinear Polariton Pulse Propagation<sup>1</sup>

#### 4.1.1 Introduction

Nonlinear propagation of optical pulses through an extended bulk semiconductor is investigated using the coupled semiconductor Maxwell-Bloch equations including excitation induced correlations. For short pulse excitation around the exciton resonance, the theory describes the development of polariton beats and their suppression at increasing input pulse intensities due to coupling of single exciton states to the Coulomb-correlated continuum of two-exciton states. The theoretical results are compared to experimental observations for CdSe bulk material showing good agreement.

The exciton-polariton is the quasi-particle emerging from the coupling of the electric field and excitonic states in semiconductor bulk material [33]. Its dispersion relation is separated by a gap into an upper and lower branch. If both branches are coherently excited by an optical pulse, the interference of the excited polariton modes leads to a beating in the transmitted temporal pulse shape. Experimentally, several beating periods are observable and can be explained with the interference of the two polariton branches [34]. Additionally, depending on the sample thickness, the influence of the sample boundaries must be included for a quantitative description. For samples large compared to the exciton Bohr radius, Pekar's boundary conditions [35] can be used, whereas for shorter samples microscopic boundary conditions must be incorporated [36]. Polariton beating has also been experimentally observed in multiple quantum well structures (Refs. [37], also see section 5.1.4) and for localized excitons [38].

In the nonlinear regime, where the response is dominated by Coulomb mediated interactions due to the increased carrier density, the polariton beating is found to be suppressed. Experimentally, the suppression can be realized either by the presence of an incoherent electron-hole density before the arrival of the pulse [39], or by an intensity increase of the pulse itself [40]. The first situation can be explained theoretically within a theory for incoherent Coulomb-correlated electron-hole pairs [41], which induce a density dependent dephasing of the excitonic polarization, thus suppressing the coherence of the polariton.

The second situation is different, because the suppression of the polariton beats is related to interaction among coherently excited excitons. In this case, the beat suppression is observed experimentally via a faster decay of the propagated pulse tail as well as a reduction of the modulation depth of the polariton beats [40]. A semiconductor Maxwell-Bloch theory is evaluated to understand the

<sup>1</sup>Sections 4.1.1-4.1.4 are based on Refs. [16, 31]. Section 4.1.5 is based on Ref. [32].

suppression of the polariton beating for increasing pulse intensities microscopically.

### 4.1.2 Theoretical approach

The material model is based on the density matrix approach introduced in chapter 2. In addition to the band structure Hamiltonian (Eq. 2.3), coupling to the classical light field according to Eq. 2.14 and Coulomb electron-electron interaction (Eq. 2.17) is included. Due to the missing confinement, the electronic wavevectors are three-dimensional and the form factor  $F$  evaluates to 1 leading to the Semiconductor Bloch Hamiltonian[2]. The theory is evaluated in a correlation expansion approach beyond the Hartree-Fock approximation. Within a dynamically controlled truncation scheme all contributions which (DCT) are third order in the electric field are taken into account[42, 43, 44, 45]. This is demonstrated for a two-level system in section A.1.3. In addition to single particle coherences also two-particle coherences, i.e. four-point expectation values consisting of two electron creation and two annihilation operators, occur. The DCT procedure allows a controlled derivation of the equations of motion by discarding all quantities which are beyond the  $\chi^{(3)}$ -response to the electric field. In this regime special relations ensuring conservation hold, e.g. one can express single particle intraband coherences in terms of interband coherences, e.g. for conduction band electrons one can derive  $\langle a_{i,\mathbf{k}}^+ a_{i,\mathbf{k}'}^+ \rangle = \sum_{k'', j \neq i} \langle a_{i,\mathbf{k}}^+ a_{j,\mathbf{k}''}^+ \rangle \langle a_{j,\mathbf{k}}^+ a_{i,\mathbf{k}'}^+ \rangle$ . Similar equations hold for other density-like one- and two-particle quantities. Since propagation in an extended medium is considered, the excitation cannot be assumed to be homogeneous. Within a gradient expansion weak inhomogeneities are considered and a spatial dependence of all coherences is introduced. Boundary conditions according Pekar have been implemented [46]. The details of the derivation of the equations of motion are given in Ref. [16]. For the polarization one obtains:

$$\begin{aligned}
-i\hbar \dot{p}_{\mathbf{k}}^{ii'} &= -\left(\varepsilon_{\mathbf{k}}^{ii'} + \Xi_{\mathbf{k}} \partial_z^2 - i\gamma\right) p_{\mathbf{k}}^{ii'} + \sum_{\mathbf{q}} V_{\mathbf{k}-\mathbf{q}} P_{\mathbf{q}}^{ii'} + \hbar \Omega^{ii'}(t) \left(1 - 2 \left|P_{\mathbf{q}}^{ii'}\right|^2\right) \\
&+ 2 \sum_{\mathbf{q}} V_{\mathbf{k}-\mathbf{q}} p_{\mathbf{k}}^{ii'} p_{\mathbf{q}}^{ii'} \left(p_{\mathbf{k}}^{ii'} - p_{\mathbf{q}}^{ii'}\right)^* \\
&+ \sum_{\mathbf{q}, \mathbf{k}, j, j'} V_{\mathbf{q}} P_{\mathbf{k}'}^{jj'*} \left(B_{\mathbf{q}, \mathbf{k}', \mathbf{k}}^{jjj'i'} - B_{\mathbf{q}, \mathbf{k}' - \mathbf{k}, \mathbf{k}}^{jjj'i'} + B_{\mathbf{q}, \mathbf{k}' - \mathbf{q}, \mathbf{k} - \mathbf{q}}^{jjj'i'} - B_{\mathbf{q}, \mathbf{k}', \mathbf{k} - \mathbf{q}}^{jjj'i'}\right).
\end{aligned} \tag{4.1}$$

For the numerical evaluation, two bands are considered. Additionally spin degeneracy is included. A tight-binding model is used for the description of the energy dispersion and leads to  $\xi_{\mathbf{k}} = \varepsilon_g/2 + \Delta_p^i/2 \cos(ka_0)$  where  $\Delta_p^i$  is the energetic width of band  $i$ , the transition energies are thus given by  $\varepsilon_{\mathbf{k}}^{ii'} = \varepsilon_{\mathbf{k}}^i + \varepsilon_{\mathbf{k}}^{i'}$ . The gradient expansion leaves only the wavevector  $\mathbf{k}$  of the relative motion, the center of mass motion is transformed into a spatial dependence of the microscopic polarization. A link between polarizations at different spatial positions appears as a second order spatial derivative with a dispersion prefactor  $\Xi_{\mathbf{k}}$  (see appendix B of Ref. [16] for details). A phenomenological dephasing  $\gamma$  has been introduced. Optical selection rules between the valence bands ( $v^+$  with spin  $-\frac{3}{2}$ ,  $v^-$  with spin  $+\frac{3}{2}$ ) and the conduction ( $c^+$  with spin  $-\frac{1}{2}$ ,  $c^-$  with spin  $+\frac{1}{2}$ ) bands lead to a reduced set on non-vanishing dipole transition elements. Consequently only  $\mathbf{d}^{+c^+}$ ,  $\mathbf{d}^{v^-c^-}$  and their complex conjugates occur and additionally select electric field with specific polarization. If  $\mathbf{E}^+(t)$  and  $\mathbf{E}^-(t)$  are the circular polarized parts of the electric field, the Rabi frequency is therefore given by  $\Omega^{ii'}(t) = \delta_{i', v^+ c^+} \mathbf{d}^{v^+ c^+} \cdot \mathbf{E}^+(t) + \delta_{i', v^- c^-} \mathbf{d}^{v^- c^-} \cdot \mathbf{E}^-(t) + c.c..$  Via the Coulomb interaction the polarization couples to the two-particle correlations  $B_{\mathbf{q}, \mathbf{k}', \mathbf{k}}^{jjj'i'} \equiv \langle a_{i, \mathbf{k}' - \mathbf{q}}^+ a_{j, \mathbf{k} + \mathbf{q}}^+ a_{j', \mathbf{k} - \mathbf{q}} a_{i', \mathbf{k}' + \mathbf{q}} \rangle^c$ .

The linear part of Eq. 4.1 is given by the transition energies and spatial dispersion of free particles and by a Coulomb-induced electron-hole-coupling ( $\sim VP$ ). The Coupling to the electric field consists

of a linear ( $\sim\Omega$ ) and a nonlinear ( $\sim\Omega PPP^*$ ) part. The first describes the single-particle transitions whereas the latter introduces Paul-blocking. All other quantities describe exciton-exciton interactions on mean-field ( $\sim VPPP^*$ ) and correlation ( $\sim V P^* B$ ) level. The correlation part describes the interaction between a single exciton and a biexciton represented by the biexcitonic amplitudes  $B$ . The equation of motion for these four-point quantities is derived analogous to the microscopic polarization by using the dynamics controlled truncation scheme and applying a gradient expansion:

$$\begin{aligned}
-i\hbar\dot{B}_{\mathbf{q},\mathbf{k}',\mathbf{k}}^{ijj'i'} &= -\left(\varepsilon_{\mathbf{k}'}^{i'} + \varepsilon_{\mathbf{k}}^{jj} + \varepsilon_{\mathbf{q}}^L + \Xi_{\mathbf{q}}\partial_z^2 - 2i\gamma\right) B_{\mathbf{q},\mathbf{k}',\mathbf{k}}^{ijj'i'} \\
&+ \sum_{\mathbf{k}''} \{ B_{\mathbf{q}+\mathbf{k}'',\mathbf{k}'+\mathbf{k}'',\mathbf{k}-\mathbf{k}''}^{ijj'i'} - B_{\mathbf{q}+\mathbf{k}'',\mathbf{k}'-\mathbf{k}'',\mathbf{k}+\mathbf{k}''}^{ijj'i'} + B_{\mathbf{q}-\mathbf{k}'',\mathbf{k}'+\mathbf{k}'',\mathbf{k}+\mathbf{k}''}^{ijj'i'} \\
&\quad - B_{\mathbf{q}+\mathbf{k}'',\mathbf{k}'+\mathbf{k}'',\mathbf{k}+\mathbf{k}''}^{ijj'i'} + B_{\mathbf{q},\mathbf{k}',\mathbf{k}+\mathbf{k}''}^{ijj'i'} + B_{\mathbf{q},\mathbf{k}'+\mathbf{k}'',\mathbf{k}}^{ijj'i'} \} \\
&+ V_{\mathbf{q}} \left( p_{\mathbf{k}'-\mathbf{q}}^{i'} - p \right) \left( p_{\mathbf{k}-\mathbf{q}}^{jj} - p_{\mathbf{k}+\mathbf{q}}^{jj} \right) + \delta_{ij} V_{\mathbf{k}'-\mathbf{k}} \left( p_{\mathbf{k}-\mathbf{q}}^{i'} - p_{\mathbf{k}'-\mathbf{q}}^{i'} \right) \left( p_{\mathbf{k}+\mathbf{q}}^{i'} - p_{\mathbf{k}'+\mathbf{q}}^{i'} \right).
\end{aligned} \tag{4.2}$$

The energetic structure and spatial dispersion of these correlated two-electron-two-hole pairs are given by direct extension of the single-particle properties. In agreement with factorization rules, the dephasing is scaled by a factor of 2 [42]. Furthermore the equation contains the coherent coupling between different electron-hole pairs ( $\sim VB$ ). Since the biexcitonic amplitude  $B$  is introduced as a correction, it is only driven by single particle coherences ( $\sim VPP$ ) but not explicitly by the electric field [4]. Due to the complexity of the equations the Coulomb interaction is modeled using a simplified model based on a nearest-neighbor-coupling (tight-binding) approach. In this model, the full three-dimensional Coulomb potential is approximated by the one-dimensional potential  $V(x) = \frac{V_0}{|x+\delta|}$  with is sampled on a regular spatial grid. This is a strong simplification of the physical situation and is only justified by the good agreement to experimental results.

The material boundaries which get relevant for the gradient expansion have been modeled using Pekar's boundary condition [46], which assumes an instantaneous drop of the wavefunctions at the material borders. This phenomenological approach is appropriate for samples which extend of more than about ten Bohr radii, as can be concluded from microscopic calculations [47].

### 4.1.3 Numerical Results and Discussion

The material equations have been self-consistently evaluated together with Maxwell's equations, which are simulated using the 1d-FDTD method (see section 3.12). Radiative decay due to material-light coupling is handled microscopically due to the interaction with the radiation field. The explicit phenomenologic dephasing constant is only used to represent additional dephasing processes such as phonons or disorder phenomenologically. The theory is evaluated for parameters corresponding to a CdSe material (see table 4.1). The validity of the  $\chi^{(3)}$ -approximation was continuously checked by observing the corresponding conservation law between polarization and density [42, 43, 44]. The peak amplitude  $E_0$  of the circularly polarized Gaussian pulse has been varied over a range from the linear to the nonlinear regime of the observed material. Fig. 4.1a shows the normalized time-resolved signals of the transmitted pulses for the input pulse areas  $\theta = 0.01\pi$  (linear material response),  $\theta = 0.17\pi$  (nonlinearities begin to get clearly observable) and for  $\theta = 0.56\pi$ . At low intensity, the pulse splitting due to polariton interference is clearly visible (two-peak-structure). For  $\theta = 0.17\pi$  a weak suppression of the polariton beat (second peak) is visible. For even higher intensities ( $\theta = 0.56\pi$ ) the transmission of the original pulse peak is continuously increased and, simultaneously the polariton beat is suppressed. The evaluated theory matches the most important signatures reported in the corresponding

| quantity          | value                                | meaning                                 |
|-------------------|--------------------------------------|---|
| $d_{vc}$          | $0.21e\text{nm}$                     | dipole transition element               |
| $\epsilon_b$      | 9                                    | background dielectric constant          |
| $\epsilon_g$      | $1.850e\text{V}$                     | band gap energy                         |
| $\hbar\gamma_0$   | $0.13\text{meV}$                     | additional dephasing constant           |
| $\Delta_p^i$      | $35.2\text{meV} \frac{m_v+m_c}{m_i}$ | band width of TBA bands                 |
| $m_c : m_v$       | 1 : 10                               | ratio of electron to hole masses        |
| $a_0$             | $13.5\text{nm}$                      | exciton Bohr radius                     |
| $V_0$             | $16\text{meV}$                       | amplitude of Coulomb potential          |
| $\delta$          | $2.5\text{nm}$                       | screening length of Coulomb potential   |
| $w$               | $5\text{nm}$                         | sampling distance for Coulomb potential |
| $\rightarrow E_x$ | $15\text{meV}$                       | exciton binding energy                  |

Table 4.1: Parameters corresponding to a CdSe material based on a tight binding model for the band structure and the Coulomb interaction [48, 45].

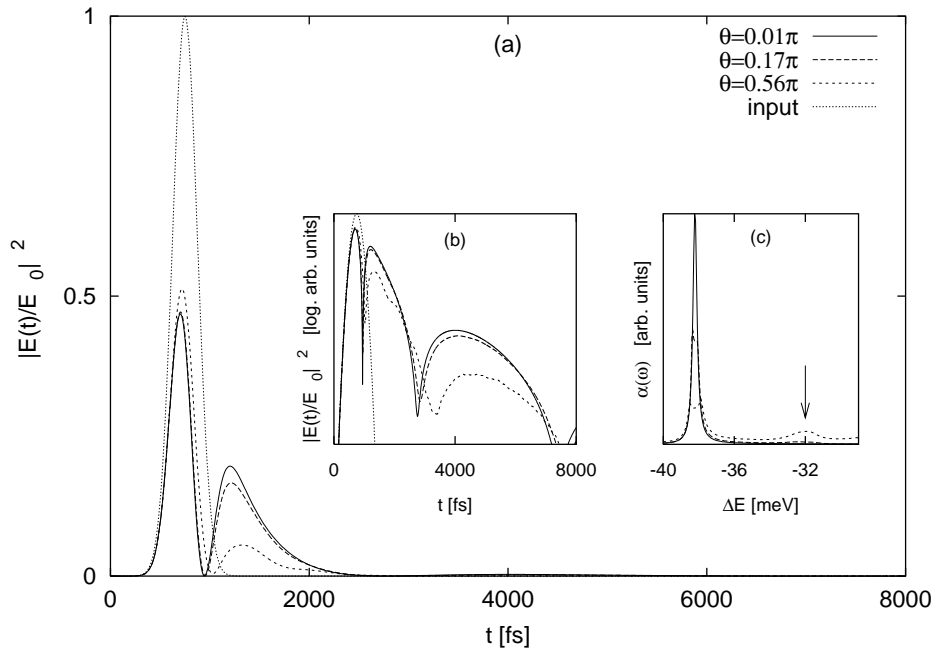


Figure 4.1: (a) linear, (b) logarithmic scale: Time resolved intensities of transmitted optical pulses for different input pulse areas after propagation through  $2\mu\text{m}$  of the CdSe model material. The polariton beating, clearly visible in the linear case, is suppressed for increasing input pulse areas. The normalized input pulse is given as dashed curve. The spectral absorption (c) shows an increase of the biexciton continuum at  $\Delta E \simeq 32\text{meV}$  and a suppression of the exciton resonance for growing pulse intensity. Published in Ref. [31].

experiments [40]. In particular, the reduced modulation of the polariton beating and the increased mean signal decay with increasing input intensity can be reproduced. This is illustrated in the inset (4.1b), showing the pulse shapes on a logarithmic scale.

To investigate the origin of the polariton damping, numerical simulations, especially a comparison to Hartree-Fock and constant damping rate calculations have been performed. It can be concluded that within the chosen description the continuum of two-exciton states is responsible for the decrease of the polariton beating observed. This interpretation is supported by the spectral absorption plotted in Fig. 4.1c. For increasing intensities parts of the two-exciton continuum around  $\Delta E \simeq -32\text{meV}$  grow continuously while the exciton resonance peak at  $\Delta E \simeq -38\text{meV}$  is suppressed.

#### 4.1.4 Experimental Results and Comparison

The theoretical calculations for pulse propagation through a CdSe sample is compared to experimental results over a range of input intensities. The experiments were conducted by H. Giessen et al. using a setup described in detail in Ref. [49]. The influence of the sample strain has been modeled assuming an inhomogeneous broadening of the band gap energy by averaging the polarization over a Gaussian distribution. The corresponding inhomogeneous broadening of  $6\text{meV}$  (FWHM) can be estimated from a linear spectrum obtained with a spectral broad input pulse [49]. For a direct comparison of the theoretical and the experimental results, the computed time resolved signal was convoluted with a  $50\text{fs}$  Gauss pulse in correspondence with the experimental setup.

The experimental and theoretical cross-correlation signals are compared in Fig. 4.2. At low intensity, a single polariton beat can be observed about  $500\text{fs}$  after the pulse maximum in this experiment. Further polariton beats are suppressed because of inhomogeneous broadening in the sample. The observed polariton beats show the characteristic decrease for increasing intensities. For even higher intensities the beats vanish completely and except for a small shoulder, the original shape of the input pulse is restored.

The spectral intensity for the transmitted pulses as given in Fig. 4.2 can be obtained in experiment directly by a spectrum analyzer and for the theoretical results by Fourier transformation of the temporal evolution of the electric field. For low intensity the center part of the pulse spectrum is depleted by the excitonic absorption. At higher intensities the center part increases and the spectral hole is filled up until the original input shape is nearly recovered. For both, temporal and spectral signatures, good agreement between experiment and theory is observed.

It should be noted that the presented theory is especially suited for intermediate intensities, because at higher intensities (not shown) the used  $\chi^{(3)}$  approximation breaks down. In this self-induced transmission regime theories based on cluster expansion like a second Born approach (used e.g in section 5.2) are more appropriate and can explain according experiments [49].

#### 4.1.5 Hole burning within the exciton resonance

The model system of a semiconductor bulk material without inhomogeneous broadening has already been briefly discussed in Fig. 4.3 and is investigated in more detail here. In a first step the formation of exciton-polaritons during propagation is studied in the linear optical regime. The insets in Fig. 4.3 displays the slowly varying envelope function of the transmitted electric field  $\tilde{E}(t)$  for different propagation lengths. During propagation the exciton-resonant  $250\text{fs}$ -Gauss input pulse is continuously reshaped. This reshaping is minor for small propagation lengths but increases for larger distances leading to an oscillating structure. These oscillations are attributed to the temporal beating of two polariton branches which travel with different velocity [27]. During these beatings, the phase of the

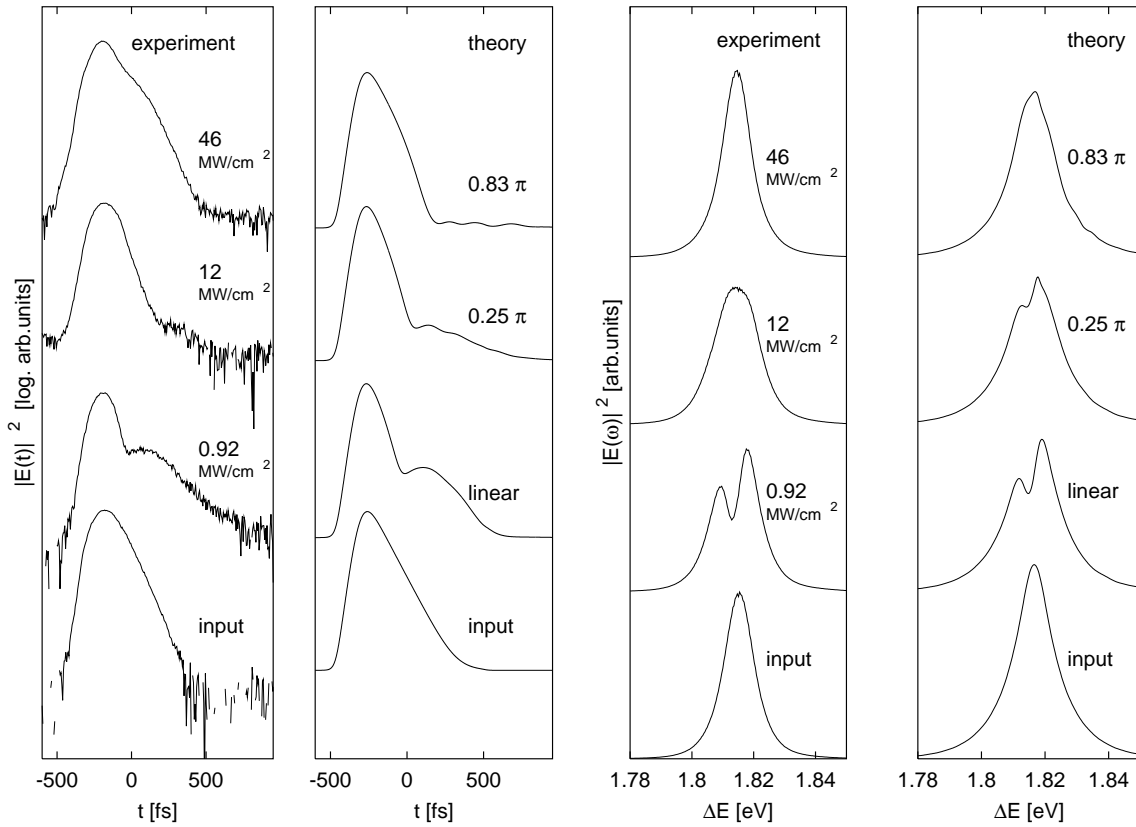


Figure 4.2: Experiment-theory comparison of the cross-correlations (left) and spectral intensities (right) of the transmitted intensities of a 180ps pulse propagated through  $L = 1.7\mu\text{m}$  of CdSe bulk material. The input intensity is varied from 0.92 to  $46\text{ MW/cm}^2$ . Both show the development and the suppression of the polariton beat for increasing intensities. The excitonic absorption in the center for increasing intensities is depleted. Published in Ref. [31].

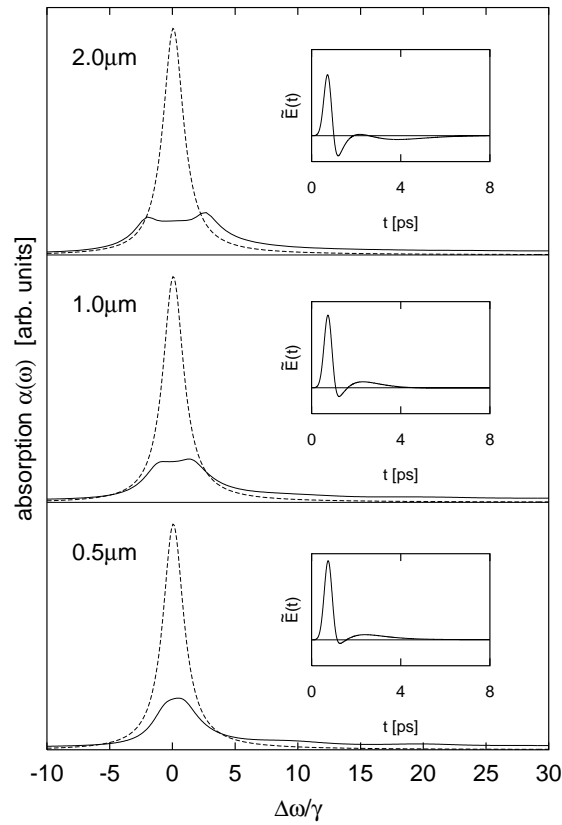


Figure 4.3: The spectral absorption after propagation of a 250fs Gaussian input pulse at different sample length (dashed line: linear excitation, solid: nonlinear excitation  $\Theta = 0.56\pi$ ). The development of the exciton line splitting due to the simultaneous action of optical nonlinearity and the formation of a small area pulse is shown. The insets shows the formation of polariton beating for increasing sample length. From Ref. [32].

|                                    | a          | b         | A                 | B         |
|------------------------------------|------------|-----------|-------------------|-----------|
| positive definite pulses           | $1/2000fs$ | $1/150fs$ | $a\Theta/2$       | $b\tau/2$ |
| small area pulses with $F = 0.12$  | $1/2000fs$ | $1/150fs$ | $-0.95a\Theta/2$  | $b\tau/2$ |
| small area pulses with $F = 0.012$ | $1/2000fs$ | $1/150fs$ | $-0.995a\Theta/2$ | $b\tau/2$ |

Table 4.2: Pulse parameters for Fig. 4.4.

envelope function exhibits several jumps by  $\pi$ . These phase jumps can be observed in the graphs as sign changes occurring around the zero-crossing points. Since some parts of the envelopes are negative the pulse area is reduced compared to the input pulse. As a function of propagation length the pulse area can be defined as  $\Theta(z) = \frac{d^{vc}}{\hbar} \int_{-\infty}^{+\infty} \tilde{E}(z, t) dt$ . For linear propagation in undamped two-level systems one can show analytically, that this pulse area decreases and converges to  $0\pi$  for increasing propagation [50, 51, 27]. As can be concluded from the graphs, this formation of  $0\pi$ -pulses also occurs for exciton-resonant propagation in semiconductors. This is also observed in experiments [34]. For excitation with nonlinear pulses, which have a large pulse area  $\Theta \geq 2\pi$ , the polariton picture breaks down. Instead lossless propagation is possible. For a pulse area of  $\Theta = 2\pi$  even soliton solutions are possible. In this regime the pulse area does not decrease during propagation, instead the McCall area theorem holds and describes the lossless propagation via self-induced transmission [52, 53]. In the intermediate regime, i.e. for  $0 < \Theta < 2\pi$  this self-induced transmission is not achieved. Hence the exciton-polariton picture is still valid, however, the polariton beating is increasingly suppressed for growing pulse areas (see section 4.1.3). Nevertheless as already seen in the previous section, formation of  $0\pi$ -pulses is still possible for this weakly nonlinear excitation regime [40, 31]. Such pulses, which have a vanishing pulse area but simultaneously have a nonlinear intensity are further investigated in the following.

The spectral absorption for linear excitation (dashed,  $\Theta(0) \simeq 0$ ) is compared to that obtained for the weakly nonlinear regime (solid,  $\Theta(0) = 0.56\pi$ ) in Fig. 4.3. As discussed in section 3.3 the spectral absorption  $\alpha(\omega) = -\frac{1}{L} \ln(T)$  with  $T = |E_T|^2/|E_{in}|^2$  is a material specific functions for linear excitation and is therefore independent of the propagation length. Only the Lorentzian shaped resonance of the 1s-exciton is visible in the shown graph, further resonances and the continuum states of the semiconductor spectrum are located at higher energies. For nonlinear excitation, the spectral absorption function can depend on the propagation length. At a sample length of  $L = 1\mu m$ , and even more pronounced for  $L = 2\mu m$ , a spectral hole within the homogeneous linewidth is visible in the absorption spectrum. Detailed analysis reveals that two ingredients are necessary in order to produce this spectral hole-like feature: A coherent nonlinearity and an oscillating pulse envelope with small pulse area  $\Theta$ . In this example the small area pulse is evolving during the propagation in the sample (see insets of Fig.1). Such small area pulses have been experimentally observed for the linear regime [34] but also occur in weakly nonlinear situations [40, 31].

To understand the formation of spectral hole burning within the homogeneous exciton line it is necessary to keep in mind that small area pulses with oscillating envelopes can induce nonlinear effects, because the field strength at an individual time  $t$  can take large values. This property contrasts with the characteristics of positive definite envelopes ( $\tilde{E}(t) \geq 0$ ), where pulse areas much smaller than unity cover the limit of linear optics [27] and only large pulse areas  $\Theta$  induce optical nonlinearities. To have a measure for the ability to induce nonlinear optical effects in the case of oscillating envelopes,  $\bar{\Theta} = \int_{-\infty}^{+\infty} dt |\Omega(t)|$ , the area of the field modulus is introduced.

In the analysis of the nonlinear spectral signatures induced by small area pulses one can separate

the pulse formation problem from the absorption lineshape problem. Hence, in the following model study we eliminate the propagation part and concentrate on the spectral absorption  $\alpha(\omega)$  for an optically thin sample where the input is a small area pulse with oscillatory amplitude. In this case, the (local) spectral absorption is given by  $\alpha(\omega) \propto \text{Im}(P(\omega)/\tilde{E}(\omega))$  [2, 27] with the macroscopic spectral polarization  $P(\omega)$  and the input pulse spectrum  $\tilde{E}(\omega)$ . In order to obtain partly analytical results we approximate the oscillating pulse envelope by a double-sided exponential  $\Omega(t) = \theta(-t)B e^{bt} + \theta(t)A e^{-at}$ . We have checked numerically that the spectra obtained with this pulse shape reproduce the results of the full propagation study. For the double exponential pulse we investigate the influence of the relevant material nonlinearities such as Pauli Blocking, Hartree-Fock mean-field nonlinearities as well as Coulomb correlations up to the third order in field in detail (see section 4.1.2 and [42, 43, 44, 54, 16]).

Figs. 4.4a-c show the spectral absorption in the presence of the different nonlinearities (a: Pauli blocking, b: Pauli blocking + mean-field, c: Pauli blocking + mean-field + correlations) each for linear and nonlinear excitation with positive definite and the double exponential pulse envelopes. Besides the Lorentzian shaped homogeneous absorption line for linear excitation, the well-known results for positive definite nonlinear excitation are reproduced: A Pauli blocking nonlinearity uniformly suppresses the resonance, the Hartree-Fock mean-field nonlinearity blue-shifts the resonance whereas including correlations partly compensates the mean-field effects leading to a much weaker shift and an additional uniform reduction [48]. Note, that the input pulse area has been chosen considerably larger for pure Pauli blocking ( $\Theta = 0.2\pi$ , 4.4a) than for the other nonlinearities ( $\Theta = 0.05\pi$ ) in order to obtain a comparable magnitude of the respective nonlinear responses (see table 4.2 for parameters). If a small area nonlinear pulse with oscillating envelope is applied, in all three cases pronounced structures within the homogeneous line are induced. These structures, while being spectrally much narrower, show features reminiscent of those for positive definite input pulses: For Pauli blocking a symmetric hole, for mean-field a dispersive structure, and for all nonlinearities including correlations a mix of both can be seen.

Using the above double sided exponential as input pulse, one can derive an analytic expression for the linear part and the third-order nonlinear part of the polarization in time-domain (by using the linear result as first-order solution for the nonlinear part). After Fourier transformation and fractional expansion in the equation of the the absorption  $\alpha$ , the spectral contributions can be analyzed. One finds Lorentz-like contributions in the nonlinear absorption with a characteristic width  $F$ , independent of the homogeneous line width  $\gamma$ , which are responsible for the spectrally sharp features shown above. Interestingly, the width  $F$  of the induced spectral structure does not depend on material properties but only on the input pulse parameters:

$$F = \frac{\Theta ab}{(|A| + |B|)},$$

where  $A$  and  $B$  are the amplitudes, and  $a$  and  $b$  are the spectral widths of the above defined double sided exponential pulse. Therefore, by varying the input pulse parameters the width of the structure can be directly controlled. For  $F < \gamma$ , hole-burning-like signatures smaller than the homogeneous linewidth can be created. While the width is solely determined by the input pulse parameters, the shape and magnitude also depends on the specific nonlinearity. The Pauli blocking nonlinearity shows narrow symmetric Lorentzian contributions proportional to  $\frac{F}{\Delta\omega^2 + F^2}$  with a width  $F$ . In the presence of a mean-field nonlinearity, the narrow structures are dominated by dispersive contributions. With correlations a mixture of symmetric and dispersive contributions is predicted. These differences may serve as a useful application to identify the origin of nonlinear optical effects. The advantage of such a spectroscopic tool is that the structure induced by nonlinear small area pulses can be sharp and of large magnitude and may be controlled by varying the input pulse parameters.

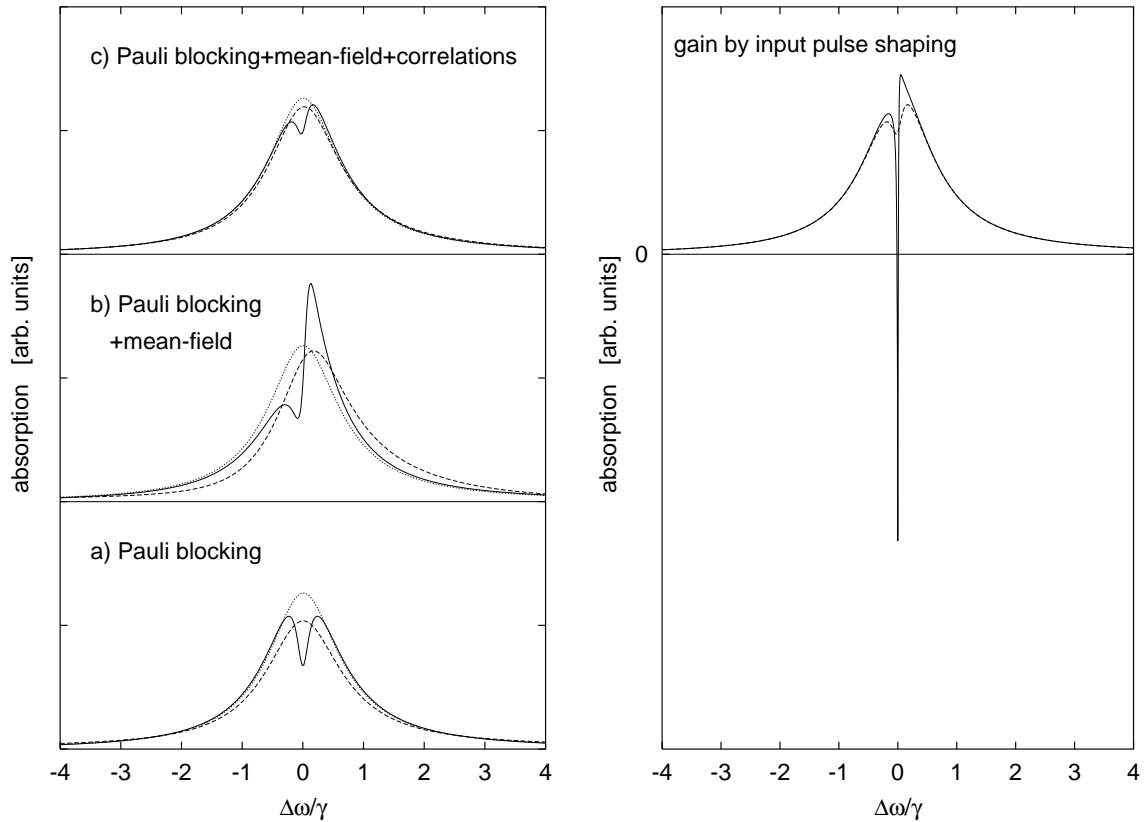


Figure 4.4: Left: For three types of nonlinearity (Pauli blocking, mean-field, correlation) the spectral absorption for different excitation conditions with a double-sided exponential, (for parameters see table 4.2) is given. In contrast to the known results for linear (dotted) and positive definite (dashed) excitation, nonlinear small area pulses (solid) induce spectral structures narrower than the homogeneous line-width. Right: By changing the input pulse parameters (see table 4.2) of a small area input pulse, the width  $f$  and magnitude (proportional to  $1/f$ ) of the spectral hole can be influenced. This way, it is possible to produce narrow spectral regions with optical gain (solid:  $F = 0.012\gamma$ ). For comparison the spectrum from for  $F = 0.12\gamma$  is given (dashed). All nonlinearities are taken into account. Published in Ref. [32].

The sign of the new nonlinear absorption contributions are determined by a complex combination of material and pulse properties, and can therefore cause an enhancement or reduction of the spectral absorption. This opens the door to another interesting feature, which is illustrated in Fig. 4.4d: Regardless of the actual strength of the nonlinearity, by varying the input pulse parameters, it is possible to increase the strength of the interaction at  $\Delta\omega = 0$  until a partially negative absorption occurs (solid line:  $F = 0.012\gamma$ , compare to dashed line with  $F = 0.12\gamma$  - as in Fig. 4.4). This generation of optical gain for certain spectral components is possible for any strength of the nonlinearity and can be reached without any material inversion, i.e. the electron-hole occupations remain smaller than unity, as has been checked numerically. Applications like optical amplifiers emitting in a spectrally very narrow region seem possible.

The analogy of the observed effect with the well-known spectral hole burning spectroscopy restricts to a macroscopically observable spectral hole for nonlinear excitation. Whereas in the classical sense of hole burning spectroscopy, a certain transition out of a inhomogeneously broadened line is saturated, in case a homogeneous line exhibits a spectral hole due to a combined effect of pulse propagation and nonlinearity. We would like to comment, that we know of no physical phenomena with the possible exception of interference effects that could explain the observed features. In this sense we consider the presented spectral signatures to be a novel physical effect.

In conclusion, it has been shown that small area pulses with oscillating pulse envelopes induce nonlinear structures in the spectral absorption that are narrower than the homogeneous linewidth. The width and strength of the structures can be controlled by varying input pulse properties alone. The pulses may evolve due to propagation, as e.g. in a bulk semiconductor due to polaritonic effects, or may be obtained through proper pulse shaping techniques. Since the shape of the narrow spectral features is characteristic for the underlying material nonlinearity, absorption measurements with small area pulses should be useful as a diagnostic spectroscopic technique. Furthermore, it has been shown that it is possible to create spectral narrow regions with optical gain.

The observed effect is not restricted to a semiconductor material but can be found in all materials where pulse propagation effects result in the formation of a low area, oscillating pulse shape and optical nonlinearities. Examples are the Pauli blocking nonlinearity in atomic systems as well as Förster-type interactions in dense atomic gases or molecular systems. These general aspects are discussed in the next section.

## 4.2 Hole-burning within the homogeneous linewidth<sup>2</sup>

The general characteristics of the hole-burning effect, which has been discussed for the special case of a semiconductor material in the previous chapter, are investigated in the following. For this the nonlinear absorption of a homogeneously broadened two-level transition is investigated using  $0\pi$ -pulses ( $\Theta = 0$ ) containing sufficient large fields envelope amplitudes ( $\Theta \geq 1$ ). In particular, analytical insight into the material dynamics is gained and the observed effects like field induced line narrowing, spectral hole burning and gain at the transition frequency are explained with a nonlinear wave-mixing process.

The macroscopic spectral polarization (slowly varying envelope)  $\tilde{P}_m(\omega)$  represents the nonlinear response to a input pulse  $\tilde{E}(\omega)$ . According to Eq. 3.9 the spectral absorption is the given by  $\alpha(\omega) = \text{Im}(\tilde{P}_m(\omega)/\tilde{E}(\omega))$ . The corresponding two-level equations used to calculate the polarization  $\tilde{P}_m(\omega)$  in

---

<sup>2</sup>This section is based on Ref. [55].

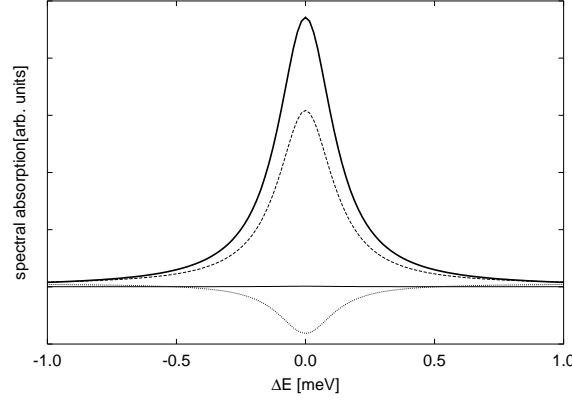


Figure 4.5: The spectral absorption of a two-level system excited with a positive definite Gaussian input pulse  $\Omega^>$  for increasing pulse area  $\bar{\Theta} = \Theta = 0.01\pi$  (linear case, strong solid),  $0.5\pi$  (dashed),  $1.5\pi$  (dotted),  $2\pi$  (thin solid line). For nonlinear excitation, the homogeneous line is uniformly suppressed and finally gain is generated. Published in Ref. [55].

time domain (within rotating frame) have been derived in as derived in section A.1.4 [27]:

$$\tilde{P}_m = d\rho_d \tilde{P}, \quad (4.3)$$

$$\dot{\tilde{P}} = -\gamma \tilde{P} - i\Delta \tilde{P} + i\frac{\Omega}{2}(1 - 2f), \quad (4.4)$$

$$\dot{f} = -2\gamma f + \frac{i}{2}(\Omega \tilde{P}^* - c.c.), \quad (4.5)$$

where the electron density of the upper level is denoted by  $n$  and the polarization amplitude by  $\tilde{P}$  (diagonal and off-diagonal part of the density matrix),  $\rho_d$  is the number density of two-level systems,  $\Delta = \omega_0 - \omega_l$  is the detuning of the two level transition  $\omega_l$  with respect to the light frequency  $\omega_l$ , and  $\gamma$  is the radiative decay constant, which accounts for the homogeneous broadening of the transition and the population decay. The Rabi-frequency of the field is  $\Omega(t) = d\tilde{E}(t)/\hbar$ .

First, to illustrate the hole burning effects in the homogeneously broadened two-level absorption, Eqs. 4.3-4.5 are solved numerically. The close-to- $0\pi$  pulse for the numerical calculations is represented by  $\Omega(t) = A_1 \exp(-[t/\tau]^2) - A_2 \exp(-[(t - t_o)/\tau]^2)$ , i.e. a series of two Gaussian pulses. The results are contrasted against a standard positive definite pulse shape  $\Omega^>(t) = A^> \exp(-[t/\tau]^2)$ . As numerical parameters,  $\gamma = 1/5ps$ ,  $\Delta = 0$ ,  $\tau = 100fs$  and  $t_o = 2\tau$  where used. The excitation conditions for the nonlinear case can be classified with respect to  $\Theta$  and  $\bar{\Theta} = \frac{d^2c}{\hbar} \int_{-\infty}^{+\infty} |\tilde{E}(t)| dt$ . Whereas  $\Theta$  is the standard area of the pulse,  $\bar{\Theta}$  measures its capacity to induce nonlinear effects for a close to zero area pulse. Fig. 4.5 shows the spectral absorption for a standard positive definite Gaussian shaped pulse, where  $\bar{\Theta} = \Theta$ . Here, as expected, an overall suppression of the absorption is observed for increasing  $\bar{\Theta}$ . Gain is reached for inversion ( $\bar{\Theta} = 1.5\pi$ ) and transparency for a  $2\pi$ -pulse. In contrast Fig. 4.6 shows the spectral absorption for a close to  $0\pi$ -pulse ( $\Theta \approx 0$ ) with different  $\bar{\Theta}$  having either  $\Theta = +0.003\bar{\Theta}$  (left graph) or  $\Theta = -0.003\bar{\Theta}$  (right graph, corresponds to first pulse smaller than second one). In the case of linear optics, i.e.  $\bar{\Theta} \approx 0$ , the spectral absorption shows in both cases the usual Lorentzian shape reflecting the homogeneous broadening  $\gamma$ . In the nonlinear case, in contrast to Fig.1, additional spectral structures, i.e. a sharp spectral hole (Fig. 4.6, left) and even gain, or a sharp absorption line (Fig. 4.6, right) occur at the transition frequency  $\omega = 0$  in the rotating frame. Obvi-

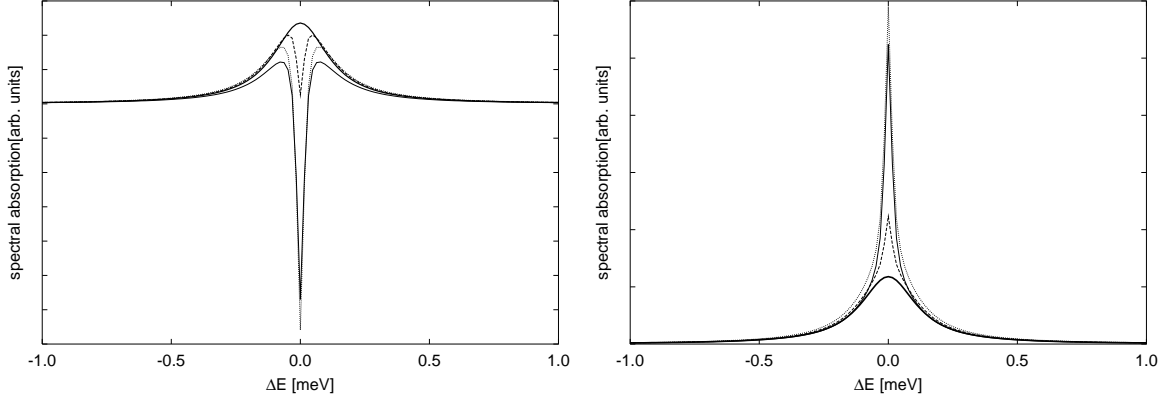


Figure 4.6: Left: Hole burning effect in the spectral absorption of a two-level system for 1 with positive small area pulse ( $\Theta = 0.003\bar{\Theta}$ ) for increasing pulse area  $\bar{\Theta} = 0.01\pi$  (linear case, strong solid),  $0.5\pi$  (dashed),  $1.5\pi$  (dotted),  $2\pi$  (thin solid line). Right: Line narrowing of the spectral absorption of a two-level system excited with negative small area pulse ( $\Theta = -0.003\bar{\Theta}$ ) for increasing pulse area  $\bar{\Theta} = 0.01\pi$  (linear case, strong solid),  $0.5\pi$  (dashed),  $1.5\pi$  (dotted),  $2\pi$  (thin solid line). Published in Ref. [55].

ously, the sharp spectral structures within the homogeneous linewidth of the two-level atom results from a combination of small area pulse and optical nonlinearity. The sign of the pulse area determines the specific structure (spectral hole for  $\Theta > 0$  or line narrowing for  $\Theta < 0$ ).

To understand the numerical results and to extract the basic physical process of the structure formation, an analytical solution for the spectral absorption in the low density limit is discussed. For this purpose, the material equations are iterated up to third order in the optical field envelope to obtain the lowest optical nonlinearity. In first order, i.e. linear optics (l), and for vanishing detuning  $\Delta$ , the  $P$ -equation Eq. 4.4 can be written as:

$$\dot{P}_l = -\gamma P_l + i\frac{\Omega}{2}. \quad (4.6)$$

Using the corresponding conservation law for polarization and density:  $\dot{f} = |P_l|^2$ , the nonlinear (nl) third order polarization is determined by the equation:

$$\dot{P}_{nl} = -\gamma P_{nl} - i\Omega|P_l|^2. \quad (4.7)$$

To obtain the spectral absorption  $\alpha(\omega) = \alpha_l(\omega) + \alpha_{nl}(\omega)$ , Eqs. 4.4, 4.5 are solved in the Fourier-domain. The linear absorption coefficient reads:

$$\alpha_l = \frac{\gamma}{\gamma^2 + \omega^2}. \quad (4.8)$$

Due to the nonlinearity, no exact analytical solution for the nonlinear part is possible. However, the most interesting frequency range for a spectral hole at the transition frequency allows to solve the nonlinear absorption approximately in the limit  $\omega \rightarrow 0$ . For instance, for the envelope of the Rabi-

frequency  $\tilde{\Omega}$  the expansion reads:

$$\begin{aligned}\tilde{\Omega}(\omega) &= \int_{-\infty}^{+\infty} dt \tilde{\Omega}(t) e^{i\omega t} \\ &\approx \int_{-\infty}^{+\infty} dt \Omega(t) + i\omega \int_{-\infty}^{+\infty} dt \Omega(t) t \\ &= \Theta + i\omega M,\end{aligned}\tag{4.9}$$

where for close to  $0\pi$ -pulses,  $\Theta \ll \omega M$ . Within the described approximation scheme the nonlinear absorption coefficient reads:

$$\alpha_{nl} = -\frac{2}{M} \frac{\tilde{f}}{\gamma + \gamma_p} \left( \frac{\gamma}{\omega^2 + \gamma^2} + \frac{\gamma_p}{\omega^2 + \gamma_p^2} \right).\tag{4.10}$$

The nonlinear absorption contains two Lorentzian contributions where the first has the width of the original transition. The second contains a width parameter  $\gamma_p = \Theta/M$  which depends only on pulse parameters such as pulse area  $\Theta = \int_{-\infty}^{+\infty} dt \Omega(t)$  and the first momentum  $M = \int_{-\infty}^{+\infty} dt t \Omega(t)$ . The sharp spectral features within the homogeneous linewidth (Fig. 4.6) can be explained as follows: For vanishing pulse area the broadening  $\gamma_p$  approaches zero and from Eq. 4.10 it can be recognized that in this limit, the nonlinear absorption  $\alpha_{nl}$  contains a sharp, delta-like contribution  $\lim_{\gamma_p \rightarrow 0} \frac{\gamma_p/\pi}{\omega^2 + \gamma_p^2} \approx \delta(\omega)$  directly at the transition frequency ( $\omega = 0$  in the rotating frame) for resonant excitation. This contribution which results directly from the  $0\pi$ -property of the input pulse can be significantly sharper than the homogeneous linewidth contribution:  $\gamma_p \ll \gamma$ , and leads to the spectral structures observed in the numerical results in Fig. 4.6. More importantly, the nonlinear coefficient  $\tilde{f} = \int_{-\infty}^{+\infty} dt \Omega(t) |P_l|^2$  allows a direct physical interpretation of the features.  $\tilde{f}$  accounts for a nonlinear, retarded ( $P_l \propto \int^t dt' E(t')$ ) wave-mixing process [56] by the incident optical field  $\Omega$  and the linear first order polarization  $P_l$ . The wave-mixing process is due to the two-level saturation nonlinearity of the two-level transition. Of course, to understand Fig. 4.6 in detail, the sign of the delta-like contribution is important, because the original absorption in Fig. 4.6 is reduced (right graph, hole burning) or increased (left graph, line narrowing). The value of  $\alpha_{nl}$  at the transition frequency is given by  $\alpha_{nl}(\omega = 0) = -\frac{2\tilde{f}}{\Theta\gamma}$ . Therefore, its sign is determined by the sign of  $\tilde{f}/\Theta$ . Whereas  $\Theta$  is directly determined by the pulse properties, the sign of the factor  $\tilde{f}$  is not trivially given and must be calculated. Here we note that by a detailed analysis, using delta-like pulse envelopes in time domain, it can be shown that the sign of  $\tilde{f}$  is always positive for the conditions used in this paper. Therefore  $\alpha_{nl}(\omega = 0) < 0$  for  $\Theta > 0$  and  $\alpha_{nl}(\omega = 0) > 0$  for  $\Theta < 0$ , which is consistent with the numerical results.

In conclusion, the nonlinear spectral absorption of two-level transitions excited by large envelope  $0\pi$ -pulses exhibits sharp hole burning or line narrowing structures, depending on the used pulses. These phenomena can be used as a tool for nonlinear spectroscopy within the homogeneous linewidth of a transition and to develop frequency filters of extreme quality.

## Chapter 5

# Quantum wells

Semiconductor quantum wells are created by embedding a thin film of one semiconductor material between another semiconductor material. If the well material has a band gap energy smaller than the surrounding a potential minimum is created into which carriers can be confined. Using methods like the molecular beam epitaxy it is possible to control the layers thickness of these heterostructures on the atomic scale and even below with negligible fluctuations. Important for the theoretical modelling is, that the motion of the carriers is only confined in one direction, in the plane of the well motion of the electrons is still possible. This reduction to a two-dimensional plasma leads to a modified density of states which is one of the most important reasons, why most commercial semiconductor lasers are based on quantum well heterostructures. Additionally the confinement leads to a splitting of the band into several subbands.

All in all, the electron dynamics of interband transitions in quantum wells does not qualitatively differ from that in bulk material. The modified density of states and the different rates for scattering events between electrons and between electrons and phonons of course leads to quantitative differences in the electron dynamics, but apparently not to completely new effects. This changes, if several quantum wells are considered. In these multiple quantum well (MQW) structures one can use interference effects to strongly couple the different wells via the electromagnetic field. Since the material response changes the light field one obtains a very strong recursive light-matter coupling that is investigated in section 5.1.

A qualitatively new situation compared to bulk semiconductors is given due to the presence of subbands as result of the quantum confinement of carriers in quantum wells. The physics of optical transitions between these subbands is discussed in section 5.2 considering both a Markovian and a quantum kinetic theory.

### 5.1 Interband transitions in MQW Bragg structures<sup>1</sup>

A system of multiple quantum wells (MQW) is considered in order to study strong light-matter coupling. It is assumed that the quantum wells are thin compared to the wave length of the incident light and that they are separated by a constant distance  $l$ . This type of MQW structure is closely related to Bragg reflectors: They have the linear optical property to reflect light with a specific wavelength [15]. Based on destructive interference, they are usually modeled by alternating layers of two materials with different (mostly frequency independent) refractive indices and are technologically utilized

---

<sup>1</sup>Results, especially graphs of this section are partly published in Refs. [57, 58, 59].

for lossless mirrors of high quality. Since resonant excitation of a semiconductor material is considered here, also the energetic position of the optically allowed transitions becomes relevant. In order to study strong optical coupling between the quantum wells, a Bragg scheme is chosen, where the spacing between the wells is given by half the wavelength of light with the transition energy  $\hbar\omega_g$  (i.e.  $l = \lambda/2$  with  $\lambda = c_0 n_b / \omega_g$ ). For these distances it is plausible to assume that the different quantum wells are coupled only by the light field via Maxwell's equations and that there is no wavefunction overlap or direct many-body interaction between the wells.

The  $z$ -axis has been selected as confinement and propagation direction, the  $n$ -th quantum well is therefore positioned at  $z_n = nl$  (with  $l = \lambda/2$ ). Hence, each well leads to a polarization contribution as described in Eq. 2.32. Assuming identical quantum wells and homogeneous excitation in the unconfined dimensions the total polarization can be expressed:

$$P(\mathbf{r}, t) = \sum_n \delta(z - z_n) P_n(t)$$

$$\text{with } P_n(t) = \frac{1}{V_f} \sum_{\mathbf{k}} \mathbf{d}_{vc}(0) p_{n\mathbf{k}}(t) + c.c.$$

In principle the microscopic coherence  $\bar{p}_{n,\mathbf{k}} = \langle a_{n\mathbf{k}}^+ a_{n\mathbf{k}} \rangle$  and all electronic operators are labeled by the quantum well index  $n$ . However the equations of motion are identical (with the exception the spatial coordinate of the driving electric field  $\mathbf{E}_n = \mathbf{E}(z_n)$  differs, hence for simplicity the quantum well index  $n$  is no longer explicitly written in the following. Nevertheless the dynamics of these quantities has to be calculated independently for each quantum well.

### 5.1.1 Material description

Based on the expectation that the radiative coupling between the quantum wells dominates the relaxation dynamics of the system, in addition to the electron-field coupling only the Coulomb interaction is included and evaluated in mean-field approximation, i.e. both electron-electron scattering and electron-phonon coupling are not considered. Taking one subband in each of two bands (v,c) into account, the equations of motion of the microscopic polarization and for each quantum well can be derived from the combined Hamiltonian of Eqs. 2.3, 2.14, 2.17 using the Heisenberg equation. In the rotating wave approximation (see section A.2) they read [2]:

$$\begin{aligned} \dot{p}_{\mathbf{k}} &= -i(\omega_{\mathbf{k}} + \Delta - i\gamma_0) p_{\mathbf{k}} + \frac{i}{2} \tilde{\Omega}(1 - 2f_{\mathbf{k}'}) \\ &\quad - \frac{i}{\hbar} p_{\mathbf{k}} \sum_{\mathbf{q}_f \neq 0} V_{\mathbf{q}_f} (1 - 2f_{\mathbf{k}+\mathbf{q}_f}) + \frac{i}{\hbar} (1 - 2f_{\mathbf{k}}) \sum_{\mathbf{q}_f \neq 0} V_{\mathbf{q}_f} p_{\mathbf{k}+\mathbf{q}_f}, \\ \dot{f}_{\mathbf{k}} &= -2\gamma_0 f_{\mathbf{k}} - \text{Im}(\Omega^* p_{\mathbf{k}} + \frac{2}{\hbar} p_{\mathbf{k}} \sum_{\mathbf{q}_f \neq 0} V_{\mathbf{q}_f} p_{\mathbf{k}+\mathbf{q}_f}^*). \end{aligned} \quad (5.1)$$

The transition frequencies are given by  $\omega_{\mathbf{k}} = \frac{\hbar k^2}{2m_r}$  with the reduced mass  $m_r = (m_v^{-1} + m_c^{-1})^{-1}$ . Assuming a very thin layer, which confines the motion of electrons and holes into a two dimensional plane, the unscreened Coulomb matrix element is given by  $V_{\mathbf{q}_f} = \frac{e_0^2}{2\epsilon_0 \epsilon_b V_f a_0 q_f}$ , where  $a_0$  is the excitonic radius [17].

The dephasing constant  $\gamma_0$  has been introduced to account for many-body dephasing contributions but is only relevant for modelling of small structures consisting of a single or only very few wells which are not dominated by radiative decay. For such a single uncoupled quantum well the linear response can be directly solved by mode expansion and results in the 2d Elliot formula [2]. The linear absorption spectrum resulting from this formula is displayed in Fig. 5.1. It consists of a continuum

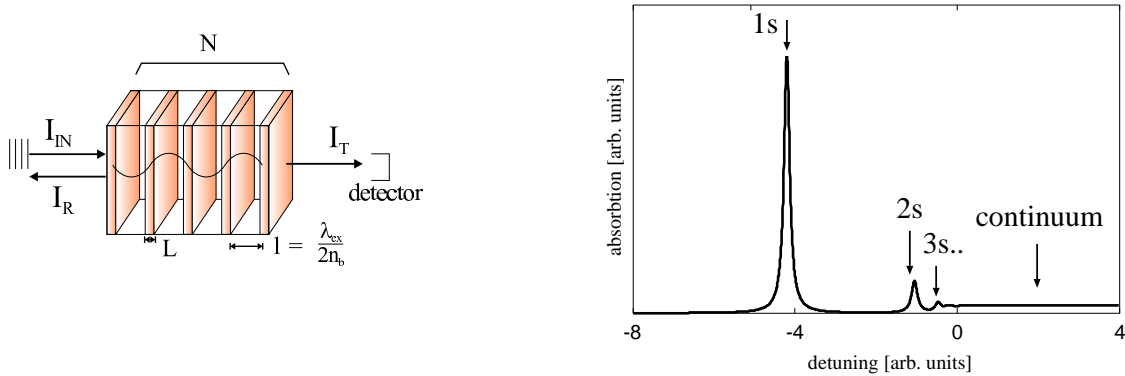


Figure 5.1: Left: Scheme of the multiple quantum well (MQW) structure fulfilling the Bragg condition. Right: Linear absorption spectrum of a single uncoupled quantum well as given by the 2d Elliot formula.

contribution and a series of excitonic resonances below the band gap (1s and 2s excitons are clearly visible, higher resonances are melted with the continuum edge). As for a two-dimensional free carrier plasma the shape of the continuum can be represented by a step function. The Elliott formula does not include the electromagnetic problem but only solves the electronic problem of single uncoupled quantum well. Hence no radiative damping emerges from the equation. Line broadening has to be taken into account by the phenomenological dephasing constant  $\gamma$ . For a correct description, the Maxwell problem has to be solved self-consistently together with the material equation of motion. This coupled problem is evaluated by a combination of the one-dimensional FDTD method (see chapter 3.4.1) for the electromagnetic part and a Runge-Kutta method for the electronic part.

### 5.1.2 Linear propagation two-level MQW structures

In order to study principal effects of the strong radiative coupling in a first step only the reduced dynamics of an isolated 1s exciton transition represented by a two-level system is considered (compare chapter A). Due to the recursive coupling to the light field an additional radiative broadening  $\Gamma_1$  occurs in addition to the phenomenologically introduced dephasing  $\gamma$ . For a single well which is coupled to the light field it is given by [57]:

$$\Gamma_1 = \frac{\omega_g d_{vc}^2}{2\epsilon_0 n_b c \pi a_0^2 \hbar}.$$

For parameter values (see table 5.1) adapted to an InGaAs heterostructure[60] one obtains  $\Gamma_1 \approx 0.06 meV$ . If instead of a single quantum well a MQW Bragg structure with  $N$  wells is considered, the collective radiative coupling between the quantum wells changes the absorption spectra and leads to an enhancement of the radiative decay, called superradiance [61]. Using a SVEA approach (as described in section 3.5, for details see Ref. [62, 63, 64, 57]) which is valid for a structure consisting of only a few wells ( $N < 20$  for these parameters), one can show that the line broadening is proportional to the number of wells. In this limit the absorption (defined in Eq. 3.5) can be represented by a Lorentzian resonance curves. Hence MQW systems with a strongly limited number of quantum wells behave exactly like a single quantum well with an enhanced dipole moment. Fig. 5.2, showing the linear absorption for  $N = 1, 10, 20$ , illustrates this line width enhancement by superradiance. Evidently the overall dephasing dynamics is dominated by radiative broadening even for small MQW systems consisting of only a relatively small number of wells. It can be seen, that in contrast to propagation in

| quantity        | value                       | meaning                                       |
|-----------------|-----------------------------|---|
| $d_{vc}$        | $0.42e\text{nm}$            | dipole transition element                     |
| $\epsilon_b$    | 12.7                        | background dielectric constant                |
| $\epsilon_g$    | $1.5eV$                     | band gap energy                               |
| $\hbar\gamma_0$ | $0.55meV$                   | additional dephasing constant                 |
| $m_c$           | $0.067m_0$                  | effective mass of conduction band electron    |
| $m_v$           | $0.377m_0$                  | effective mass of valence band hole           |
| $\rho_d$        | $4.1 \times 10^{12}cm^{-2}$ | oscillator density for two-level calculations |
| $L$             | $8.5nm$                     | width of a single quantum well                |

Table 5.1: Parameters for MQW calculations representing InGaAs quantum wells. Dipole moment  $d_c$  and dephasing constant  $\gamma_0$  are obtained by comparing simulated absorption spectra with experimental findings[60].

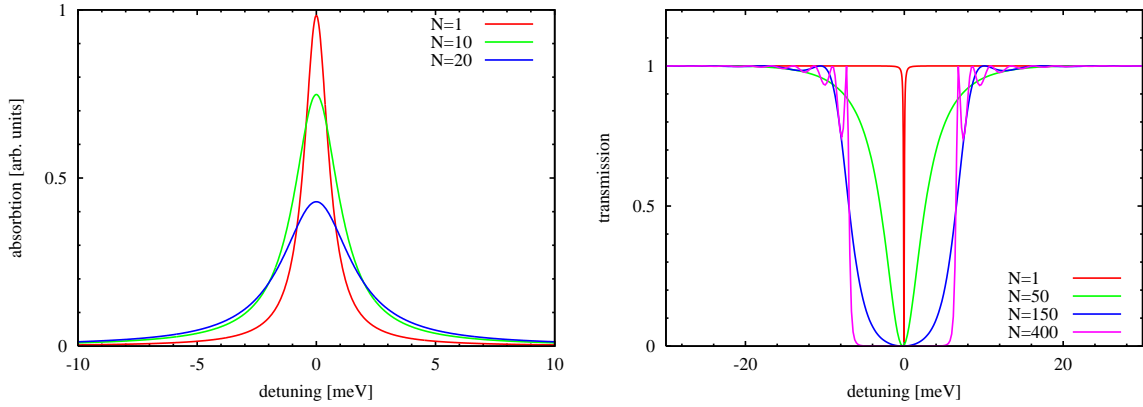


Figure 5.2: Spectra for MQW structure consisting of quantum well modelled using a two-level scheme. Left: Absorption spectrum calculated using the SVEA approach for MQW structures consisting of  $N=1, 10$  and  $20$  quantum wells, Right: Linear transmission spectra calculated with the one-dimensional FDTD method for  $N=1, 50, 150$  and  $400$ . After [57].

bulk media (compare chapter 4) the linear absorption function  $\alpha(\omega)$  is no longer independent of the propagation length. Hence the spectral transmission  $T(\omega) = \frac{|E_T|^2}{|E_{in}|^2}$  as introduced in chapter 3 will be studied in the following.

For a higher number of wells the SVEA –neglecting backscattering and retardation effects– breaks down. Then the response of the system has to be calculated a method which numerically evaluates the full Maxwell equations without further approximations, like the FDTD approach (see chapter 3.4.1). The effects beyond the SVEA can be seen in Fig. 5.2 which shows the transmission spectrum for MQW structures with up to 400 radiatively coupled quantum wells. A roughly Lorentzian shape with increasing line width can be identified for up to 50 quantum wells, but for larger structures the line width does not further increase and the shape of the transmission begins to converge into a rectangular shape. Hence only components of an incident pulse, which lie outside this frequency range can propagate. All other components are reflected and do not contribute to the transmission signal. The shape and width (10meV) of the stop band is in good agreement with experimental results which have been reported for an InGaAs MQW structures[65].

### 5.1.3 Nonlinear propagation two-level MQW structures

Solitary traveling waves exist in many extended systems and are of special interest not just because they are often the only analytical solution which can be found, but also for their technological impact as a lossless light transport mechanism [66]. While a solitary solution is difficult to derive for a system of finite size, one can map the coupled light-matter problem onto a Sine-Gordon equation if an infinite number of quantum wells in Bragg condition is assumed [27, 66]. The emerging Sine-Gordon equation  $c^2 \partial_z^2 \Theta(z, t) - \partial_t^2 \Theta(z, t) = -2\tau_c^{-2} \sin \Theta(z, t)$  with  $\tau_c = \sqrt{\frac{8\pi\epsilon_0\epsilon_b\hbar c}{\omega^2 \sigma d_{vc}^2}}$  has several known solutions (which are connected via the Bäcklund transformations). Considering only the simplest solution, the Rabi oscillation  $\Omega(z, t) = \dot{\Theta}(z, t)$  reads:

$$\Omega(z, t) = 2\sqrt{\frac{2}{\tau_c^2(u^2 - 1)}} \operatorname{sech} \left( \sqrt{\frac{2}{\tau_c^2(u^2 - 1)}} \left( t - \frac{u}{c}z \right) \right).$$

It describes a sech-shaped wave (defined in appendix B.1) which travels with the speed  $c/u$ . The parameter  $u$  must fulfill  $u > 1$  to ensure a real-valued solution and in addition to the travelling speed it determines the width of the pulse. Independently of  $u$  the time-integrated pulse area always evaluates to  $\Theta = \int_{-\infty}^{\infty} \Omega(t) dt = 2\pi$ , hence it coincides with the pulse area needed for one complete Rabi oscillation of the density in a two-level system (see section A.2).

Real systems are of course limited in size. Specifically MQW Bragg structures can only reliably be manufactured with up to several hundred quantum well layers. From propagation of Bragg grating solitons in fibre it is known that very long distances are needed for soliton formation [67]. Hence, to answer the question, whether solitary waves can exist in real, finite MQW Bragg structures, the problem has to be investigated numerically. Hence, the nonlinear propagation of a  $2\pi$ -sech-pulse has been simulated using the combined Runge-Kutta-FDTD approach described above (with zero phenomenological dephasing) and is displayed in Fig. 5.3 (left column) for different pulse durations. The calculation shows, that very short pulses ( $\tau = 20fs$ , top) travel without alterations shape or amplitude. This is in contrast to linear optics where the pulse is strongly distorted into polariton beats during propagation. For the nonlinear excitation with a  $2\pi$  pulse the transmission is almost exactly equal to the incident pulse and only a very small signal can be seen in reflection. This effect is known as self-induced transparency (SIT) in unstructured atomic vapor[27]. The opposite extreme of long pulses

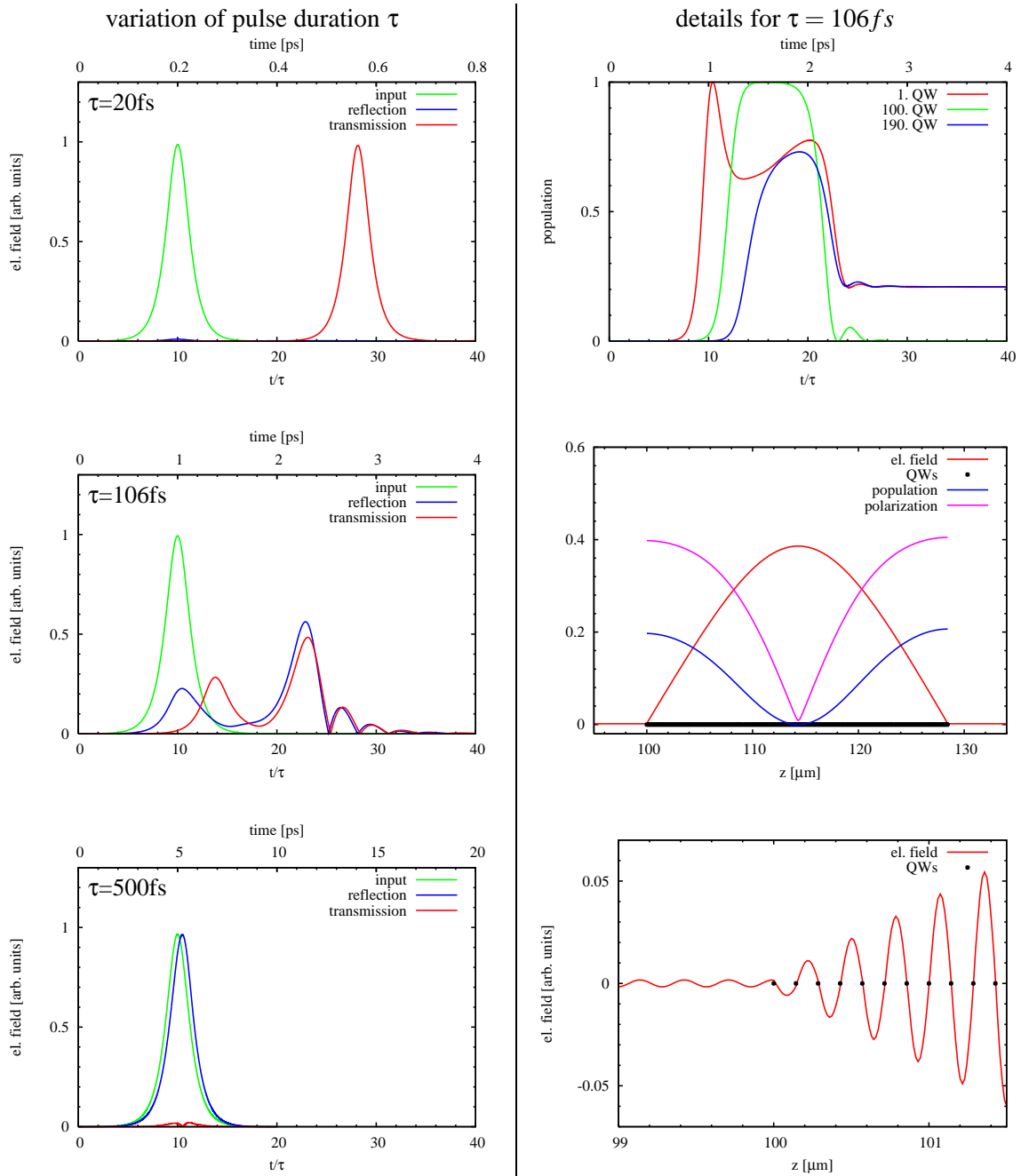


Figure 5.3: Nonlinear excitation of two-level MQW structure. Left column: Temporal dynamics of the reflected (blue curve) and transmitted (red curve) electric field in comparison with the incident pulse (green curve) for pulse durations  $\tau = 20, 106, 500$  fs (from top to bottom). Right column (details for 106fs pulse): top: Occupation dynamics in the 1st, 100th and 190th quantum well, middle: spatially resolved electric field, occupation and polarization for stationary situation, bottom: magnification of the electric field at the left boundary of the MQW structure. After [57].

( $\tau = 500fs$ , bottom) corresponds to spectral excitation completely within the stop band. As one would expect, the propagation in this spectral region is strongly suppressed. Most of the light is reflected back and only a small part is transmitted through the sample. The intermediate situation of a pulse which has roughly the same spectral width as the band gap ( $\tau = 106fs$  corresponding to a spectral FWHM of about  $10meV$ ) whereas lying mostly in the stop band shows a different behavior: As initial response the MQW structure immediately reflects and transmits parts of the pulse. Additionally, after about 2ps time delay a second response is emitted in both reflection and transmission direction. To understand this result, Fig. 5.3 (right column) gives further information about the processes in the system for this excitation situation. The top graph displays the dynamics of the upper level occupation of quantum wells at different positions. During pulse excitation all quantum wells are first completely inverted and subsequently coherently depopulated to some extent. The 100th quantum well, lying in the center of the structure, is pumped into complete inversion and stays there for a substantial time (1ps) until decaying back into its ground state. Quantum wells at the beginning and the end of the structure first show a partial decay but subsequently a second increase of the upper level population, that is not directly induced by the incident pulse, occurs. However, this decay is only partial and the upper level occupation remains on a nonvanishing constant value. In contrast to chapter 6.8 also the polarization (not shown) does not vanish (but only oscillates with a constant amplitude), therefore one would still expect radiative decay. All in all, the system converges into a stationary solution in which the excited states and therefore energy (population) and coherent excitation (polarization) can be stored. This is further illustrated in Fig.5.3(e) showing the spatially resolved electric field, polarization and upper state population for the stationary situation, i.e. few ps after pulse excitation. Both the polarization and occupation have their maxima at the boundaries of the structure and vanish in the middle. The electric field forms an oscillating standing wave within the structure with a profile that has its maximum in the middle and declines towards the boundaries. A magnification of the electric field as given in Fig. 5.3 finally helps to understand why a stationary solution exists and how it is preserved. First, one can observe that the electric field is zero at the quantum well positions (with only small deviations at the MQW boundaries). Therefore the material equations are not driven and remain stationary. However the polarization is nonvanishing and occurs in the Maxwell equations as a driving term. In the balanced stationary condition it exactly cancels out propagating fields from the surrounding which enter the quantum well, hence stabilizing the stationary solution. Further studies have shown, that inclusion of a phenomenologic dephasing, which has not been considered in the shown calculations, would lead to a decay the trapped excitation.

#### 5.1.4 Two-band semiconductor quantum wells

Especially for ultrashort pulses, which are spectrally broad, the two-level approximation is inappropriate as it corresponds to a truncation of the mode expansion by taking only the 1s exciton into account. For spectrally broader pulses, however, also exciton states and the band continuum are coherently excited. Hence the full material dynamics as described by Eqs. 5.1 has to be evaluated together with the Maxwell equations. This coupled system describing propagation in a semiconductor MQW system has been evaluated for parameters given in Table 5.1 resembling an InGaAs material. The results for MQW structures consisting of  $N = 60$  and  $N = 200$  quantum wells are given in Fig. 5.4. As for the simplified two-level system a stop band located around the exciton resonance at  $-11meV$  forms. As above, the band gap is stronger and converges towards a rectangular shape for a larger number of quantum wells. Exactly at the spectral position of the 1s exciton resonance a small dip, known from structured atomic vapor[68], can be seen within the stop band for  $N = 200$ . In addition to the main band gap around the 1s excitonic resonance the transmission is also reduced for higher energies in

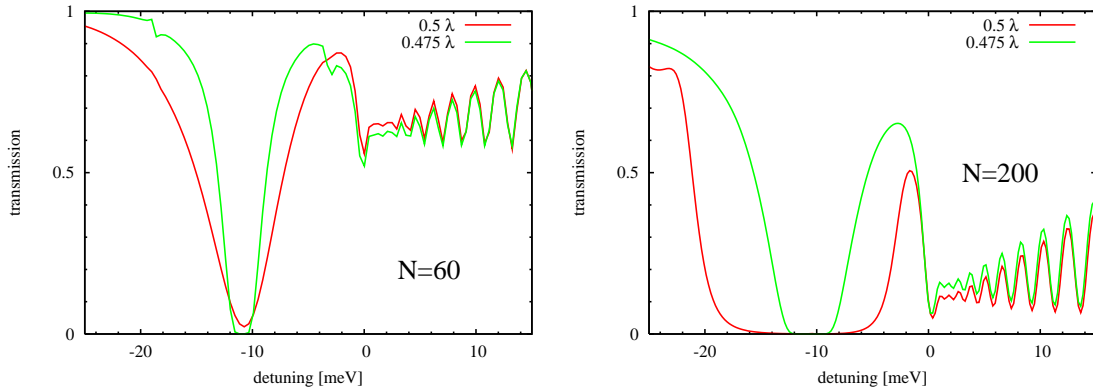


Figure 5.4: Simulated transmission spectra for a semiconductor MQW structure consisting of  $N = 60$  (left) and  $N = 200$  (right) quantum wells. [57]

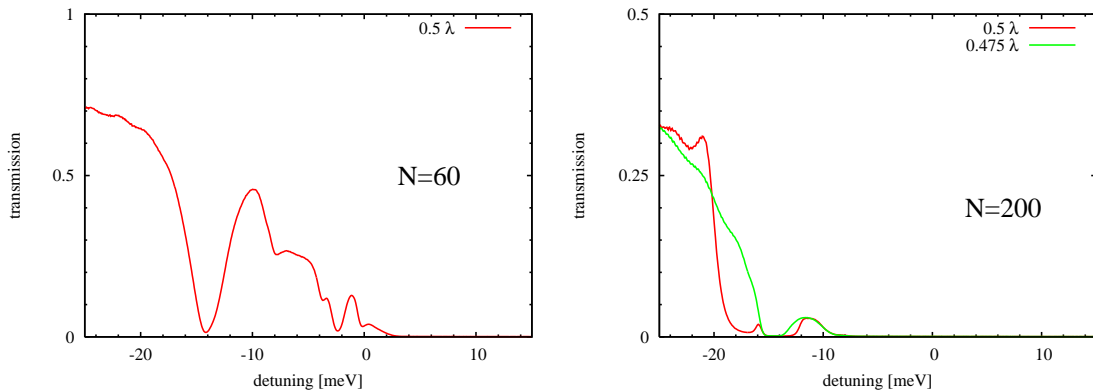


Figure 5.5: Experimental transmission spectra for InGaAs MQW structures consisting of  $N = 60$  (left) and  $N = 200$  (right) quantum wells. Data provided by N. Nielsen [59, 69].

the continuum region. While the spectral oscillations are mainly artifacts from the finite numerical discretization, the 2s exciton resonance can still be clearly identified. For comparison, Fig. 5.5 shows experimental transmission spectra provided by N. Nielsen [59, 69]. They were obtained using wedged InGaAs MQW structures, which allow to study deviations from the Bragg condition. The experimental transmission spectra show the same qualitative structure as predicted by theory: In addition to a pronounced stop band around the 1s exciton resonance also the continuum states lead to a reduction of the transmission. Also other features, like the small dip in the 1s exciton stop band for the MQW structure consisting of  $N = 200$  quantum wells are nicely reproduced. However, the spectral width of the stop band is smaller than simulated and the transmission suppression in the continuum region is much stronger. All in all no quantitative but good qualitative agreement is reached.

The wedge geometry of the MQW sample allows to study effects in geometries deviating from the exact Bragg condition. The experimental transmission spectrum for a quantum well spacing of  $l = 0.475\lambda$  is additionally displayed in Fig. 5.5 (green curve) and shows that the deviation from the exact Bragg condition leads to a considerable reduction of the spectral width of the stop band. This effect is in good agreement with theoretical calculations (given in Fig. 5.4, green curves) and

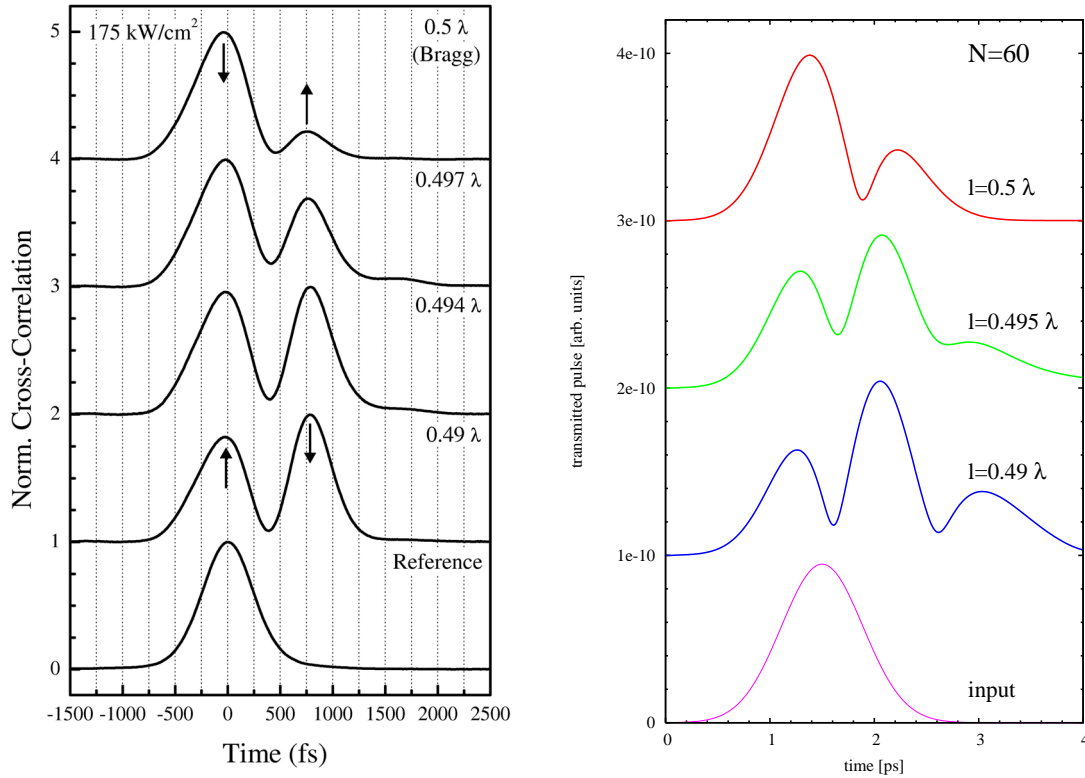


Figure 5.6: Comparison of experimental (left) and simulated (right) dynamics of the transmitted field for deviations from the exact Bragg condition ( $l = 0.5\lambda$ ). Experimental data from a InGaAs MQW structures consisting of 60 quantum wells provided by N. Nielsen [59, 69], theory after [57].

results from the very sensitive dependence on the exact destructive interference condition for collective radiative dampening, as e.g. known from the dielectric Bragg reflector. Since it is difficult to maintain the perfect Bragg condition in experiment and the stop band width is very sensitive to deviations, this may at least partly explain the differences between the predicted and measured stop band widths, which have been discussed above. This sensitivity of the system with respect to fulfillment of the Bragg condition is further studied in the temporal dynamics of the transmission signal for linear excitation and is displayed in Fig. 5.6 comparing experiment (left) with simulation (right). For all well spacings the transmission signal exhibits pulse beatings as known from propagation in atomic vapor [27]. However, for deviation from Bragg condition the structure of the beating changes: For  $l = 0.5\lambda$  only two maxima are visible and the first oscillation is much larger than the second one. For decreasing quantum well spacing, the second maximum becomes stronger than the first and further oscillations occur. This additional beating is very weak in the experimental signal but very clear in the simulations. This modification in the polariton beating structure is mainly caused by changes in the phase relations between the polarizations in the quantum wells.

Fig. 5.7 shows the experimental (left) and simulated (right) transmission dynamics of a MQW structure consisting of 60 wells in exact Bragg geometry for transition from the linear to the nonlinear optical excitation regime. In both, theory and experiment one can observe a reduction of polariton beating for increasing pulse intensities. For strong excitation the beating completely vanishes and the original pulse shape is restored and for even higher intensities shoulders occur in the signal. These

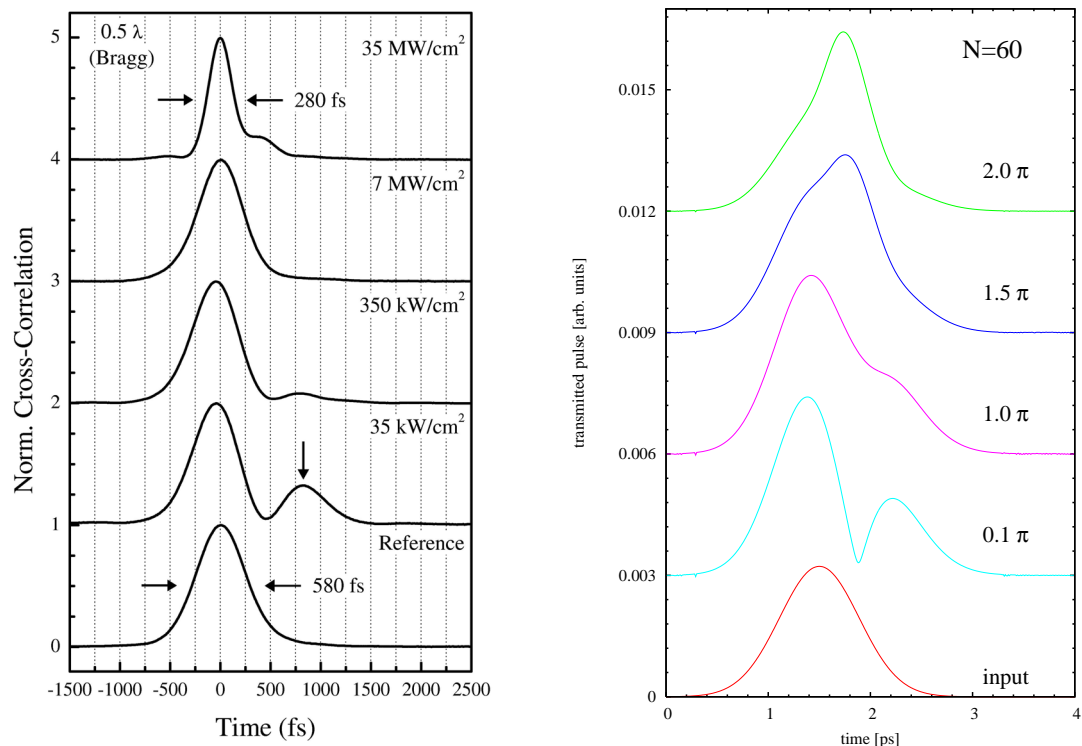


Figure 5.7: Dynamics of the transmitted field for nonlinear excitation. Compared are experimental (left) and simulated (right) results for a InAs MQW structure consisting of 60 wells. Experimental data provided by N. Nielsen[59, 69], theory after [57].

results are in agreement with nonlinear resonant pulse propagation in bulk semiconductors. However, for a pulse intensity of  $35 \text{ MW/cm}^2$  the experiment shows a strong pulse compression which is not predicted by the simulations. Further studies have shown that this temporal compression can be attributed to near-resonant self-phase modulation effects in the GaAs substrate of the experimentally investigated sample [59, 70].

## 5.2 Intersubband transitions<sup>2</sup>

Besides a different density of states and other coupling functions, the main feature of a quantum well compared to bulk material is the existence of subbands which form due to the quantum confinement of the electronic wavefunctions. Transitions between these subbands shows qualitatively new effects mainly resulting from the very similar curvatures of the energy dispersion of subbands in a band [75]. While e.g. valence and conduction band in a direct semiconductor have opposite curvatures, the different subbands of the conduction band all have a positive curvature, i.e. they all have a minimum at the  $\Gamma$ -point. Subband transitions can of course only be induced if the initial states is at least partially populated and the final states is not completely occupied. This situation is not naturally encountered in a semiconductor, but can easily be reached either by a preceding interband transition which transfers electrons from the valence into the conduction band leaving holes in specific subbands of the valence band and populating some subbands of the conduction bands with electrons. Also, one can induce carriers using electric current. Alternatively, one can directly implant electrons or holes, e.g. by adding a doped material in the vicinity of the quantum well. Whereas the first two methods require continuous external pumping in order to reach a (floating) equilibrium situation, the doping method naturally leads to a stationary state and is therefore used in the following.

The possibility to directly control the energetic spacing between subbands by variation of the well width has lead to a considerable technological interest in intersubband transitions in quantum wells. Today's manufacturing methods allow a precise control of the layer width on and below the atomic scale. Within the limits of the used material this allows to design the intersubband transition frequencies with great precision and flexibility. Especially in the low infrared and THz regime applications as laser or detector have been proposed and several commercial products are already available. For these applications not only the quantum wells, in which intersubband transitions occur, are designed but also the surrounding structure. In so called quantum cascade laser (QCL) a series of active layers successively converts the potential energy of the electrons into a cascade of photons [76]. These structures consists of a complex series of layers of different materials which provide not only the several active layers but also a super-lattice for the electronic transport and an optical waveguide. In addition to their technological potential, intersubband transition provide a unique possibility to study many-particle effects, since parameters like the subband dispersions and well widths allow direct control over many-body interactions like the electron-electron and electron-phonon coupling.

In this work only intersubband transition in single quantum wells are considered. Extensions of the theory towards a multiple well structure, nonlinear excitation and quantum optics are given in Refs. [73, 72, 18, 77]. The material dynamics is considered in several steps: First, the influence of different subband dispersions is discussed for the interaction-free two-dimensional electron gas. In a next step, Coulomb interaction is included on a Hartree-Fock approximation level. Afterwards, dephasing is microscopically calculated by considering electron-electron in second Born approximation and electron-phonon scattering in a Markovian first order correlation expansion. Finally effects beyond the Markov approximation are studied for the electron-phonon coupling. The impact of the quantum

<sup>2</sup>Parts of the data and discussions of this section are published in Refs. [71, 58, 72, 18, 73, 74].

kinetic electron-phonon interaction is investigated for both linear absorption spectra and intersubband Rabi oscillations.

### 5.2.1 Description of confinement, energetic structure

The two-dimensional confinement is assumed to lie in the  $z$ -direction and is modeled by a potential with width  $L$  and infinite borders:

$$V_{conf}(z) = \begin{cases} 0 & |z| \leq L/2 \\ \infty & \text{else} \end{cases}.$$

Only transitions between the lowest two subbands of the conduction band are considered. Hence, the occurring confinement wave functions are  $\phi_1(z) = \sqrt{2/L} \sin \frac{2\pi z}{L}$  for the upper subband and  $\phi_2(z) = \sqrt{2/L} \cos \frac{\pi z}{L}$  for the lower subband [2, 17]. The difference of the subband energy offsets, i.e. subband energy gap, is given by

$$\varepsilon_g = \frac{3\pi^2 \hbar^2}{2m_z L^2}.$$

The two-dimensional in-plane motion is described by a quadratic dispersion as defined in Eq. 2.4. Due to non-parabolic curvature of the bands, the effective masses for the different subbands are not necessarily the same but can slightly differ [78, 79]. For the used model system (see table 5.2) the effective masses of the upper band are higher than for the lower band. This results in transition energies  $\varepsilon_k = \varepsilon_{1,k} - \varepsilon_{2,k} = \varepsilon_g + \frac{\hbar k^2}{2m_r}$  with a negative reduced mass  $m_r = (m_1^{-1} - m_2^{-1})^{-1}$ . Hence the transition energy reduces for increasing wavenumber  $\mathbf{k}$ . This is in contrast to interband transitions, where the band curvatures are always opposite ensuring a positive reduced mass [2].

Since the electrons are prepared into the conduction band by doping they cannot transit into the completely filled valence bands. However, by scattering processes within the conduction band the electrons can relax into Fermi distributions

$$f_{i,\mathbf{k}} = \frac{1}{\exp(\beta(\varepsilon_{i\mathbf{k}} - \mu)) + 1},$$

with  $\beta = \frac{1}{k_B T}$  [3]. The chemical potential  $\mu$  is implicitly determined by the carrier density  $n$ , which has to fulfill  $n = \frac{1}{V_f} \sum_{i\mathbf{k}} f_{i\mathbf{k}}$ . For occupation of only the lower subband the chemical potential is therefore given by  $\mu = \frac{1}{\beta} \ln \left( e^{2\pi \hbar^2 \beta n / m_2} - 1 \right)$  [2].

The Hamiltonian describing the physical situation consists of the kinetic energy (Eq. 2.3), the classical electron-light coupling (Eq. 2.14), the Coulomb interaction (Eq. 2.17) and the Fröhlich coupling of electrons to LO phonons (Eq. 2.21). The equations of motion described in the following are used for the calculations in sections 5.2.2 to 5.2.4 and rely on the Markov approximation. The electron-phonon coupling is treated within in a first order correlation expansion using a Markovian coupling to the phonon bath. The Coulomb interaction is divided into a Hartree-Fock part describing effects on the mean-field level, and an electron-electron scattering part, which is derived in second Born approximation. Extraordinary about this system is the presence of macroscopic charges leading to a nonvanishing Coulomb interaction for  $\mathbf{q} = 0$ . This results in an additional depolarization contribution already occurring on mean-field level. The emerging equation for the intersubband coherence  $p_k^{21}$  resembles that of the interband quantity (Eq. 5.1) but additionally include the depolarization and correlation contributions [1, 71, 73]:

$$\frac{d}{dt}p_{\mathbf{k}}^{12} = \underbrace{\frac{i}{\hbar}(\varepsilon_{\mathbf{k}}^1 - \varepsilon_{\mathbf{k}}^2)p_{\mathbf{k}}^{12}}_{\text{transition energies}} + \underbrace{i\Omega(t)[f_{\mathbf{k}}^1 - f_{\mathbf{k}}^2]}_{\text{coupling to light field}} \quad (5.2)$$

$$+ \underbrace{\frac{i}{\hbar} \sum_{\mathbf{k}'' \neq 0} (V_{\mathbf{k}''}^{1221} - V_{\mathbf{k}''}^{1111})f_{\mathbf{k}-\mathbf{k}''}^1 p_{\mathbf{k}}^{12} - \frac{i}{\hbar} \sum_{\mathbf{k}'' \neq 0} (V_{\mathbf{k}''}^{1221} - V_{\mathbf{k}''}^{2222})f_{\mathbf{k}-\mathbf{k}''}^2 p_{\mathbf{k}}^{12}}_{\text{exchange}} \quad (5.3)$$

$$+ \underbrace{\frac{i}{\hbar} \sum_{\mathbf{k}'' \neq 0} V_{\mathbf{k}''}^{2121} p_{\mathbf{k}-\mathbf{k}''}^{12} [f_{\mathbf{k}}^1 - f_{\mathbf{k}}^2]}_{\text{exciton}} - \underbrace{\frac{2i}{\hbar} \sum_{\mathbf{k}'' \neq 0} V_0^{2112} p_{\mathbf{k}''}^{21} [f_{\mathbf{k}}^1 - f_{\mathbf{k}}^2]}_{\text{depolarisation}} \quad (5.4)$$

$$+ \underbrace{\frac{2\pi}{\hbar} \sum_{i=1,2} \left[ -\Gamma_{\mathbf{d}}^{i,\text{cc}} p_{\mathbf{k}}^{12} + \sum_{\mathbf{k}',\mathbf{q}} \Gamma_{\text{nd1}}^{i,\text{cc}} p_{\mathbf{k}'-\mathbf{k}''}^{12} + \sum_{\mathbf{k}''} \Gamma_{\text{nd2}}^{i,\text{cc}} p_{\mathbf{k}+\mathbf{k}''}^{12} - \sum_{\mathbf{k}'} \Gamma_{\text{nd3}}^{i,\text{cc}} p_{\mathbf{k}'}^{12} \right]}_{\text{Coulomb correlations}} \quad (5.5)$$

$$+ \underbrace{\frac{2\pi}{\hbar} \sum_{i=1,2} \left[ -\Gamma_{\mathbf{d}}^{i,\text{cp}} p_{\mathbf{k}}^{12} + \sum_{\mathbf{q}_f} \Gamma_{\text{nd}}^{i,\text{cp}} p_{\mathbf{k}+\mathbf{q}_f}^{12} \right]}_{\text{electron-phonon correlations}}. \quad (5.6)$$

The various diagonal (d) and nondiagonal (nd) scattering elements  $\Gamma$  are given in appendix C.1. The two main parameters whose influence is studied in the following are the well width  $L$  and the temperature. Directly determined by the well width but not important for the calculation, which have been evaluated using the rotating frame approximation (A.8), is the gap energy. Via the form factor, which contains of the wave functions, also the Coulomb matrix element  $V_{\mathbf{q}_f}^{i1,i2,i3,i4}$  (Eq. 2.17) and the electron-phonon coupling elements  $g_{\mathbf{q}}^{ij}$  (Eq. 2.21) are influenced by the well width. The dependence of the effective subband masses on the well width is neglected. The temperature describes the equilibrium state of the particles and enters the equations as distribution functions of the electrons (Fermi distribution) and the phonons (Bose distribution). In order to study the influence of the subband masses, two different material models are considered (see table 5.2). The InAs/AlSb system exhibits a strong difference between the two subband masses, in the GaAs/AlGaAs system both masses are very similar [80]. The equation of motion is evaluated in the random frame (see section A.1.4) using a Runge-Kutta differential equation solver (section B.2.2).

## 5.2.2 Free dynamics

If neither Coulomb interaction nor electron-phonon coupling is considered (Eq. 5.2), the absorption spectrum, i.e. the linear response of the system, is solely determined by the energy structure and the occupation of the energetic states. Fig. 5.8 shows absorption spectra for the InAs and GaAs systems for different temperatures. Since no microscopic dephasing effects are included in these calculations, a phenomenological dephasing with  $\gamma = 1\text{meV}$  has been applied in order to be able to perform a numerical Fourier transformation. The absorption spectra show several similarities between both material systems: First, both spectra are located below the gap energy (detuning  $0\text{meV}$ ). For low temperatures the shape of the absorption spectra is almost rectangular with a width of about  $25\text{meV}$  for InAs and about  $5\text{meV}$  for GaAs. The higher-energy edge at the gap energy is broadened with a constant value of about  $1\text{meV}$  whereas the lower-energy edge increasingly broadens with higher temperature. The schematic illustration in Fig. 5.9 helps to understand these features of the linear absorption spectra.

| quantity           | (a) InAs/AlSb           | (b) GaAs/AlGaAs         | meaning                                      |
|--------------------|-------------------------|-------------------------|--|
| $m_1$              | $0.039m_0$              | $0.073m_0$              | effective mass of the upper subband          |
| $m_2$              | $0.027m$                | $0.069m_0$              | effective mass of the lower subband          |
| $n$                | $5 \times 10^{10}/cm^2$ | $6 \times 10^{11}/cm^2$ | carrier density                              |
| $\epsilon_b$       | 15.68                   | 10.9                    | background dielectric constant               |
| $\epsilon_s$       | 16.8                    | 12.9                    | static dielectric constant                   |
| $\hbar\omega_{LO}$ | 24meV                   | 36meV                   | LO phonon energy                             |
| $L$                | 10nm                    | 10nm                    | quantum well width                           |
| $\epsilon_g$       | 100meV                  | 100meV                  | difference of subband offsets, “subband gap” |

Table 5.2: Default parameters used for intersubband simulations. (a) InAs/AlSb [80], (b) GaAs/Al<sub>0.35</sub>Ga<sub>0.65</sub>As material. Different effective subband masses occur due to non-parabolicity effects [78, 79].

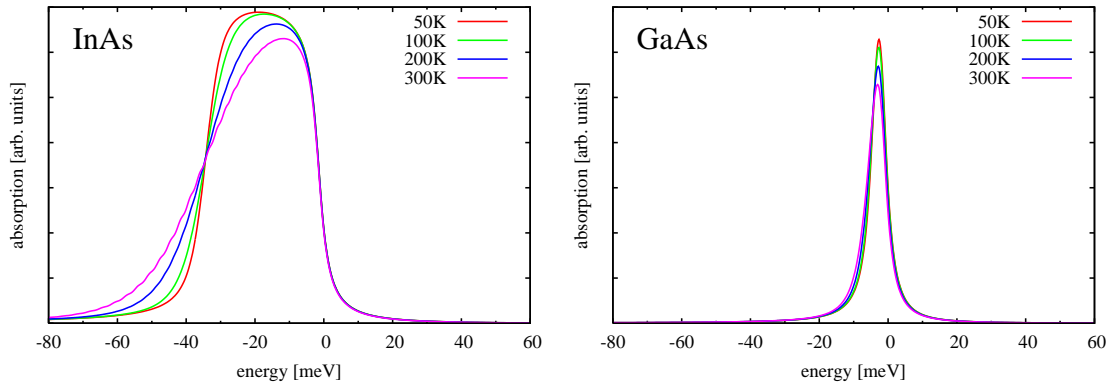


Figure 5.8: Absorption spectra of InAs (left) and GaAs (right) materials for different temperatures without any interaction mechanisms. Parameters are given in table 5.2.

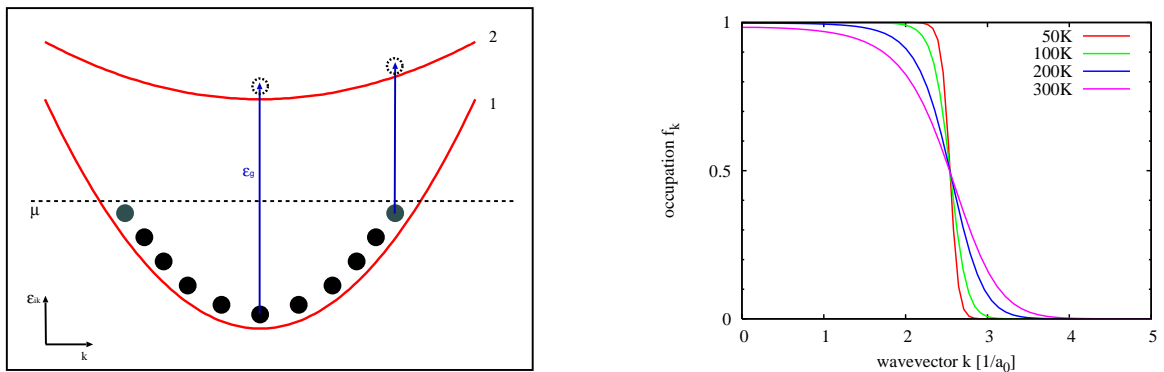


Figure 5.9: Left: scheme of intersubband transition, Right: Transformation of the Fermi distribution (of the InAs material) from a rectangular shape towards the Boltzmann distribution for increasing temperatures.

Since the effective masses of the upper subband is larger than for the lower subband in both materials, the curvature of the lower band is stronger. Consequently the maximum energy difference between two states with same wavevector is encountered for  $k = 0$ , hence the highest transition energy equals the gap energy  $\epsilon_g$ . For growing wavevectors the energy differences gets smaller and therefore contribute to absorption at frequencies below the gap energy in the spectrum. Since the lower subband is only filled up to a specific wavevector (Fermi level) for temperatures around  $T = 0K$ , a minimum transition energy exists and determines the lower-energy edge of the spectrum (temporarily disregarding effects due to the phenomenological broadening). The smallest energy occurring is given by  $\epsilon_{min} = \epsilon_g + \frac{\hbar k_F^2}{2m_r}$  with the Fermi wavevector  $k_F = \sqrt{2m_r\mu/\hbar}$  and a reduced mass  $m_r$ , which is negative for the considered systems. Due to the different reduced masses of the two systems, also the spectral widths of the absorption spectra differ. For the GaAs material the small difference between the subband masses leads to a very narrow absorption spectrum with edges mainly broadened by the phenomenological dephasing  $\gamma$ , for the InAs material the mass difference is larger. Hence the absorption spectrum covers a larger frequency range and only the edges are broadened. For increasing temperatures, the Fermi distribution –determining the occupation of the lower subband– transforms from a rectangular shape towards a Boltzmann distribution (see Fig. 5.9, for InAs). Thus also the low-energy edge of the absorption spectra broadens with increasing temperature. This effect is strong for the InAs material and only minor for GaAs.

### 5.2.3 Hartree-Fock contributions

In the following the influence of the various Coulomb contributions emerging from a Hartree-Fock factorization (Eqs. 5.3-5.4) is discussed [80, 71]. The well width is the main parameter determining the strength of the Coulomb matrix elements. Absorption spectra for simulations, which separately include the different Hartree-Fock contributions, are shown in Fig. 5.10 for several well widths  $L = 5, 10, 15, 20nm$  (InAs material,  $T = 77K$ ).

(a) The *exchange* contributions leads to a uniform blue-shift, i.e. a shift to higher energies, of the absorption spectrum. This shift is also called self-energy and decreases with growing well widths, since the Coulomb matrix elements get smaller. The rectangular shape of the absorption spectrum remains mainly unaltered.

(b) The *excitonic* contribution results in the formation of a collective resonance and a renormalization of the continuum. This effect occurs similar in interband transitions (see section 5.1) and can be explained with the intuitive picture of binding of electron-hole pairs into the hydrogen-like exciton particle. Since the lower subband is not completely filled one usually only considers the electrons as carriers [80]. Nevertheless a collective binding between the carriers in the upper and the lower subband is possible leading to the observed resonance. This structure is less pronounced than in interband transitions since the resonance lies within the (renormalized) continuum, which is located below the band gap for the considered InAs material as discovered above. The related Coulomb matrix elements decrease for growing well widths thus the excitonic formation gets weaker for broader wells.

(c) The *depolarization* contribution only occurs due to the presence of macroscopic charge imbalances. The electron surplus is needed to populate the lower conduction subband while preserving a completely filled valence band. The depolarization leads to a non-uniform shift of the absorption spectrum and appears to create a resonance structure [81, 80]. However the mechanism is different to excitonic formation. The excitonic resonance is a correlated superposition of all states. The depolarization on the other hand is only a  $k$ -dependent compression of the single particle states. Only Coulomb matrix elements with vanishing wavevector contribute to the depolarization. Since these matrix elements scale linearly with the well width, the depolarization contribution is stronger for broader

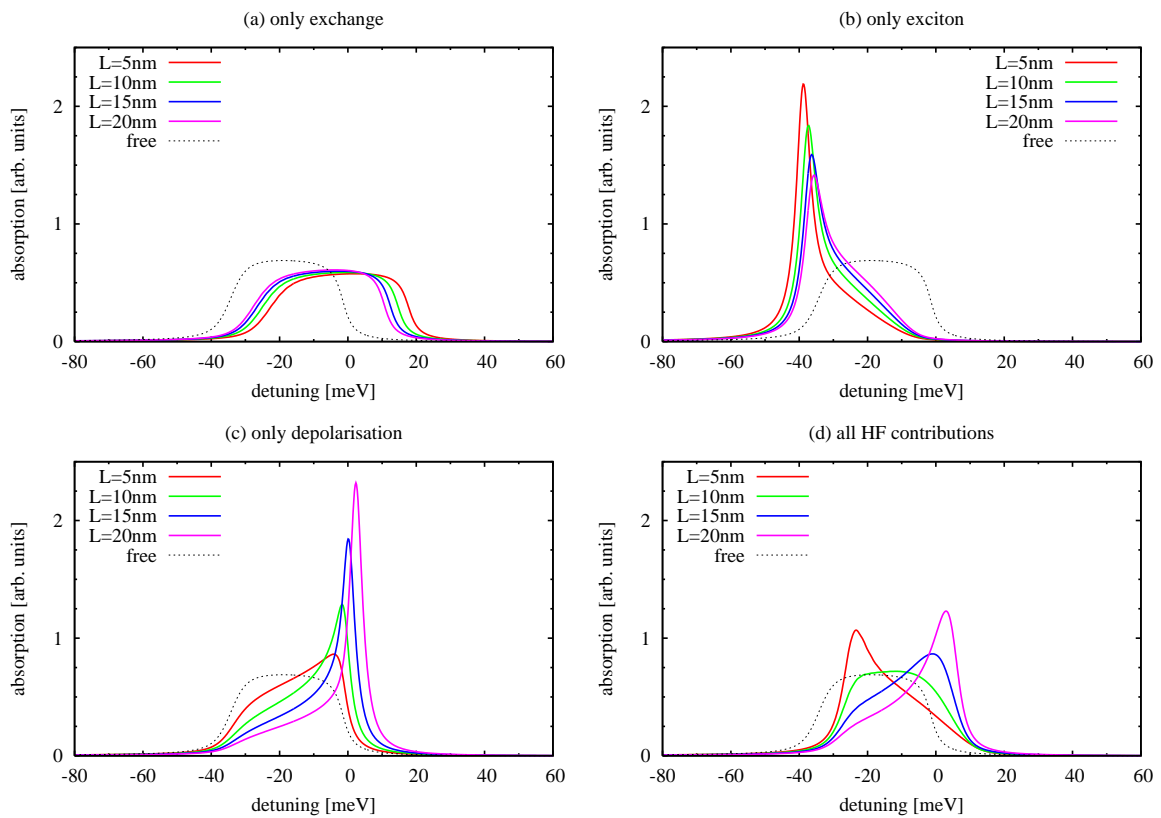


Figure 5.10: Effects of the various Hartree-Fock contributions for different well widths  $L = 5, 10, 15, 20\text{nm}$  for the InAs parameters at  $T = 50\text{K}$ . For comparison also the spectrum calculated without Coulomb interaction is given (“free”). After 5.2.

wells in opposite to all other Coulomb contributions.

(d) If *all* Coulomb contributions on Hartree-Fock level are included, one can observe that the different effects partly cancel each other. E.g. the blue-shift induced by the exchange term is to good extend compensated by the (red-shifting) binding energy of the exciton. Also, the non-uniform transformation toward a peak around the gap energy is counteracted by the exciton formation. Depending on the well width one of the contributions is stronger. For narrow wells, the exciton contribution dominates and a resonance at lower energies appears. For intermediate widths ( $L = 10nm$ ) the contributions almost exactly cancel leaving a structure similar to a shifted free spectrum. For broader wells, the linear dependency of the depolarization matrix elements dominates and a peak forms at the higher-energy continuum edge around the gap energy.

As can be seen in the equation of motion, the Coulomb contributions scale with the difference of subband occupations. Thus, for an inverted system where the upper subband is stronger populated than the lower one the sign of the contributions will switch and lead to shifts in the opposite direction, e.g. the exchange contribution will lead to a red shift. Also the electric field couples via a subband occupation difference. For an inverted system one therefore obtains negative absorption, i.e. gain [80, 71].

#### 5.2.4 Electron-electron and electron-phonon scattering

Inclusion of Coulomb effects beyond the Hartree-Fock approximation can be obtained within a second order Born approach by including all electron-electron correlations that can be projected on a products of single-particle quantities. Thus these interactions only describe electron-electron scattering but not many-particle states like biexcitons. A similar approach can be followed for the electron-phonon coupling by factorizing phonon-assisted expectation values into products of single-electron and single-photon quantities. A subsequent Markov approximation selects processes which obey strict energy conservation and leads to the compact form as given in Eqs. 5.5, 5.6. One should note, that the scattering rates  $\Gamma$  (given in appendix C.2) depend on the occupation functions, which are themselves dynamic quantities if nonlinear excitation is considered. In linear optics they are solely determined by equilibrium populations and hence the temperature. This temperature dependence and the general impact of the electron-electron and electron-phonon scattering is studied in Fig. 5.11 showing absorption spectra of InAs (left) and GaAs (right) for different temperatures including the electron-electron and electron-phonon scattering contributions. In both materials the absorption line broadens for increasing temperature. However, for InAs this broadening is mainly caused by the temperature dependence of the Fermi distribution (see Fig. 5.9 and related discussion) as can be seen in comparison with spectra evaluated in Hartree-Fock approximation (also shown in Fig. 5.11). For all temperatures the linewidth broadening by scattering processes at the higher-energy edge is smaller than the phenomenological broadening of  $\hbar\gamma = 1meV$  used for the Hartree-Fock calculations for the InAs material. In the GaAs model the situation is different due to the similar subband masses. There, the temperature dependence is negligible in Hartree-Fock approximation. However, if scattering processes are included the width of the absorption line is strongly temperature dependent and changes from a very narrow to a very broad line for increasing temperatures.

This broadening of the absorption spectrum for growing temperatures is caused by an increase of scattering events. Regarding electron-electron scattering this increase is solely caused by the Fermi distribution broadening for higher temperatures (see Fig. 5.9) providing to larger phase space for scattering events which would not be possible otherwise due to Pauli-blocking [82]. In addition to the larger phase space available for scattering the electron-phonon scattering also increases due to the growing phonon population for higher temperatures. Because of the coherent many-particle na-

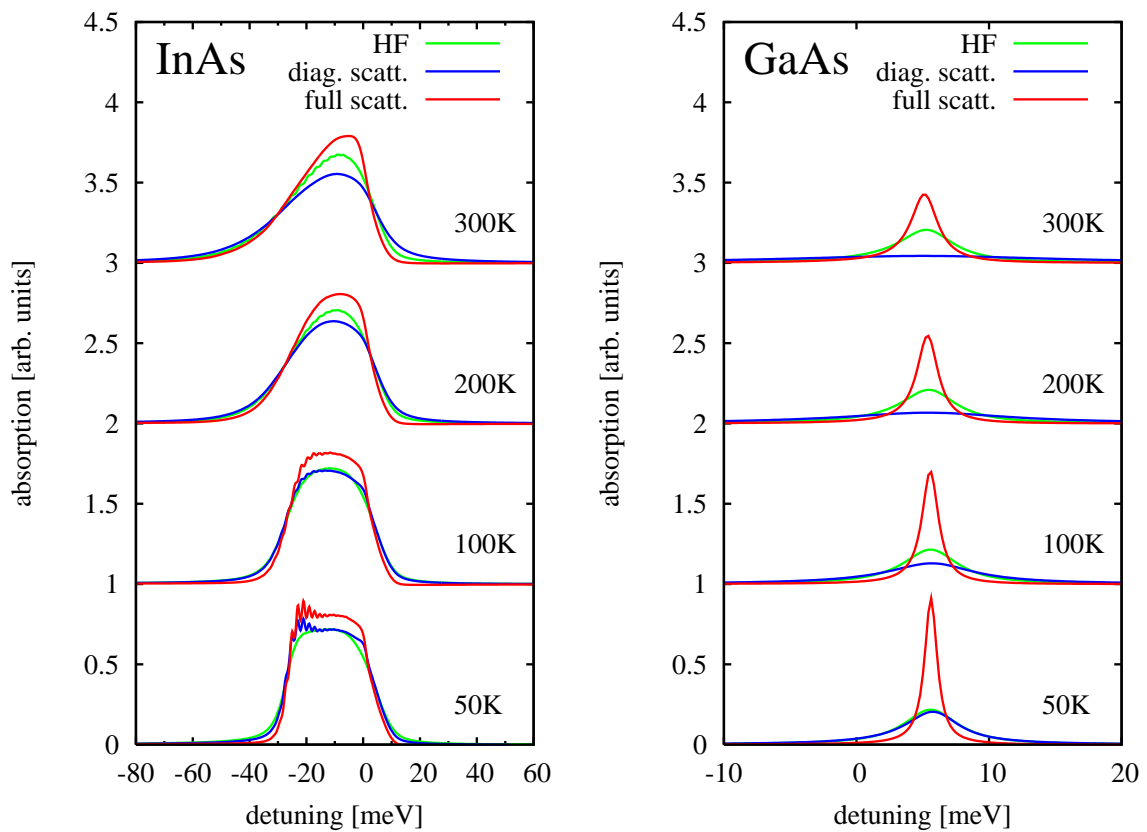


Figure 5.11: Comparison of absorption spectra of InAs (left) and GaAs (right) materials for inclusion of only Hartree-Fock contributions (green curve), only diagonal scattering rates  $\Gamma_d$  (blue curve) and all scattering terms (red curve) for different temperatures [77].

ture of the scattering events, the electron-phonon and electron-electron scattering processes are not independent but interfere with each other. Therefore, the linewidth including both scattering types simultaneously is smaller than the direct sum of the line widths for inclusion of electron-electron and electron-phonon separately (not shown) [18, 73].

Fig. 5.11 additionally displays absorption spectra for numerical evaluations which do not include the non-diagonal scattering rates  $\Gamma_{nd}$ . Neglecting these processes and inclusion of only diagonal terms considerably simplifies the structure of the equations of motion (Eqs. 5.2-5.6) and is therefore a very common approximation. Especially phenomenological rate models, which are often used to fit experimental results, are based on the assumption of solely diagonal scattering rates. However, as Fig. 5.11 illustrates, this approximation leads to qualitatively very different results in comparison to the complete inclusion of both diagonal and nondiagonal scattering processes. In most cases it results in a strong overestimation of the linewidth of the absorption, being stronger for higher temperatures especially in the GaAs system. This shows that the diagonal and nondiagonal scattering process are effectively counteracting, as known from interband transition [83, 84, 85, 86]. Calculating the Coulomb and electron-phonon coupling elements under the assumption of an infinitesimal small well width one can show that the diagonal and nondiagonal scattering processes exactly cancel each other for equal subband masses [71, 73, 18]. This cancellation is related to Kohn's theorem and also applies to the Hartree-Fock part of the equation of motion, resulting in a complete coherent countervail of all interactions leaving a dynamics exactly equal to that of free particles [80, 87, 88].

### 5.2.5 Quantum kinetic electron-phonon coupling

For the derivation of Eqs. 5.2-5.6 the Markov approximation has been applied. Physically this implies, that only processes which strictly obey energy conservation are included. This condition is mathematically expressed in a Dirac  $\delta$  function of the energies of the involved particle which emerges after Markov approximation of the memory kernel of the interaction (see section 2.8). This approach considerably simplifies the structure of the equations of motion (leaving only the microscopic polarization equation) and allows to express the coupling problem in terms of diagonal and nondiagonal scattering rates.

In this section the impact of the Markov approximation is studied by deriving quantum kinetic equations which are beyond the rigorous approximation of the memory kernel. For this investigation of principal effects only the electron-phonon coupling is considered, i.e. the Coulomb interaction is not included. In a correlation expansion approach phonon-assisted correlations including up to one phonon operator are dynamically evaluates. This is roughly equivalent to a second order series expansion of the memory kernel. The resulting equation for the intersubband coherence  $p_{2\mathbf{k}} = \langle a_{1\mathbf{k}}^+ a_{2\mathbf{k}} \rangle$  reads [74]:

$$\begin{aligned} \frac{d}{dt} p_{12,\mathbf{k}} &= \frac{1}{i\hbar} (\epsilon_{2,\mathbf{k}} - \epsilon_{1,\mathbf{k}}) p_{12,\mathbf{k}} + \Omega (f_{1,\mathbf{k}} - f_{2,\mathbf{k}}) - \frac{1}{i\hbar} \sum_{\mathbf{q}} g_{\mathbf{q}}^{11} (s_{\mathbf{k}+\mathbf{q},\mathbf{q},\mathbf{k}}^{12} - s_{\mathbf{k},\mathbf{q},\mathbf{k}+\mathbf{q}}^{21*}) \\ &+ g_{\mathbf{q}}^{22} (s_{\mathbf{k}+\mathbf{q},\mathbf{q},\mathbf{k}}^{21*} - s_{\mathbf{k},\mathbf{q},\mathbf{k}+\mathbf{q}}^{12}) + g_{\mathbf{q}}^{12} (s_{\mathbf{k}+\mathbf{q},\mathbf{q},\mathbf{k}}^{22} + s_{\mathbf{k},\mathbf{q},\mathbf{k}+\mathbf{q}}^{22*} - s_{\mathbf{k},\mathbf{q},\mathbf{k}+\mathbf{q}}^{11} - s_{\mathbf{k}+\mathbf{q},\mathbf{q},\mathbf{k}}^{11*}). \end{aligned} \quad (5.7)$$

Due to the chosen approach phonon-assisted correlations  $\xi_{\mathbf{k}',\mathbf{q},\mathbf{k}}^{ij} = \langle a_{\mathbf{k}}^+ b_{\mathbf{q}} a_{\mathbf{j},\mathbf{k}} \rangle^c$  occur and enter the equations via the Fröhlich electron-phonon coupling element  $g_{\mathbf{q}}^{ij}$  for LO phonons (see Eq. 2.23). The respective equations for the non-diagonal ( $i \neq j$ ) and diagonal phonon-assisted quantities are given

by:

$$\begin{aligned} \frac{d}{dt} s_{\mathbf{k}',\mathbf{q},\mathbf{k}}^{ij} &= \frac{i}{\hbar} (\varepsilon_{i,\mathbf{k}'} - \varepsilon_{j,\mathbf{k}} - \hbar\omega_{LO}) s_{\mathbf{k}',\mathbf{q},\mathbf{k}}^{ij} - \frac{1}{i\hbar} g_{\mathbf{q}}^{ii*} [(n_{\mathbf{q}} + 1) f_{i,\mathbf{k}'} + n_{\mathbf{q}} (1 - f_{i,\mathbf{k}'})] \rho_{ij,\mathbf{k}} \\ &\quad + \frac{1}{i\hbar} g_{\mathbf{q}}^{jj*} [(n_{\mathbf{q}} + 1) (1 - f_{j,\mathbf{k}}) + n_{\mathbf{q}} (f_{j,\mathbf{k}})] \rho_{ij,\mathbf{k}'} - \gamma_s s_{\mathbf{k},\mathbf{q},\mathbf{k}'}^{ij}, \end{aligned} \quad (5.8)$$

$$\begin{aligned} \frac{d}{dt} s_{\mathbf{k},\mathbf{q},\mathbf{k}'}^{ii} &= \frac{i}{\hbar} (\varepsilon_{i,\mathbf{k}} - \varepsilon_{i,\mathbf{k}'} - \hbar\omega_{LO}) s_{\mathbf{k},\mathbf{q},\mathbf{k}'}^{ii} + \frac{1}{i\hbar} g_{\mathbf{q}}^{ij*} [(n_{\mathbf{q}} + 1) (1 - f_{ii,\mathbf{k}'}) + n_{\mathbf{q}} f_{ii,\mathbf{k}'}] \rho_{ij,\mathbf{k}} \\ &\quad - \frac{1}{i\hbar} g_{\mathbf{q}}^{ij*} [(n_{\mathbf{q}} + 1) f_{ii,\mathbf{k}} + n_{\mathbf{q}} (1 - f_{jj,\mathbf{k}})] \rho_{ij,\mathbf{k}'}^* - \gamma_s s_{\mathbf{k},\mathbf{q},\mathbf{k}'}^{ii}. \end{aligned} \quad (5.9)$$

Inclusion of the phonon assisted correlations represents the quantum kinetic (retarded) character of the electron-phonon scattering and correspond to new quasi particle resonances (polarons). A phenomenological damping constant  $\hbar\gamma_s = 1meV$  for the assisted quantities is added to assure numerical stability. This parameter represents higher order correlations and it has been verified that this parameter only enhances the numerical convergence. It does not affect the optical spectra as long as the overall linewidth induced by the electron-phonon interaction is larger than  $\hbar\gamma_s$ . This prerequisite is fulfilled for the used parameter space.

For direct comparison, absorption spectra based on the Markovian and quantum kinetic theory are displayed in Fig. 5.12. GaAs parameters according to table 5.2 have been used. In general an increase of the linewidth can be observed for higher temperatures. For  $T = 200K$  and  $T = 300K$  the line shapes of the Markovian and quantum kinetic theories are very similar with slightly narrower lines for the quantum kinetic simulation. For lower temperatures the linewidth is strongly overestimated by the theory based on the Markov approximation. This effect of a smaller linewidth for the quantum kinetic theory has also been reported to occur in interband transitions of quantum dots interacting with their surrounding wetting layer [89]. At first sight this is counterintuitive as one would expect an increase in scattering processes due to the extended possibility of scattering events which do not obey strict energy conservation. However these processes are not additional but only replace other, energy-balanced events. Therefore it depends on the detailed structure of the interaction, whether inclusion of quantum kinetic processes increases the broadening in comparison to Markovian processes alone. As a general rule, the quantum kinetic effects, which go beyond Markov approximation, are more pronounced if the population shows steeper edged like for lower temperatures or more similar subband masses (see next section). Further differences between the theories can be observed on a logarithmic scale. In contrast to the Markovian theory the spectrum of quantum kinetic simulation exhibits an additional resonances at one LO phonon energy  $\hbar\omega_{LO}$  above and below the gap energy  $\varepsilon_g$  [74]. These peaks at  $\varepsilon_g \pm \hbar\omega_{LO}$  are associated with the formation of a polaron which contribute to the absorption and only the quantum kinetic approach is able to properly resolve their spectral positions.

## 5.2.6 Intersubband Rabi oscillations

Intersubband transitions in semiconductor quantum wells provide a good basis for the study of intersubband density Rabi oscillations, i.e. for the coherent population and depopulation of the upper subband. Subband transitions are well suited for these investigations because of their weak wavevector dependence of the optical transition energies resulting from the similar subband masses (almost parallel subbands). Also as a consequence of Kohn's theorem (see discussion in section 5.2.4) it is expected that the dephasing due to many-particle interactions is reduced in comparison to interband transitions. Recently, such intersubband Rabi oscillations have been experimentally observed in GaAs/AlGaAs quantum wells [90] in the THz regime.

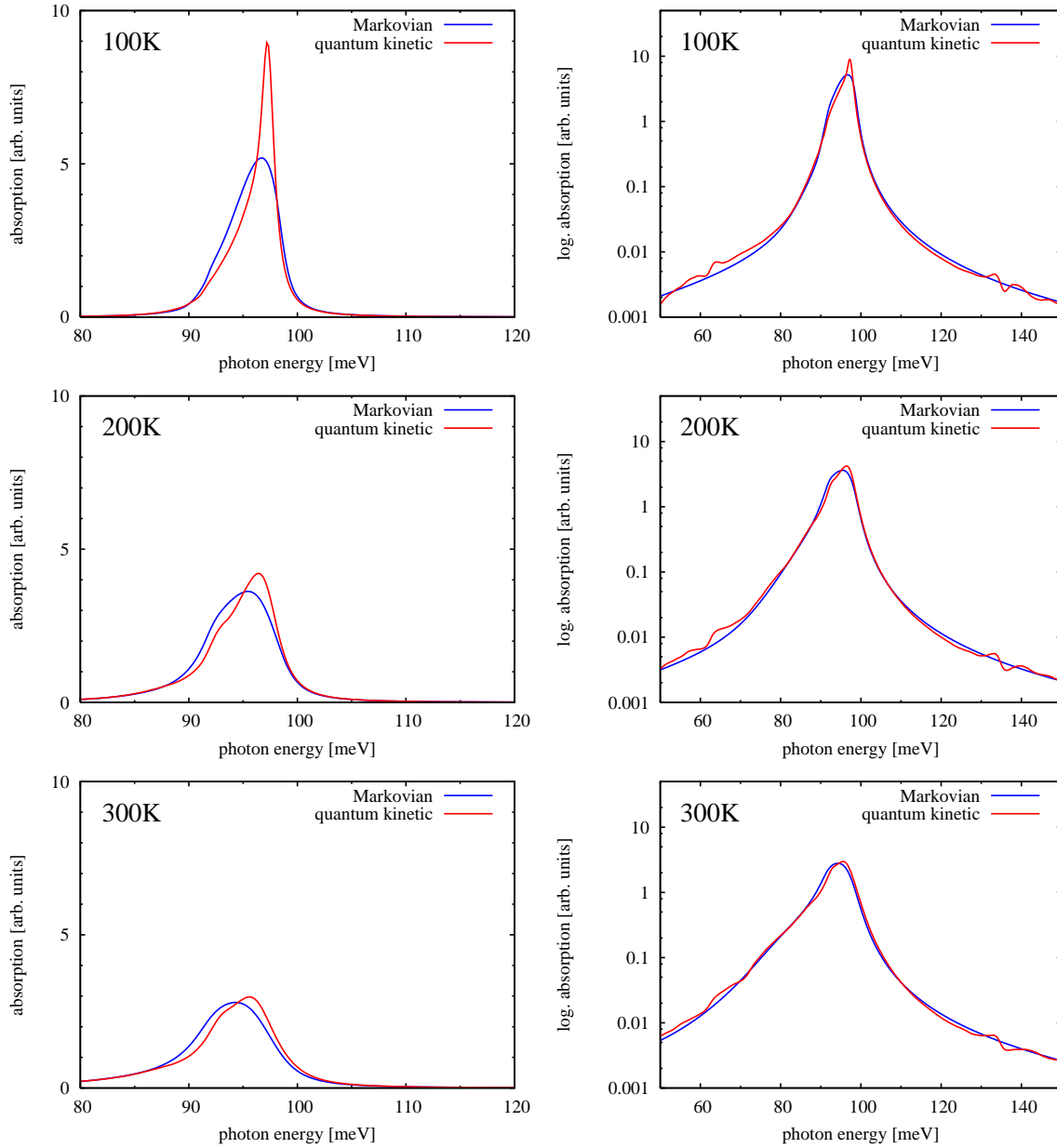


Figure 5.12: Absorption spectra of quantum kinetic simulations (red curves) in comparison with the Markovian theory (blue curves) on linear (left) and logarithmic (right) scale for different temperatures  $T = 100, 200, 300K$ .

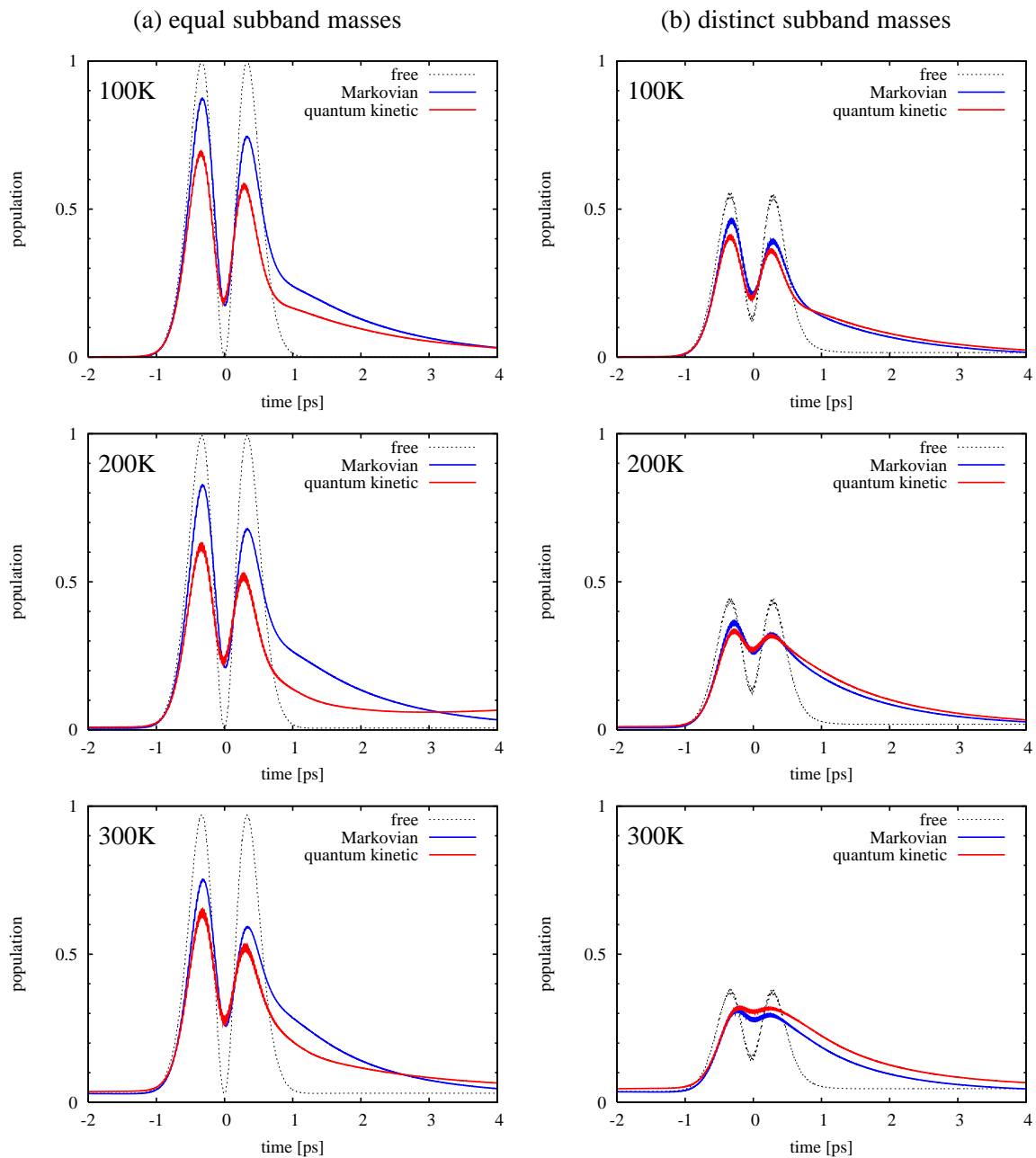


Figure 5.13: Influence of the electron-phonon damping on the population dynamics during excitation with a nonlinear Gaussian pulse ( $\Theta = 4\pi$ ,  $\tau = 700fs$ ). Comparison of quantum kinetic simulations (red curves), the Markovian theory (blue curves) and an undamped system (dashed curve). A system with equal subband masses (left) and with distinct masses (right) is considered for different temperatures  $T = 100, 200, 300K$ .

Here the influence of Markovian and quantum kinetic coupling of electrons to phonons is studied. In a systematic investigation the dynamics of the upper subband population is shown in Fig. 5.13 for nonlinear excitation with a Gaussian pulse ( $\Theta = 4\pi$ ,  $\tau = 700fs$ ) and increasing temperatures ( $T = 100, 200, 300K$ ). For comparison, systems with exactly equal subband masses (left) and slightly distinct masses (right) are considered. If no electron-phonon interaction is present (“free”), the system with equal masses exhibits two full density Rabi flops, as expected for excitation with a  $4\pi$  pulse in an undamped dispersion-less system [27]. If the subband masses do not coincide the transition frequency depends on the wavevector. Then a gap-resonant pulse with carrier frequency  $\omega_g$  only induces ideal Rabi oscillation for electrons at the  $\Gamma$ -point, i.e. for  $\mathbf{k} = 0$ . With respect to all other wavevectors the pulse is detuned leading to modification of the Rabi oscillation [27]. Consequently the subband population as superposition of all state occupations of the subband does not exhibit perfect Rabi oscillations but appears damped, as can be seen in Fig. 5.13. Broadening of the Fermi distribution for higher temperatures leads to population of higher states in the subbands increasing the number of distinct transition energies and consequently further reducing the Rabi oscillations.

Another type of damping is introduced by the electron-phonon interaction. For low temperatures (not shown) the Rabi oscillations of the phonon-damped systems resemble those of the free systems. For higher temperatures the increase of phonon-induced polarization dephasing leads to a reduction of all coherent processes including Rabi flopping. For 300K the modulation of the Rabi oscillations is almost completely suppressed. As can be observed in Fig. 5.13, also the population itself can relax into the lower subband by phonon emission. Additionally, it can be seen, that the population dynamics is considerably different for the quantum kinetic evaluation in comparison with to theory based on Markov approximation. In the Markovian simulations the temperature dependence is generally weaker and still exhibits clear oscillations for room temperature in contrast to the quantum kinetic system which undergoes much stronger damping. This difference between Markovian and quantum kinetic theory is more pronounced in the system with equal masses, where softening of the energy conservation allows additional scattering processes.



---

## Chapter 6

# Quantum dots

In this chapter optical excitation of quantum dots within the strong confinement regime is considered. Due to the presence of different materials a barrier potential exists and leads to a three dimensional confinement for carriers. Bloch electrons and holes are captured in the quantum dot and can no longer move freely but are localized in a small spatial region if the confinement region is smaller than their Bohr radius (strong confinement regime). For strong confinement, i.e. for a deep confinement potential, the delocalized continuum states reaching into the surrounding semiconductor (wetting layer) can be neglected. In the mathematical description the quasi-continuous wave vector of the confined carriers is then replaced by a single discrete subband index strongly simplifying the semiconductor Hamiltonian. The emerging energetic structure is equivalent to a simple multi-level scheme if a non-interacting electronic system is considered. Because of this discrete energy level structure, quantum dots are often compared to atoms. While this picture is instructive as a first approach, quantum dots are -in contrast to atoms- embedded in a solid state matrix with which they interact and therefore have to be described including the interaction to these many-body systems.

Despite to their similarity in the Hamilton operators representing the coupling of electrons to photons and to phonons is of very different character. Photons as particles of the quantized light field have a very broad energy range and can bridge the electronic band gap which lies in the eV range. This allows strictly energy conserving transition processes which can to good extent be described in Markov approximation. Even in the presence of a photon bath only spontaneous emission plays a significant role, since at realistic temperatures the photon occupation, described by the Bose statistics, is negligible for typical gap energies. These scattering processes of electrons with photons lead to simultaneous energy and phase relaxation (optical dephasing). In quantum dots the electron-light coupling is relatively weak and results in (effectively temperature independent) radiative decay times of several hundred picoseconds [91, 92, 93].

Phonons on the other hand have typical energies well below  $100\text{meV}$ . Depending on the specific energy structure, at least the optical phonon energies (e.g.  $36\text{meV}$  in GaAs) may be able to bridge intersubband gaps within the same band, but compared to usual interband gap energies the phonon energies are typically much smaller. Therefore strictly energy conserving interband phonon absorption and emission processes are suppressed due to the discrete energy level structure. Nevertheless, quantum kinetic processes relying on energy-time uncertainty are possible and lead to so-called pure dephasing of the quantum dot polarization not accompanied by energy relaxation. With the exception of an initial comparison only results for interactions with acoustic phonons are presented since in comparison the coupling to optical phonons is very weak in the considered systems [94].

In the linear optical regime and for a two-level system (i.e. one electron-hole pair is excited),

these pure dephasing processes can be investigated by applying the independent Boson model to the electron-phonon interaction. This allows analytical summation of the electron-phonon many-body hierarchy if no other interactions are considered. For comparison, the solutions of this approach will be presented and discussed. For nonlinear excitation and restriction to electron-phonon interaction it is possible to derive closed-form non-perturbative solutions for excitation with  $\delta$ -pulses [95]. Since this assumption prevents observation of the nonlinear electronic dynamics like Rabi flopping during excitation with pulses of finite duration, a correlation expansion approach has been chosen for most parts of this chapter. This approach has the additional advantage of allowing inclusion of other interactions and being able to handle more than two electronic levels. Furthermore it can be evaluated with standard numerical methods. The drawback of the approach is its limitation to systems and temperatures where the electron-phonon interaction is not too strong. For material parameters of GaAs quantum dots it will be shown that results obtained with a second order expansion in the electron-phonon coupling are in good agreement with the nonperturbative solutions for temperatures up to 200K. As a first result of the correlation expansion approach, that is not achievable with known nonperturbative methods, damping of Rabi oscillations (i.e. the coherent population and depopulation of levels) of a single electron-hole pair coupled to an acoustic phonon bath is studied.

In a further approach the independent Boson model solution and properties of the expansion approach are combined into an integro-differential equation which allows simulations for the strong-coupling regime and excitation with arbitrary pulses. It is shown that the approach reproduces the results of the analytic solutions and the expansion approach in their respective areas of validity.

In a next step, again using the expansion approach for the electron-phonon coupling, Coulomb interaction between electrons in one quantum dot will be discussed. In contrast to higher dimensional semiconductors in quantum dots the many-body hierarchy naturally truncates if only excitation of a finite number of electron-hole pairs is assumed. E.g. in a system with two spin-degenerated levels (i.e. effectively four levels) only two electron-hole pairs are expected, hence three-electron correlations vanish by definition. This allows the study of the Coulomb interaction in a non-perturbative manner and leads to novel properties compared to higher-dimensional semiconductors where correlation expansion of the electron-electron interaction like mean-field approximation is crucial.

Since the electron-phonon coupling effectively creates virtual states around the real levels one expects changes in the nonlinear dynamics for excitation which is off-resonant with respect to the level gap. Nonlinear detuning spectra, which can be obtained by systematic variation of the carrier frequency of the excitation light pulses, show a structure strongly resembling the electron-phonon coupling function which enters the Hamiltonian. By controlled selection of the pulse strength contributions of the direct transition (zero phonon line) can be suppressed in such nonlinear detuning spectra. As an application, steady-state solutions for a system in which both electron-phonon coupling and Coulomb interaction are important is presented and compared to experimental results from a saturation spectroscopy setup.

Coherent phonons which are generated during optical excitation can be neglected in comparison to bath phonons for most realistic cases (like isolated quantum dots and not to dense or unordered ensembles). But, for strongly ordered dense quantum dot arrays theory predicts that analogous to a photonic crystal most phonon modes should be suppressed and the system should only be able to couple to a few selected phonon modes. In such a situation it could at least in principle be possible that coherent phonons become relevant and could potentially be used as long-range coupling mechanism between quantum dots. This idea is discussed in section 6.7.

In order to describe nonlinear light propagation through a medium which contains an ensemble of quantum dots, Maxwell Equations have to be evaluated simultaneously with the material equations. Results for unidirectional propagation (using the SVEA method) are presented in section ???. The

influence of the different interaction mechanisms (electron-phonon, Coulomb) is studied and the possibility of self-induced transmission and related pulse propagation effects known from atomic vapor are discussed. For comparison with experimental conditions the model is extended to include inhomogeneous broadening (of energies and dipole strengths) and optical confinement by a waveguide structure.

In section 6.8 radiative coupling of quantum dots arranged in an ordered two dimensional array are considered. For these simulations the three dimensional vector Maxwell equations have been evaluated using the Finite Difference Time Domain (FDTD) approach. The material's response to light pulses is coined by the strong electromagnetic coupling between the dots leading to pronounced interference effects. The radiative dampening is studied for different dot sizes and distances in the linear and nonlinear regime.

## 6.1 The Independent Boson Model<sup>1</sup>

In a first step a simplified quantum dot model described by a two level system that is coupled to a phonon bath is considered. Only intraband processes (electron-phonon coupling element which is diagonal in the band indices) and no further contributions like coupling to a light field are included. Adapting the respective Hamiltonians from chapter 2 and using the three dimensional confinement situation encountered in the quantum dot ( $\dim \mathbf{k} = 0$ ,  $\mathbf{q} = \mathbf{q}_\pm$ ), one obtains:

$$H_{ibm} = \sum_i \varepsilon_i a_i^\dagger a_i + \sum_{\mathbf{q}} \hbar \omega_{\mathbf{q}} b_{\mathbf{q}}^\dagger b_{\mathbf{q}} + \sum_{i,\mathbf{q}} g_{\mathbf{q}}^{ii} a_i^\dagger (b_{\mathbf{q}} + b_{-\mathbf{q}}^\dagger) a_i. \quad (6.1)$$

This Hamiltonian is known from the Independent Boson Model (ibm) and represents one of the few many-particle problems which can be solved exactly in the sense that an explicit expression for the dynamics of the system can be derived without any approximation [3]. Using Feynman's disentanglement theorem one can derive [98, 99, 94, 96, 97]:

$$p_{vc}^{ibm}(t) = p_{vc}(0) \theta(t) \exp \left( -i(\omega_g - \Delta_p)t + \sum_{\mathbf{q},\pm} A_{\mathbf{q}}^\pm (e^{\pm i\omega_{\mathbf{q}}t} - 1) \right), \quad (6.2)$$

$$\text{with } A_{\mathbf{q}}^\pm = \frac{|\tilde{g}_{\mathbf{q}}|^2 (n_{\mathbf{q}} + \delta_{\pm,-})}{\hbar^2 \omega_{\mathbf{q}}^2}$$

$$\text{and } \Delta_p = \sum_{\mathbf{q},\pm} \frac{|\tilde{g}_{\mathbf{q}}|^2}{\hbar^2 \omega_{\mathbf{q}}}.$$

Here, an electron-phonon coupling element  $\tilde{g}_{\mathbf{q}} = g_{\mathbf{q}}^{vv} - g_{\mathbf{q}}^{cc}$  combining both levels has been introduced. The temperature of the phonon bath enters the equation via the Bose distribution  $n_{\mathbf{q}}$  (see chapter 2.6). The polaron shift  $\Delta_p$ , which results from an additional rotation of the polarization, represents the binding energy of the polaron quasi particle which forms due to the coupling of electrons and phonons. Apparently it is independent of the phonon population which changes with temperature. The gap energy is defined here as the direct energy level difference  $\omega_g = \omega_c - \omega_v$  but may later additionally include renormalizations like the polaron shift. The polarization  $p_{vc}^{ibm}(t)$  can be considered as the linear response for excitation with a delta pulse  $\delta(t)$ . Hence, using it as Green's function in a convolution approach one can calculate the general polarization for arbitrary linear excitation, see section 6.4. In this section only excitation with  $\Omega(t) = \delta(t)$  leading to the initial condition  $p_{vc}(0) = i$  is investigated.

<sup>1</sup>Results from sections 6.1-6.3 have been partially published in Refs. [94, 96, 58, 97].

| quantity               | value                 | meaning               |
|------------------------|-----------------------|-----------------------|
| $\omega_g$             | 1.5eV                 | gap energy            |
| $D_v$                  | -4.8eV                | Deformation potential |
| $D_c$                  | -14.6eV               | “                     |
| $a_v$                  | 3.19nm                | Gaussian radius       |
| $a_c$                  | 5.8nm                 | “                     |
| $c_{LA}$               | 5110m/s               | velocity of sound     |
| $\rho$                 | 5370kg/m <sup>3</sup> | density               |
| $\rightarrow \Delta_p$ | 15.8 $\mu$ eV         | polaron shift         |

Table 6.1: Parameters describing the electron-phonon problem in GaAs quantum dots.

For explicit numerical calculations the electron-phonon coupling elements  $g_{\mathbf{q}}^{ij}$  have to be specified. The theory was evaluated for LO phonons described by Fröhlich coupling and deformation potential LA phonons [94]. Calculations have shown, that the interaction is orders of magnitudes stronger for deformation potential LA phonons than for LO phonons in the considered material system (GaAs), see Fig. 6.5. This dominance also holds in comparison to other possible phonon types [98]. Hence, only results for deformation potential LA phonons are discussed in the following. However, one should be aware that the polaron shift for other phonons (Fröhlich LO phonons in GaAs:  $\Delta_p^{LO} \approx 410\mu\text{eV}$ ) can be much larger than the LA polaron shift (GaAs:  $\Delta_p^{LA} \approx 15.8\mu\text{eV}$ ). This does not essentially affect the polarization dynamics since in linear optics one can assume that these temperature independent shifts are already included in the gap energy  $\omega_g$ .

For a spherical parabolic confinement potential which leads to Gaussian wave function envelopes, i.e.  $\phi_i(\mathbf{r}) = \alpha_i e^{-r^2/a_i^2}$  with Gaussian radius  $a_i$  and normalization factor  $\alpha_i$ , the electron-phonon coupling element (Eq. 2.24) evaluates to [94]:

$$g_{LA,\mathbf{q}}^{ii} = \sqrt{\frac{\hbar q}{2\rho c_{LA} V}} D_{\bar{i}} e^{-q^2 a_i^2 / 4} \quad (6.3)$$

The parameters used for simulating a GaAs quantum dot are listed in table 6.1 . Fig. 6.1 displays the wavevector dependence of the coupling elements  $|g_{\mathbf{q}}^{vv}|$ ,  $|g_{\mathbf{q}}^{cc}|$  and  $|\tilde{g}_{\mathbf{q}}| = |g_{\mathbf{q}}^{vv} - g_{\mathbf{q}}^{cc}|$  for these parameters. The coupling functions have maxima between 0 and  $1/nm$  and are essentially zero for wavevectors beyond  $1.5/nm$ . Hence the assumption of a exactly linear dispersion relation for the LA phonons can be expected to be valid to good extent.

Fig. 6.2 shows the polarization dynamics  $|p_{vc}(t)|$  for different temperatures. One can observe that the polarization drops from an initial value of 1 to a lower but nonzero value in which it stays without substantial further decay for all except for very low temperatures. While the time scale ( $\approx 2ps$ ) of the drop is mainly constant the final value of the polarization strongly varies with temperature: For 4K almost 90% of the polarization is preserved, for increasing temperature the final value gets less and less and is nearly zero for 300K. Additionally one can observe that the initial slope of the decay is zero, which is a typical signature of non-Markovian dephasing processes. All in all, the dephasing dynamics is very distinct from a typical exponential decay. Such an exponential decay is for example expected for Markovian energetic coupling to a bath as demonstrated in chapter 2.9. In the considered system application of the Markov approximation would lead to no dephasing at all, since the typical phonon energies (few  $meV$ ) are not able to bridge the band gap ( $eV$ ) and also strictly energy conserving intraband transitions are not possible because of the discrete energy level structure

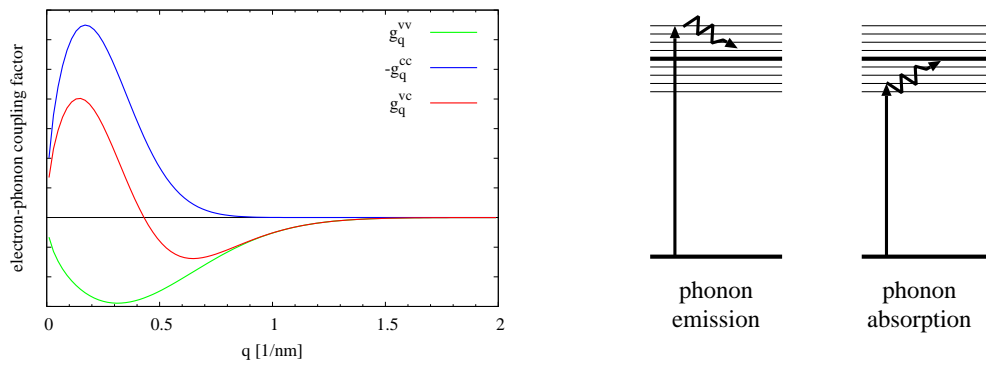


Figure 6.1: Left: Wavevector dependence of the electron-LA phonon coupling elements in GaAs. Right: Illustration of phonon-assisted interband transitions (via phonon emission and absorption)

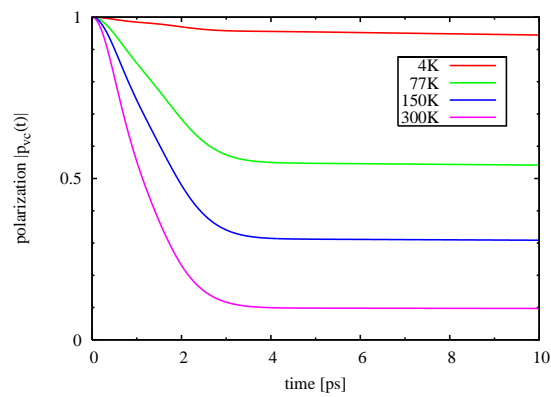


Figure 6.2: Polarization dephasing dynamics for different temperatures calculated using the Independent Boson Model.

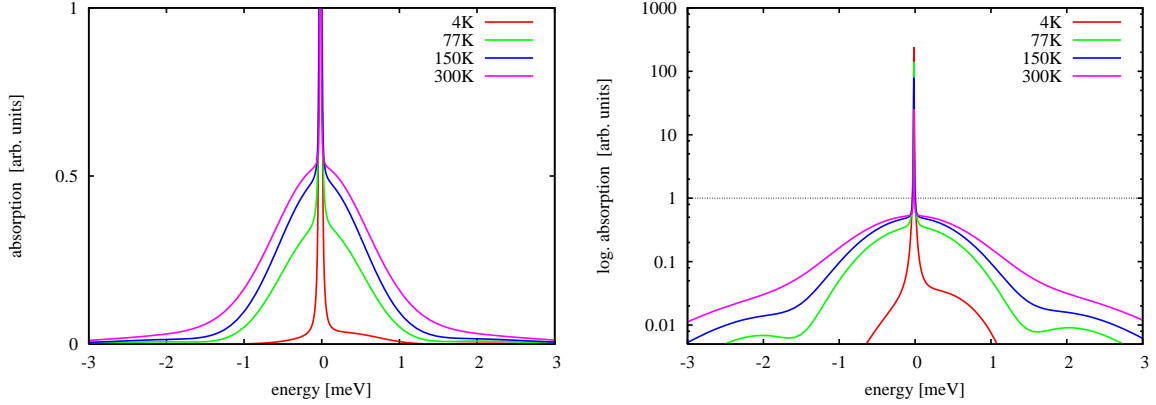


Figure 6.3: Absorption spectra for different temperatures calculated using the Independent Boson Model. The linear scale (left) is truncated to magnify the phonon sidebands. On the logarithmic scale (right) the complete peak is displayed and further details of the sidebands are visible. After [94].

that quantum dots have in contrast to higher dimensional semiconductors. This so-called phonon bottleneck is not present if non-Markovian processes are allowed. These processes make use of the energy-time uncertainty and consequently also enable transitions which would not be possible with strict energy conservation.

Since the polarization decay (also called phase relaxation) is not accompanied by energy relaxation (shown in section 6.2) one speaks of pure dephasing. As one can see from the structure of Eq. 6.2 the overall dynamics is internally composed of an interference of a spectrum of oscillators. Hence, the polarization reduction can be explained as destructive interference effect of the optically excited phonon-assisted virtual states. While the interference process itself is coherent and in principle reversible, permanent dephasing occurs due to the coupling to an incoherent phonon bath. For not too low temperatures, where  $n_{\mathbf{q}} \ll 1$  holds, the oscillations cancel out each other after some time and the decoherence process stops leaving some residual polarization in the system. This symmetry (between phonon emission and absorption) also leads to the initially zero slope of the decay. For low temperatures ( $\lesssim 10K$ ) the phonon population vanishes and the spontaneous phonon emission gets dominant, breaking the absorption-emission symmetry.

If in addition to the electron-phonon coupling also spontaneous emission of photons is considered (compare 2.9), one gets an additional  $e^{-\gamma_0 t}$  factor in the polarization dynamics (Eq. 6.2), describing radiative decay. The radiative relaxation via photon emission can be well described as a Markovian process since the band gap can be bridged by proper photons in the optical regime. However, the emerging radiative decay rate  $\gamma_0$  for a typical GaAs quantum dot is very small, corresponding to a long time scale of about  $T_2 = 1/\gamma_0 \approx 500ps$ . While this decay is hardly visible on the time scale of the phonon dynamics (few ps) it is important when considering the Fourier transformation of the polarization which is needed for calculation of absorption spectra via  $\alpha(\omega) \propto \text{Im} \frac{P(\omega)}{\Omega(\omega)}$ . Without radiative decay the nonvanishing final value would lead to a Dirac delta function in frequency space. But, including radiative decay, this line broadens to a Lorentzian curve with a FWHM of  $\gamma$ . The electron-phonon coupling contributes with a variety of oscillations and is therefore expected to lead to satellite contributions and not only broadening of the Lorentzian curve. The absorption spectra for different temperatures are displayed in Fig. 6.3 (the linear plot is truncated as indicated in logarithmic graph). The radiatively broadened Lorentzian part, usually called zero-phonon-line (ZPL), is very slightly

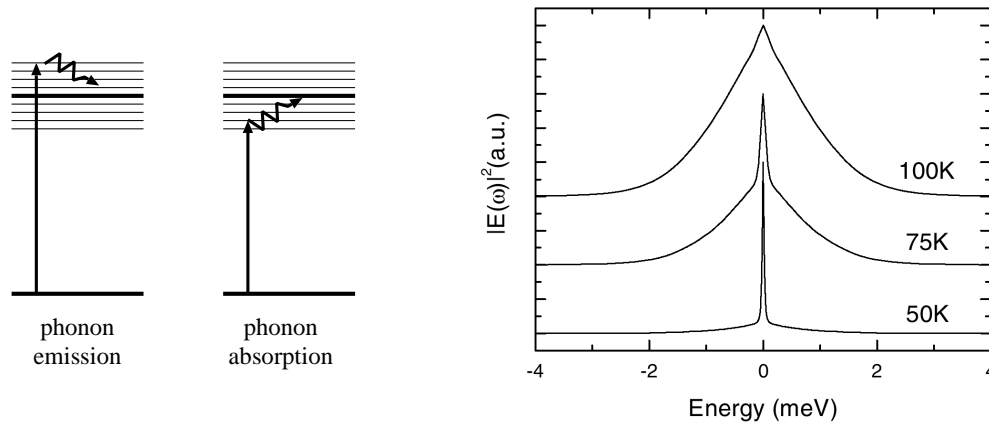


Figure 6.4: Left: Illustration of phonon-assisted interband transitions (via phonon emission and absorption). Right: Experimentally obtained absorption spectra of GaAs quantum dots, taken from [93].

( $15.8\mu\text{m}$ ) polaron-shifted to lower energies relative to the gap energy. Additionally, broad sidebands around the ZPL are visible. These phonon sidebands are symmetric around the ZPL for higher temperatures, but for very low temperatures the sidebands are visibly stronger on the higher energy side. The ZPL describes absorption of light by direct transitions between the levels and is therefore only possible for frequencies which match the Polaron-renormalised band gap energy. The phonon sidebands are formed by phonon-assisted absorption processes (and have a reduced density of states compared to the ZPL). As illustrated in Fig. 6.4, this absorption of light is possible by transitions into virtual levels, which according to energy-time uncertainty can only exist temporarily. Nevertheless long term energy conservation must be fulfilled, which can be ensured by emission or absorption of phonons. For very low temperatures only spontaneous phonon emission occurs, for higher temperatures both absorption and emission processes are possible and grow with increasing population. Hence the lower energy sidebands are suppressed for low temperatures but symmetry is reached for higher temperatures. In contrast to the height of the sidebands which increase with temperature, the width is independent of temperature and localized within  $\pm 1\text{meV}$  around the ZPL for the considered system.

In experiments the same structure of a sharp zero-phonon line surrounded by phonon sidebands has been reported, see Fig. 6.4 [93]. Specifically in these experiments the increase of the phonon sidebands for higher temperatures was observed. Not predicted by independent boson model [96, 98] but present in the experiment is a strong temperature dependence of the ZPL width. For low temperatures the ZPL is narrow with very long dephasing times of about  $630\text{ps}$  in agreement with theory, but the ZPL width strongly increases with temperature and even gets stronger than the phonon decay for room temperature (about  $6\text{meV}$  for  $300\text{K}$ ). Explanations for this ZPL broadening with damping mechanisms based on phonon-phonon scattering have been proposed [99, 100]. These calculations are able to reproduce the experimental evidence of temperature dependent ZPL broadening but unsatisfyingly they do not describe the phonon-phonon scattering microscopically but rely on phenomenological models and experimental data. Because no conclusive investigation on the validity of these models is available, phonon-induced broadening of the ZPL has not been included in this work. All in all, a convincing microscopic theory for the description of the temperature dependent ZPL broadening is desired but not yet available.

To illustrate that longitudinal optical phonons are relatively weak compared to acoustical phonons

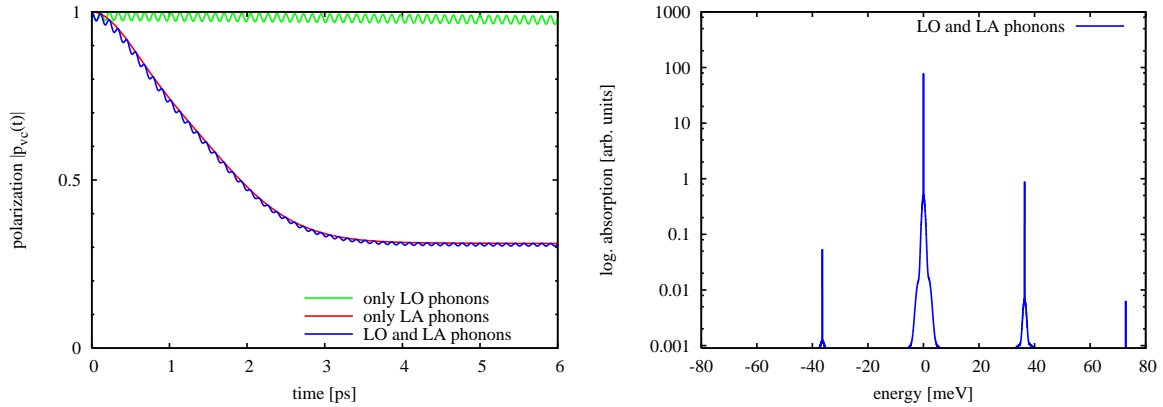


Figure 6.5: Polarization dynamics (left) and absorption spectra (right) for a simulation including Fröhlich-LO-phonons in addition to the deformation potential LA phonons. After [94].

in the considered GaAs quantum dots, Fig. 6.5 displays the polarization dynamics and absorption spectra obtained with a simulation that also includes Fröhlich-LO phonons in addition to the deformation potential LA phonons (for  $T = 150K$ ). The absorption spectrum exhibit additional satellite resonances which can be attributed to the LO phonons. The resonances are energetically located at multiples of the LO phonon energy  $\hbar\omega_{LO} = 36meV$  and show sidebands caused by LA-phonon similar to the ZPL. However, the satellites are by a factor 100 smaller than the ZPL. The dominance of LA phonons over LO phonons can also be observed in the polarization dynamics: If only LO phonons are considered (green curve), the polarization shows only negligible dephasing and oscillations with a small amplitude. The LA coupling alone (red curve), leads to a very strong decay of the polarization as described above. Hence, if both phonon types are included (blue curve) the polarization dephasing dynamics is strongly dominated by the acoustical phonons and the optical phonons contribute by small oscillations. Additionally, these oscillations even vanish for pulses of finite duration, if the satellite resonances are not spectrally excited. Therefore, only LA phonons are considered in the following.

Fig. 6.6 shows the polarization dynamics and absorption spectrum using more realistic wavefunctions from an 8-band  $\mathbf{k} \cdot \mathbf{p}$ -calculation for pyramidal-shaped quantum dots [94]. These calculations have been performed based on anisotropic wavefunctions and matrix elements for a pyramidal GaAs quantum dot, which have been provided by A. Schliwa ([101, 102, 103], also see section 6.8). In correspondence with experimental conditions[93] the originally radiative dephasing time is adjusted to  $T_2 = 11ps$  in order to include the additional exponential damping effects. Comparison to the case of Gaussian wavefunctions (isotropic parabolic potential) reveals a slightly slower polarization decay for pyramidal dots. Also, as can be seen in the absorption spectra, the phonon sidebands contain energetically higher contributions and are generally broader for the pyramidal dots. Since the differences are mainly quantitatively, in the following only calculations for Gaussian wavefunctions being computational less expensive are discussed.

The Independent Boson Model, which has been considered up to now, is only able to describe the linear response of the quantum dots. In order to allow nonlinear excitation which induces not only a polarization but also an occupation dynamics, different approaches have to be taken. Axt et al. have shown that a solution nonperturbative with respect to the electron-phonon coupling can be derived using a generating function approach if excitation is restricted to a finite series of  $\delta$ -pulses[95]. For excitation with a single  $\delta$ -pulse, i.e.  $\Omega = \Theta\delta(t)$  with pulse area  $\Theta$ , the polarization is still described

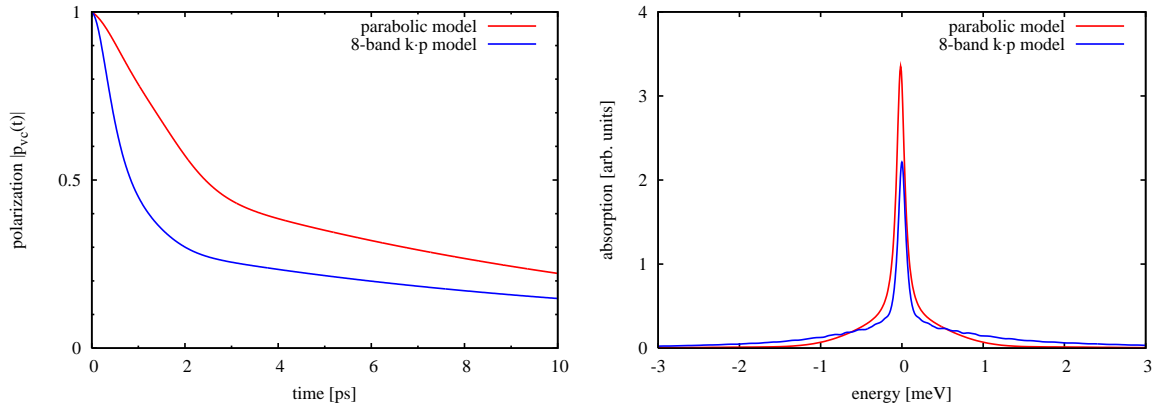


Figure 6.6: Polarization dynamics (left) and absorption spectra (right) of the spherical parabolic model (red) in comparison with an anisotropic 8-band- $k \cdot p$  model. Simulations based on the Independent Boson Model for temperature  $T = 77K$  and pulse duration  $\tau = 11ps$ .

by Eq. 6.2 but with  $p_{vc}(0) = \frac{i}{2} \sin \Theta$  as the initial condition (for numerical results see section 6.4, Fig. 6.12). The electron density, given by  $f(t) = \theta(t) \sin^2(\Theta/2)$ , depends on the pulse area exactly as known from Rabi flopping in pure two-level systems (compare Eq. A.9) and is not directly influenced by the phonons, as to expect considering the structure of the interaction. Hence, after excitation the polarization amplitude decays, but the occupation does not. This decoherence of the polarization without energy relaxation of the occupation (pure dephasing) is a direct consequence of the non-Markovian nature of the process. However, if a series of  $\delta$ -pulses (see Ref. [95]) or a pulse with nonvanishing duration is considered (see below), the phonon-induced decay reduces the polarization and consequently the coherent build-up of the density needing both polarization and light field is modified as well. Hence, the occupation dynamics is indirectly influenced by the electron-phonon interaction.

While the explicit nonperturbative solution for  $\delta$ -pulse excitation provides insight into the structure of the system, it fails to describe real pulses with a duration that cannot be assumed to be infinitesimal. For pulses of nonvanishing duration the polarization and density continuously affect each other leading to a possibly very distinct dynamics. Also, by construction the theory is not able to describe Rabi oscillation during pulse excitation and inclusion of further interactions is not feasible. Therefore a perturbative correlation expansion approach as described in the next section was chosen for most of the simulations in this chapter. A comparison of the nonperturbative  $\delta$ -pulse solutions with the correlation expansion and a nonperturbative convolution approach allowing arbitrary pulses is presented in section 6.4.

## 6.2 Correlation expansion

As discussed in chapter 2.25 a hierarchy of differential equations describing the dynamics of the system can be derived using the Heisenberg equation together with a correlation expansion approach. In order to describe excitation with arbitrary light fields, the Hamiltonian used for the independent Boson model is extended by the electron-light contributions (Eqs. ?? and 2.14):

$$\begin{aligned}
H = & \sum_i \varepsilon_i a_i^\dagger a_i + \sum_{\mathbf{q}} \hbar \omega_{\mathbf{q}} b_{\mathbf{q}}^+ b_{\mathbf{q}} + \sum_{i\mathbf{q}} g_{\mathbf{q}}^{ii} a_i^\dagger (b_{\mathbf{q}} + b_{-\mathbf{q}}^+) a_i \\
& + \sum_{ii'\mathbf{q}\lambda} G_{\mathbf{q}}^{ii'\lambda} a_i^\dagger (c_{\mathbf{q}} + c_{-\mathbf{q}}^+) a_{i'} - \sum_{ii'} \mathbf{d}^{ii'} \cdot \mathbf{E}(t) a_i^\dagger a_{i'}.
\end{aligned} \tag{6.4}$$

An external electric field  $E(t)$  constant over the quantum dot region has been assumed. Despite the fact that the correlation expansion itself is not an approximation, it would lead to an infinite hierarchy of equations, which therefore has to be truncated since no method for an analytical summation like the Independent Boson Model is known for arbitrary nonlinear excitation. Hence, in the following a second order expansion with respect to the electron-phonon coupling is applied by neglecting correlations with more than two phonon operators like  $\langle a_1^\dagger a_2 b_{\mathbf{q}}^{(+)} b_{\mathbf{q}'}^{(+)} b_{\mathbf{q}''}^{(+)} \rangle^c$ . Calculations have shown that creation of coherent and hot phonons is a very minor effect and can therefore be neglected for typical situations of unordered or not to dense quantum dot ensembles. Hence, with the exception of section 6.7, where electron-phonon interdot coupling in a perfectly regular grid of quantum dots is considered, a phonon bath, not influenced by the phonon dynamics, is assumed (see section 2.6). Analogous to the treatment in section 2.9 the interaction of electrons with the quantized light field is solved within Markov approximation under the assumption that the photons (with exception of the external electric field) form a bath with negligible occupation at optical frequencies. Hence only phase and energy relaxation via spontaneous photon emission is considered. As discussed in section 6.1 applying the Markov approximation to the electron-phonon coupling would eliminate the essential parts of the interaction and is therefore only used on the electron-photon problem.

The full set of differential equations is given in appendix C.2. A subset of these equations for a two level system with valence (v) and conduction (c) band pair is given for illustration and discussion [96, 94]:

$$\dot{p}_{vc} = -i\omega_g p_{vc} - i\Omega(1 - 2f_c(t)) + \frac{i}{\hbar} \sum_{q,\pm} \tilde{g}_q (S_q + T_q) - \gamma_0 p_{vc}, \tag{6.5}$$

$$\dot{f}_c = -i(\Omega^* p_{vc} - \Omega p_{vc}^*) - 2\gamma_0 f_c, \tag{6.6}$$

$$\begin{aligned}
\dot{S}_q(t) = & \frac{i}{\hbar} (-\varepsilon_g - \hbar\omega_q) S_q + i\Omega(t) (\langle a_v^\dagger a_v b_q \rangle^c - \langle a_c^\dagger a_c b_q \rangle^c) - \gamma_0 S_q \\
& + \frac{i}{\hbar} \tilde{g}_{vc}^{-q} \rho_{vc}(t) (n_q + 1) + \frac{i}{\hbar} \sum_{q'} \tilde{g}_{vc}^{q'} (\langle a_v^\dagger a_c b_q b_{q'} \rangle^c + \langle a_v^\dagger a_c b_{-q'} b_q \rangle^c),
\end{aligned} \tag{6.7}$$

$$\begin{aligned}
\dot{T}_q(t) = & \frac{i}{\hbar} (-\varepsilon_g + \hbar\omega_q) T_q + i\Omega(t) (\langle a_v^\dagger a_v b_{-q}^+ \rangle^c - \langle a_c^\dagger a_c b_{-q}^+ \rangle^c) - \gamma_0 T_q \\
& + \frac{i}{\hbar} \tilde{g}_{vc}^{-q} \rho_{vc}(t) n_{-q} + \frac{i}{\hbar} \sum_{q'} \tilde{g}_{vc}^{q'} (\langle a_v^\dagger a_c b_{q'} b_{-q}^+ \rangle^c + \langle a_v^\dagger a_c b_{-q'}^+ b_{-q}^+ \rangle^c).
\end{aligned} \tag{6.8}$$

The radiative dephasing contributions, which contain the parameter  $\gamma$ , emerge from the electron-photon interaction by using Markov and bath approximation (see section 2.9). Thus it is calculated microscopically and not a phenomenological parameter. Several conclusions can already be drawn from the structure of these equations: (1) The equation of motion for the occupation  $f$  does not depend on any phonon quantities but only on the polarization and the electric field. Hence it is identical to

that of an atomic system (Eq. A.4). This reflects the fact that no direct interband transitions by phonon emission or absorption are possible. However, the occupation dynamics depends on the polarization, which is directly connected to the phonon system. Hence the occupation is indirectly influenced by the electron-phonon coupling. (2) Performing Markov approximation on the first order phonon-assisted interband coherences results in a Delta function  $\delta(\pm\omega_q)$ , i.e. a condition that can never be met. In second order Delta functions like  $\delta(\omega_q \pm \omega_{q'})$  emerge and can be fulfilled with  $\omega_q = \omega_{q'}$ . This condition is met for interband transitions during which one phonon is emitted and another with the same energy is absorbed. However, these processes do not have an enhanced probability and only contribute to transitions with an energy equal to the band gap and consequently only affect the ZPL line in absorption spectra, as expected from a Markovian process.

Fig. 6.7 shows results from a numerical evaluation of the equations of motion for excitation with an ultrashort linear pulse at different temperatures. For comparison, the polarization dynamics and absorption spectra of the nonperturbative theory based on the Independent Boson Model (see section 6.1) are displayed together with results from the first order and second order correlation expansion. For very low temperatures (4K, top row) all three curves coincident almost exactly: The polarization drops on a 2ps timescale and decays very slowly afterwards. In the absorption spectra one gets a sharp zero-phonon line which is surrounded by phonon sidebands. As discussed in section 6.1 these sidebands are very asymmetric with more weight at higher energies. For increasing temperatures, the correlation expansion results shows deviations from the nonperturbative curves. While the first order correlation expansion already differs from the i.b.m. at moderate temperatures (77K) the second order expansion shows good agreement for up to 200K but fails for even higher temperatures (300K, bottom row). Therefore all following simulations based on the correlation expansion are evaluated for temperatures well below 300K. Other materials may have a stronger electron-phonon coupling reducing the critical temperatures up to which the second order correlation expansion can be considered to be valid.

The advantages of the correlation expansion in contrast to the nonperturbative theories from section 6.1 result from the possibility to excite the system with arbitrary nonlinear pulses and to extend the model with further coupling mechanisms (like electron-electron interaction). Several applications will be discussed in the following.

### 6.3 Rabi oscillations

In isolated two-level systems it is well known that nonlinear coherent excitation leads to Rabi oscillations, i.e. to coherent flopping of the density during excitation with a strong optical pulse (see Ref. [27] or section A.2). Rabi flopping can be used for the preparation of specific quantum mechanical states. As a precursor of coherent control it is therefore considered to be an important ingredient for quantum information processing. Quantum dots have been proposed as basis element for quantum computing for several reasons: Besides their compactness, discrete level structure and easy manufacturing one original reason was the expectation of very few decoherence channels. Due to the discrete level structure it was expected that most intraband scattering processes were not allowed due to energy conservation. But, as discussed in section 6.1 this decoherence bottleneck can only be postulated for *strict* energy conservation. Quantum kinetic motion, i.e. processes beyond Markov approximation, provide dephasing channels which lead to at least partial reduction of optically induced coherence. Obviously, damping of Rabi oscillations has direct impact on the usability of quantum dots as quantum computing devices. In addition, Rabi flopping is also of general interest as it describes the fundamental nonlinear dynamics of system. Also, as discussed in section 6.5, it is possible to extract information about the many-body system by a nonlinear detuned excitation scheme.

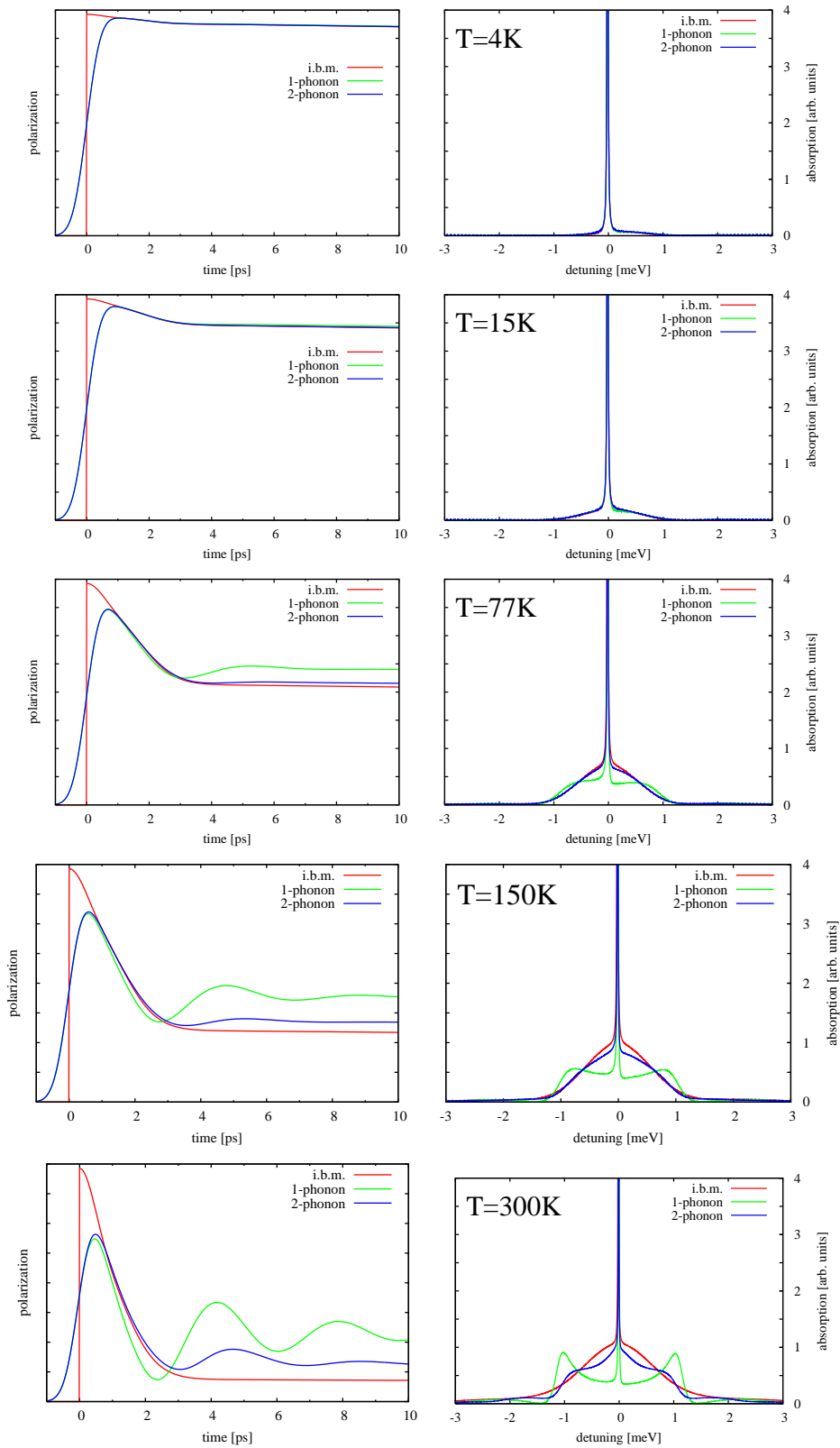


Figure 6.7: Comparison of the correlation expansion of first order (green) and second order (blue) to the nonperturbative i.b.(red) in linear optics. Left: linear polarization, Right: absorption spectra. The second order correlation expansion shows good agreement to the i.b.m. solutions for temperatures up to 200K, first order calculations differ already for much lower temperatures  $>15\text{K}$ . For simulations based on the correlation expansion a Gaussian  $500\text{fs}$  pulse has been applied.

The nonlinear polarization and occupation dynamics, specifically its dependence on the essential parameters pulse area, temperature and pulse duration, is therefore studied in the following. For comparison also results for an undamped two-level system are given. Fig. 6.8 shows the polarization and occupation dynamics for excitation with a  $5ps$  Gaussian pulse at  $T = 77K$  for different pulse areas ( $\Theta = 0.2\pi, 1\pi, 2\pi, 4\pi$  from top to bottom). In an undamped system (gray curve) the conduction level occupation increases only very slightly and thereafter remains on a constant value for very low pulse areas ( $\Theta = 0.2\pi$ ). For  $\Theta = 1\pi$  the isolated two-level system exhibits half a Rabi flop leaving a completely inverted system. In the phonon-damped quantum dot no complete inversion but only an occupation of about 0.8 is reached. This behavior continues for higher pulse areas: The undamped system performs perfect Rabi oscillations (compare section A.2). In the quantum dot the phonon-assisted dephasing leads to incomplete oscillations, e.g. for  $\Theta = 2\pi$  a density of about 0.4 remains in the upper level in contrast to the undamped system. However, the fundamental structure of an oscillating density is preserved with a strong first and increasingly reduced maxima. The polarization mainly shows the same structure, but still dephases for about one picosecond after pulse excitation. This dephasing at later times does not influence the occupation, since presence of both polarization and field is needed for changes in the occupation. However, during the pulse excitation the phonon-induced dephasing of the polarization strongly influences the temporal development of the occupation, leading to the described damping of Rabi oscillations.

Since the phonon population strongly depends on the temperature via the Bose-Einstein distribution, it is expected that also the dephasing dynamics changes with temperature. This is investigated in Fig. 6.9, which shows the polarization (left column) and occupation (middle column) dynamics of the phonon-damped quantum dot (red curve) for a  $5ps$  Gaussian  $4\pi$ -pulse at different temperatures ( $T = 4, 15, 77, 150K$  from top to bottom) in comparison to an undamped two-level system (gray curve). As in linear optics the dynamics of the quantum dot system is very similar to the undamped system at low temperatures (4K) due to the minimal phonon activity and exhibits two complete density Rabi flops. In the same time, the polarization performs four oscillations for the chosen  $4\pi$  pulse. For growing temperatures the phonon population and accordingly the phonon-assisted damping increases and both the polarization and occupation oscillations are reduced. While the polarization amplitude is damped as a whole for higher temperatures, the occupation only shows reduction of the modulation amplitude but still reaches a partial level inversion. For higher temperatures it converges towards the situation of equal occupation of upper and lower band as expected for incoherent pumping [27].

While the detailed study of the temporal dynamics helps to understand how the electron-phonon interaction affects the system, the most important information of such simulations with respect to coherent control is the final state of the system after excitation with a light pulse. As seen above the upper state occupation is only modified while a pulse is present, afterwards it remains constant and does not decay, assuming no other damping mechanisms are included. From Fig. 6.8 it can be concluded, that the final occupation will depend on the pulse area in an oscillating manner, i.e. it will show Rabi flopping as a function of the pulse area. As shown in section A.2 this dependence is exactly sinusoidal for undamped two-level-systems. Fig. 6.9 displays this function in comparison with the final upper state occupation of phonon-damped quantum dots for different lattice temperatures. For low temperatures (4K), the final occupation shows an oscillating behavior almost identical to the that of the (temperature independent) undamped two-level system. This is expected, since the polarization itself is barely influenced by the phonons at this temperature (compare Fig. 6.2). For higher temperatures the electron-phonon interaction becomes important due to increased phonon population and, as already seen before, no full inversion is possible anymore. Unexpectedly the minimal and maximal values of the oscillation vary with the pulse area. The first maximum (around  $1\pi$ ) is very pronounced in contrast to the following (at  $3\pi, 5\pi, \dots$ ). While the maxima get reduced for higher pulse areas at first,

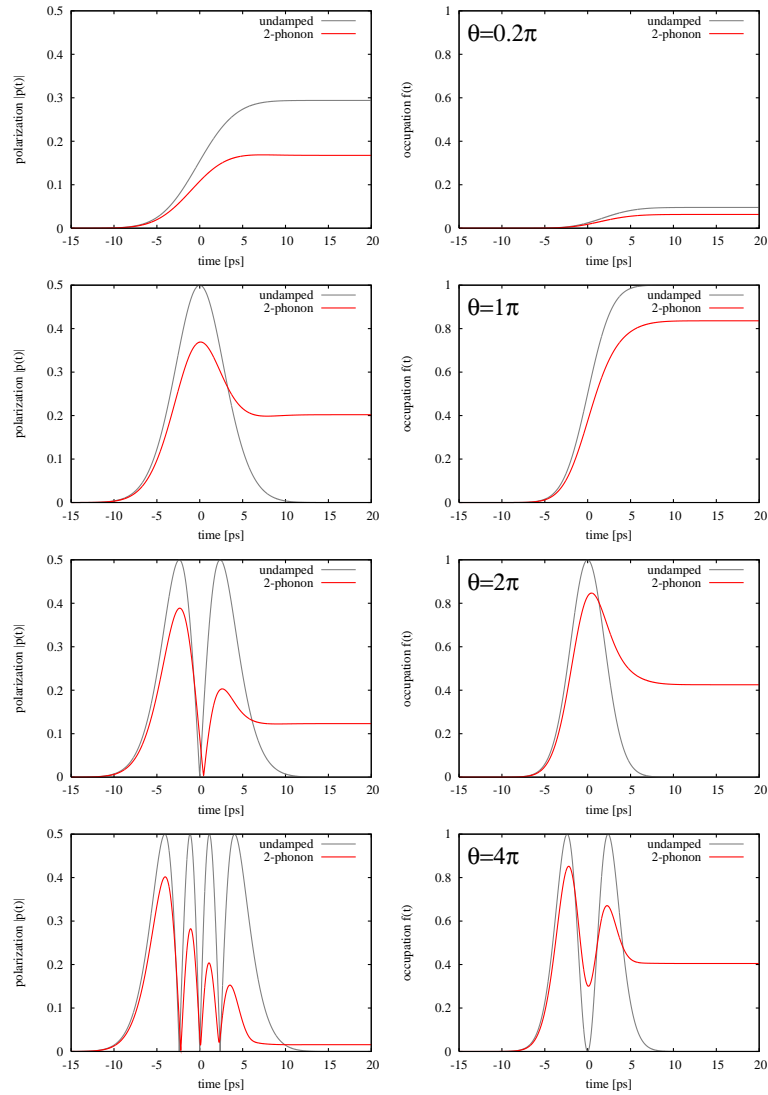


Figure 6.8: Pulse area dependence of the nonlinear polarization (left) and occupation (right) dynamics for excitation with a Gaussian 5 ps pulse at  $T = 77K$ .

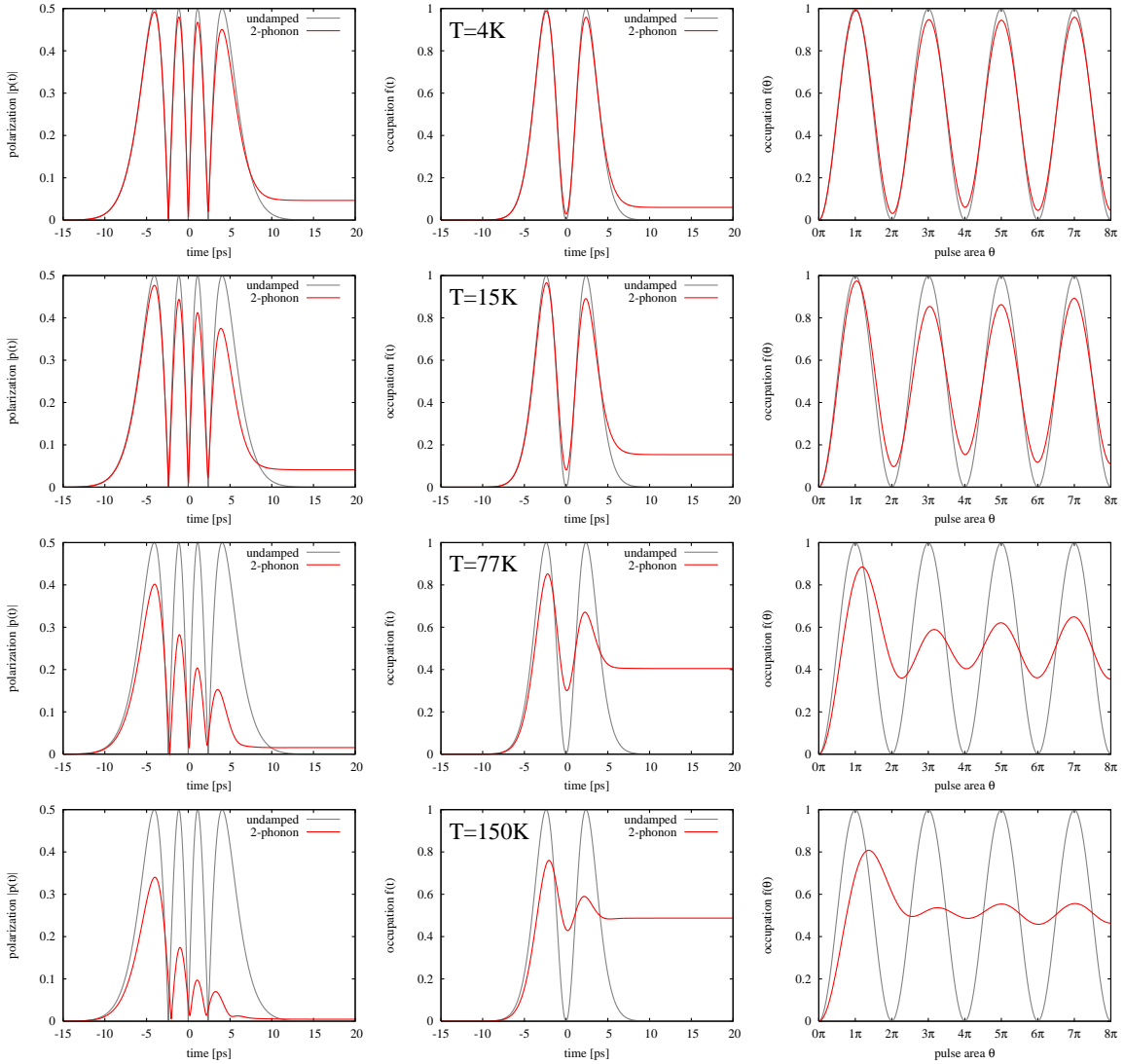


Figure 6.9: Temperature dependence of Rabi oscillations: Nonlinear polarization (left), occupation dynamics (middle) and occupation after pulse excitation (right) for an undamped two-level system (grey) and for the phonon-induced dephasing in second order correlation expansion (red). Left and middle: excitation with a  $4\pi$  pulse, Right: occupation after pulse excitation as a function of the pulse area. (pulse duration  $\tau = 5\text{ps}$ )

the modulation for  $7\pi$  is even higher than for  $5\pi$ . Additionally a pulse area renormalization occurs and can be observed as a slight shift of the minima and maxima to higher pulse areas.

From other dephasing mechanisms (like radiative dephasing) it is known, that the ratio between pulse duration and typical dephasing time is an essential parameter which allows classification of the system's behavior into different regimes. To study this effect for in the quantum dot system, Fig. 6.10 shows the pulse-area-dependent final upper level occupation  $f(\Theta)$  for different pulse durations. For comparison also results for the undamped two-level-system and a system with an exponential pure dephasing ( $T_2 = 4ps$ ) are displayed for a temperature of  $T = 77K$ . For very short pulses (500fs), none of the dephasing mechanisms is able to affect the dynamics resulting in perfectly oscillating final occupation as for an undamped system. However, for longer pulses the final occupation is increasingly modified: For the exponentially damped system the oscillation amplitudes are uniformly damped. If the pulse duration is considerably longer than the dephasing time (e.g. for  $\tau = 20ps \gg T_2 = 4ps$ ) the occupation even shows no more oscillations but only saturates into an equilibrium position where the upper and lower level are equally populated ( $f = 0.5$ ) as expected for incoherent pumping. The behavior for the phonon-induced dephasing is considerably distinct: For pulse durations up to about  $10ps$  the oscillations are increasingly damped. But only the modulation for higher pulse areas are strongly reduced, the first maximum around  $1\pi$  is barely affected, indicating that almost full inversion can be achieved for even very long pulse durations. For pulse duration beyond  $10ps$  the oscillation amplitudes even get stronger again, with a very pronounced first maximum and subsequently damped modulations. While this behavior is surprisingly at first, it can be understood by basic considerations: For short pulses the electron-phonon dynamics which acts on a time scale of about  $2ps$  is too slow to considerably affect the occupation. For increasing pulse duration this is no longer the case and strong damping can be expected. This damping is strongest, if the spectral width of the pulse coincides with the width of the phonon sidebands. For even longer durations the pulse gets spectrally very narrow and therefore decreasingly excites the phonon sidebands. However the pulse still has overlap with the ZPL and is therefore able to induce clear Rabi oscillations.

Experimentally the inversion can be obtained by pump-probe techniques or current measurements. The presented theory may provide a microscopically motivated explanation for the overshoot behavior, i.e. the strong first density Rabi oscillation maximum, found in several recent experiments [104, 105, 106]. However, the different experimental setups are not completely covered by theory: In Ref. [104] a large ensemble of quantum dots was measured, hence averaging effects over quantum dots with different sizes and therefore varying gap energies and dipole moments could be important and potentially be solely responsible for the overshooting behavior. In the experiment described in Ref. [105] scattering with excitons from delocalized states have been attributed to explain the observed overshooting dependency. The experimental setup from Ref. [106] is closest to the presented theoretical model since the experiments are performed on single quantum dots. However, only the excitation regime up to about  $3\pi$  is covered. While in this region the measurements are in good agreement with the theory, further experimental data is desired for verification of the theoretical predictions.

## 6.4 Convolution approach

### 6.4.1 Nonperturbative linear solution for finite pulses

The nonperturbative solution for linear excitation with a  $\delta$ -pulse, that has been derived 6.1 using the Independent Boson Model, can be used to construct the solution for excitation with an arbitrary pulse  $\Omega(t)$ . In linear optics the spectral functions of the polarization depends linearly on the light field

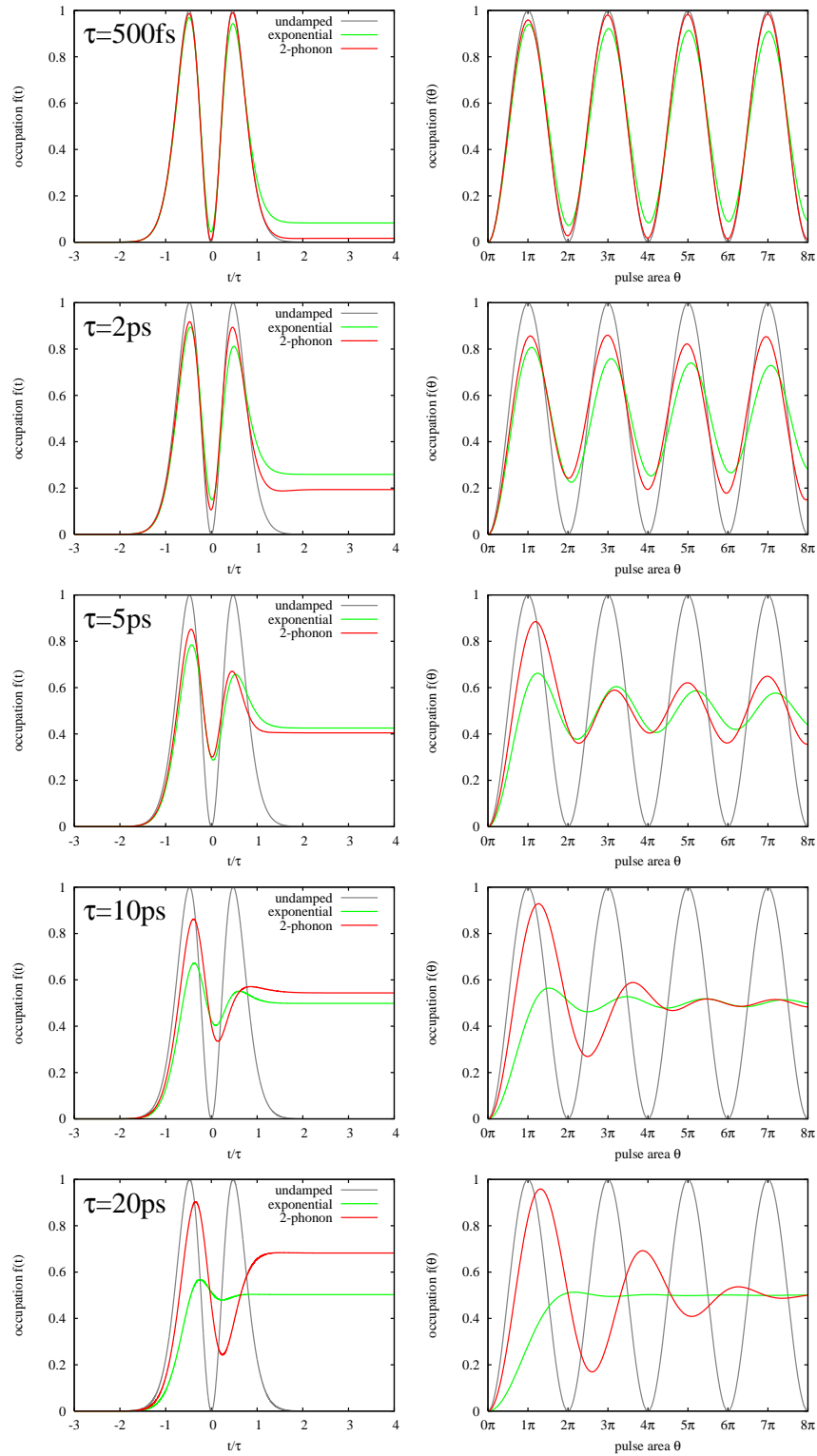


Figure 6.10: Pulse duration ( $\tau$ ) dependence of the occupation dynamics for  $\Theta = 4\pi$  (left) and the area-dependent occupation after pulse excitation. Different dephasing mechanisms (see text for details) are compared ( $T = 77\text{K}$ ).

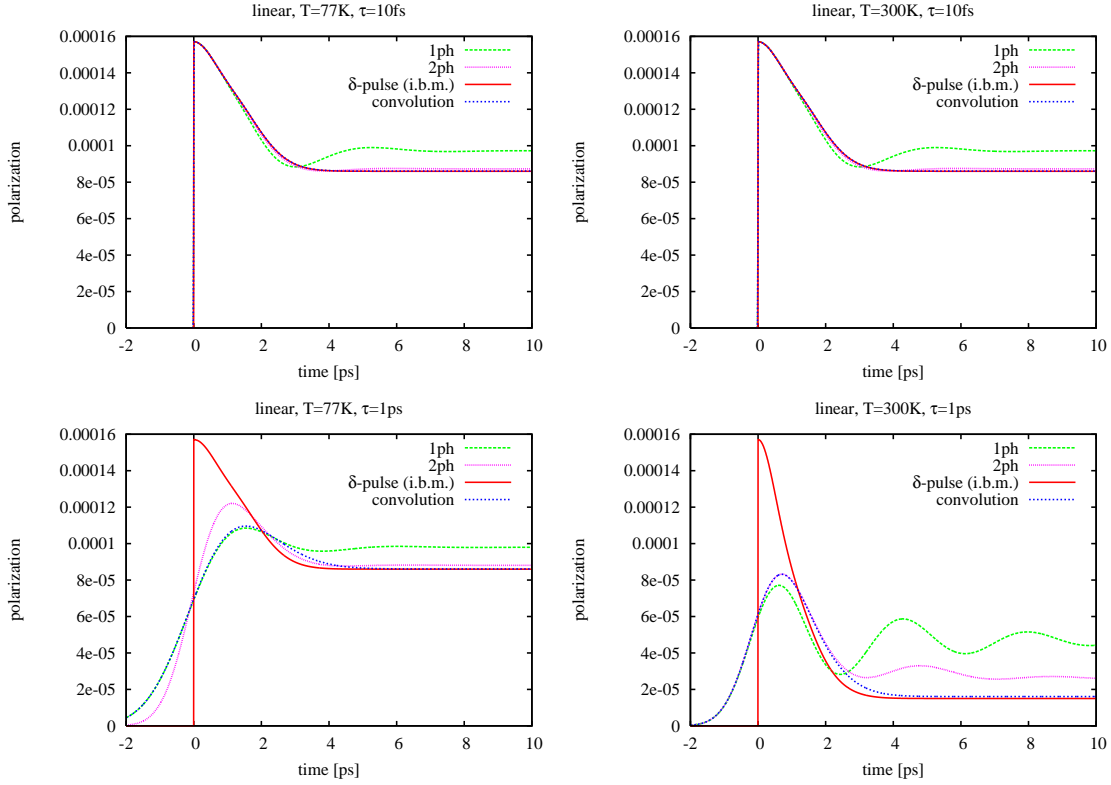


Figure 6.11: Polarization for linear excitation. Convolution approach in comparison to independent Boson model and correlation expansion. top: 10fs pulse, bottom: 1ps pulse. left: 77K, right: 300K

through the proportionality function  $\chi(\omega)$ :  $P(\omega) = \chi(\omega)\Omega(\omega)$ . Hence the polarization dynamics can be written as convolution:

$$P(t) = \int_{-\infty}^{\infty} dt' \chi(t-t') \Omega(t').$$

According to the Green's function formalism (or Fourier transformation, see section B.1) the linear response function  $\chi$  is defined as the system's response to  $\delta$ -pulse excitation and is given by the ibm polarization from Eq. 6.2 for the considered problem, i.e.  $\chi(t) = P_{vc}^{ibm}(t)$ . Hence the general polarization dynamics for excitation with an arbitrary pulse shape  $\Omega(t)$  can be written (in rotating frame) as:

$$P(t) = i \int_{-\infty}^{\infty} dt' \theta(t-t') \exp\left(\sum_{q,\pm} A_q^{\pm} (e^{\pm i\omega_q(t-t')} - 1)\right) \Omega(t'). \quad (6.9)$$

Numerical evaluation (Fig. 6.11) shows that the solution from the independent Boson model is reproduced for short pulses. For longer pulses the independent Boson model is no longer valid, but the convolution approach and the independent Boson model converge after long times. For not too high temperatures and coupling strengths (Fig. 6.11, left column: 77K) the second order correlation expansion is expected to be valid and indeed shows good agreement with the convolution approach. All in all the convolution approach is a direct extension of the independent Boson model solution and produces (at least in the linear regime) the result of known approaches for arbitrary temperatures and coupling strengths and pulses of finite duration.

### 6.4.2 Integro-differential approach

In nonlinear optics in addition to the polarization also densities are built up. The dynamics of these quantities is coupled and no approach to decouple them with help of mathematical transformations is known. Hence, the pursued approach is based on a rewrite of the linear convolution-integral solution into a differential equations. This equation is modified to include the density dynamics analogous to the correlation expansion framework, in which the equation of motion for the density only directly couple to the polarization and therefore only indirectly to the phonon dynamics. Hence it is expected, that the equations of motion of the density is not affected by a summation over the electron-phonon coupling hierarchy.

In a first step the linear convolution-integral solution is transformed into an integro-differential equation by taking the calculating the temporal derivative:

$$\begin{aligned} \dot{P}(t) &= i\Omega(t) + i \int_{-\infty}^t dt' W(t-t') \Omega(t'), & (6.10) \\ \text{with } W(t) &= \sum_{q,\pm} (\pm i\omega_q) A_q^\pm e^{\pm i\omega_q t} \exp\left(\sum_{q,\pm} A_q^\pm (e^{\pm i\omega_q t} - 1)\right). \end{aligned}$$

The function  $W(t)$  resembling a memory kernel contains the complete electron-phonon interaction and serves as additional inhomogeneity in the polarization equation.

The general validity of the convolution approach can only be proved for linear optics which has been considered so far. Calculations using the TCL (time-convolution-less) approach, which has been evaluated up to  $K_3$  order<sup>2</sup>, suggest that a convolution-integral solution may exist in which the pure Rabi frequency  $\Omega(t)$  is modified with a Pauli blocking term and therefore replaced by  $\Omega(t)(1 - 2f(t))$ . From the correlation expansion, which also supports this substitution, one knows that the equation of motion of the density does not contain any phonon-assisted quantities. Hence, the integro-differential equation describing the nonlinear dynamics non-perturbatively for arbitrary excitation can be guessed to be:

$$\dot{P}(t) = i\Omega(t)(1 - 2f(t)) + i \int_{-\infty}^t dt' W(t-t') \Omega(t')(1 - 2f(t')) \quad (6.11)$$

$$\dot{f}(t) = \text{Im}(\Omega^*(t)P(t)) \quad (6.12)$$

These equations have been numerically evaluated by direct discretization of the integral and are compared to the analytical  $\delta$ -pulse solution and the correlation expansion in Fig. 6.12. For excitation with a very short  $10fs$  pulse (top row) one gets very good agreement with the analytical  $\delta$ -pulse solution for low and high temperatures. For longer pulses ( $1ps$ , bottom row) the analytical solution is no longer valid, but in the low temperature range ( $77K$ , left column) the second order correlation expansion is expected to be correct and shows good agreement with the convolution approach results. Whereas the theory is not derived by direct mathematical deduction, these comparisons support the convolution approach and strengthen its validity - at least as good extrapolation method. All in all, the theory allows predictions in the regime of strong electron-phonon coupling for nonlinear excitation with pulses of finite duration, which was not covered by any previous theory. Fig. 6.12 ( $1ps$ ,  $77K$ : bottom,right) displays results for this region showing both damped Rabi flopping during the pulse duration and a smooth non-oscillating behaviour for long times.

<sup>2</sup>Calculations by Nikolaos Gortsas, unpublished.

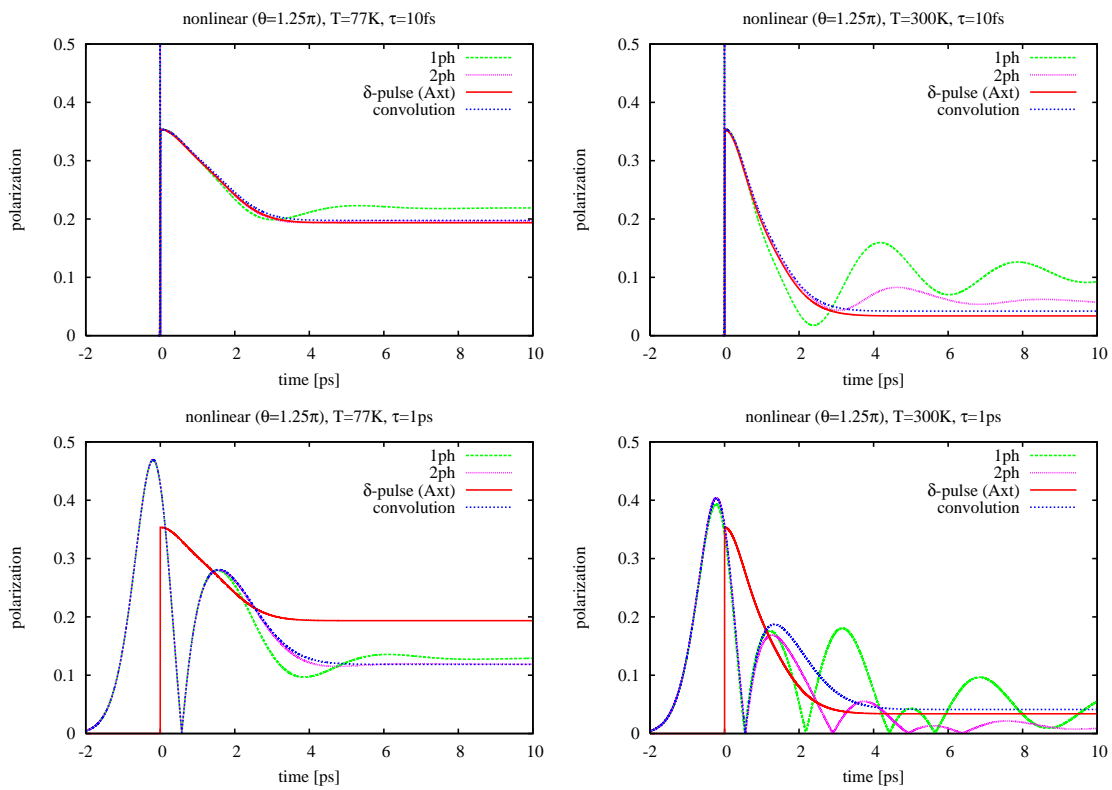


Figure 6.12: Polarization for nonlinear excitation (pulse area  $\theta = 1.25$ ). Convolution approach in comparison to the analytical  $\delta$ -pulse solution [95] and the correlation expansion. top: 10fs pulse, bottom: 1ps pulse. left: 77K, right: 300K.

### 6.4.3 Frequency domain approach

A differential set of equations without an integral part can be constructed starting from the linear convolution integral (Eq. by introducing a new quantity  $S_q^\pm(t)$ ):

$$\dot{P}(t) = i\Omega(t) + i \sum_{\mathbf{q}, \pm} (\pm i\omega_{\mathbf{q}}) A_{\mathbf{q}}^\pm S_{\mathbf{q}}^\pm(t)$$

The integral has been absorbed into the new quantity  $S_{\mathbf{q}}^\pm(t) = \int dt' \theta(t-t') e^{\pm i\omega_{\mathbf{q}}(t-t')} \beta(t-t') \Omega(t')$  with  $\beta(t-t') = \exp\left(\sum_{\mathbf{q}, \pm} A_{\mathbf{q}}^\pm (e^{\pm i\omega_{\mathbf{q}}(t-t')} - 1)\right)$ . Comparing this equation to Eq. 6.5, the quantity  $S_{\mathbf{q}}^\pm(t)$  strongly resembles the phonon assisted density matrix elements from the correlation expansion approach. In order to eliminate all explicit integrals and hoping to obtain a closed set of equations one derives the differential equation for  $S_{\mathbf{q}}^\pm(t)$ :

$$\begin{aligned} \Rightarrow \dot{S}_{\mathbf{q}}^\pm(t) &= \pm i\omega_{\mathbf{q}} S_{\mathbf{q}}^\pm(t) + i\Omega(t) + \sum_{\mathbf{q}', \pm'} (\pm' i\omega_{\mathbf{q}'}) A_{\mathbf{q}', \pm'}^\pm S_{\mathbf{q}', \pm'}^\pm(t) \\ \text{with } S_{\mathbf{q}, \mathbf{q}'}^{\pm, \pm'} &= \int_{-\infty}^{\infty} dt' \theta(t-t') e^{i(\pm\omega_{\mathbf{q}} \pm' \omega_{\mathbf{q}'}) (t-t')} \beta(t-t') \Omega(t') \end{aligned}$$

By transformation from wavevector to frequency representation one can represent both  $S_{\mathbf{q}}^\pm(t)$  and  $S_{\mathbf{q}, \mathbf{q}'}^{\pm, \pm'}(t)$  by the same quantity  $T(t, \omega) = \int_{-\infty}^{\infty} dt' \theta(t-t') e^{i\omega(t-t')} \beta(t-t') \Omega(t')$ :  $S_{\mathbf{q}}^\pm(t) = T(t, \pm\omega_{\mathbf{q}})$ ,  $S_{\mathbf{q}, \mathbf{q}'}^{\pm, \pm'}(t) = T(t, \pm\omega_{\mathbf{q}} \pm' \omega_{\mathbf{q}'})$ . These substitutions lead to a formally closed set of differential equations:

$$\begin{aligned} \dot{P}(t) &= i\Omega(t) + i \sum_{\mathbf{q}, \pm} (\pm i\omega_{\mathbf{q}}) A_{\mathbf{q}}^\pm T(t, \pm\omega_{\mathbf{q}}) \\ \dot{T}(t, \omega) &= i\omega T(t, \omega) + i\Omega(t) + \sum_{\mathbf{q}, \pm} (\pm i\omega_{\mathbf{q}}) A_{\mathbf{q}}^\pm T(t, \omega \pm \omega_{\mathbf{q}}) \end{aligned}$$

Practically  $T(t, \omega)$  would have to be calculated for an infinite number and range of frequencies  $\omega$ , which renders a complete numerical evaluation impossible. But for a linear or constant phonon dispersion the complexity with respect to the wavenumber discretization could be reduced from exponential to linear scale, drastically reducing the computational effort.

Again motivated by the correlation expansion equations, one can introduce the density as a dynamic quantity and substitute the Rabi frequency  $\Omega(t)$  by  $\Omega(t)(1-2f)$  leading to a closed set of differential equations describing the nonlinear electron-phonon dynamics:

$$\begin{aligned} \dot{P}(t) &= i\Omega(t)(1-2f(t)) + i \sum_{\mathbf{q}, \pm} (\pm i\omega_{\mathbf{q}}) A_{\mathbf{q}}^\pm T(t, \pm\omega_{\mathbf{q}}) \\ \dot{T}(t, \omega) &= i\omega T(t, \omega) + i\Omega(t)(1-2f(t)) + \sum_{\mathbf{q}, \pm} (\pm i\omega_{\mathbf{q}}) A_{\mathbf{q}}^\pm T(t, \omega \pm \omega_{\mathbf{q}}) \\ \dot{f}(t) &= \text{Im}(\Omega^*(t)P(t)) \end{aligned}$$

Further studies could determine, whether these equations can be derived by a rigorous calculation and if one can extend the approach to a multi-level system and if it is possible to include other interactions like electron-electron coupling.

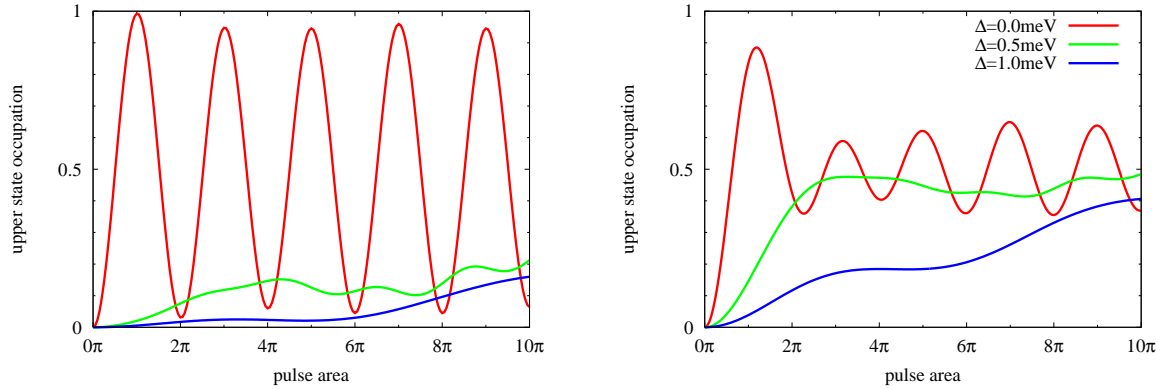


Figure 6.13: Occupation after pulse excitation ( $\tau = 5ps$ ) for different detunings ( $\Delta = 0, 0.5, 1.0$ ) of the input pulse relative to the ZPL resonance for  $T = 4K$  (left) and  $T = 77K$  (right).

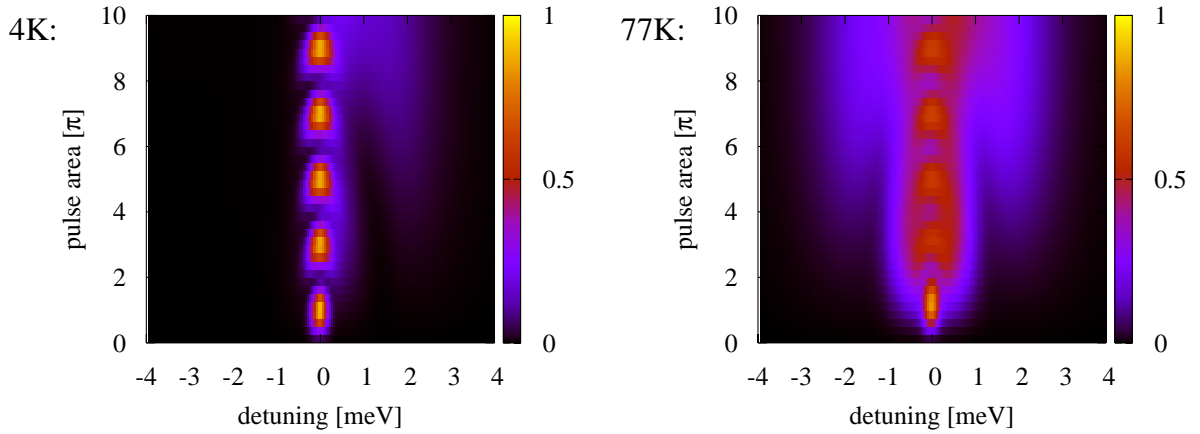


Figure 6.14: Final occupation (encoded as color: black=0, yellow=1) for variation of pulse area and detuning. Left: 4K, Right: 77K

## 6.5 Nonlinear detuning spectra

An additional degree of freedom that has not been considered in the previous discussions is the frequency of the incident light pulse. Instead of a resonant excitation where the energy of the light frequency matches the gap energy, the pulse can be detuned from the exact frequency. This off-resonant excitation allows to extract further information about the electron-phonon interaction by optical methods.

Fig. 6.13 shows the pulse area dependent occupation after excitation for different detunings. For zero detuning ( $\Delta = 0\text{meV}$ ) the results from Fig. 6.9 are reproduced showing an oscillating behavior with strong first and reduced subsequent maxima. For increasing detuning ( $\Delta = 0.5\text{meV}$ ) the modulations of the oscillations are suppressed and the system is simply brought into an equal occupation situation ( $f \approx 0.5$ ) for stronger pulses ( $\Theta > 2\pi$ ) and higher temperatures (77K). For far off-resonant excitation ( $\Delta \geq 1\text{meV}$  for 77K,  $\Delta \geq 0.1\text{meV}$  for 4K) not only the oscillations but also the occupation itself is strongly suppressed reaching nonvanishing values ( $f \approx 0.3$ ) only for very strong pulses.

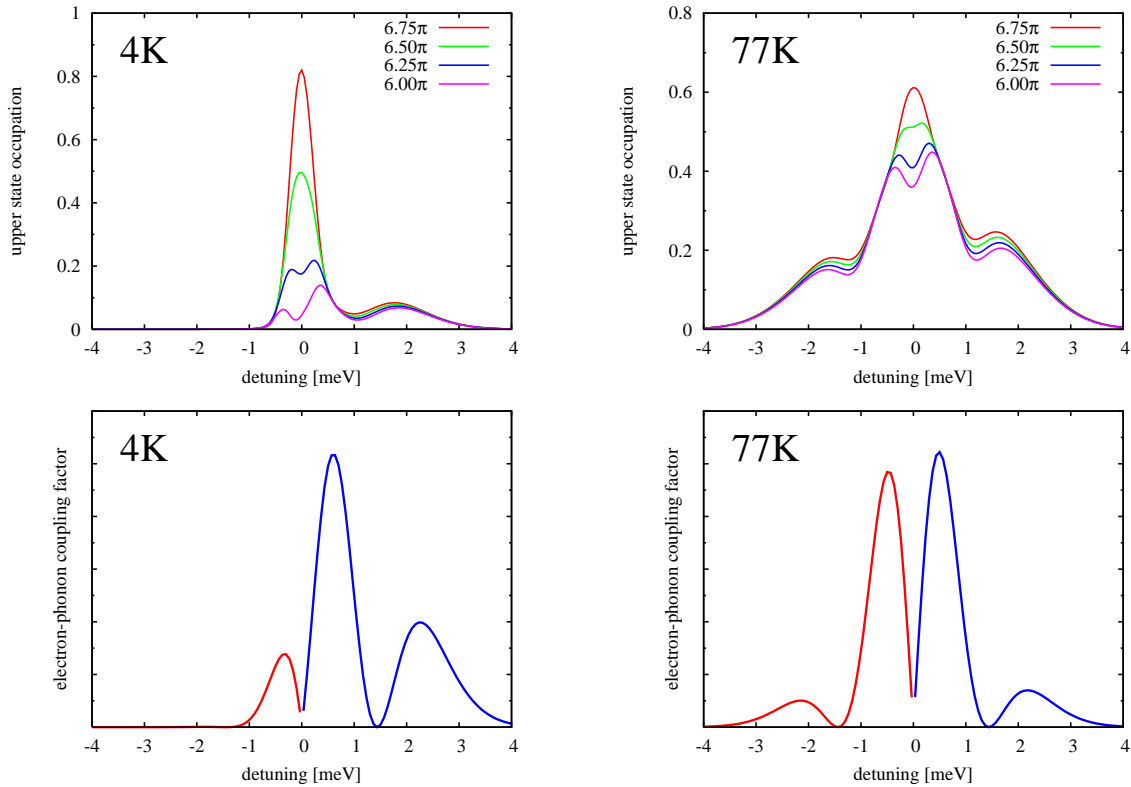


Figure 6.15: Top row: Occupation as a function of detuning for selected pulse areas. Bottom Row: Effective electron-phonon coupling element modified by phonon population factor. Left: 4K, Right: 77K

This dependency of the upper state occupation on the detuning is systematically plotted in Fig. 6.14 showing the occupation encoded as color (black=0, yellow=1) for variation of both the pulse area and detuning. At low temperatures (left, 4K) a pronounced Rabi flopping structure in the vicinity of  $\Delta = 0$  is visible. These oscillations with increasing pulse area do not only occur for exactly  $\Delta = 0$  but also in a small vicinity. Generally the modulation of the oscillation is weaker for  $\Delta \neq 0$ , but the modulation range increases for higher pulse areas. Additionally one can observe a small region of nonvanishing occupation for detunings around 2meV at higher pulse areas. While the strong structure around  $\Delta = 0$  can be attributed to Rabi flopping at the ZPL, the structure at nonvanishing detuning can be identified as phonon assisted transitions. Due to the small phonon activity at low temperatures the process is considerably suppressed and therefore needs high pulse areas. Also for higher temperatures (right, 77K) strong oscillations occur around zero detuning for increasing pulse areas. Additionally the sidebands which occur due to phonon-assisted transitions get more pronounced, but show no oscillating structure. Since the phonons are coupled to an incoherent phonon bath no coherent Rabi flopping but incoherent pumping is possible.

The fact that only transitions at the ZPL and not at the phonon sidebands show oscillating behavior could be used in an experimental setup in order to gain detailed information about the electron-phonon interaction. For this, the occupation has to be obtained as a function of the detuning for a pulse area where the oscillation at the ZPL has a minimum. Then the detuning spectrum consists only of phonon sidebands without the direct (ZPL) transition part. To illustrate this, Fig. 6.15 (top row) shows such

detuning-spectra of the occupation for different pulse areas. For cases where the ZPL part is small the curves strongly resemble the electron-phonon coupling element shown in Fig. 6.1. The asymmetry can be explained with different effective weighting factors for phonon absorption and emission. To illustrate this, Fig. 6.15 (bottom row) displays an effective electron-phonon coupling factor

$$G(\omega) = \begin{cases} |\tilde{g}_{\mathbf{q}}^{vc}|^2 n_{\mathbf{q}} q^2 & \text{for } \omega < 0 \\ |\tilde{g}_{\mathbf{q}}^{vc}|^2 (n_{\mathbf{q}} + 1) q^2 & \text{for } \omega \geq 0 \end{cases},$$

which consists of the coupling element  $\tilde{g}_{\mathbf{q}}^{vc} = g_{\mathbf{q}}^{cc} - g_{\mathbf{q}}^{vv}$ , the phonon occupation modified to include spontaneous emission for positive detunings and a phase space factor (note:  $q = |\Delta|/c$  has been used). All in all detailed information about the electron-phonon coupling can be retrieved by this nonlinear detuning scheme.

## 6.6 Intradot Coulomb coupling (biexcitonic effects)

Up to now, only excitation of a single electron-hole pair has been investigated. This is a valid good description for a quantum dot if only two levels and excitation with circular polarized light is considered. If more than a single electron-hole pair is excited, it is expected that Coulomb interaction between the electrons leads to many-body coupling. For the special three dimensional confinement situation encountered in quantum dots the Hamiltonian from Eq. 2.17 describing electron-electron Coulomb interaction (see section 2.2.4) reduces to:

$$H_c = \frac{1}{2} \sum_{12} V_{12} a_1^\dagger a_2^\dagger a_2 a_1.$$

Due to the three-dimensional confinement, the compound indices only contain band, subband and spin indices. If only a constant background screening is assumed the Coulomb matrix element can be most compactly expressed in space domain:

$$V_{12} = \frac{e^2}{4\pi\epsilon_0\epsilon_b} \int d^3r \int d^3r' \frac{\phi_1^*(\mathbf{r})\phi_1(\mathbf{r})\phi_2^*(\mathbf{r}')\phi_2(\mathbf{r}')}{|\mathbf{r} - \mathbf{r}'|}.$$

Apparently the Coulomb matrix element obeys the symmetry condition  $V_{12} = V_{21}$ . Hence, in a system with two levels (v,c) each spin degenerated (i.e. no splitting) only three distinct matrix elements occur. One can show that the Coulomb matrix elements for Gaussian wavefunctions with radii  $q$  are given by  $V_{12} = \frac{e^2}{4\pi\epsilon_0\epsilon_b} \frac{4}{\sqrt{2\pi}\sqrt{a_1^2+a_2^2}}$ . For the used parameters (Table 6.1) one would obtain values (e.g.  $V_{cc} \approx 22meV$ ) which are much larger than observed in experiments [107, 108] or calculated using more realistic wavefunctions from  $k \cdot p$ -calculations [108]. These high values are artifacts from the Gaussian wavefunctions, which result from the artificial parabolic confinement potential and which have their maxima at the same position for valence and conduction level. Hence the matrix elements have been adjusted to be in agreement with experimental findings while maintain the ratio of the theoretical result. If not stated otherwise  $V_{vv} = 8meV$ ,  $V_{cc} = 4meV$  and  $V_{vc} = 5meV$  has been used.

If excitation of up to two electrons is investigated, the hierarchy of equations of motion naturally truncates with respect to the Coulomb interaction because all expectation values with three or more electron creation/annihilation operator pairs in normal order (acting on a two-particle state) must vanish. Therefore the Hartree-Fock approximation does not have to be applied and would lead to errors as large as the quantities itself, as the underlying assumption of a mean field is no longer fulfilled. The equations of motion have been derived including Markovian electron-photon interaction

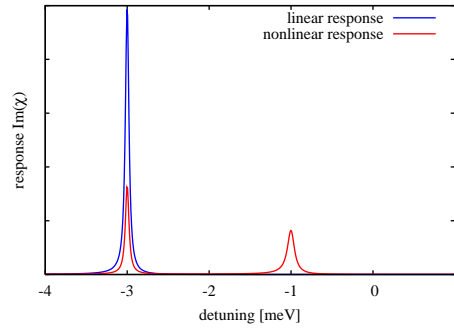


Figure 6.16: Linear (blue) and nonlinear (red,  $\Theta = 0.5\pi$ ) response of the quantum dot system for inclusion of Coulomb interaction.

and non-Markovian electron-phonon coupling in a first order correlation expansion. They are given in appendix C.2. In an alternative approach one could be tempted to diagonalize the given Hamiltonian. This is feasible if only the Coulomb interaction is included, but not for additional many-body coupling to photons and phonons. Also the coupling to the classical light field would exhibit different transition elements and therefore only approximatively map to a simple multi-level scheme.

The equations of motions are first evaluated without inclusion of phonon-induced dephasing to study effects by the electron-photon and Coulomb interaction. Fig. 6.16 shows the response of the system for linear and weakly nonlinear ( $\Theta = 0.5\pi$ ) excitation. For illustration, the radiative decay constant has been increased by a factor of ten (i.e.  $\gamma = 50ps$ ). As expected, the linear absorption line is shifted to lower energies ( $E_A = V_{vc} - V_{vv} = -3meV$  relative to the band gap). This energetic shift corresponds to the Coulomb binding energy of a single electron-hole pair. For higher excitation a biexcitonic state is built from two Coulomb correlated electrons and holes and leads to a second absorption line at  $E_B = V_{cc} - V_{vc} = -1meV$  relative to the band gap. Apparently the biexcitonic resonance is shifted to a higher energy relative to the exciton resonance for the used model wavefunctions. This antibinding effect of biexcitons has been observed in experiments and is in agreement with  $\mathbf{k} \cdot \mathbf{p}$  calculations [108]. As can be seen in the graph, the biexcitonic line is by a factor of 2 broader than the excitonic line, corresponding to a faster decay time of the biexcitonic transition due to radiative decay.

If the system is excited with a nonlinear pulse the electrons are transferred into the upper states. This is displayed in Fig. 6.17 showing the population of the upper level for one spin orientation, the biexcitonic population  $B(\Theta) = \langle a_{c0}^+ a_{c1}^+ a_{c1} a_{c0} \rangle$  and the product  $H(\Theta) = \langle a_{c0}^+ a_{c0} \rangle \langle a_{c1}^+ a_{c1} \rangle = f(\Theta)^2$  which would be used as approximation for  $B(\Theta)$  in a Hartree-Fock approach. Normal (non-enhanced) radiative decay with  $T_2 = 500ps$  has been included. For excitation with a spectrally broad pulse ( $\tau = 100fs$ ) the system shows clear Rabi oscillations. Since both transition energies are available in the input pulse, the electrons are uniformly transferred to the upper state immediately building a partial biexcitonic state. The Hartree-Fock product  $H(\Theta)$  directly follows  $B(\Theta)$  showing that the correlation  $B(\Theta) - H(\Theta)$  is zero for this broadband excitation. If a spectrally narrow pulse ( $\tau = 10ps$ ) tuned on the excitonic resonance is applied, the situation changes and according to Fig. 6.17 only half inversion for each electron can be reached. This corresponds to the fact that apparently two electrons with two holes cannot exist as two separate excitons but must form a biexciton in quantum dots. If the spectral components for building this biexcitonic state are not present, the pulse can only excite the system from its initial ground state  $|00\rangle$  into the highly entangled state  $|\psi_m\rangle = \frac{1}{\sqrt{2}}(|01\rangle + |10\rangle)$ ,

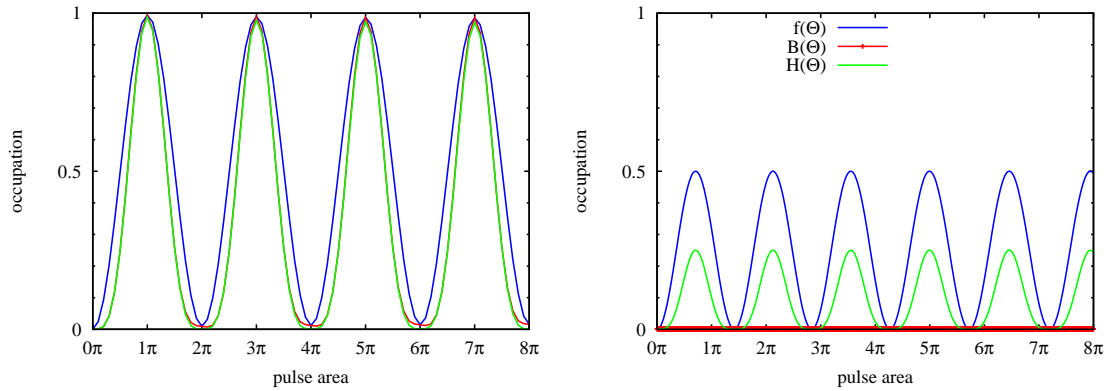


Figure 6.17: Pulse area dependence of the upper level occupation  $f(\Theta)$  (blue curve), the biexcitonic occupation  $B(\Theta)$  (red curve), and the Hartree-Fock product  $H(\Theta) = f(\Theta)^2$  (green curve) for excitation of a spectrally narrow  $10ps$ -pulse tuned on the exciton resonance ( $-3meV$ )

which has a single particle population of  $\frac{1}{2}$ , i.e. below 1. This is also observable in the biexcitonic population  $B(\Theta)$  which stays zero and therefore considerably differs from the Hartree-Fock product  $H(\Theta)$  which oscillates between 0 and  $\frac{1}{4}$ . Hence, the correlation  $C(\Theta) = B(\Theta) - H(\Theta)$  is equal to the quantity  $-H(\Theta)$  itself. This confirms that the Hartree-Fock approximation would fail to describe the physical situation and should therefore not be used for such a few-particle system. Despite the impossibility of full Rabi flopping the density still shows an oscillating behavior, but it flops between 0 and  $\frac{1}{2}$  and the frequency is by a factor of  $\sqrt{2}$  faster compared full Rabi flops. It already reaches its maximum state  $|\Psi_m\rangle$  with  $f_{c0} = \frac{1}{2}$  for  $\Theta = \pi/\sqrt{2}$  and returns to its ground state  $|00\rangle$  with  $f_{c0} = 0$  for  $\Theta = \sqrt{2}\pi$ .

The question arises whether it is possible to induce optical transitions if the frequency of the light pulse does not exactly match the excitonic resonance frequency. In order to study this problem, analogous to the nonlinear detuning spectra shown in section 6.5, in Fig. ?? the upper level occupation is displayed in a color encoded map for variation of detuning and pulse area for the spectrally narrow  $10ps$ -pulse (corresponding to a FWHM of about  $0.2meV$ ). Around the exciton resonance at  $-3meV$  one can see oscillations along the pulse area axis as discussed above. For small deviation from the exact resonance excitation oscillations are possible, however only reduced. The width of these features in detuning direction is just given by the spectral width of the pulse which still has overlap with the excitonic line even for small deviations. Consequently one has to use spectrally narrow pulses (like the applied Gaussian  $10ps$  pulse) in order to resolve small spectral features. As one would expect, excitation at the position of the biexcitonic resonance ( $-1meV$ ) alone does not lead to any excitonic population  $f$ , therefore also no biexcitonic density  $B$  (not shown) can be built up. Unexpectedly another oscillation of the occupation with increasing pulse area occurs around  $-2meV$  exactly between the excitonic and biexcitonic resonances. In contrast to excitation with the spectrally broad  $100fs$  pulse as has been used above for calculation of the nonlinear response, the overlap of the spectrally narrow  $10ps$  pulse with the resonances is marginal ( $10^{-12}$ ) and can therefore not explain the features. Also, since the occupation exhibits very clear oscillations it does not comply with adiabatic following effects which are known for non-zero detuning [27]. Hence, the features can only be understood in a many-particle picture and not by projection on a multi-level effective single-particle scheme. In order to investigate the effect in detail, Fig. ?? shows a cut along the pulse-area-axis for a detun-

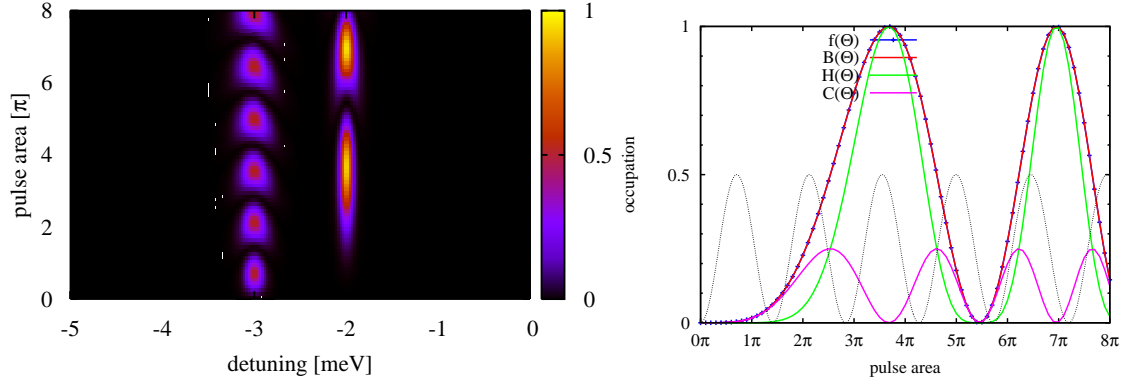


Figure 6.18: Upper level occupation after excitation with a nonlinear (spectrally narrow)  $10ps$  pulse. Left: variation of detuning and pulse area, occupation is color encoded. Right: population  $f(\Theta)$  (blue curve), biexcitonic occupation  $B(\Theta)$  (red curve), Hartree-Fock product  $H(\Theta) = f(\Theta)^2$  (green curve) and correlation  $C(\Theta) = B(\Theta) - H(\Theta)$  (magenta curve) as function of the pulse area for a detuning of  $-2meV$ .

ing of  $-2meV$ . While the occupations only varies between 0 and  $\frac{1}{2}$  for excitation at the excitonic resonance, full Rabi flops from 0 to 1 are performed by the system for a  $-2meV$  detuning. However, the oscillation period, which is  $\sqrt{2}\pi$  for exciton-resonant excitation, is not constant and much larger for off-resonant excitation. In contrast to the Rabi oscillation which are induced by a spectrally broad pulse, here the biexcitonic occupation  $B$  builds up exactly matching the exciton density, i.e.  $B(\Theta) = f(\Theta)$ . Hence, a nonvanishing correlation contribution  $C(\Theta) = B(\Theta) - H(\Theta) = B(\Theta) - f(\Theta)^2$  occurs in comparison to a broad band excitation.

Fig. 6.19 shows the impact of a nonlinear pulse on the occupation, if the system is initially prepared in the highly entangled  $|\psi_m\rangle$  state (e.g. by a  $\pi/\sqrt{2}$  pulse tuned on the exciton resonance). For excitation around the excitonic resonance ( $-3meV$ ) the system is oscillating between  $\frac{1}{2}$  and 0 as already observed above. However if the pulse is tuned in the vicinity of the biexcitonic resonance ( $-1meV$ ) it is possible to induce upper level populations above  $\frac{1}{2}$ . This is further illustrated in Fig. 6.17 showing the pulse area dependence for exact excitation of the biexcitonic resonance. It shows the system performs transitions between the initial state  $|\psi_m\rangle$  and the fully biexcitonic state  $|11\rangle$ . The upper level occupation flops between  $\frac{1}{2}$  and 1 with a periodicity of  $\sqrt{2}\pi$ . The biexcitonic amplitude  $B(\Theta)$  oscillates with the same frequency between 0 to 1. Hence, the system exhibits pure exciton-biexciton Rabi oscillations. In strong contrast to the observations for a system initially prepared into the ground state, excitation with a pulse which is tuned on  $-2meV$  the system does not show any response at all. Further studies could determine, whether these frequency selective flopping effects can be utilized for optical gates or even qubit operations.

In a next step, electron-phonon coupling is again included using the correlation expansion approach described in section 6.2. The full set of equations is derived in first order with respect to the electron-phonon interaction and is given in appendix C.2. Fig. 6.20 shows the results of a simulation performed for a lattice temperature of  $T = 77K$  and excitation with a Gaussian  $10ps$  pulse. Essentially the occupation as a function of detuning and pulse area is a direct combination of the results for electron-phonon coupling (Fig. 6.14) and Coulomb interaction (Fig. 6.18). However, not only the exciton resonance is surrounded by phonon sidebands, but also the structure at  $-2meV$ . The sideband around  $-2meV$  are spectrally narrower than for the exciton resonance. This is in contrast to the non-

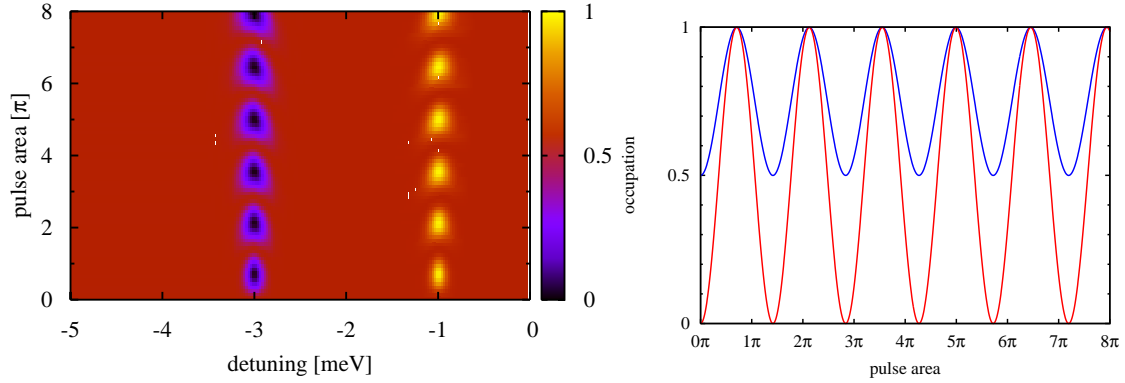


Figure 6.19: Upper level occupation for a quantum dot system that is initially in the highly entangled state  $|\Psi_m\rangle = \frac{1}{\sqrt{2}}(|01\rangle + |10\rangle)$ . Left: nonlinear detuning scan, Right: excitonic population  $f(\Theta)$  (blue curve) and biexcitonic occupation  $B(\Theta)$  for excitation tuned on the biexcitonic resonance ( $-1\text{meV}$ ). Response of the quantum dot system for linear (blue) and weakly nonlinear (red) excitation. Simulation includes two-electron-coherences and Coulomb interaction

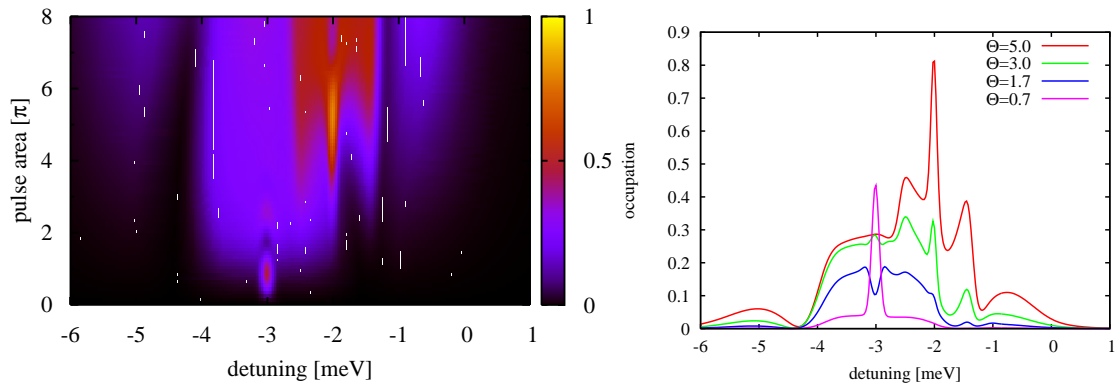


Figure 6.20: Upper level occupation after excitation with  $10\text{ps}$  pulse for a quantum dot model including both Coulomb and electron-phonon interaction. Left: occupation scan for variation of detuning and pulse area, Right: detuning dependence of the occupation for different pulse areas.

linear response  $\text{Im}\chi$  (not shown) which exhibits phonon sidebands around the excitonic and around the biexcitonic resonance with the same spectral width.

## 6.7 Interdot coupling by phonons

For GaAs quantum dots which are solely considered in this work, the generation of non-equilibrium phonon populations and pure phonon-correlations is negligible for single quantum dots based on realistic parameters[97]. However, if a large ordered ensemble of quantum dots is considered, the situation is different. Then it is possible to create macroscopic phonon populations beyond the equilibrium bath distribution. In order to describe this situation, the formalism of chapter 2 has to be extended to allow an ensemble of quantum dots. Introducing a quantum dot index  $n$ , the overall wave function can be expanded into individual single dot solutions  $\phi_{i,n}$ :

$$\psi(\mathbf{r}) = \sum_{i,n} \phi_{i,n}(\mathbf{r}) u_{ik}(\mathbf{r}) a_{i,n}.$$

Assuming that the wavefunctions of different dots do not overlap, the Hamiltonian accordingly changes to:

$$H = \sum_{i,n} E_{i,n} a_{i,n}^+ a_{i,n} + \sum_{i,j,n} \mathbf{d}_{i,j,n} \mathbf{E}_c(t, \mathbf{r}) a_{i,n}^+ a_{j,n} + \sum_{\mathbf{q}} \hbar \omega_{\mathbf{q}} b_{\mathbf{q}}^+ b_{\mathbf{q}} + \sum_{i,j,\mathbf{q},n} g_{\mathbf{q},n}^{ij} a_{i,n}^+ a_{j,n} (b_{\mathbf{q}} + b_{\mathbf{q}}^+).$$

As one would expect, the quantum dot index  $n$  appears in all matrix elements because the related integrals have to be performed over the respective quantum dot wave function. Assuming that all quantum dot wave functions have the same shape  $\phi(\mathbf{r})$  and are only translated to different position, so  $\phi_{i,n}(\mathbf{r}) = \phi_i(\mathbf{r} - \mathbf{R}_n) e^{i\zeta_n}$ , the matrix elements can be written as:

$$E_{i,n} = E_i,$$

$$d_{i,j,n} \mathbf{E}_c(t, \mathbf{r}) = d_{i,j} \mathbf{E}_c(t, \mathbf{r}_n),$$

$$g_{\mathbf{q},n}^{i,j} = g_{\mathbf{q}}^{i,j} e^{i\mathbf{q} \cdot \mathbf{R}_n},$$

As special case, all quantum dots could be equally excited by an homogeneous light field. Then all dots would be indistinguishable and all expectation values should behave equally. This assumption can then be used to rewrite the Hamiltonian:

$$H = N \sum_i E_i a_i^+ a_i + N \sum_{i,j} \mathbf{d}_{i,j} \mathbf{E}_c(t) a_i^+ a_j + \sum_{\mathbf{q}} \hbar \omega_{\mathbf{q}} b_{\mathbf{q}}^+ b_{\mathbf{q}} + \sum_{i,j,\mathbf{q}} G_{\mathbf{q}}^{ij} a_i^+ a_j (b_{\mathbf{q}} + b_{\mathbf{q}}^+),$$

Hence, the main difference in contrast to a single quantum dot occurs in the electron-phonon coupling  $G_{\mathbf{q}}^{ij} = g_{\mathbf{q}}^{ij} \sum_n e^{i\mathbf{q} \cdot \mathbf{R}_n}$  which now additionally includes a summation over phase factors. If the quantum dots form a regular grid with distance  $R_0$ , the wave vectors  $\mathbf{q}$  have to be inverse (super)lattice vectors (in the dimensions in which the dots form a grid), i.e. it evaluates to  $\sum_m \delta(\mathbf{q} \cdot \mathbf{R} - 2\pi m)$  and by that selects specific wave vectors in the Hamiltonian. In effect this considerably reduces the number of phonon modes to which the quantum dots can couple.

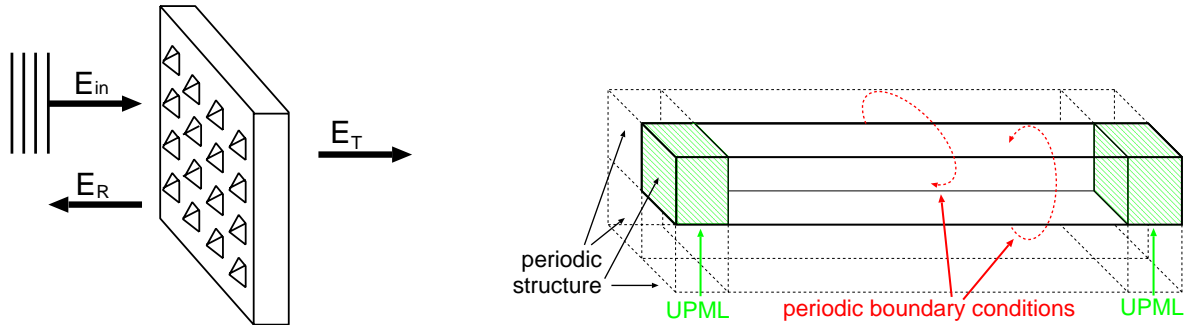


Figure 6.21: Left: Setup of the coherently excited quantum dot array investigated in section 6.8. Right: Boundary condition schematics for the utilized FDTD approach.[26]

## 6.8 Array of quantum dots: radiative coupling<sup>3</sup>

In the following light propagation through a two-dimensional grid of identical quantum dots is considered. As Fig. 6.21 illustrates, the quantum dot array is coherently excited by a laser pulse incident orthogonal on the grid plane. Due to their coupling to the electromagnetic field the quantum dots re-emit light, which is observed as transmitted and reflected signal. Since the re-emitted light can again be absorbed by neighboring quantum dots one expects a strong coupling between the quantum dots mediated by the electromagnetic field. In addition to the linear response of such a system, which is mainly characterized by radiative decay times, the nonlinear excitation and dephasing dynamics is investigated[26].

### 6.8.1 Theoretical Background

Because also the nonlinear dynamics of the system shall be described, a time-space domain method which naturally includes retardation effects is most suitable for evaluating Maxwell's Equation. Therefore the FDTD method in conjunction with the Uniaxial Perfectly Matched Layer (UPML) approach, as described in section 3.4.2 is used, as it has proven to be a reliable method for providing numerical solutions for the three-dimensional Maxwell problem. Since the quantum dot grid constitutes a periodic structure in two dimensions the FDTD method is modified to reflect these symmetry conditions by applying a cyclic boundary in two directions as illustrated in Fig. 6.21. The boundaries in the propagation direction are modeled using UPMLs, which absorb the incident light field ideally reflection-less and by that simulate an open space into which the light disappears.

Due to the expected strong recursive coupling of the dots via the electromagnetic field one can no longer assume a homogeneous light field over the quantum dots. Also, the FDTD method being evaluated in space-domain is not based on plane waves, therefore one has to resolve the light carrier oscillations in both space and time domain. This leads to specific constraints on the numerical spatial resolution and also has impact on the material description. E.g. the Hamiltonian which describes coupling of electrons to the classical light field is best expressed as space domain integral. Modifying Eq. 2.14 under these conditions, specializing it to the quantum dot confinement situation and only

<sup>3</sup>This Section 6.8 is based on simulations from Ref. [26].

| quantity         | value            | meaning  |
|------------------|------------------|--|
| $\mu_{vc}^{IB}$  | $1.25e\text{nm}$ | interband dipole element   |
| $\epsilon_b$     | 12.7             | background dielectric constant                                   |
| $\epsilon_{gap}$ | 1.217eV          | interband gap energy   |
| $\sigma_{max}$   | 2.239mS/nm       | maximum conductivity of the (artificial) UPML layer              |
| $\lambda$        | 285.7nm          | resulting wavelength in material for bandgap-resonant excitation |

Table 6.2: Parameters representing an InAs/GaAs material used for the quantum dot array simulations of section 6.8.

considering interband transitions leads to:

$$H_{e.m.} = -\sum_{i,i'} \hbar \bar{\Omega}_{ii'}(t) a_i^+ a_{i'}. \quad (6.13)$$

The modified Rabi frequency  $\bar{\Omega}(t)$  is given by the electric field spatially integrated together with the wave functions:

$$\bar{\Omega}_{ii'}(t) = \frac{1}{\hbar} \mu_{i,i'}^{IB} \cdot \int dr_c \phi_i^*(\mathbf{r}_c) \mathbf{E}(t, \mathbf{r}_c) \phi_{i'}(\mathbf{r}_c). \quad (6.14)$$

Due to the expected strong coupling of the quantum dots via the electromagnetic field the electron-light interaction is supposed to be dominant over other effects like electron-phonon interaction which therefore have been neglected here as a first approach to describe the system. Considering only interband transition of a single electron between two states (v,c) the emerging material equations of motions are therefore equivalent to those of a two-level atomic system with a Rabi frequency as defined above. Since the FDTD method always resolves the carrier oscillations of the light field on its temporal discretization grid the RWA cannot be applied in contrast to previous calculations. The polarization as given by Eq 2.31 describes the material response and occurs as driving force in Maxwell's equations. For the special situation it can be written as:

$$\mathbf{P}(t, \mathbf{r}) = 2\mu_{vc}^{IB} \cdot \text{Re}(\langle a_v^+ a_c \rangle \phi_v^*(\mathbf{r}) \phi_c(\mathbf{r})). \quad (6.15)$$

The wave functions  $\phi_c(\mathbf{r})$  and  $\phi_v(\mathbf{r})$  have been modeled using different approaches. The simulations presented in this work utilize wave function from an 8-band  $k \cdot p$  theory which were kindly provided by A. Schliwa[101]. The underlying model for these calculations assumes roughly pyramidal InAs/GaAs quantum dots as expected for self-assembled fabrication[102, 103].

The simulation of the coupled FDTD-material problem has been performed using parameters typical for GaAs as given in table 6.2. Fig. 6.22c shows a typical example for the spatially resolved electric field in the  $(x, 0, z)$ -plane of a single simulation cell at a time shortly (1ps) after excitation with a ultrashort plane wave laser pulse. For comparison Fig. 6.22a+b displays the corresponding electron probability density  $|\psi(\mathbf{r})|^2$ . Because of the recursive coupling between the light field and the material's polarization the quantum dots re-emit light after the excitation is gone as can be seen in Fig. 6.22c. Evidently the emitted electric field is by no means constant over the quantum dot, it does not even scale with the probability density but apparently strongly varies from minimal to maximal value within the quantum dot region. While variation of the electric field is a known near-field effect occurring in structured material the actual strength was not anticipated. In retrospective these results support the chosen approach of considering arbitrarily varying electric fields which require numerical calculation of the integral as given by Eq. 6.14 in each time step of the evaluation.

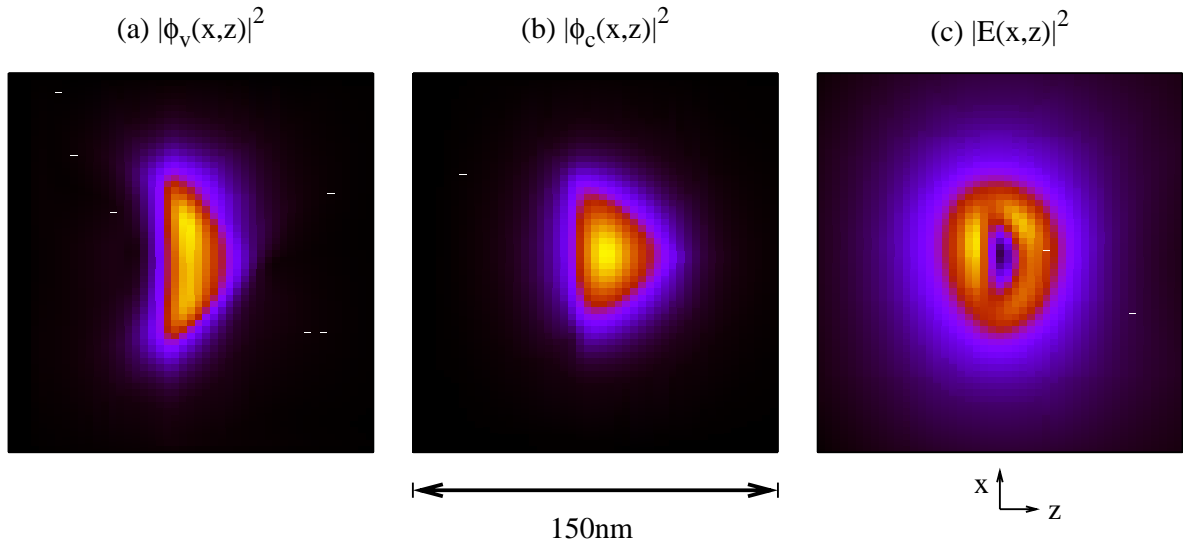


Figure 6.22: (a) Square of wave functions of the lower and (b) upper state of an electron/hole confined in a pyramidal quantum dot (from a 8-band  $k \cdot p$  calculation, provided by A. Schliwa [101]). (c) spatial intensity ( $|\mathbf{E}|^2$ ) around the quantum dot  $1ps$  after excitation.

In the near surrounding of the quantum dot the shape of the electric field is roughly spherical and less structured. These spherical waves emitted by each quantum dot superpose in the far field. This leads to a formation of a plane wave front by interference of these individual spherical light waves emitted by each quantum dot in the array. Despite the relatively large dot separation the wave front is formed on a very small length scale [26].

### 6.8.2 Linear properties

In a first step the linear response of the quantum dot ensemble is considered. For this, the system is excited with ultrashort laser pulses and the subsequent relaxation dynamics is monitored. In linear optics the laser pulse does not lead to substantial transfer of electron occupation from the ground state into the upper level but only excites a coherent optical polarization which can be radiatively re-emitted through light emission. This decoherence by radiative dampening gives rise to a homogeneous broadening of the spectral linewidth. In time domain it leads to an exponential decay of the macroscopic polarization with a decay time depending on material and geometry. This dependency will be analyzed in the following by varying the quantum dot size and the distance between the quantum dots.

Fig. 6.23 shows the polarization relaxation dynamics for the two cases of (a) very strong decoherence (dense array with dot distance of  $0.1\lambda$ ) and (b) a more typical weaker coupling and damping (dot distance  $\approx 1.1\lambda$ ). Both decays are exponential. For case (a) this is well recognizable and the decay time  $T_2$  can be easily extracted by using  $T_2 = (t_b - t_a) \ln(|P(t_b)| - |P(t_a)|)$ . For the slow dephasing situation (case (b)) the exponential decay can only be directly observed on very long time scales. Since the FDTD method is computational very demanding, simulations of such long periods above a few picoseconds are not feasible. Additionally, oscillations being small compared to the absolute signal but comparable to the observed decay effect occur due to the imperfect representation by the FDTD discretization. Nevertheless the decay time can be reliably extracted by using the well-established

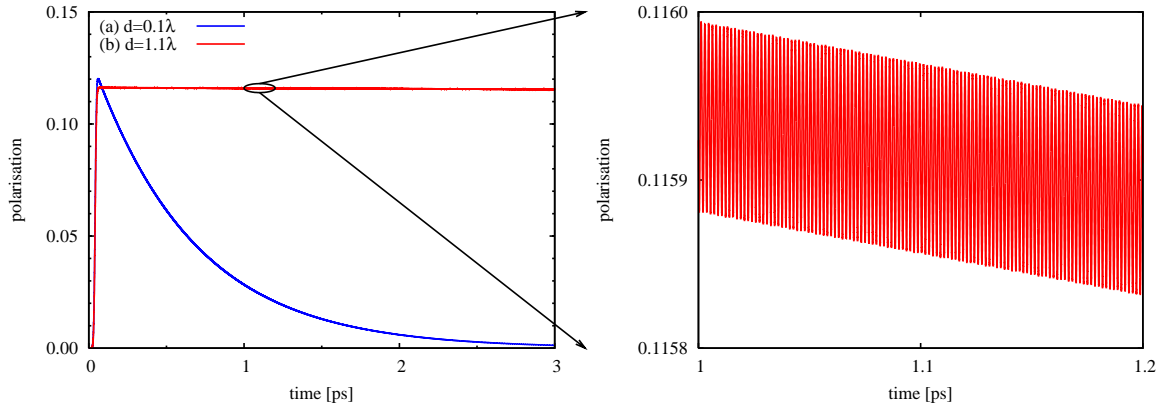


Figure 6.23: Left: Radiative polarization dephasing of a dense quantum dot array (distance  $d = 0.1\lambda$ ) with visible exponential decay (blue curve) and an array with distance  $d \approx 1.1\lambda$  showing only a weak decay of about  $300ps$  (red curve). Right: magnification of the slow decay showing the necessity for the linear regression method for extraction of decay times. After [26].

linear regression method for  $\ln(|P(t)|)$ .

First the dependence of the dephasing time  $T_2$  on the distance between the dots is investigated. As one can see in Fig. 6.24 (left) the dephasing time increases approximately quadratically for distances below  $\lambda$ . This is further illustrated in Fig. 6.24 (right) where additionally the dephasing time of a quantum well with the same dipole area density is plotted. The dephasing time of an infinitesimally thin two-level-system quantum well with dipole area density  $n = 1/d^2$  can be analytically derived and is given by:

$$T_2^{qw} = \frac{2\varepsilon_0\sqrt{\varepsilon_b}c_0\hbar d^2}{\omega_g (\mu_{vc}^{IB})^2}.$$

Additionally Fig. 6.24b displays the dephasing of a numerically simulated quantum well with finite width which shows the same quadratic dependence on  $d$  but has slightly smaller dephasing times compared to the infinitesimal quantum well. For interdot distances  $d$  below about  $0.4\lambda$  the quantum dot array shows the same dephasing times as the finite-width quantum well but deviates for larger distances. Then, as can be seen in Fig. 6.24a, interference effects between the quantum dots become important. For distances around  $\lambda$  the dephasing time changes very rapidly from an almost infinite dephasing time (no radiative decay due to destructive interference) to relatively short times of about  $250ps$  (constructive interference leading to collective radiation enhancement). The dephasing dependence is strongly influenced by the interference pattern also for distances beyond the wavelength ( $d > \lambda$ ). Since a two-dimensional grid is considered, the radiation enhancement by constructive interference does not necessarily only occur for distances which are multiples of  $\lambda$  but also if diagonal interdot spacings are in resonance. Due to the finite quantum dot size further deviations occur. In general the variations of the dephasing time get weaker for increasing dot distances. For very large dot distances of several wavelength the radiative decay time converges towards that of a single dot, i.e. about  $500ps$ .

The changes in the dephasing time for variation of the quantum dot size are displayed in Fig. 6.25. For the chosen interdot distance of  $1.3\lambda$  an array consisting of very small quantum dots has a dephasing time of about  $300ps$ . For increasing dot size the dephasing time first grows rapidly but converges towards a saturation limit of about  $1100ps$  for dot sizes above  $30nm$ .

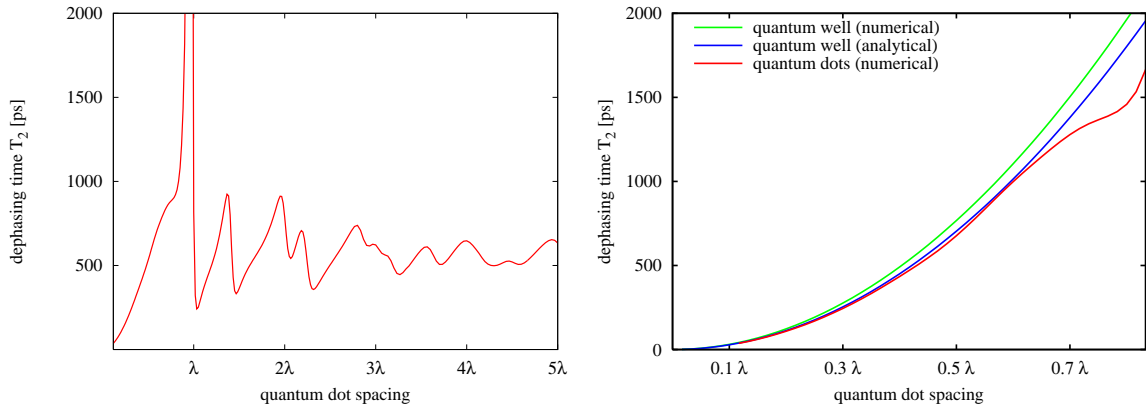


Figure 6.24: Left: Dependence of the radiative dephasing time on the quantum dot spacing. Right: Dephasing times for the quantum dot array compared to an infinitesimal quantum well and a finite width quantum well with equivalent dipole density.[26]

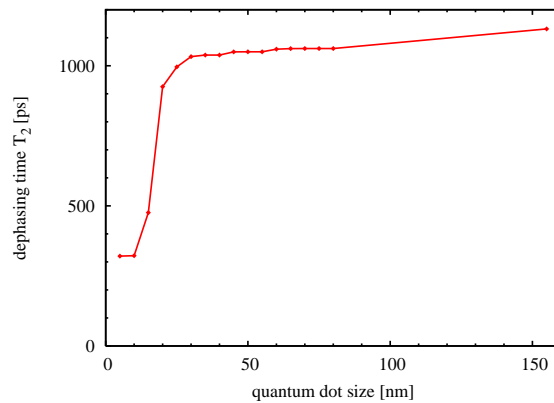


Figure 6.25: Radiative dephasing time as a function of the quantum dot size. After [26].

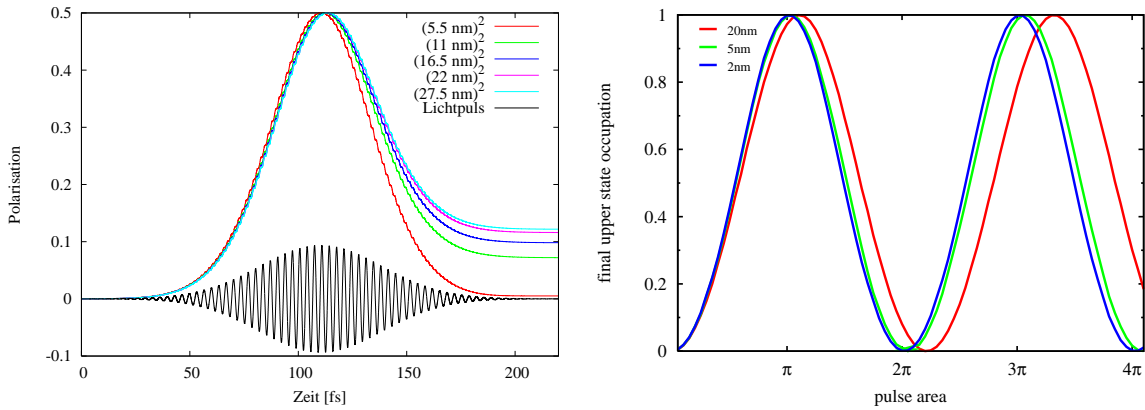


Figure 6.26: Left: Density Rabi flopping during nonlinear excitation with  $2\pi$ -pulse for different quantum dot sizes. Right: Upper state occupation after excitation for different quantum dot sizes. After [26].

### 6.8.3 Nonlinear properties

If the quantum dot array is illuminated with stronger light pulses nonvanishing electron transfer between the states is possible in addition to excitation of a dipole polarization. As in other two-level systems Rabi oscillations can be observed, but as Fig. 6.26a shows (for a weak dephasing situation) the finite size of the quantum dots changes the quantitative results. Also, small oscillations with the carrier frequency expectedly occur due to the non-RWA treatment. In very small dots a pulse with pulse area  $\theta = 2\pi$  induces one complete Rabi cycle pushing the electron completely into the upper level and coherently bringing it back into the lower level. For increasing dot size ( $10\text{nm}$ ,  $50\text{nm}$ ) the Rabi flops are less and less complete. E.g. the occupation of the upper state after excitation is still about 7% after the  $2\pi$ -pulse for the  $50\text{nm}$  dot. This is further quantified in Fig. 6.26b, where the final occupation of dots with different size is displayed for varying pulse area. It can be seen that it is still possible to induce full Rabi flops for larger quantum dots, but that the required pulse area is renormalised. This is a direct consequence of the modified Rabi frequency  $\bar{\Omega}$  which enters the equation of motion. While this complex valued quantity is calculated as an average of the electric field weighted with the wave functions, the unrenormalized pulse area is given by integral over original input pulse envelope as  $\theta = \int_{-\infty}^{\infty} \mu_{v,c}^{AB} \bar{E}(t) / \hbar$ .

Knowing that coherent control of the quantum dot array is in principle possible, the nonlinear relaxation dynamics is investigated. For this, a dense quantum dot array (distance  $0.1\lambda$ ) with strong radiative dephasing ( $T_2 \approx 200\text{fs}$ ) is excited with  $\pi$ -pulses of different duration. Fig. 6.27 shows input pulse, polarization and upper state occupation for excitation with Gaussian  $\pi$ -pulses with duration of 1000, 300, 100 and 10fs. The slow 1000fs-pulse is not able to induce a complete inversion of the occupation because of the strong damping which is on a shorter timescale than the pulse itself. Therefore the occupation and polarization adiabatically follow the input pulse and hence have the same Gaussian shape and only very reduced amplitude compared to a weaker damped system. The intermediate 300fs pulse already inverts the system almost completely (occupation up to 0.8). After the excitation, the occupation decays while the polarization first decays, then increases again and finally extincts completely. This behaviour is even more pronounced for the 100fs pulse. For the 10fs one can study this effects in its pure form. The short pulse induces an almost undamped half Rabi cycle, which in-

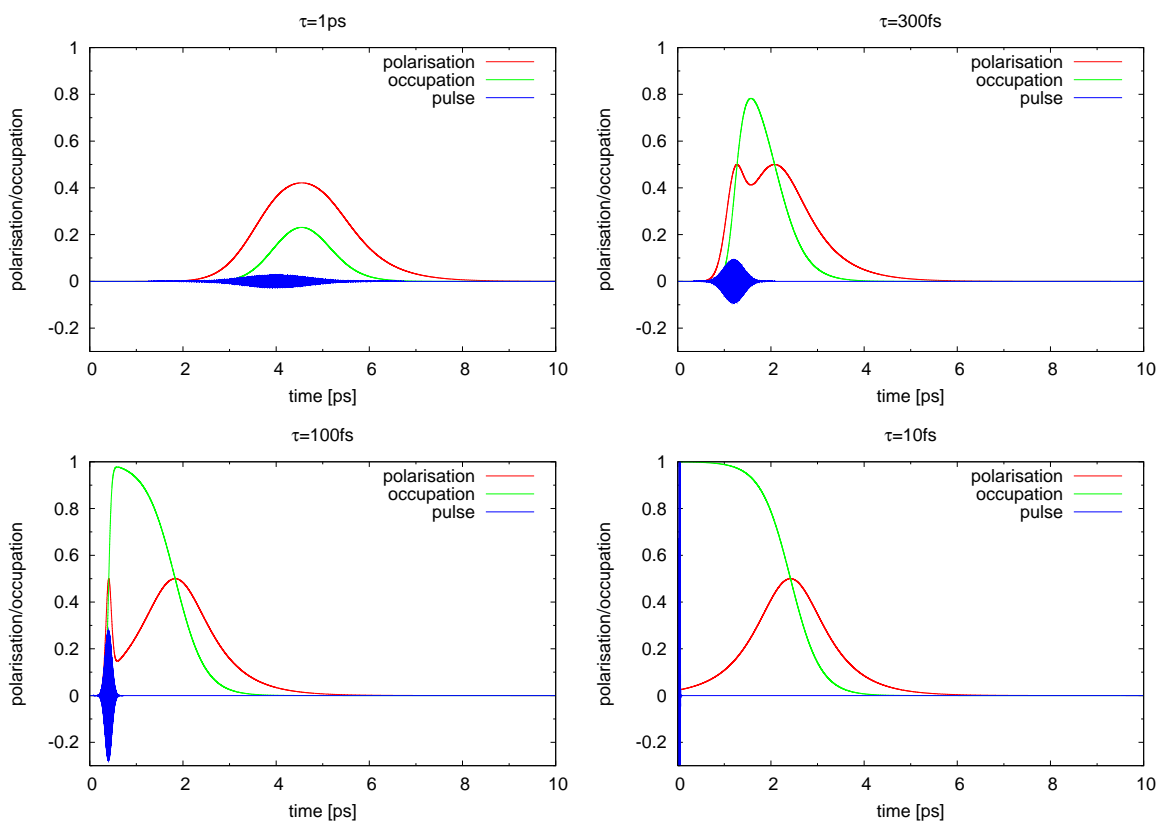


Figure 6.27: Dynamics of polarization and upper state occupation for excitation with  $2\pi$ -pulses of different duration  $\tau$  in a dense quantum dot array with strong radiative dephasing. Transition from adiabatic following ( $\tau = 1ps$ ) to suppressed density relaxation regime ( $\tau = 10fs$ ). After [26].

verts the occupation to the upper level ( $\approx 1$ ) and flops the polarization to its maximum (0.5) and back to almost zero. Since the radiative decay is driven by the polarization in the Maxwell equations a vanishing polarization leads to a blocking of the energy relaxation. For a perfect inversion with exactly zero polarization the energy would therefore never be emitted by the coherent radiative coupling. A quantized treatment of the light field would of course allow spontaneous emission of photons and by that energy relaxation. Since this perfect condition is not fulfilled in the shown calculations due finite dot size (see Fig. 6.26), the small polarization remainder is amplified on the dephasing time scale allowing energy relaxation of the occupation. This process begins slowly but is self-enhancing until the occupation drops below 0.5. Then the occupation decays exponentially on half the dephasing time scale.

Further calculations could determine, whether the polarization self-amplification only occurs due to the strong interdot coupling or if it also possible in other system. The relaxation blocking itself should occur in all systems where the dominant damping mechanism is polarization driven like the coherent radiative emission. Additionally, investigation of a pump-probe scheme with controlled preparation and subsequent sampling could be interesting with respect to an optical memory functionality. Then of course, other dephasing mechanisms like electron-phonon coupling should be included.



## Chapter 7

# Conclusion and Outlook

Various semiconductor structures have been investigated using an adaptable density matrix approach. Depending on the specific problem this material description is combined with one of several methods for evaluating Maxwell's equations.

Despite their differences all systems have a common denominator. All systems can be coherently excited and show linear absorption spectra which represent their inner energetic structure. In an interaction-free system this is simply given by a continuum of transitions according to the band structure. The Coulomb interaction in general leads to a shift contributed to the exchange self energy and to formation of collective states which can be seen in the spectra as exciton resonances. As electron-electron scattering the Coulomb interaction additionally induces a line broadening. Quantum dots with their intrinsic discrete level structure pose an exception there. A broadening of the absorption spectrum can also result from electron-phonon coupling or by interaction with the radiation field. In the nonlinear regime all systems exhibit Rabi oscillations, i.e. coherent flopping of the occupation during coherent nonlinear excitation. Depending on the relevant interaction these oscillations are damped. Apart from these similarities the systems have their own characteristics emerging from a combination of the structure of the electronic confinement and the geometry which determines the radiative coupling.

For nonlinear polariton propagation in a bulk semiconductor from chapter 4.1 the formation of an exciton-polariton has been shown. For increasing intensities the occurring polariton beating is reduced by excitation-induced dephasing via exciton-exciton scattering. Good agreement to experimental findings is achieved. For long propagation distances structures within the homogeneous line width appear. These have been further discussed within an analytical two-level model system. It has been shown that due to nonlinear wave-mixing novel effects like narrowing of the line shape, hole burning within the homogeneous line width and ultranarrow gain structures can occur.

In multiple quantum well structures in Bragg geometry formation of an optical stop gap is observed and the conditions for self-induced-transmission during nonlinear light propagation have been studied, showing that only pulses which are spectrally broader than the stop band can travel in the structure. A stationary solution exists, allowing storage of light and optical excitation in a two-level MQW structure. The effect of the Coulomb interaction and electron-phonon coupling has been investigated in detail for intersubband transitions showing that systems with very similar subband masses (like GaAs) are only very weakly affected by the Coulomb interaction on Hartree-Fock level. Electron-electron and electron-phonon scattering however leads to strong broadening of the absorption spectrum. It has been shown that the common approximation of neglecting the nondiagonal scattering processes leads to an immense overestimation of the line broadening. For systems with

more distinct subband masses (like InAs) the system already shows a strong temperature dependent broadening in the interaction-free model caused by broadening of the electronic Fermi distribution. For quantum-kinetic treatment of the electron-phonon interaction line narrowing and additional resonances attributed to polaron formation could be observed. The differences between a Markovian and quantum kinetic dynamics have also been discussed for nonlinear excitation by studying damping of Rabi oscillations.

The quantum kinetic description of the electron-phonon coupling has also been discussed in detail for quantum dots in chapter 6. It has been shown that a second-order correlation expansion shows good agreement with experiments and a nonperturbative solution, which can be derived in the linear optical regime. Damping of density Rabi oscillations has been studied showing that the phonon-induced dephasing is pulse area dependent with a nearly undamped first maximum around  $1\pi$  and successively damped oscillation. A finite pulse duration exists for which the reduction of the Rabi oscillations is maximal. A nonperturbative approach was presented which is able to describe the dynamics induced by an arbitrary nonlinear pulse for high temperatures and strong electron-phonon coupling. It was shown that systematic variation of the detuning and pulse area can be used to extract details of the electron-phonon couplings. This method is proposed as an possible experimental technique to directly obtain information about the structure of the electron-phonon interaction. It is shown that the Coulomb interaction has to be included in a rigorous many-particle scheme and that mean-field approximations fail in these systems. In the nonlinear optical regime a biexcitonic resonance forms. However, the strongest response on a spectrally narrow pulse is obtained for a pulse tuned exactly between the excitonic and biexcitonic resonance. Finally the radiative coupling between an ordered array of quantum dots was investigated showing strong interference effects for the radiative decay rate. In the nonlinear regime, the fact that the decay is polarization-driven can be used to store optical excitation by suppression of the radiative decay.

The density matrix theory has proven to be a powerful tool for describing linear and nonlinear optical processes in semiconductor nanostructures. However, the infinite hierarchy of equations of motion which emerges from usage of Heisenberg's equations requires perturbative approaches and truncation schemes leading to an exponentially growing numerical complexity. Only the likewise exponentially growing availability of computation power allows a steady refinement of the description of the semiconductor quantum mechanics. Several methods like the time-convolution-less approach or the generating function method promise to overcome this problem, but so far only solutions for special problems could be derived. Deriving a generally applicable non-perturbative approach is certainly one of the greatest challenges for semiconductor optics theory today. Ultimately it may be, that only quantum computers can solve this problem.

However, there are still many problems which are interesting and can be reached with the existing theoretical framework. Quantum optics, describing the dynamics of the quantized light field, has only been considered as a dephasing process in this work. Description of further quantum optical effects like squeezing, luminescence or few-photon emission would be the next logical step and work in this area is in progress.

So far the impact of structuring on the nanometer scale has been mainly discussed for the electronic motion. However nanostructures are also small compared to the wavelength of the light field leading to novel effects in the near-field. This region has been visited in this work by considering the near-field coupled quantum dot array but is certainly worth further studies as also the experimental possibilities grow. In this technologically relevant context a combined description of transport and optics phenomena is desirable and appears reachable using the density matrix framework together with a numerical Maxwell solver.

## Appendix A

# Two-Level Systems

### A.1 Introduction

The *two-level system* (TLS) model has its origin in atomic physics where the equivalent model is called *two-level atom* (TLA). However it is often used in semiconductor optics as well. The main reason for this is the simplicity of the model and the existence of analytical solutions, even for several situations in nonlinear optics. An extension to more levels can sometimes be useful and leads to a *multi-level system* (MLS). The applicability of these models to represent a semiconductor strongly depends on the considered system: For quantum dots a level structure naturally arises [92], therefore it serves well in the low-temperature limit, where many-particle interactions, most of all with phonons, are suppressed (see chapter 6). In higher-dimensional systems the MLS model may be applicable because the Coulomb interaction leads to bound excitons with discrete energy eigenstates [2]. If the energy difference between the various exciton levels is big enough and if only a single or few exciton resonances are optically excited, the TLS or MLS can represent the otherwise very complex dynamics in good approximation. In general, the TLS/MLS can be a good starting point to understand the material dynamics if only a very qualitative description is required or a microscopic theory is unreachable. The most complete and simultaneously compact treatment on two-level systems can be found in Ref. [27], which covers all effects described in this appendix. The most relevant results regarding this work are recited here for a seamless notation and to give a brief overview. It also provides an opportunity to discuss some approximations and approaches which are frequently used in this work on a simple model system.

#### A.1.1 The Hamiltonian

The equations of motion for the polarization, which is the driving quantity in the Maxwell equations, are derived from the Hamiltonian of the TLS/MLS model. The general procedure to obtain this Hamiltonian, is to first solve the problem of a single electron in a static potential without coupling to the light field or other systems. In the case of atomic systems or semiconductor quantum dots, this already gives a discrete energy level structure. For higher dimensional semiconductors one will usually achieve a continuous band structure [11, 5, 4, 2]. Either the resulting Hamiltonian already is in its final simple discrete level form, or has to be brought to it either by complete neglecting of the many-body interactions or by solving at least parts of them analytically leading to new quasi-particles with renormalized energies. Next, the Hamiltonian of the complete problem is written down in second

quantization giving:

$$H = \sum_j \varepsilon_j a_j^\dagger a_j - \sum_{ij} \mathbf{d}_{ij} \cdot \mathbf{E}(t) a_i^\dagger a_j. \quad (\text{A.1})$$

Here  $\varepsilon_j = \hbar\omega_j$  are the discrete energy levels of the chosen quasi particle, which may include renormalization due to many-body interactions. The creation/annihilation operators  $a_j^\dagger/a_j$  also refer to the quasi particles. Due to the transformation the dipole matrix elements  $\mathbf{d}_j$  can in principal have diagonal contributions, but in the following non-diagonality (i.e.  $\mathbf{d}_i = 0$ ) is assumed for simplicity.

### A.1.2 Equations of motion

From the Hamiltonian the equations of motion for the single-particle coherences  $\sigma_j = \langle a_i^\dagger a_j \rangle$  can easily be derived using Heisenberg's equation (Eq. 2.25):

$$i\hbar \frac{d}{dt} \sigma_{ij} = (\varepsilon_j - \varepsilon_i) \sigma_{ij} + \mathbf{E}(t) \cdot \sum (\mathbf{d}_{ik} \sigma_{kj} - \mathbf{d}_{kj} \sigma_{ik})$$

Assuming only two levels (v,c) and non-diagonal dipole matrix elements  $\mathbf{d}_{vc} = \mathbf{d}_{cv}$  the equation can be reduced to:

$$\frac{d}{dt} \sigma_{cv} = -i(\omega_v - \omega_c) \sigma_{cv} - i\mathbf{E}(t) \cdot \mathbf{d}_{vc} / \hbar (\sigma_{vv} - \sigma_{cc}), \quad (\text{A.2})$$

$$\frac{d}{dt} \sigma_{cc} = -i\mathbf{E}(t) \cdot \mathbf{d}_{vc} / \hbar (\sigma_{vc} - \sigma_{cv}),$$

$$\frac{d}{dt} \sigma_{vv} = -i\mathbf{E}(t) \cdot \mathbf{d}_{vc} / \hbar (\sigma_{cv} - \sigma_{vc}). \quad (\text{A.3})$$

The *microscopic polarization* is given by  $p = \sigma_{vc}$ , the *occupation* of the upper level by  $f = \sigma_{cc}$ . Due to particle number conservation  $f = 1 - \sigma_{vv}$  is fulfilled. Introducing the *Rabi frequency*  $\Omega(t) = \mathbf{E}(t) \cdot \mathbf{d}_{vc} / \hbar$  and the *gap frequency*  $\omega_g = \omega_c - \omega_v$ . the equations of motion can be written as

$$\begin{aligned} \dot{p} &= i\omega_g p + i\Omega(1 - 2f), \\ \dot{f} &= 2\text{Im}(\Omega p). \end{aligned} \quad (\text{A.4})$$

These equations represent a set of two coupled linear differential equations with  $\Omega$  as inhomogeneity. Their solutions are discussed in the following.

### A.1.3 Field expansion

For weak excitation one can simplify the equations with the help of a perturbation expansion in the field  $\Omega$ . For this, an expansion parameter  $\lambda$  is introduced and the quantities are expanded according to  $\Omega = \lambda \bar{\Omega}$ ,  $p = \sum_{i=0}^{\infty} \lambda p_i$ ,  $f = \sum_{i=0}^{\infty} \lambda f_i$ . Inserting this into Eq. A.4 and sorting according to the order in  $\lambda$  leads to:

$$\begin{aligned} \dot{p}_0 &= i\omega_g p_0, & \dot{f}_0 &= 0, \\ \dot{p}_1 &= i\omega_g p_1 + i\bar{\Omega}(1 - 2f_0), & \dot{f}_j &= \text{Im}\bar{\Omega} p_{j-1}, \text{ for } j \geq 1, \\ \dot{p}_j &= i\omega_g p_j + i2\bar{\Omega} f_{j-1}, \text{ for } j \geq 2. \end{aligned} \quad (\text{A.5})$$

If the system is initially in the unexcited ground state ( $p(-\infty) = 0$ ,  $f(-\infty) = 0$ ) one can show by formal integration that only  $p_1, p_3, p_5 \dots$  and  $f_2, f_4, f_6 \dots$  are nonzero. Thus in first order of the field only  $p_1$  is excited (and no density  $f$  is build up) leading to a linear response (see section 3.6). The

lowest nonlinear response is in third order of the field, where the density builds up with second order in the field and polarization according to  $f = |p|^2$ . For semiconductors, this kind of expansion can be used to obtain a truncation criterion when handling the hierarchy problem introduced by the Coulomb interaction. In chapter 4.1.2 this is performed up to the third order in the field in the framework of the dynamic controlled truncation (DCT) scheme [42, 43, 44, 45]. All other parts of this work either use the linearized (first order) form or the full nonlinearity which has no limitations for the field amplitude.

In first order (linear excitation) and assuming that the system is initially in the ground state ( $f(-\infty) = 0$ ) the equations of motion reduce to  $\dot{p} = i\omega_g p + i\Omega(t)$ . This simple differential equation can either be solved by integration explicitly giving  $p(t) = e^{-i\omega_g t} \int_{-\infty}^t e^{i\omega_g t'} \Omega(t') dt'$ , or by Fourier transformation after introducing a convergence factor  $\gamma$ :

$$\dot{p} = i(\omega_g + i\gamma)p + i\Omega(t). \quad (\text{A.6})$$

The factor  $\gamma$  leads to an exponential decay of the polarization after excitation with an optical pulse and is introduced phenomenologically here. In reality, no system is completely isolated but always coupled to its environment in some way. Hence one always encounters dissipation or dephasing, i.e. finite lifetimes of excited states and coherence. Often, including the commonly found case of energetic, i.e. Markovian, coupling to an external bath, this dephasing can be described by an exponential decay with a constant  $\gamma$  as introduced above.

Eq. A.6 can be instantly solved by Fourier transformation (see section B.1), giving:

$$p(\omega) = \frac{\Omega(\omega)}{\omega - \omega_g - i\gamma} = \Omega(\omega) \frac{(\omega - \omega_g) + i\gamma}{(\omega - \omega_g)^2 - \gamma^2}.$$

From this the macroscopic polarization  $\mathbf{P}(\omega) = n_0 \mathbf{d}_{vc} FT\{p(t) + p^*(t)\} = n_0 \mu_{vc} (p(\omega) + p^*(-\omega))$  can be calculated. The spectral absorption is then given by:

$$\alpha(\omega) = \frac{F}{\omega} \text{Im} \frac{P(\omega)}{\Omega(\omega)} = \frac{F}{\omega} \left( \frac{\gamma}{(\omega - \omega_g)^2 - \gamma^2} + \frac{-\gamma}{(-\omega - \omega_g)^2 - \gamma^2} \right).$$

It is composed of two Lorentzian peak functions of width  $\gamma$  and height  $F/\gamma$ , one at  $\omega = \omega_g$  and one at  $\omega = -\omega_g$ . In the limit of  $\gamma \rightarrow 0$  the absorption can be formally written as:

$$\alpha(\omega) = \frac{F}{\omega} [\delta(\omega - \omega_g) - \delta(\omega + \omega_g)].$$

#### A.1.4 The Rotating Wave Approximation

Assuming monochromatic excitation of an optical pulse with a carrier frequency  $\omega$ , i.e.  $\Omega(t) = 2B \cos(\omega t) = B(e^{i\omega t} + e^{-i\omega t})$ , the solution of the linear Eq. A.6 can be constructed as a sum  $p = p_+ + p_-$  of two special solutions  $p_+$  and  $p_-$  reflecting the two rotational parts of the driving field:

$$\dot{p}_+ = i(\omega_g + i\gamma)p_+ + iB e^{i\omega t} \quad \dot{p}_- = i(\omega_g + i\gamma)p_- + iB e^{-i\omega t}.$$

These equations are solved by  $p_{\pm} = A_{\pm} e^{\pm i\omega t}$  with amplitudes  $A_{\pm} = \frac{B}{\pm\omega_l - \omega_g - i\gamma}$ . Therefore, if resonantly excited ( $\omega_l \approx \omega_g$ ), only  $p_+$  is relevant because  $A_+ \approx \frac{B}{i\gamma}$  is much larger than  $A_- \approx -\frac{B}{2\omega_g}$  under the assumption that  $\gamma \ll \omega_g$ , which is valid in most materials<sup>1</sup>. Then it is plausible to neglect the

<sup>1</sup>Typical numbers are  $\hbar\omega_g \approx 1.5\text{eV}$  compared to  $\hbar\gamma \approx 0.001\text{eV}$ .

mismatching rotational part  $p_-$  of the driving field at all, which is the essence of the *rotating wave approximation* (RWA). For excitation with a Gaussian pulse (spectral width  $\sigma$ ), one can show that the RWA for the above model system is good as long as  $\sigma \ll 2\omega_g$ . This requires that the off-resonant spectral components must be sufficiently small. In the time picture this is fulfilled, if there are several carrier oscillations under the pulse envelope. Except for the subband transition which are discussed in section 5.2, this requirement is fulfilled for all situations considered in this work. Effects beyond RWA, like carrier-wave Rabi flopping have been studied in the visible optical regime with ultra-short laser pulses [109]. In the THz regime, where the frequencies are very small, non-RWA effects are expected to be of importance [90].

The RWA, i.e. the neglect of the mismatching rotational part of the driving field, is usually accompanied by a transformation of the equations of motion into the rotating frame of the relevant part of the driving field. In the nonlinear equation of the TLS (Eq. A.4), this affects the polarization, but not the (non-rotating) density.

The most general description of a real-valued field  $\Omega(t)$  with envelope  $\hat{\Omega}(t)$ , time dependent phase  $\phi(t)$  and carrier oscillation frequency  $\omega$  can be rewritten as:

$$\Omega(t) = \hat{\Omega}(t) \cos(\omega t + \phi(t)) = \frac{1}{2} \hat{\Omega}(t) \left( e^{i(\omega t + \phi(t))} + e^{-i(\omega t + \phi(t))} \right) = \frac{1}{2} \tilde{\Omega}(t) e^{i\omega t} + \frac{1}{2} \tilde{\Omega}^*(t) e^{-i\omega t}. \quad (\text{A.7})$$

Here, the complex envelope function  $\tilde{\Omega}(t) = \hat{\Omega}(t) e^{i\phi(t)}$ , which contains the phase factor, has been introduced. Defining  $\tilde{p} = p e^{-i\omega t}$  Eqs. A.4 can be transformed into the rotating frame:

$$\begin{aligned} \dot{\tilde{p}} &= i\Delta \tilde{p} + i\frac{\tilde{\Omega}}{2}(1 - 2f), \\ \dot{f} &= \text{Im}(\tilde{\Omega}^* \tilde{p}). \end{aligned} \quad (\text{A.8})$$

For exact resonant excitation, the detuning  $\Delta = \omega_g - \omega_l$ , as the difference between the carrier frequency of the pulse and the gap frequency, evaluates to zero, further simplifying the equation. For the numerical evaluation it is advantageous that the dynamics in the rotating frame is slow compared to the carrier oscillations which therefore no longer have to be resolved. Also, some analytical solution can only be derived for the simple RWA equations with zero detuning.

## A.2 Rabi flopping

If the Rabi frequency  $\tilde{\Omega}(t)$  is a real-valued function, i.e. if there is no time dependent phase factor (except for  $180^\circ$  phase jumps which lead to a sign change), and if one assumes zero detuning ( $\Delta = 0$ ) then it is possible to give a closed solution to the nonlinear RWA equations of motion (Eq. A.8):

$$p(t) = \frac{i}{2} \sin \Theta(t), \quad f(t) = \sin^2 \frac{\Theta(t)}{2}. \quad (\text{A.9})$$

This is possible by introducing the time-dependent pulse area  $\Theta(t) = \int_{-\infty}^t \tilde{\Omega}(t') dt'$ , which can be calculated analytically for many pulse shapes. Since  $\Theta(t)$  is the argument of sine functions it is usually expressed in units of  $\pi$ . As a function of (increasing)  $\Theta(t)$  the density and the polarization oscillate sinusoidal. These oscillations are called *Rabi flops/oscillations*: The density varies between zero and one and is zero for  $\Theta = 2\pi n$ . The polarization oscillates with twice the frequency between the values  $-\frac{1}{2}$  and  $\frac{1}{2}$  and gets zero for all  $\Theta = n\pi$ ,  $n = 0, 1, 2, 3, \dots$ . As direct functions of time, the density and polarization still perform Rabi oscillations but not necessarily sinusoidal, strongly depending on the specific pulse shape.

Additionally, one can define the (total) pulse area  $\Theta = \lim_{t \rightarrow \infty} \Theta(t)$ , which can be calculated analytically for even more pulse shapes and is useful to determine the final state of a system after pulse excitation. For positive pulse envelopes, i.e.  $\tilde{\Omega}(t) \geq 0 \forall t$ , it represents the overall strength/nonlinearity of the given pulse. A  $2\pi$  pulse, e.g., can induce one complete density Rabi flop, a  $4\pi$  pulse two density fops, etc. Pulses with phase variations are not necessarily positive semidefinite, and can lead to novel effects like compression of the linewidth or hole-burning within the homogeneous line, see section 4.2.



## Appendix B

# Mathematical Tools

The following mathematical definitions and derived formula can be found in basic textbooks and are repeated here to ensure a consistent notation and as a compact overview.

### B.1 Fourier transformation

Basic definitions and properties of the Fourier transformation (FT) used in this work:

|   |  |                         |
|---|--|-------------------------|
| $f(t) = FT^{-1}\{f(\omega)\}$   | $f(\omega) = FT\{f(t)\}$                                     |                         |
| $f(t)$  | $f(\omega) = \int_{-\infty}^{\infty} e^{-i\omega t} f(t) dt$ | definition of the FT    |
| $f(t) = \frac{1}{2\pi} \int_{-\infty}^{\infty} e^{i\omega t} f(\omega) d\omega$ | $f(\omega)$  | inverse FT              |
| $a f(t) + b g(t)$   | $a f(\omega) + b g(\omega)$                                  | linearity               |
| $f(t - t_0)$  | $e^{-i\omega t_0} f(\omega)$                                 | FT of shifted function  |
| $e^{i\omega_0 t} f(t)$  | $f(\omega - \omega_0)$                                       | FT of rotating function |
| $\frac{d}{dt} f(t)$   | $i\omega f(\omega)$  | FT of derivative        |
| $f^*(t) = (f(t))^*$   | $f^*(-\omega) = (f(-\omega))^*$                              | FT of conjugate         |
| $e^{i\omega_0 t}$   | $2\pi\delta(\omega - \omega_0)$                              | FT of rotation          |
| $\delta(t - t_0)$   | $e^{-i\omega t_0}$   | FT Dirac delta          |
| $(f * g)(t) = \int_{-\infty}^{\infty} f(t - t') g(t') dt'$                      | $f(\omega) g(\omega)$  | convolution             |

FT and properties of some functions often used for describing light pulses:

| $f(t)$                        | $f(\omega)$                                    | $\theta$           | $\tau_{FWHM}$                   | $\tau_{IFWHM}$                      | $\Gamma_{FWHM}$                       | $\Gamma_{IFWHM}$                      |
|-------------------------------|--|--------------------|---------------------------------|-------------------------------------|---------------------------------------|---------------------------------------|
| $e^{-(\frac{t}{\tau})^2}$     | $\sqrt{\pi\tau} e^{-(\frac{\omega\tau}{2})^2}$ | $\sqrt{\pi\tau}$   | $2\tau\sqrt{\ln 2}$             | $2\tau\sqrt{2\ln 2}$                | $\frac{4\sqrt{\ln 2}}{\tau}$          | $\frac{2\sqrt{2\ln 2}}{\tau}$         |
| $\text{sech}(\frac{t}{\tau})$ | $\pi\tau \text{sech}(\frac{\pi\tau\omega}{2})$ | $\pi\tau$          | $2\tau \ln(2 + \sqrt{3})$       | $2\tau \ln(1 + \sqrt{2})$           | $\frac{4 \ln(2 + \sqrt{3})}{\pi\tau}$ | $\frac{4 \ln(1 + \sqrt{2})}{\pi\tau}$ |
| $e^{-\gamma t} \theta(t)$     | $\frac{1}{i\omega + \gamma}$                   | $\frac{1}{\gamma}$ | $\tau_H = \frac{\ln 2}{\gamma}$ | $\tau_{IH} = \frac{\ln 2}{2\gamma}$ | $\sqrt{12\gamma}$                     | $2\gamma$                             |
| $\delta(t)$                   | 1  | 1                  | 0                               | 0                                   | $\infty$                              | $\infty$                              |
| 1                             | $2\pi\delta(\omega)$                           | $\infty$           | $\infty$                        | $\infty$                            | 0                                     | 0                                     |
| $\Pi(t)$                      | $\frac{\sin(\omega a)}{\omega a}$              | 1                  | $2a$                            | $2a$                                | $\approx 3.98/a$                      | $\approx 2.78/a$                      |
| $\theta(t)$                   | $\pi\delta(\omega) - \frac{i}{\omega}$         | $\infty$           | -                               | -                                   | -                                     | -                                     |

$f(t)$ : temporal pulse shape,  $f(\omega)$ : Fourier transformation,  $\theta = \int_{-\infty}^{\infty} f(t) dt$ : pulse area,  $\tau_{FWHM}$ ,  $\tau_{IFWHM}$ ,  $\Gamma_{FWHM}$ ,  $\Gamma_{IFWHM}$ : full width at half maximum (i.e. where  $g(x/2) = \frac{1}{2}g(0)$ ) of  $|f(t)|$ ,  $|f(t)|^2$ ,  $|f(\omega)|$ ,  $|f(\omega)|^2$ ,  $\text{sech}(x) = \frac{1}{\cosh(x)} = \frac{2}{e^x + e^{-x}}$ ,  $\Pi(t) = \frac{1}{2a}$  if  $|t| \leq a$ , 0 otherwise.

Numerically the Fourier transformation can be simply performed by Euler discretization of the Fourier integral, i.e.  $g(\omega_j) = \sum_n e^{-i\omega_j n \Delta t} g(n \Delta t) \Delta t$  for a set of chosen  $\omega_j$ . Alternatively the Fourier integral can be rewritten as differential equation  $\dot{\tilde{g}}_{\omega_j}(t) = e^{-i\omega_j t} g(t)$  which can then be solved using the Euler or Runge Kutta methods as presented in the next section. The FT of  $g(t)$  is then given by  $g(\omega_j) = \lim_{t \rightarrow \infty} \tilde{g}_{\omega_j}(t)$ . These approaches allow output of preliminary FTs during a simulation which can be very useful for long-running calculations. If this is not needed, the most efficient numerical method is the Fast Fourier Transform (FFT) algorithm [110, 111] which reduces the computational effort from  $O(N^2)$  to  $O(N \log N)$  if  $N$  time steps are used. Since all numerical methods instead of calculating the real Fourier integral effectively perform a discrete Fourier transformation (discrete time grid, finite interval) the Nyquist-Shannon sampling theorem must be regarded. It states that for a limited sampling time interval a critical spectral resolution exists, below which spectral features cannot be resolved. For a given time interval  $T = t_{max} - t_{min}$  the smallest useful frequency difference (which does not lead to spectral aliasing effects) is given by [112, 113]:

$$\Delta\omega = \frac{\pi}{T}$$

Analogous, the maximum spectral interval of a discrete Fourier transformation is given by  $\omega_{max} - \omega_{min} = \frac{4\pi}{\Delta t}$  if  $\Delta t$  is the discrete time step. Beyond this spectral interval the function repeats periodically.

The sampling theorem also has to be considered in other situations where integrals of oscillation functions have to be calculated. This is e.g. the case for integrals over phonon-assisted density matrix elements, which are usually converted into sums for numerical evaluation. Each phonon-assisted density element oscillates with a frequency  $\omega_\alpha$ . If the largest frequency step is given by  $\Delta\omega_{max}$  one can deduce from the Nyquist sampling theorem that the temporal interval in which one can properly simulate the equations is limited to  $T = \frac{\pi}{\Delta\omega_{max}}$ . For calculations beyond this interval it is likely that artifacts from the insufficient discretization appear in the signal.

## B.2 Numerical methods for solving differential equations

### B.2.1 Euler method

The simplest approach for numerically solving a (set of coupled) first order differential equations  $\dot{g}(t) = f(g(t), t)$  is the Euler method which is obtained by expressing the time derivative  $\dot{g}$  as forward finite difference:  $\dot{g}(t) \approx (g(t + \Delta t) - g(t)) / \Delta t + O(\Delta t^2)$ . Knowing the values of  $g(t)$  at time  $t$ , one can then calculate the values at a later time  $t + \Delta t$ : [114]

$$g(t + \Delta t) = g(t) + f(g(t), t) \Delta t \quad (\text{B.1})$$

From the construction it is clear, that the Euler method is only accurate to first order. While this may be sufficient for some applications, the Optical Bloch Equations, which are evaluated in this work, would require such a small time step  $\Delta t$  and therefore so many iterations that not only the computation time would be enormous but also the numerical rounding errors due to limited floating point precision would most likely sum up and lead to instability.

### B.2.2 Runge-Kutta method

Because of the shortcomings of the Euler approach, a fourth-order Runge-Kutta method is used in this work to solve the first order differential equation  $\dot{g}(t) = f(g(t), t)$ . Generally, Runge-Kutta methods use a quadrature formula to approximate the formal integral solution of the differential equation between two times  $t$  and  $t + \Delta t$ : [114]

$$g(t + \Delta t) = g(t) + \int_t^{t+\Delta t} f(g(t'), t') dt' \approx g(t) + \Delta t \sum_{l=1}^m \gamma_l f(g(t_l), t_l)$$

This  $m$ -stage quadrature approximation with weights  $\gamma$  at positions  $t_l \in [t, t + \Delta t]$  needs the values  $g(t_l)$  which are not all known at all times  $t$ . Therefore the values of the function  $f$  at these times  $t_l$  are approximated by using values (of  $g$ ) which have been already calculated at earlier times:  $f(g(t_l), t_l) \approx k_l(g(t), t)$ . An iterative, explicit approach assuming  $t_l = t$  leads to:

$$k_l(t) = f \left( \left[ g(t) + \sum_{j=1}^{l-1} (t_l - t_j) k_j \right], t_l \right)$$

The above differential equation can therefore be integrated/iterated over a time step from  $t$  to  $t + \Delta$  using:

$$g(t + \Delta t) \approx g(t) + \Delta t \sum_{l=1}^m \gamma_l k_l(t)$$

By choosing appropriate positions/weights of the quadrature approximation, one can obtain an precision order (with regard to  $\Delta t$ ) of the Runge-Kutta method that equals the stage of the quadrature approximation, which in turn is just the number of function evaluations needed per time step and as that the normally most time consuming part when solving differential equations. As limiting case, the Euler method (Eq. B.1) can also be reproduced by choosing  $m = 1$  and  $t_l = t$  ( $\Rightarrow \gamma_1 = 1, k_1 = f(g(t), t) \Rightarrow g(t + \Delta t) = g(t) + k_1 \Delta t$ ). An excellent balance of precision and simplicity is obtained by the standard fourth order Runge-Kutta method with positions  $\{t_l - t\}_l = \{0, \frac{1}{2}, \frac{1}{2}, 1\} \Delta t$  and weights  $\{\gamma_l\}_l = \{\frac{1}{6}, \frac{1}{3}, \frac{1}{3}, \frac{1}{6}\}$ , which are very similar to the ones used in Simpson's integration rule. Using these weights one obtains:

$$\begin{aligned} k_1 &= f(g(t), t) \\ k_2 &= f(g(t) + k_1/2, t + \Delta t/2) \\ k_3 &= f(g(t) + k_2/2, t + \Delta t/2) \\ k_4 &= f(g(t) + k_3, t + \Delta t) \\ g(t + \Delta t) &= g(t) + \frac{\Delta t}{6} (k_1 + 2k_2 + 2k_3 + k_4) \end{aligned} \tag{B.2}$$

If  $g, f$  and  $k_l$  are defined as  $n$ -tuples/vectors, the above derivation is still valid and the resulting equations can be used for numerical evaluation of a coupled set of differential equations. Experience has shown that for solving optical Bloch equations, especially if evaluated beyond RWA, the reduction of computational effort gained by using an adaptive time step scheme, which is recommended by some textbooks, does not countervail the increased complexity and possible instabilities which arise with such a method.



## Appendix C

# Equations of motion

### C.1 Markovian subband scattering rates

The electron-electron and electron-phonon scattering rates which have been introduced in Eqs. 5.5-5.6 are listed here in detail.

Only results for the subband  $i = 1$ , are given here. The terms for  $i = 2$  are obtained by exchanging all subband indices 1 and 2. The diagonal and diagonal scattering rates resulting from the electron-phonon coupling are given by:

$$\Gamma_d^{1,\text{cp}} = 2 \sum_{\mathbf{q}} \left[ \delta(-\varepsilon_{\mathbf{k}}^1 + \varepsilon_{\mathbf{k}+\mathbf{q}_f}^1 - \hbar\omega_{\text{LO}}) |g_{\mathbf{q}}^{11}|^2 \left\{ n_{\mathbf{q}}(1 - f_{\mathbf{k}+\mathbf{q}_f}^1) + (n_{\mathbf{q}} + 1) f_{\mathbf{k}+\mathbf{q}_f}^1 \right\} \right. \\ \left. + \delta(-\varepsilon_{\mathbf{k}}^1 + \varepsilon_{\mathbf{k}+\mathbf{q}_f}^1 + \hbar\omega_{\text{LO}}) |g_{\mathbf{q}}^{11}|^2 \left\{ (n_{\mathbf{q}} + 1)(1 - f_{\mathbf{k}+\mathbf{q}_f}^1) + n_{\mathbf{q}} f_{\mathbf{k}+\mathbf{q}_f}^1 \right\} \right. \\ \left. + \delta(-\varepsilon_{\mathbf{k}}^2 + \varepsilon_{\mathbf{k}+\mathbf{q}_f}^1 - \hbar\omega_{\text{LO}}) |g_{\mathbf{q}}^{12}|^2 \left\{ n_{\mathbf{q}}(1 - f_{\mathbf{k}+\mathbf{q}_f}^1) + (n_{\mathbf{q}} + 1) f_{\mathbf{k}+\mathbf{q}_f}^1 \right\} \right. \\ \left. + \delta(-\varepsilon_{\mathbf{k}}^2 + \varepsilon_{\mathbf{k}+\mathbf{q}_f}^1 + \hbar\omega_{\text{LO}}) |g_{\mathbf{q}}^{12}|^2 \left\{ (n_{\mathbf{q}} + 1)(1 - f_{\mathbf{k}+\mathbf{q}_f}^1) + n_{\mathbf{q}} f_{\mathbf{k}+\mathbf{q}_f}^1 \right\} \right] \quad (\text{C.1})$$

$$\Gamma_{\text{nd}}^{1,\text{cp}} = \delta(-\varepsilon_{\mathbf{k}}^1 + \varepsilon_{\mathbf{k}+\mathbf{q}_f}^1 - \hbar\omega_{\text{LO}}) g_{\mathbf{q}_f}^{11*} g_{\mathbf{q}_f}^{22} \left\{ (n_{\mathbf{q}_f} + 1)(1 - f_{\mathbf{k}}^1) + n_{\mathbf{q}_f} f_{\mathbf{k}}^1 \right\} \\ + \delta(-\varepsilon_{\mathbf{k}}^1 + \varepsilon_{\mathbf{k}+\mathbf{q}_f}^1 + \hbar\omega_{\text{LO}}) g_{\mathbf{q}_f}^{11*} g_{\mathbf{q}_f}^{22} \left\{ n_{\mathbf{q}_f}(1 - f_{\mathbf{k}}^1) + (n_{\mathbf{q}_f} + 1) f_{\mathbf{k}}^1 \right\}, \quad (\text{C.2})$$

The diagonal part of the electron-electron scattering reads:

$$\begin{aligned}
\Gamma_{\text{d}}^{1,\text{cc}} &= 2 \sum_{\mathbf{k}',\mathbf{q}} \left[ \delta(\epsilon_{\mathbf{k}}^1 + \epsilon_{\mathbf{k}'}^1 - \epsilon_{\mathbf{k}'-\mathbf{q}}^1 - \epsilon_{\mathbf{k}+\mathbf{q}}^1) V_{\mathbf{q}}^{1111} (2V_{\mathbf{q}}^{1111} - V_{\mathbf{k}'-\mathbf{k}-\mathbf{q}}^{1111} - V_{\mathbf{k}'-\mathbf{q}}^{1111}) \{ f_{\mathbf{k}'}^1 (1 - f_{\mathbf{k}'-\mathbf{q}}^1) (1 - f_{\mathbf{k}+\mathbf{q}}^1) + f_{\mathbf{k}'-\mathbf{q}}^1 f_{\mathbf{k}+\mathbf{q}}^1 (1 - f_{\mathbf{k}'}^1) \} \right. \\
&\quad + \delta(\epsilon_{\mathbf{k}}^1 + \epsilon_{\mathbf{k}'}^1 - \epsilon_{\mathbf{k}'-\mathbf{q}}^2 - \epsilon_{\mathbf{k}+\mathbf{q}}^2) V_{\mathbf{q}}^{1122} (2V_{\mathbf{q}}^{1122} - V_{\mathbf{k}'-\mathbf{k}-\mathbf{q}}^{1122} - V_{\mathbf{k}'-\mathbf{q}}^{1122}) \{ f_{\mathbf{k}'}^1 (1 - f_{\mathbf{k}'-\mathbf{q}}^1) (1 - f_{\mathbf{k}+\mathbf{q}}^2) + f_{\mathbf{k}'-\mathbf{q}}^2 f_{\mathbf{k}+\mathbf{q}}^2 (1 - f_{\mathbf{k}'}^1) \} \\
&\quad + \delta(\epsilon_{\mathbf{k}}^1 + \epsilon_{\mathbf{k}'}^2 - \epsilon_{\mathbf{k}'-\mathbf{q}}^1 - \epsilon_{\mathbf{k}+\mathbf{q}}^1) V_{\mathbf{q}}^{1221} (2V_{\mathbf{q}}^{1221} - V_{\mathbf{k}'-\mathbf{k}-\mathbf{q}}^{1221} - V_{\mathbf{k}'-\mathbf{q}}^{1221}) \{ f_{\mathbf{k}'}^2 (1 - f_{\mathbf{k}'-\mathbf{q}}^1) (1 - f_{\mathbf{k}+\mathbf{q}}^1) + f_{\mathbf{k}'-\mathbf{q}}^1 f_{\mathbf{k}+\mathbf{q}}^1 (1 - f_{\mathbf{k}'}^2) \} \\
&\quad \left. + \delta(\epsilon_{\mathbf{k}}^1 + \epsilon_{\mathbf{k}'}^2 - \epsilon_{\mathbf{k}'-\mathbf{q}}^2 - \epsilon_{\mathbf{k}+\mathbf{q}}^2) V_{\mathbf{q}}^{1212} (2V_{\mathbf{q}}^{1212} - V_{\mathbf{k}'-\mathbf{k}-\mathbf{q}}^{1212} - V_{\mathbf{k}'-\mathbf{q}}^{1212}) \{ f_{\mathbf{k}'}^2 (1 - f_{\mathbf{k}'-\mathbf{q}}^2) (1 - f_{\mathbf{k}+\mathbf{q}}^1) + f_{\mathbf{k}'-\mathbf{q}}^1 f_{\mathbf{k}+\mathbf{q}}^1 (1 - f_{\mathbf{k}'}^2) \} \right]. \tag{C.3}
\end{aligned}$$

The nondiagonal part of the Coulomb correlations is given by:

$$\begin{aligned}
\Gamma_{\text{nd1}}^{1,\text{cc}} &= \delta(\epsilon_{\mathbf{k}}^1 + \epsilon_{\mathbf{k}'}^2 - \epsilon_{\mathbf{k}'-\mathbf{q}}^1 - \epsilon_{\mathbf{k}+\mathbf{q}}^2) V_{\mathbf{q}}^{2222} (2V_{\mathbf{q}}^{1221} - V_{\mathbf{k}'-\mathbf{k}-\mathbf{q}}^{1212} - V_{\mathbf{k}'-\mathbf{q}}^{1212}) \{ f_{\mathbf{k}+\mathbf{q}}^2 (1 - f_{\mathbf{k}'}^1) (1 - f_{\mathbf{k}'}^2) + f_{\mathbf{k}'}^1 f_{\mathbf{k}'}^2 (1 - f_{\mathbf{k}+\mathbf{q}}^2) \} \\
&\quad + \delta(\epsilon_{\mathbf{k}}^1 + \epsilon_{\mathbf{k}'}^1 - \epsilon_{\mathbf{k}'-\mathbf{q}}^1 - \epsilon_{\mathbf{k}+\mathbf{q}}^1) V_{\mathbf{q}}^{1221} (2V_{\mathbf{q}}^{1111} - V_{\mathbf{k}'-\mathbf{k}-\mathbf{q}}^{1111} - V_{\mathbf{k}'-\mathbf{q}}^{1111}) \{ f_{\mathbf{k}+\mathbf{q}}^1 (1 - f_{\mathbf{k}'}^1) (1 - f_{\mathbf{k}'}^1) + f_{\mathbf{k}'}^1 f_{\mathbf{k}'}^1 (1 - f_{\mathbf{k}+\mathbf{q}}^1) \}, \tag{C.4}
\end{aligned}$$

$$\begin{aligned}
\Gamma_{\text{nd2}}^{1,\text{cc}} &= \sum_{\mathbf{k}'} \left[ \delta(\epsilon_{\mathbf{k}}^1 + \epsilon_{\mathbf{k}'}^2 - \epsilon_{\mathbf{k}'-\mathbf{q}}^2 - \epsilon_{\mathbf{k}+\mathbf{q}}^1) V_{\mathbf{q}}^{2222} (2V_{\mathbf{q}}^{1212} - V_{\mathbf{k}'-\mathbf{k}-\mathbf{q}}^{1212} - V_{\mathbf{k}'-\mathbf{q}}^{1212}) \{ f_{\mathbf{k}'-\mathbf{q}}^2 (1 - f_{\mathbf{k}'}^1) (1 - f_{\mathbf{k}'}^2) + f_{\mathbf{k}'}^1 f_{\mathbf{k}'-\mathbf{q}}^2 (1 - f_{\mathbf{k}+\mathbf{q}}^1) \} \right. \\
&\quad \left. + \delta(\epsilon_{\mathbf{k}}^1 + \epsilon_{\mathbf{k}'}^1 - \epsilon_{\mathbf{k}'-\mathbf{q}}^1 - \epsilon_{\mathbf{k}+\mathbf{q}}^1) V_{\mathbf{q}}^{2121} (2V_{\mathbf{q}}^{1111} - V_{\mathbf{k}'-\mathbf{k}-\mathbf{q}}^{1111} - V_{\mathbf{k}'-\mathbf{q}}^{1111}) \{ f_{\mathbf{k}'-\mathbf{q}}^1 (1 - f_{\mathbf{k}'}^1) (1 - f_{\mathbf{k}'}^1) + f_{\mathbf{k}'}^1 f_{\mathbf{k}'-\mathbf{q}}^1 (1 - f_{\mathbf{k}+\mathbf{q}}^1) \} \right], \tag{C.5}
\end{aligned}$$

$$\begin{aligned}
\Gamma_{\text{nd3}}^{1,\text{cc}} &= \sum_{\mathbf{q}} \left[ \delta(\epsilon_{\mathbf{k}}^1 + \epsilon_{\mathbf{k}'}^2 - \epsilon_{\mathbf{k}'-\mathbf{q}}^2 - \epsilon_{\mathbf{k}+\mathbf{q}}^1) V_{\mathbf{q}}^{1221} (2V_{\mathbf{q}}^{1212} - V_{\mathbf{k}'-\mathbf{k}-\mathbf{q}}^{1212} - V_{\mathbf{k}'-\mathbf{q}}^{1212}) \{ f_{\mathbf{k}}^1 (1 - f_{\mathbf{k}'-\mathbf{q}}^2) (1 - f_{\mathbf{k}+\mathbf{q}}^1) + f_{\mathbf{k}'-\mathbf{q}}^2 f_{\mathbf{k}+\mathbf{q}}^1 (1 - f_{\mathbf{k}}^1) \} \right. \\
&\quad \left. + \delta(\epsilon_{\mathbf{k}}^1 + \epsilon_{\mathbf{k}'}^2 - \epsilon_{\mathbf{k}'-\mathbf{q}}^1 - \epsilon_{\mathbf{k}+\mathbf{q}}^2) V_{\mathbf{q}}^{1212} (2V_{\mathbf{q}}^{1221} - V_{\mathbf{k}'-\mathbf{k}-\mathbf{q}}^{1221} - V_{\mathbf{k}'-\mathbf{q}}^{1221}) \{ f_{\mathbf{k}}^1 (1 - f_{\mathbf{k}'-\mathbf{q}}^1) (1 - f_{\mathbf{k}+\mathbf{q}}^2) + f_{\mathbf{k}'-\mathbf{q}}^1 f_{\mathbf{k}+\mathbf{q}}^2 (1 - f_{\mathbf{k}}^1) \} \right]. \tag{C.6}
\end{aligned}$$

## C.2 Quantum dots: correlation expansion

The correlation expansion of the electron-phonon interaction in second order is given by:

$$\dot{P}_{vc} = -i\omega_g P_{vc} + i\Omega(1 - 2f_c(t)) + \frac{i}{\hbar} \sum_{q,\pm} \tilde{g}_q (S_q + T_q) - \gamma_0 P_{vc} \quad (\text{C.7})$$

$$\dot{f}_c = -i(\Omega^* P_{vc} - \Omega P_{vc}^*) - 2\gamma_0 f_c \quad (\text{C.8})$$

$$\begin{aligned} \dot{S}_q(t) = & \frac{i}{\hbar}(-\varepsilon_g - \hbar\omega_q) S_q + i\Omega(t) \langle \langle a_v^+ a_v b_q \rangle \rangle^c - \langle a_c^+ a_c b_q \rangle^c - \gamma_0 S_q \\ & + \frac{i}{\hbar} \tilde{g}_{vc}^{-q} P_{vc}(t) (n_q + 1) + \frac{i}{\hbar} \sum_q \tilde{g}_{vc}^q (\langle \langle a_v^+ a_c b_q b_q \rangle \rangle^c + \langle a_v^+ a_c b_{-q}^+ b_q \rangle^c), \end{aligned} \quad (\text{C.9})$$

$$\begin{aligned} \dot{T}_q(t) = & \frac{i}{\hbar}(-\varepsilon_g + \hbar\omega_q) T_q + i\Omega(t) \langle \langle a_v^+ a_v b_{-q}^+ \rangle \rangle^c - \langle a_c^+ a_c b_{-q}^+ \rangle^c - \gamma_0 T_q \\ & + \frac{i}{\hbar} \tilde{g}_{vc}^{-q} P_{vc}(t) n_{-q} + \frac{i}{\hbar} \sum_q \tilde{g}_{vc}^q (\langle \langle a_v^+ a_c b_q b_{-q}^+ \rangle \rangle^c + \langle a_v^+ a_c b_{-q}^+ b_{-q}^+ \rangle^c). \end{aligned} \quad (\text{C.10})$$

$$\begin{aligned} \langle a_v^+ a_c b_q b_d \rangle^c = & \frac{i}{\hbar}(-\varepsilon_g - \hbar\omega_q - \hbar\omega_d) \langle a_v^+ a_c b_q b_d \rangle^c + i\Omega (\langle \langle a_v^+ a_v b_q b_d \rangle \rangle^c - \langle a_c^+ a_c b_q b_d \rangle^c) \\ & + \frac{i}{\hbar} S_q \tilde{g}_{vc}^{-d} (n_d + 1) + \frac{i}{\hbar} S_d \tilde{g}_{vc}^{-q} (n_q + 1) \end{aligned} \quad (\text{C.11})$$

$$\begin{aligned} \langle a_v^+ a_c b_q^+ b_d \rangle^c = & \frac{i}{\hbar}(-\varepsilon_g + \hbar\omega_q - \hbar\omega_d) \langle a_v^+ a_c b_q b_d \rangle^c + i\Omega (\langle \langle a_v^+ a_v b_{-q}^+ b_d \rangle \rangle^c - \langle a_c^+ a_c b_{-q}^+ b_d \rangle^c) \\ & + \frac{i}{\hbar} T_q \tilde{g}_{vc}^{-d} (n_d + 1) + \frac{i}{\hbar} S_d \tilde{g}_{vc}^{-q} n_{-q} \end{aligned} \quad (\text{C.12})$$

### C.2.1 Coulomb interaction

If spin degeneracy of the quantum dot levels is allowed, two electron-hole pairs are considered and Coulomb interaction is included the emerging set equations of motion is very large. Therefore only the generic equations without explicit evaluation of the indices are given here. The microscopic coherences are denoted as:

$$S_{12} = \langle a_1^+ a_2 \rangle \quad (\text{C.13})$$

$$S_{12q}^{\pm} = \langle a_1^+ a_2 b_q^{\pm} \rangle^c$$

$$S_{12qd}^{\pm,\pm'} = \langle a_1^+ a_2 b_q^{\pm} b_d^{\pm'} \rangle \quad (\text{C.14})$$

For notation  $b_q^- = b_q$  is used. With these definitions the equation of motion can be written as:

$$i\hbar\dot{S}_{12} = (\varepsilon_2 - \varepsilon_1)S_{12} - E(t) \sum_j (d_{1j}S_{j2} - d_{2j}S_{1j}) + \sum_{q,\pm} \hat{g}_q^{21} S_{12q}^\pm + \sum_t W_{12}^i S_{12i} \quad (\text{C.15})$$

$$i\hbar\dot{S}_{11'22'} = (\varepsilon_2 + \varepsilon_{2'} - \varepsilon_1 - \varepsilon_{1'} + V_{11'}^{22'})S_{11'22'} + E(t) \sum_j (d_{1j}S_{j1'22'} + d_{1'j}S_{1j22'} - d_{2j}S_{11'j2'} - d_{2'j}S_{11'2j'}) + \sum_{q,\pm} \hat{g}_q^{21} S_{11'22'q}^\pm \quad (\text{C.16})$$

$$i\hbar\dot{S}_{12q}^\pm = (\varepsilon_2 - \varepsilon_1 \mp \hbar\omega_q)S_{12q}^\pm - E(t) \sum_j (d_{1j}S_{j2q}^\pm - d_{2j}S_{1jq}^\pm) + S_{12} \hat{g}_q^{21} n_q^\pm + S_{12} \sum_{q',\pm'} \hat{g}_{q'}^{21} S_{qq'}^{\pm\pm'} \\ + \sum_{q',\pm'} \hat{g}_{q'}^{21} S_{12qq'}^{\pm\pm'} + \sum_{q',\pm'} \hat{g}_{q'}^{21} S_{12iq'}^{\pm\pm'} + \sum_t W_{12}^i S_{12i} \mp \sum_{q'} \hat{g}_{q'}^{22} S_{12} \pm \sum_{q'} \hat{g}_{q'}^{ii} S_{12i} \quad (\text{C.17})$$

$$i\hbar\dot{S}_{11'22'q}^\pm = (\varepsilon_2 + \varepsilon_{2'} - \varepsilon_1 - \varepsilon_{1'} + V_{11'}^{22'} \mp \hbar\omega_q)S_{11'22'q}^\pm + E(t) \sum_j (d_{1j}S_{j1'22'q}^\pm + d_{1'j}S_{1j22'q}^\pm - d_{2j}S_{11'j2'q}^\pm - d_{2'j}S_{11'2j'q}^\pm) \\ + S_{11'22'} \hat{g}_q^{21} n_q^\pm + S_{11'22'} \sum_{q',\pm'} \hat{g}_{q'}^{21} S_{qq'}^{\pm\pm'} + \sum_{q',\pm'} \hat{g}_{q'}^{21} S_{11'22'qq'}^{\pm\pm'} \mp (\hat{g}_q^{22} + \hat{g}_q^{2'2'}) S_{11'22'} \mp \sum_{q'} \hat{g}_{q'}^{ii} S_{11'22'i} \quad (\text{C.18})$$

For a compact notation the following definitions are used:

$$n_q^{\pm\pm'} = \begin{cases} n_q & + - [\pm = +, \pm' = -] \\ n_q + 1 & - + [\pm = -, \pm' = +] \\ 0 & \text{otherwise} \end{cases} \quad (\text{C.19})$$

$$n_q^\pm = \sum_{\pm'} n_q^{\pm\pm'} = n_q^{\pm+} + n_q^{\pm-} = \begin{cases} n_q & + [\pm = +] \\ n_q + 1 & - [\pm = -] \end{cases} \quad (\text{C.20})$$

The above equations do not include electron-photon interaction. In fact, the simulations in chapter 6.6 use equations of motion which are computer generated using a self-written program. This program is able to derive equations of motion for a given Hamiltonian and can perform the RWA and Markov approximation automatically. Also it allows evaluation of all necessary index combinations. The program is restricted to problems with simple wavevector dependency. The resulting equations are directly encoded in Fortran 90 allowing direct numerical evaluation.

## Appendix D

# Notation, Symbols

### D.1 Notation

| Notation                     | description   |
|------------------------------|---|
| $\partial_x g(x)$            | derivative of function $g$ with respect to $x$ : $\partial_x g(x) = \frac{d}{dx}g(x)$ |
| $\dot{g}(t)$                 | temporal derivative of $g(t) = \partial_t g(t) = \frac{d}{dt}g(t)$                    |
| $\mathbf{r}$                 | vector  |
| $\mathbf{q}_c, \mathbf{q}_f$ | confinement, free sub-vector, see section 2.1   |
| $\underline{\chi}$           | tensor  |
| $[A, B] = [A, B]_-$          | (bosonic) commutator of two operators $A$ and $B$ , $[A, B] = AB - BA$                |
| $[A, B]_+$                   | (fermionic) anti-commutator of two operators $A$ and $B$ , $[A, B]_+ = AB + BA$       |

See section 2.1 for the special notation of vectors and band indices.

### D.2 Fundamental constants

| symbol       | meaning                               |
|--------------|---------------------------------------|
|              |                                       |
|              |                                       |
| $e_0$        | elementary charge                     |
| $c_0$        | vacuum velocity of light              |
| $\epsilon_0$ | permittivity of free space            |
| $\mu_0$      | (magnetic) permeability of free space |
| $m_0$        | restmass of an electron               |
| $k_B$        | Boltzmann constant                    |

### D.3 Symbols

Some symbols which are frequently used in chapters 4- are given here:

| Symbol   | description   | details       |
|--|---|---------------|
| $\delta(t - t_0)$                              | Dirac $\delta$ -function, $\int f(t)\delta(t - t_0)dt = f(t_0)$ , $\delta(t) = \dot{\theta}(t)$   |               |
| $\delta_{ij}$                                  | Kronecker delta, $\delta = \begin{cases} 0 & i = j \\ 1 & i \neq j \end{cases}$   |               |
| $\theta(t)$                                    | Heaviside step function, $\theta(t) = \begin{cases} 0 & t < 0 \\ 1 & t \geq 0 \end{cases}$  |               |
| $\Omega_{i,i'}(t)$                             | Rabi frequency, $\Omega(t) = \mathbf{d}_{i,i'} \cdot \mathbf{E}(t)/\hbar$   | Eq. 2.16      |
| $\mathbf{E}(t)$                                | electric field  |               |
| $\mathbf{d}_{i,i'}(\mathbf{q}_c)$              | dipole transition element, $\mathbf{d}_{i,i'}(\mathbf{q}_c) = F_{i,i'}(\mathbf{q}_c)\mu_{i,i'}^{IB} + \delta_{i,i'}\mu_{i,i'}^{ISB}(\mathbf{q}_c)$        | Eq. 2.15      |
| $F_{ij}(\mathbf{q}_c)$                         | confinement form factor $F_{i,i'}(\mathbf{q}_c) = \int d\mathbf{r}_c \phi_i^*(\mathbf{r}_c) e^{i\mathbf{q}_c \cdot \mathbf{r}_c} \phi_{i'}(\mathbf{r}_c)$ | Eq. 2.9       |
| $\mu_{i,i'}^{IB}$                              | interband (IB) dipole matrix elements   | Eq. 2.8       |
| $\mu_{i,i'}^{ISB}(\mathbf{q}_c)$               | intersubband (ISB)dipole matrix elements  | Eq. 2.10      |
| $\Theta(t)$                                    | time-dependent pulse area $\Theta(t) = \int_{-\infty}^t \Omega(t') dt'$   |               |
| $\Theta$                                       | pulse area, $\Theta = \lim_{t \rightarrow \infty} \Theta(t) = \int_{-\infty}^{\infty} \Omega(t') dt'$   |               |
| $\epsilon_b$                                   | (relative) background dielectric constant   |               |
| $\epsilon_{st}$                                | (relative) static dielectric constant   |               |
| $\epsilon_{i\mathbf{k}}$                       | energy of an interaction free Bloch electron  | section 2.3   |
| $\epsilon_g = \hbar\omega_g$                   | $\epsilon_{c,0} - \epsilon_{v,0}$ , if a two band system (v,c) is considered  |               |
| $V_{\mathbf{q}_f}^{i1,i2,i3,i4}$               | Coulomb coupling element  | Eq. 2.18      |
| $g_{\mu,\mathbf{q}}^{ij}$                      | Electron-phonon coupling element  | Eq. 2.22      |
| $\omega_{LO}$                                  | LO phonon frequency   | Eq. 2.22      |
| $G_q^{i,i',\lambda}$                           | Electron-photon coupling element  | Eq. 2.12      |
| $\Phi_i(\mathbf{r}_c)$                         | confinement wavefunction of electron in band $i$  | section 2.3   |
| $V_f$  | extension (“volume”) of crystal in free dimension   |               |
| $a_{i\mathbf{k}}^+, a_{i\mathbf{k}}$           | creation/destruction operator of an <i>electron</i> in band $i$   | section 2.2.1 |
| $b_{\mu,\mathbf{q}}^+, b_{\mu,\mathbf{q}}$     | creation/destruction operator of a <i>phonon</i> in branch $\mu$  | section 2.2.5 |
| $c_{\lambda,\mathbf{q}}^+, c_{\mu,\mathbf{q}}$ | creation/destruction operator of a <i>photon</i> with polarizaton $\lambda$   | section 2.2.2 |
| $\sigma_{\mathbf{k},\mathbf{k}'}^{i,i'}$       | single-electron coherence $\sigma_{\mathbf{k},\mathbf{k}'}^{i,i'} = \langle a_{i\mathbf{k}}^+ a_{i'\mathbf{k}'} \rangle$                                  | section 2.4   |
| $p_{\mathbf{k}} = p_{\mathbf{k}}^{vc}$         | interband or or intersubband coherence $p_{\mathbf{k}} = \langle a_{v\mathbf{k}}^+ a_{c\mathbf{k}} \rangle$   | section 2.4   |
| $f_{\mathbf{k}} = f_{\mathbf{k}}^{cc}$         | occupation of the conduction band $f_{\mathbf{k}}^{cc} = \langle a_{c\mathbf{k}}^+ a_{c\mathbf{k}} \rangle$   | section 2.4   |
| $n_{\mathbf{q}}$                               | Bose distribution (for photons or phonons)  | Eq. 2.6       |
| $\tau$   | parameter controlling pulse duration  | appendix B.1  |

## D.4 Acronyms

| acronym | meaning                                  |
|---------|--|
| DCT     | Dynamically Controlled Truncation scheme |
| FDTD    | Finite Differences Time Domain method    |
| FT      | Fourier Transformation                   |
| FWHM    | Full Width at Half Maximum               |
| ibm     | Independent Boson Model                  |
| LA      | Longitudinal Acoustic (phonon)           |
| LO      | Longitudinal Optical (phonon)            |
| MLS     | Multi-Level System                       |
| MQW     | Multiple Quantum Wells                   |
| RWA     | Rotating Wave Approximation              |
| SVEA    | Slowly Varying Envelope Approximation    |
| TLA     | Two-Level Atom                           |
| TLS     | Two-Level System                         |
| SIT     | Self-Induced Transparency                |
| UPML    | Uniaxial Perfectly Matched Layer         |
| ZPL     | Zero-Phonon Line                         |



# Bibliography

- [1] T. Kuhn. *Theory of Transport Properties of Semiconductor Nanostructures*, edited by E. Schöll, chapter Density matrix theory of coherent ultrafast dynamics, page 173. Chapman & Hall, London, 1998.
- [2] Hartmut Haug and Stephan W. Koch. *Quantum Theory of the Optical and Electronic Properties of Semiconductors*. World Scientific, 3rd edition, 1990.
- [3] Gerald D. Mahan. *Many-Particle Physics*. Plenum Press, 1981.
- [4] Wilfried Schäfer and Martin Wegener. *Semiconductor Optics and Transport Phenomena*. Springer, 2002.
- [5] Peter Y. Yu and Manuel Cardona. *Fundamentals of Semiconductors*. Springer, second edition, 1996.
- [6] F. Bloch. *Z. Phys.*, 52:555, 1928.
- [7] D. F. Walls and G. J. Milburn. *Quantum Optics*. Springer, 1994.
- [8] H. Haken. *Quantenfeldtheorie des Festkörpers*. B.G. Teubner, 1973.
- [9] T. Förster. Zwischenmolekulare energiewanderung und fluoreszenz. *Annalen der Physik*, 6:55–75, 1948.
- [10] D.L. Dexter. A theory of sensitized luminescence in solids. *Journal of Chemical Physics*, 21:836–850, 1953.
- [11] N.W. Ashcroft and N.D. Mermin. *Solid State Physics*. Holt, Rinehart and Winston, Philadelphia, 1976.
- [12] P. Debye and E. Hückel. Zur theorie der elektrolyte. *Phys. Z.*, 185:305, 1923.
- [13] H. Fröhlich. Electrons in lattice fields. *Adv. Phys.*, 3:325, 1954.
- [14] E. Fick and G. Saueremann. *Quantenstatistik dynamischer Prozesse*, volume Band 1: Generelle Aspekte. Verlag Harri Deutsch, Thun, 1983.
- [15] John David Jackson. *Classical Electrodynamics*. John Wiley & Sons, Inc., 3rd edition, 1999.
- [16] Jens Förstner. Optische pulsausbreitung in halbleiterstrukturen unter berücksichtigung von coulombkorrelationen. Master's thesis, Universität Marburg, 2000.

- [17] W.W. Chow and S.W. Koch. *Semiconductor-Laser Fundamentals - Physics of the Gain Materials*. Springer, 1999.
- [18] I. Waldmüller, J. Förstner, and A. Knorr. *Nonequilibrium Physics at Short Time Scales*, chapter Self-consistent Projection Operator Theory of Intersubband Absorbance in Semiconductor Quantum Wells.
- [19] J.C. Ashley and R.H. Ritchie. Quantum treatment of multiple real transitions. *Phys. Rev.*, 174(5):1572, 1968.
- [20] J.C. Maxwell. A dynamical theory of the electromagnetic field. *Royal Society Transactions*, CLV:459, 1865.
- [21] A. Taflove and S.C. Hagness. *Computational Electrodynamics*. Artech House Publishers, Boston, 2nd edition, 2000.
- [22] A. Taflove. *Advances in Computational Electrodynamics*. Artech House Publishers, Boston, 1998.
- [23] K.S. Yee. Numerical solution of initial boundary value problems involving maxwell's equations in isotropic media. *IEEE Trans. Antennas and Propagation*, 14:302–307, 1966.
- [24] E. Waring. *Philos. Trans.*, 69:59–67, 1779. also see article on "Lagrange Interpolating Polynomial" at <http://mathworld.wolfram.com/LagrangeInterpolatingPolynomial.html>.
- [25] G. Mur. Absorbing boundary conditions for the numerical simulation of waves. *IEEE Trans. Electr. Compat.*, 23:377, 1981.
- [26] K. Zimmermann. Zur theorie der elektromagnetischen kopplung in periodischen quantenpunktstrukturen. Master's thesis, Technische Universität Berlin, 2003.
- [27] L. Allen and J.H. Eberly. *Optical Resonance and Two-Level Atoms*. Dover, 1975.
- [28] S. Schneider, P. Borri, W. Langbein, U. Woggon, J. Förstner, A. Knorr, R. L. Sellin, D. Ouyang, and D. Bimberg. Self-induced transparency in ingaas quantum-dot waveguides. *Applied Physics Letters*, 83:3668, 2003.
- [29] S. Schneider, P. Borri, W. Langbein, U. Woggon, J. Förstner, A. Knorr, R. L. Sellin, D. Ouyang, and D. Bimberg. Self-induced transparency in ingaas quantum dot waveguides. *phys. stat. sol. (c)*, 0:1548, 2003.
- [30] Tomobumi Mishina. Forward and backward self-consistent approach to coherent light propagation in stratified structures. *Phys. Rev. B*, 54:13630, 1996.
- [31] J. Förstner, A. Knorr, S.Kuckenburg, T. Meier, S.W. Koch, H. Giessen, S. Linden, and J. Kuhl. Nonlinear polariton pulse propagation in bulk semiconductors. *phys. stat. sol. (b)*, 211:453, 2000.
- [32] J. Förstner, A. Knorr, and S.W. Koch. Nonlinear pulse propagation in semiconductors: Hole burning within a homogeneous line. *Phys. Rev. Lett.*, 86:476, 2001.
- [33] J.J. Hopfield. Theory of the contribution of excitons to the complex dielectric constant of crystals. *Phys. Rev.*, 112:1555, 1958.

- [34] D. Fröhlich, A. Kulik, B. Uebbing, A. Mysyrowicz, V. Langer, H. Stolz, and W. von der Osten. Coherent propagation and quantum beats of quadrupole polaritons in  $\text{Cu}_2\text{O}$ . *Phys. Rev. Lett.*, 67:2343, 1991.
- [35] U. Neukirch, K. Wundke, J. Gutowski, and D. Hommel. *Phys. stat. sol (b)*, 196:473, 1996.
- [36] J. Tignon, T. Hasche, D. S. Chemla, H. C. Schneider, F. Jahnke, and S. W. Koch. Unified picture of polariton propagation in bulk GaAs semiconductors. *Phys. Rev. Lett.*, 84:3382, 1999.
- [37] D.S. Kim, J. Shah, D. A. B. Miller, T. C. Damen, W. Schäfer, and L. Pfeiffer. Femtosecond-pulse distortion in quantum wells. *Phys. Rev. B*, 48:17902, 1993.
- [38] M. Jütte, H. Stolz, and W. von der Osten. Linear and nonlinear pulse propagation at bound excitons in  $\text{Cu}_2\text{O}$ . *J. Opt. Soc. Am. B*, 13:1205, 1996.
- [39] U. Neukirch and K. Wundke. Propagation of confined excitonic polaritons at high densities. *Phys. Rev. B*, 55:15408.
- [40] D. Fröhlich, S. Spitzer, B. Uebbing, and R. Zimmermann. Polarization dependence in the intraband optical Stark effect of quantum wells. *Phys. stat. sol. (b)*, 173:31, 1992.
- [41] G. Manzke, Q.Y. Peng, U. Moldzio, and K. Henneberger. Coherent nonlinear excitonic effects and pulse propagation. *Phys. stat. sol (b)*, 206:37, 1999.
- [42] V.M. Axt and A. Stahl. The role of the biexciton in a dynamic density matrix theory. *Z. Phys. B*, 93:205, 1994.
- [43] M. Lindberg, Y. Z. Hu, R. Binder, and S. W. Koch.  $\chi^{(3)}$  formalism in optically excited semiconductors and its applications in four-wave-mixing spectroscopy. *Phys. Rev. B*, 50:18060, 1994.
- [44] W. Schäfer, D. S. Kim, J. Shah, T. C. Damen, J. E. Cunningham, K. W. Goossen, L. N. Pfeiffer, and K. Köhler. Femtosecond coherent fields induced by many-particle correlations in transient four-wave mixing. *Phys. Rev. B*, 53:16429, 1996.
- [45] S. Kuckenburger. Kohärente propagationseffekte lokaler Anregungen in Halbleiterstrukturen. Master's thesis, Philipps-Universität Marburg, 1998.
- [46] S.I. Pekar. *Sov. Phys. JETP*, 6:785, 1958.
- [47] H.C. Schneider. personal communication, 1999.
- [48] C. Sieh, T. Meier, F. Jahnke, A. Knorr, S. W. Koch, P. Brick, M. Hübner, C. Ell, J. Prineas, G. Khitrova, and H. M. Gibbs. Coulomb memory signatures in the excitonic optical Stark effect. 82:3112, 1998.
- [49] H. Giessen, A. Knorr, S. Haas, S. W. Koch, S. Linden, J. Kuhl, M. Hetterich, M. Grün, and C. Klingshörn. Self-induced transmission on a free exciton resonance in a semiconductor. *Phys. Rev. Lett.*, 81:4260, 1998.
- [50] D.C. Burnham and R.Y. Chiao. Coherent resonance fluorescence excited by short light pulses. *Phys. Rev.*, 188(667), 1969.

- [51] M.D. Crisp. Propagation of small-area pulses of coherent light through a resonant medium. *Phys. Rev. A*, 1:1604, 1969.
- [52] S.L. McCall and E.L. Hahn. Self-induced transparency by pulsed coherent light. *Phys. Rev. Lett.*, 18:908, 1967.
- [53] S.L. McCall and E.L. Hahn. Self-induced transparency. *Phys. Rev.*, 183:457, 1969.
- [54] C. Sieh, T. Meier, A. Knorr, F. Jahnke, P. Thomas, and S.W. Koch. Theoretical analysis of differential spectra including carrier-correlations and disorder. *Eur. Phys. J.*, 11:407, 1999.
- [55] J. Förstner, A. Knorr, M. Lindberg, and S. W. Koch. Line narrowing and hole burning within the homogeneous linewidth: a new wave-mixing effect in two-level systems. *Optics Letters*, 27:1830, 2002.
- [56] T. Yajima and Y. Taira. Spatial optical parametric coupling of picosecond light pulses and transverse relaxation effect in resonant media. *J. Phys. Soc. Jpn*, 47:1620, 1979.
- [57] M. Schaarschmidt. Theorie der nichtlinearen Lichtausbreitung in Halbleiter-Braggstrukturen. Master's thesis, Technische Universität Berlin, 2003.
- [58] J. Förstner, K. J. Ahn, J. Danckwerts, M. Schaarschmidt, I. Waldmüller, C. Weber, and A. Knorr. Light propagation and many-particle-induced non-Lorentzian lineshapes in semiconductor nanooptics. *Phys. Stat. Sol. (b)*, 234:155, 2002.
- [59] N. C. Nielsen, J. Kuhl, J. Förstner, M. Schaarschmidt, A. Knorr, S. W. Koch, G. Khitrova, H. M. Gibbs, and H. Giessen. Linear and nonlinear pulse propagation in a multiple-quantum-well photonic crystal. *Phys. Rev. B*, 2004. accepted.
- [60] C. Ell, J. Prineas, T.R. Nelson Jr, S. Park, H.M. Gibbs, G. Khitrova, S.W. Koch, and R. Houdre. Influence of structural disorder and light coupling on excitonic response of semiconductor microcavities. *Phys. Rev. Lett.*, 80:4795, 1998.
- [61] M. Hübner, J. Kuhl, T. Stroucken, A. Knorr, S.W. Koch, R. Hey, and K. Ploog. Collective effects of excitons in multiple quantum well Bragg and anti-Bragg structures. *Phys. Rev. Lett.*, 76:4199, 1996.
- [62] T. Stroucken, A. Knorr, P. Thomas, and S.W. Koch. Coherent dynamics of radiatively coupled quantum well excitons. *Phys. Rev. B*, 54:13630, 1996.
- [63] T. Warncke. *Coherent dynamics of radiatively coupled quantum well excitons*. PhD thesis, Universität Marburg, Verlag Görlich & Weiershäuser GmbH Marburg, 1996.
- [64] A. Knorr. *Spatial Effects in the Ultrafast Optics and Kinetics of Semiconductors*. Phillips Universität Marburg, 1997. Habilitationsschrift.
- [65] J.P. Prineas, J.Y. Zhou, and J. Kuhl. Ultrafast ac Stark effect switching of the active photonic band gap from Bragg-periodic semiconductor quantum wells. *Appl. Phys. Lett.*, 81:4332, 2002.
- [66] Chaohao Gu. *Soliton theory and its applications*. Springer Verlag, Berlin, 1995.
- [67] B.J. Eggleton, R.E. Slusher, C. Martijn de Sterke, P.A. Krug, and J.E. Sipe. Bragg grating solitons. *Phys. Rev. Lett.*, 76:1627, 1996.

- [68] I. H. Deutsch, R.J.C. Spreeuw, S. L. Rolston, and W. D. Phillips. Photonic band gaps in optical lattices. *Phys. Rev. A*, 52:1394, 1995.
- [69] N. Nielsen and J.Kuhl. Experiments conducted at max-planck-institut für festkörperforschung, stuttgart, germany. 2002.
- [70] P. A. Harten, A. Knorr, J. P. Sokolo, F. B. de Colstoun, S. G. Lee, R. Jin, E. M. Wright, G. Khitrova, H. M. Gibbs, S. W. Koch, and N. Peyghambarian. Propagation-induced escape from adiabatic following in a semiconductor. 69:852, 1992.
- [71] I. Waldmüller. Many particle theory of the optical gain of intersubband transitions. Master's thesis, Technische Universität Berlin, 2002.
- [72] I. Waldmüller, M. Woerner, J. Förstner, and A. Knorr. Theory of the lineshape of quantum well intersubband transitions: optical dephasing and light propagation effects. *phys. stat. sol. (b)*, 238(3):474, 2003.
- [73] I. Waldmüller, J. Förstner, S.-C. Lee, and A. Knorr. Optical dephasing of coherent intersubband transitions in a quasi-two-dimensional electron gas. *Phys. Rev. B*, 69:205307, 2004.
- [74] Stefan Butscher, Jens Förstner, Inès Waldmüller, and Andreas Knorr. Polaron signatures in the line shape of semiconductor intersubband transitions: quantum kinetics of the electron-phonon interaction. *Phys. stat. sol. (b) rapid research note*, 2004. submitted.
- [75] T. Elsaesser and M. Woerner. Femtosecond infrared spectroscopy of semiconductors and semiconductor nanostructures. *Phys. Rep.*, 321:253, 1999.
- [76] J. Faist, F. Capasso, D.L. Sivco, C. Sirtori, A.L. Hutchinson, and A.Y. Cho. Quantum cascade lasers. *Science*, 264:553, 1994.
- [77] I. Waldmüller. personal communication, 2004.
- [78] M. Braun and U. Rössler. Magneto-optic transitions and non-parabolicity parameters in the conduction band of semiconductors. *J. Phys. C*, 18:3365, 1985.
- [79] U. Ekenberg. Nonparabolicity effects in a quantum well: Sublevel shift, parallel mass, and landau levels. *Phys. Rev. B*, 40:7714, 1989.
- [80] D.E. Nikonov, A. Imamoglu, L.V. Butov, and H. Schmidt. Collective intersubband excitations in quantum wells: Coulomb interaction versus subband dispersion. *Phys. Rev. Lett.*, 79:4633, 1997.
- [81] R. J. Warburton, C. Gauer, A. Wixforth, J. P. Kotthaus, B. Brar, and H. Kroemer. Intersubband resonances in inas/alsb quantum wells: Selection rules, matrix elements, and the depolarization field. *Phys. Rev. B*, 53:7903, 1996.
- [82] Charles Kittel. *Einführung in die Festkörperphysik*. Oldenburg, 1991.
- [83] M. Lindberg and S. W. Koch. Effective bloch equations for semiconductors. *Phys. Rev. B*, 38:3342, 1988.
- [84] Fausto Rossi, Stefan Haas, and T. Kuhn. Ultrafast relaxation of photoexcited carriers: The role of coherence in the generation process. *Phys. Rev. Lett.*, 72:152, 1993.

- [85] F. Jahnke, M. Kira, S. W. Koch, G. Khitrova, E. K. Lindmark, T. R. Nelson, D. V. Wick, J. D. Berger, O. Lyngnes, and H. M. Gibbs. Excitonic nonlinearities of semiconductor microcavities in the nonperturbative regime. *Phys. Rev. Lett.*, 77:5257, 1996.
- [86] S. Hughes, A. Knorr, S. W. Koch, R. Binder, R. Indik, and J. V. Moloney. The influence of electron-hole scattering on the gain spectra and the saturation behaviour of highly excited semiconductors. *Solid State Commun.*, 100:555, 1996.
- [87] W. Kohn. Cyclotron resonance and de haas-van alphen oscillations of an interacting electron gas. *Phys. Rev.*, 123:1242, 1961.
- [88] L. Brey, Jed Dempsey, N. F. Johnson, and B. I. Halperin. Infrared optical absorption in imperfect parabolic quantum wells. *Phys. Rev. B*, 42:1240, 1990.
- [89] H.C. Schneider, W.W Chow, and S.W. Koch. Excitation induced dephasing in semiconductor quantum dots. arXiv:cond-mat/0310319 v2 10 Jun 2004.
- [90] C. W. Luo, K. Reimann, M. Woerner, T. Elsaesser, R. Hey, and K. H. Ploog. Phase-resolved nonlinear response of a two-dimensional electron gas under femtosecond intersubband excitation. *Phys. Rev. Lett.*, 92:047402, 2004.
- [91] M.O. Scully and M.S. Zubairy. *Quantum Optics*. Cambridge University Press, Cambridge, 1997.
- [92] D. Bimberg, M.Grundmann, and N.N. Lednetsov. *Quantum Dot Heterostructures*. John Wiley&Sons, Chichester, 1999.
- [93] P. Borri, W. Langbein, S. Schneider, U. Woggon, R. L. Sellin, D. Ouyang, and D. Bimberg. Ultralong dephasing time in ingaas quantum dots. *Phys. Rev. Lett.*, 87:157401, 2001.
- [94] Carsten Weber. On the theory of electron-phonon coupling and the optical linewidth in semiconductor quantum dots. Master's thesis, Technische Universität Berlin, 2002.
- [95] A. Vagov, V. M. Axt, and T. Kuhn. Electron-phonon dynamics in optically excited quantum dots: Exact solution for multiple ultrashort laser pulses. *Phys. Rev. B*, 66:165312, 2002.
- [96] J. Förstner, C.Weber, J. Danckwerts, and A. Knorr. Phonon-induced damping of rabi oscillations in semiconductor quantum dots. *Phys. Stat. Sol. (b)*, 238:419, 2003.
- [97] J. Förstner, C.Weber, J. Danckwerts, and A. Knorr. Phonon-assisted damping of rabi oscillations in semiconductor quantum dots. *Phys. Rev. Lett.*, 91:127401, 2003.
- [98] B. Krummheuer, V.M. Axt, and T. Kuhn. *Phys. Rev. B*, 65:195313, 2002.
- [99] R. Zimmermann and E. Runge. Dephasing in quantum dots via electron-phonon interaction. In J. H. Davies and A. R. Long, editors, *Proceedings of the 26th International Conference on the Physics of Semiconductors*. Institute of Physics Publishing, Bristol, UK, 2002.
- [100] A.V. Uskov, A.-P. Jauho, B. Tromborg, J. Mørk, and R. Lang. Dephasing times in quantum dots due to elastic lo phonon-carrier collisions. *Phys. Rev. Lett.*, 85:1516, 2000.
- [101] A. Schliwa. Elektronische eigenschaften von quantenpunktstrukturen. Master's thesis, Technische Universität Berlin, 2001.

- [102] O. Stier, M. Grundmann, and D. Bimberg. Electronic and optical properties of strained quantum dots modeled by 8-band k.p theory. *Phys. Rev. B*, 59:5688, 1999.
- [103] O. Stier. *Electronic and Optical Properties of Quantum Dots and Wires (Dissertation)*. Wissenschaft und Technik Verlag, Berlin, 2001.
- [104] P. Borri, W. Langbein, S. Schneider, U. Woggon, R. L. Sellin, D. Ouyang, and D. Bimberg. Rabi oscillations in the excitonic ground-state transition of InGaAs quantum dots. *Phys. Rev. B*, 66:081306, 2002.
- [105] T. H. Stievater, Xiaoqin Li, D. G. Steel, D. Gammon, D. S. Katzer, D. Park, C. Piermarocchi, and L. J. Sham. Rabi oscillations of excitons in single quantum dots. *Phys. Rev. Lett.*, 87:133603, 2001.
- [106] A. Zrenner, E. Beham, S. Stüfler, F. Findeis, M. Bichler, and G. Abstreiter. Coherent properties of a two-level system based on a quantum-dot photodiode. *Nature*, 418:614, 2002.
- [107] W. Langbein, P. Borri, U. Woggon, V. Stavarache, D. Reuter, and A. D. Wieck. Control of fine-structure splitting and biexciton binding in InGaAs quantum dots by annealing. *Phys. Rev. B*, 69:161301, 2004.
- [108] S. Rodt, R. Heitz, A. Schliwa, R. L. Sellin, F. Guffarth, and D. Bimberg. Repulsive exciton-exciton interaction in quantum dots. *Phys. Rev. B*, 68:035331, 2003.
- [109] S. Hughes. Breakdown of the area theorem: Carrier-wave Rabi flopping of femtosecond optical pulses. *Phys. Rev. Lett.*, 81:3363, 1998.
- [110] C.F. Gauss. *Nachlass: Theoria interpolationis methodo nova tractata*, volume Werke Band 3. Königliche Gesellschaft der Wissenschaften, Göttingen, 1866. See also M. T. Heideman and D. H. Johnson and C. S. Burrus, "Gauss and the history of the fast Fourier transform" *IEEE ASSP Magazine* 1 (4), 1421 (1984).
- [111] J.W. Cooley and J.W. Tukey. An algorithm for the machine calculation of complex Fourier series. *Mathematics of Computation*, 19(90):297–301, 1965.
- [112] H. Nyquist. Certain topics in telegraph transmission theory. *Trans. AIEE*, 47:617–644, 1928.
- [113] C. E. Shannon. Communication in the presence of noise. *Proc. Institute of Radio Engineers*, 37(1):10–21, 1949.
- [114] V. Mehrmann. *Vorlesungsskript Numerik für Ingenieure*. TU Berlin, 2001.



# Danksagung

Es sei all jenen gedankt, die das Entstehen dieser Arbeit ermöglicht oder erleichtert haben.

Im besonderen Maße gilt dies für meinen Doktorvater *Andreas Knorr*, der mich immer und mit aussergewöhnlichem Einsatz unterstützt hat und für jede Frage ein offenes Ohr hatte.

Für eine rundum nette, teilweise zwar produktionshemmende, aber dafür mittelfristig um so motivationsförderndere Arbeitsatmosphäre möchte ich der gesamten Arbeitsgruppe danken. Die Themenvielfalt dieser Arbeit konnte nur durch die Motivation und den Fleiß von vielen Diplomanden entstehen. Im Einzelnen möchte ich dafür *Inès Waldmüller* (Intersubband, QCL), *Martin Schaarschmidt* (Quantenfilme), *Carsten Weber* (Phononwechselwirkung in Quantenpunkten), *Kai Zimmermann* (radiative Kopplung von Quantenpunkten) und *Stefan Butscher* (Intersubband-Quantenkinetik) danken. Für viele weitere Diskussionen, die nicht direkt in die Arbeit eingegangen sind, sei auch *Kwang Jun Ahn* (Quantenoptik an Quantenpunkten), *Juliane Danckwerts* (Coulomb-gekoppelte Quantenpunkte), *Nikolaos Gortsas* (nichtstörungstheoretische Behandlung von Quantenpunkten) und *Andreas Zeiser* (Oberflächen) gedankt.

Auch die interessanten Gespräche innerhalb des Instituts für Theoretische Physik möchte ich hervorheben. Insbesondere danke ich *Christopher Witte* dafür, dass er mit seinem schier grenzenlosen physikalischen Wissen und Verständnis viele grundlegende Fragen erhellen konnte. *Peter Orłowski* sei gedankt für seine engagierte Pflege des Rechnernetzes und die Rücksichtnahme auf meine manchmal extravaganten Softwarewünsche.

Während der Promotionszeit haben sich viele interessante und fruchtbare Zusammenarbeiten mit anderen theoretischen Gruppen und Experimentatoren ergeben. Hervorheben möchte ich hierbei die Kooperationen mit der Marburger Theoriegruppe rund um meinen Diplomvater *Stephan Koch*, mit den "Stuttgarter" Experimentatoren (*Nils Nielsen*, *Harald Giessen*, *Tilman Höner* zu *Siederdisen*, *Prof. Kuhl*) und mit der Dortmunder Gruppe (*Paola Borri*, *Wolfgang Langbein*, *Prof. Woggon*).

Ausserhalb der Physik bin ich meiner *Familie* und meinen *Freunden*, vor allem *Inga* dafür dankbar, dass sie immer für mich da sind und mich auch in stressigeren Zeiten ertragen und unterstützen. Mein Dank für weitergehende moralische Stärkung gilt *Aldi* für sein Süßigkeitensortiment und *Tux* für seine reine Präsenz.

Abschliessend möchte ich Prof. *Dähne* für die Übernahme des Vorsitzes und Prof. *Schöll* für die Begutachtung meiner Arbeit unter schwierigen terminlichen Voraussetzungen danken.